Photoreaction dynamics of functional photoreceptor proteins

Hontani, Y.

2018

document version
Publisher's PDF, also known as Version of record

VRIJE UNIVERSITEIT

Photoreaction dynamics of functional photoreceptor proteins

ACADEMISCH PROEFSCHRIFT

ter verkrijging van de graad Doctor of Philosophy
aan de Vrije Universiteit Amsterdam,
op gezag van de rector magnificus
prof.dr. V. Subramaniam,
in het openbaar te verdedigen
ten overstaan van de promotiecommissie
van de Faculteit der Bètawetenschappen
op woensdag 4 juli 2018 om 13.45 uur
in de aula van de universiteit,
De Boelelaan 1105

door
Yusaku Hontani
geboren te Osaka, Japan

promotor: prof.dr. J.T.M. Kennis

This thesis was approved by the following reviewing committee:

Prof. Dr. Marie Louise Groot	Vrije Universiteit Amsterdam, The Netherlands
Prof. Dr. Klaas J. Hellingwerf	Universiteit van Amsterdam, The Netherlands
Prof. Dr. Peter Hildebrandt	Technische Universität Berlin, Germany
Prof. Dr. Janne Ihalainen	University of Jyväskylä, Finland
Prof. Dr. Josef Wachtveitl	Goethe-Universität, Germany

ISBN: 978-94-6295-980-4

Cover design by Haruka Watanabe

Printed by ProefschriftMaken || www.proefschriftmaken.nl

Contents

Chapter 1

Introduction

1.1. Photoreceptor proteins

Proteins are fundamental in all living organisms for their life activities: *e.g.* energy generation, recognition, reaction to environment, and metabolism. For example in humans, more than 20,000 different kinds of proteins exist, functioning as structural proteins, enzymes, transporter proteins, defensive proteins, regulatory proteins and so on[1]. Proteins are composed of hundreds of amino acids and form a specific three-dimensional (3D) structure (the size is typically a few nanometers, **Fig. 1.1**), which is governed by non-covalent interactions such as hydrogen bonds, ionic bonds, van der Waals forces and hydrophobic effects. 3D structures are crucial for their function, and atomic-scale characterization of proteins is highly required to understand their function and utilization for medical and scientific applications.

Photoreceptor proteins are indispensable for utilization of the light to interpret the surrounding environment and fuel activities of organisms (**Fig. 1.2**). For instance, animals utilize photoreceptor proteins for the visual reception and keeping circadian rhythm. Some organisms, including microbes and insects, show phototaxis to move towards or away from the light. In addition, plants have photoreceptor proteins that are involved in photosynthesis for generating carbohydrates, and also in phototropism and shade avoidance that are necessary to make the most of the sun light for efficient photosynthesis. Molecular functions

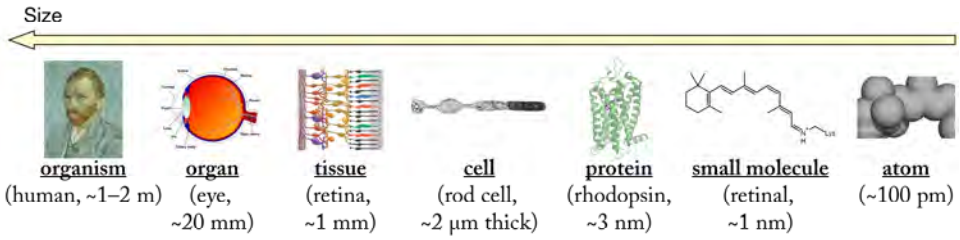

Figure 1.1.The size of proteins and cells[1-4]. Most biological functions of organs (*e.g.* the eye) are dependent on protein reactions (*e.g.* rhodopsin), whose size is typically a few nanometers. Photoreceptor proteins incorporate a small molecule called a chromophore (*e.g.* retinal), and the atomic-scale reaction triggered by a photon plays key roles for the function of cells and organs.

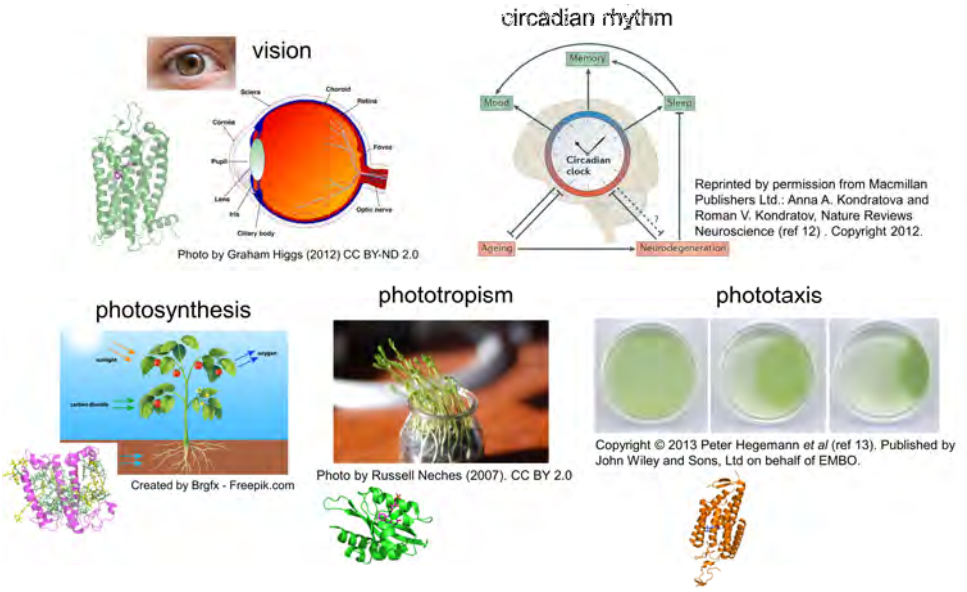

Figure 1.2. Examples of photoreceptor proteins in nature. Photoreceptor proteins are utilized in a wide domains of organisms, *e.g.* for vision, circadian rhythm[12], photosynthesis, phototropism and phototaxis[13]. Photoreceptor proteins may have various functions and utilize a wide range of wavelengths of light (PDB ID: 1F88[4], 1RWT[14], 2V0U[15], and 3UG9[16]).

of photoreceptor proteins are diverse: *e.g.* working as light-driven ion transporters[5-8], enzymes[8-10], and signal transducers[11].

Photoreceptor proteins are equipped with light-absorbing pigments called chromophores (**Fig. 1.3**). Several common chromophores may be incorporated in photoreceptor proteins: *e.g.* retinal, flavin, bilin, carotenoids and chlorophylls[17], and each chromophore has a specific wavelength range for light absorption[17,18] (**Fig. 1.4**). For example, flavin typically absorbs blue[9,19], and bilin absorbs a wide range of light from blue to far-

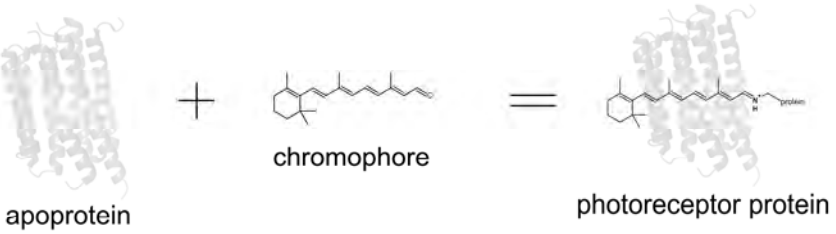

Figure 1.3. Chromophore and photoreceptor protein. Photoreceptor proteins covalently or non-covalently bind a chromophore, which absorbs near-UV, visible or near-infrared light.

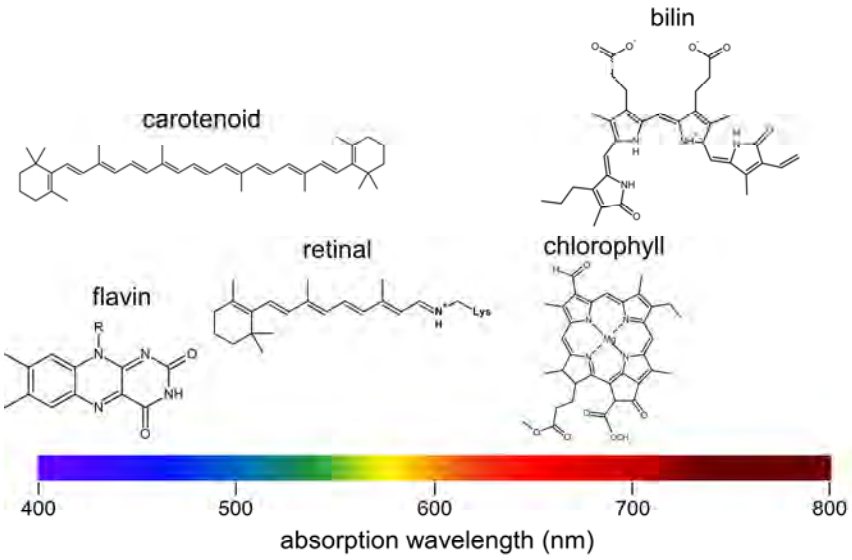

Figure 1.4. Absorption wavelengths of a variety of chromophores.

red[10,20,21]. The absorption wavelength is determined by the delocalization of π-electrons on the conjugated system. A chromophore binding pocket of the protein influences the distortion, covalent/non-covalent bindings, and electrostatic interaction of the chromophore. Hence, absorption maxima of a chromophore are tuned by the environment of the chromophore in the protein. The diverse functions and absorption energy of photoreceptor proteins are powerful not only for the utilization of light in organisms, but also for applications of these proteins in life sciences. In addition, significantly, photoreceptor proteins are suitable model systems to study structural dynamics of proteins because they can be triggered with light, ensuring spatiotemporally precise activation.

1.2. Application of photoreceptor proteins—optogenetics and fluorescent imaging—

In life science research, photoreceptor proteins are effectively employed in order to observe and manipulate molecular and cellular activities (**Fig. 1.5**). Genetically encoded fluorescent proteins enable real-time visualization of specific proteins, cells and tissues (fluorescence imaging), which is an essential technique in molecular and cellular biology[22-25]. Furthermore, several photoreceptor proteins are used for optogenetics, which is an essential tool in neuroscience, enabling manipulation of neural and regulation of protein activities with high

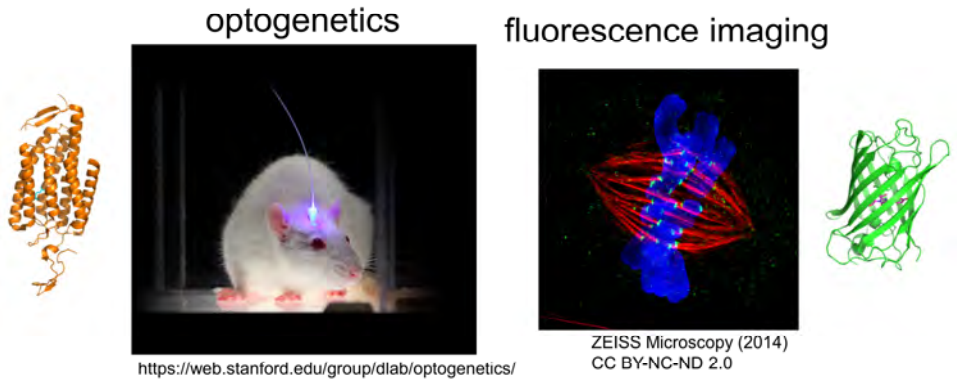

Figure 1.5. Application of photoreceptor proteins to optogenetics and fluorescent imaging. Genetically-encoded photoreceptor proteins are used for stimulating and silencing neural activities (optogenetics, left, PDB ID: 3UG9[16]), and for monitoring molecular and cellular activities (fluorescence imaging, right, PDB ID: 1EMA[33]).

spatiotemporal precision[9,26-29]. For instance, light-driven ion transporters are widely used to activate and silence signaling of specific neurons[27,30]. Moreover, photo-induced activation of enzymes is enabled, which has been a fundamental tool for molecular biologists[31,32].

Designing further functional optogenetic proteins is highly desired: *e.g.* for tuning action wavelength[34], converting functions[35], improving its quantum efficiency[36] and modifying its activation/deactivation rates[37]. For rational design of practical optogenetic tools based on currently-used proteins, clarification of their photoreactions will be substantially helpful.

1.3. Photoreactions of photoreceptor proteins

The chromophore dynamics is essential for efficient light energy utilization. Upon chromophore excitation with light, its electronically excited state is populated. On the decay from the excited state to a photoproduct state, the excess energy is used for photoisomerization, charge transfer, energy transfer, and/or bond formation which trigger a series of conformational changes of the protein that result in its activation of the protein. Competitively, chromophores may relax to the initial ground state radiatively (fluorescence) and/or non-radiatively (internal conversion). The lifetime of the excited state typically ranges from femtoseconds (10^{-15} s) to nanoseconds (10^{-9} s). After photoproduct formation, the chromophore and the protein undergo thermal structural changes in the ns-ms timescale,

and its protein function is activated. Afterwards, deactivation of the protein proceeds, returning back to the initial ground state. The series of structural and spectroscopic transitions after photon absorption and its return to its initial resting state is called a photocycle (**Fig. 1.6**).

Clarification of the molecular dynamics of the chromophore during the photocycle is highly important for understanding the activation and deactivation mechanisms of photoreceptor proteins. Since the time range of the photocycle lies from femtoseconds to seconds, minutes or hours, investigation of the photochemistry of a wide time range is required. Femtosecond temporal resolution is achieved through spectroscopy with femtosecond pulsed lasers; furthermore, a pair of electronically coupled femtosecond laser systems makes it possible to achieve a wide temporal range from femto- to milliseconds, which is a powerful way to investigate comprehensive photoreactions of photoreceptor proteins[38-46]. In this thesis, time-resolved electronic and vibrational spectroscopies are mainly applied, which give information of electronic states and bond structures of chromophores during its photoreaction, respectively.

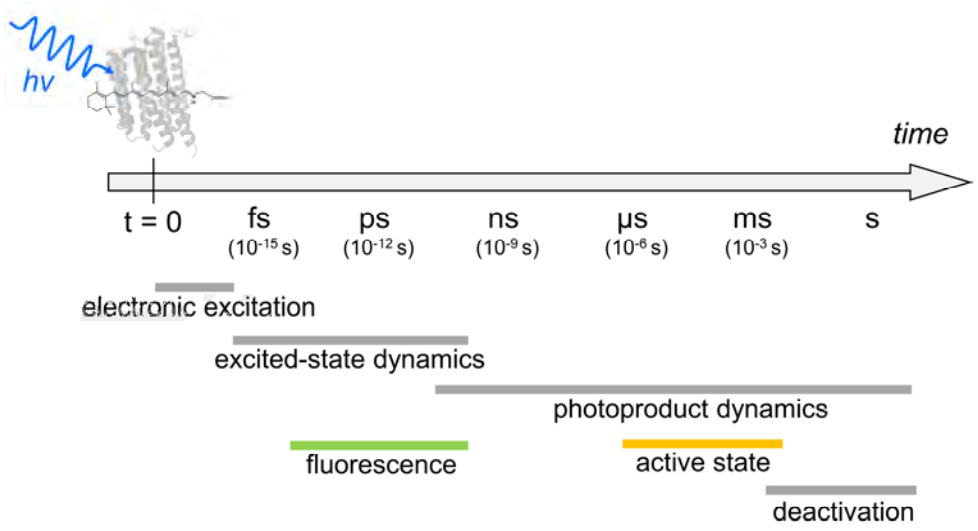

Figure 1.6. A scheme of a series of reactions of photoreceptor proteins: an example of microbial rhodopsins. Excited-state dynamics proceed on the fs–ps time range, accompanied with partial relaxation with fluorescence emission. Photoproduct dynamics is involved in a wide time range, from picoseconds to milliseconds/seconds. Protein functions are typically activated in micro- to milliseconds, and deactivation occurs in milliseconds/seconds/minutes.

1.4. Photoreceptor proteins studied in this thesis

In this section, photoreceptor proteins studied in this thesis are introduced (**Fig. 1.7**). Microbial rhodopsins having a retinal chromophore, near-infrared fluorescent proteins having a biliverdin chromophore, a blue-light using FAD (BLUF) domain having an FAD chromophore, and a high-light inducible protein with carotenoid and chlorophyll chromophores are studied by time-resolved spectroscopy.

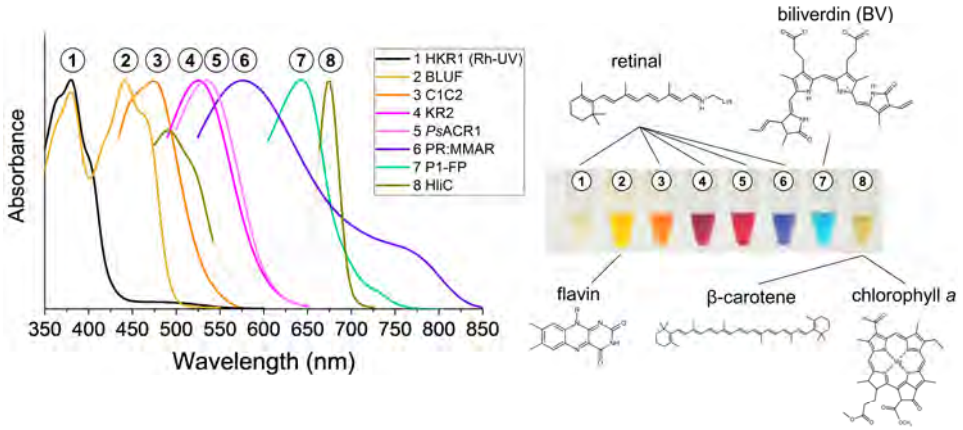

Figure 1.7. Photoreceptor proteins studied in this thesis with light-absorbing chromophores indicated. Steady-state absorption spectra of each photoreceptor proteins are shown (left panel). Colors of solubilized photoreceptor proteins and contained chromophores (right). The numbers correspond to those in the left panel.

1.4.1. Microbial rhodopsins

Rhodopsin proteins are one of the most common photoreceptors in various organisms. Animals utilize rhodopsins for visual and non-visual light sensing (animal rhodopsin), while microbes use rhodopsins as energy transducers and photosensors (microbial rhodopsins)[7,47]. Even though there is almost no sequence similarity between animal and microbial rhodopsins, both of them have seven transmembrane α-helices (TM1–TM7) and are composed of a (apo)protein called opsin , and chromophore called retinal **(Fig. 1.8a)**; it is considered that they arose through convergent evolution[48,49]. The retinal chromophore is covalently bound to a Lys residue on TM7, forming a retinal Schiff base (RSB) (**Fig. 1.8b**). When the RSB is deprotonated, the retinal absorbs near-UV light. Most rhodopsin proteins have a protonated RSB in the dark state, which delocalizes the π-conjugated system, thus achieving lower-energy light absorption (*i.e.* visible light absorption). The protonated RSB is stabilized by a counterion, *e.g.* an acidic amino acid residue (Glu and Asp) and sometimes a

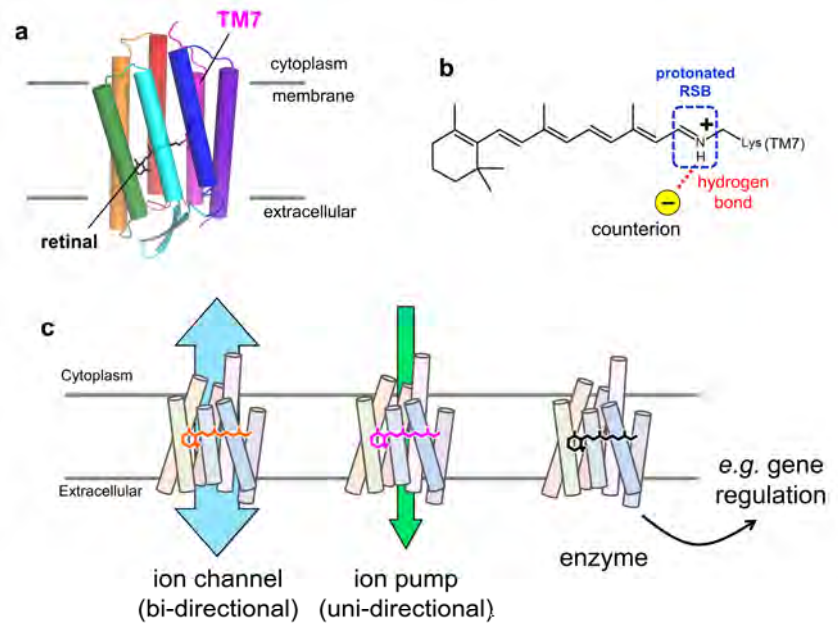

Figure 1.8. Retinal and microbial rhodopsins. (**a**) 3D structure of bacteriorhodopsin (PDB ID: 1QHJ[51]), a model system of microbial rhodopsins. Microbial rhodopsins are composed of seven transmembrane α-helices (TM1–TM7) and a retinal chromophore, which covalently binds to a Lys residue on TM7. (**b**) all-*trans* retinal bound to the protein, forming a protonated retinal Schiff base (RSB). A counterion stabilizes the protonated RSB. (**c**) Various light-driven functions of microbial rhodopsins: *e.g.* ion channels, ion pumps and enzymes.

water molecule, near the protonated RSB. The absorption energy is also affected by distortion of the polyene chain of the retinal and electrostatic interaction of the retinal in the binding pocket. Microbial rhodopsins function as light-driven ion transporters, light-driven enzymes, and photosensors[7]. Particularly, ion-transporting and enzyme microbial rhodopsins (**Fig. 1.8c**) are of great interest in optogenetics[27,50], which is an essential tool in neuroscience and molecular biology.

Ion transporting microbial rhodopsins, which are categorized into ion channels and ion pumps, are widely used in optogenetics to activate or silence neural activities. Ion channel microbial rhodopsins such as cation channelrhodopsins[52,53] (CCRs) and anion channelrhodopsins[54-56] (ACRs) transport ions bi-directionally[52-57]. Once the channel-open state is activated during the photocycle, channelrhodopsins transport a large number of ions depending on the ion gradient on the membrane. Because of the large ion flux on

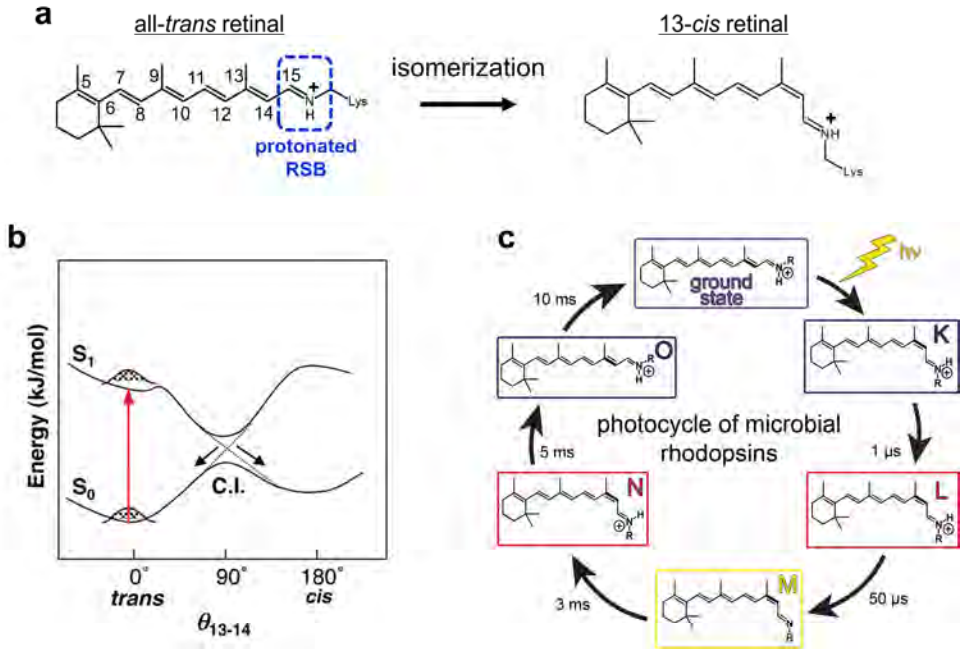

Figure 1.9. Photoreaction of microbial rhodopsins. (**a**) Retinal photoisomerization from all-*trans* to 13-*cis*. (**b**) Suggested excited-state reaction model of microbial rhodopsins. S_0 and S_1 represent the electronical ground and the first excited state, respectively. C.I. stands for conical intersection, and the red arrow shows photoexcitation. (**c**) Suggested photocycle of bacteriorhodopsin. Reprinted with permission from Oliver P. Ernst *et al. Chemical Reviews* (ref 7). Copyright 2014 American Chemical Society.

channelrhodopsins, they are extensively used in optogenetics applications[27,28,50,58]. Ion pump microbial rhodopsins such as H^+ pump[59-61], Na^+ pump[62] and Cl^- pump[63] transport ions unidirectionally. In general, only one ion is transported for one photocycle in ion pump microbial rhodopsins. Several light-active gene regulators belonging to the microbial rhodopsin family have been reported such as rhodopsin-guanylyl cyclase (RhGC[64]) and histidine kinase rhodopsin (HKR[65]), which are of interest for potential optogenetic application.

In most microbial rhodopsins, the first structural change after light absorption is all-*trans* to 13-*cis* isomerization of protonated retinal, which takes place in the time range of femtoseconds/picoseconds, in which the electronic excited state is involved (**Fig. 1.9**). The S_0–S_1 excitation occurs upon photon absorption, and the wave packet is propagated on the excited state. Retinal isomerization proceeds with relaxation via a conical intersection

between S_1 and S_0, forming the first ground-state photoproduct having 13-*cis* retinal. Notably, the excited-state dynamics is decisive for the isomerization quantum yield. In the photoproduct states, several structural changes proceed on the activation/deactivation process of the protein (**Fig. 1.9c**). The first photoproduct after the photoisomerization is named as the J intermediate, which is the vibrationally hot state of the primary 13-*cis* photoproduct. With vibrational relaxation of J in picoseconds, the K intermediate is formed. An L intermediate is considered as a distorted form of protonated retinal, and deprotonation of the retinal occurs in microseconds, resulting in formation of an M intermediate. In μs-s, reprotonation of the retinal (N intermediate) and thermal isomerization to all-*trans* (O intermediate) occur, ending up in the initial ground state. The photocycle of retinal is highly important for the function of the protein such as ion transportation. For instance in Na^+ pump rhodopsin KR2, it is reported that Na^+ intake occurs as a result of M-intermediate formation, and reprotonation (O intermediate) is significant for the one-way ion transport[66].

Elucidation of the structural dynamics during the photoreaction process is essential to understand the photochemistry. The photoreaction takes place in the wide time range from femtoseconds to seconds, and overall observation is necessary for deeper understanding of the photoreactions. In **Chapters 2–6**, the photochemistry of recently found/engineered microbial rhodopsins (cation channelrhodopsin C1C2, anion channelrhodopsin *Ps*ACR1, Na^+ rhodopsin KR2, proton pump PR with retinal analogues, and histidine kinase rhodopsin HKR1) will be studied, utilizing fs–ms time-resolved transient absorption and stimulated Raman spectroscopies.

1.4.2. Near-infrared fluorescent proteins (NIR FPs)

Fluorescence imaging is essential in life science. Green fluorescent protein (GFP)[67], and its relative species[68,69] are genetically encoded in living tissues and used for biological imaging to visualize protein expression levels and particular molecular interactions *in vitro* and *in vivo*[22-24]. Expanding the spectral palette of fluorescent proteins is highly desired for multi-color imaging[24,70], multi-photon imaging[71,72] and FRET imaging[73]. Especially, near-infrared active and emissive fluorescent proteins are in great demand for deep-tissue *in vivo* imaging because an optical transparency window of mammalian tissues ranges in the near-infrared (NIR) region, 650–900 nm, where water, hemoglobin and melanin absorption are small[74,75] (**Fig. 1.10a**). However, due to the limitation of the extent of the conjugated π-electron system, the absorption in engineered GFP-like proteins is limited at around 610 nm[76,77] and fluorescence emission at around 675 nm[78].

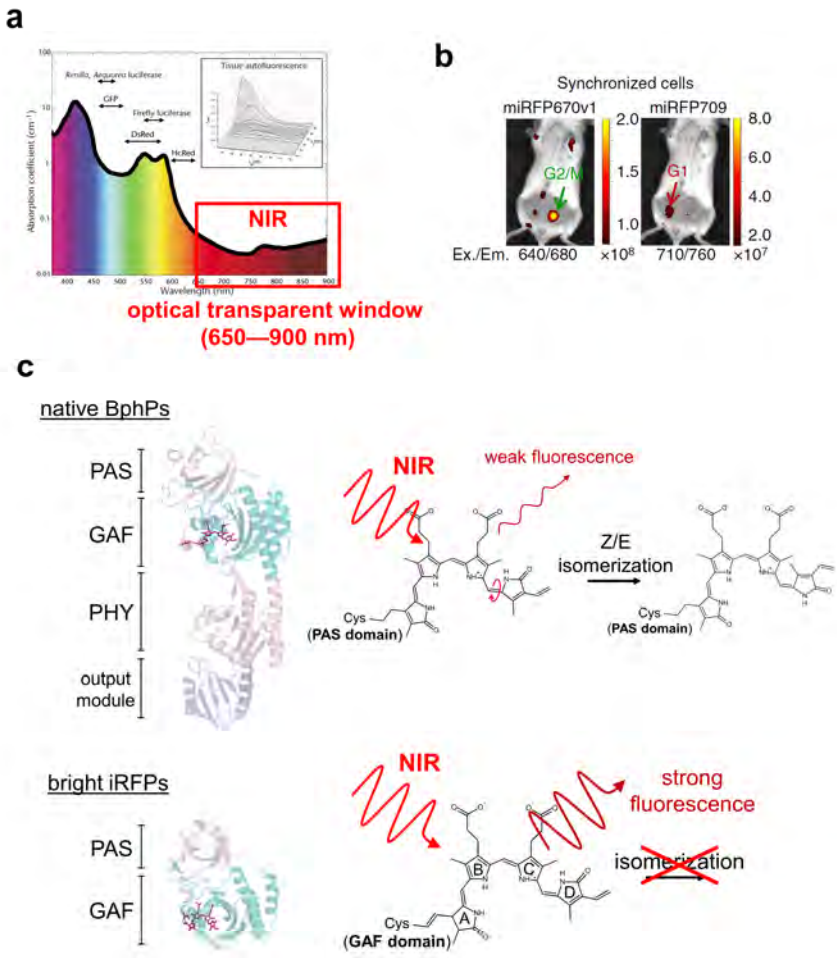

Figure 1.10. Near-infrared fluorescent proteins (NIR FPs)based on bacterial phytochromes. (**a**) Optical transparent window of biological tissues[75]. Reprinted by permission from Macmillan Publishers Ltd.: Ralph Weissleder and Vasilis Ntziachristos, *Nature Methods* (ref 75). Copyright 2003. (**b**) *In vivo* deep-tissue application of NIR FPs[79]. Representative images of mice with implanted cells expressing the NIR cell cycle reporter. The cells in G2/M and G1 phases were injected in the left and right sides of the mouse, respectively. The color bars indicate the total fluorescence radiant efficiency (photons s^{-1} cm^{-2} steradian^{-1} per $mWcm^{-2}$)[79]. (**c**) Comparison of native bacteriophytochromes (BphPs) and bright iRFPs (*e.g.* iRFP670[80], iRFP682[80], and BphP1-FP[81]). Native BphPs have the PAS, GAF and PHY domains in addition to the output module, and form a covalent bond between BV and Cys in the PAS domain (top, PDB ID: 5AKP[82]). Bright iRFPs have only PAS and GAF domains, and covalently bind BV with Cys in the GAF domain (bottom, PDB ID: 4XTQ[81]).

Recently, bright near-infrared fluorescent proteins (NIR FPs) called iRFPs have been engineered[25,79,80,83,84] based on far-red absorbing bacteriophytochromes (BphPs)[10,85,86] (**Fig. 1.10b**). BphPs are photochromic photoreceptors composed of PAS, GAF, and PHY domains in addition to the output module, and have two (meta)stable states: red absorbing (P_r) and far-red absorbing (P_{fr}) states[10,85,87]. In BphPs, a biliverdin (BV) chromophore is covalently bound to Cys in the PAS domain, and *Z*/*E* isomerization at the C15=C16 double bond occurs upon NIR (~700 nm) absorption, which triggers the photoconversion between the P_r and P_{fr} states. As a competing process of isomerization, weak fluorescence (Φ_{FL}~1–4%) in the NIR range (~720 nm) is observed[88,89]. In iRFPs, the photoisomerization is successfully prevented with induction of point mutations, and the protein size is reduced by truncation of the PHY domain and the output module (**Fig. 1.10c**)[80,81,83,84]. In some variants of iRFPs (*e.g.* iRFP670 and 682[80]), a Cys residue is introduced in the GAF domain in addition to the intrinsic Cys in the PAS domain[79-81], in which BV can form a covalent bond to the PAS and GAF domain, and also non-covalent bond to the protein. It is reported that iRFPs with BV bound to Cys in the GAF domain show blue-shifted absorption/emission features, and also bright (Φ_{FL}~15% at the maximum[79,81,84]) NIR fluorescence. It is expected that the BV binding state influences the excited-state dynamics, resulting in significant effects in the fluorescence quantum yield, but the photophysics of blue-shifted bright NIR FPs is unclear. In **Chapter 7**, ultrafast excited-state reaction dynamics of iRFPs, in which BV forms a covalent bond to the PAS/GAF domain or a non-covalent bond, will be discussed with time-resolved absorption and fluorescence spectroscopies.

1.4.3. BLUF photoreceptor

Blue-light using flavin (BLUF) photoreceptors are blue-light sensing proteins having a flavin adenine dinucleotide (FAD) as a chromophore, found mainly in prokaryotes but also in eukaryotic microbes[19,90]. Physiological functions of BLUF photoreceptors are diverse; photosynthetic gene regulation[91,92], phototaxis[93] and enzymes[94,95], and also are of great interest in optogenetics[95,96]. Upon irradiation with blue-light of the dark-adapted (DA) state of a BLUF photoreceptor, structural changes of the protein are induced[97-99], turning it into the light-adapted (LA) state in which its function is activated (**Fig. 1.11**), leading to a red-shifted FAD absorption by 10–15 nm[97,100]. A hydrogen-bond rearrangement between FAD and conserved Tyr and Gln residues underlies formation of the LA state, and is brought about by sequential photoinduced electron and proton transfer between FAD, Tyr and Gln, followed by radical pair recombination[101,102]. The LA state undergoes thermal recovery to the

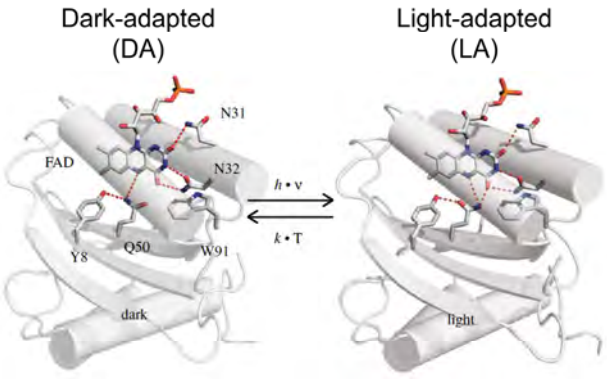

Figure 1.11. Dark- and light-adapted states of BLUF domain[19].

DA state in seconds to minutes. Since the FAD plays crucial roles on the activation/deactivation of the protein, understanding the static state chemical and the reaction dynamics of FAD is essential to understand the photoreaction of BLUF domains.

The hydrogen-bond network near the FAD with adjacent residues plays key roles in the photochemical reactions. Although many studies with X-ray crystallography[103-106], NMR[107-110], FT-IR[111-113], computational calculations[111,114-116] and time-resolved spectroscopies[97,100,101,117-119] have been performed, the hydrogen-bond patterns that connect FAD with the protein are still controversial. In **Chapter 8**, the excited-state dynamics and the hydrogen-bond network of FAD in a BLUF photoreceptor will be examined by transient stimulated Raman spectroscopy combined with band assignments with quantum chemical calculations.

1.4.4. HliC protein

Photosynthetic organisms utilize sunlight for energy production, using chlorophylls (Chls) and carotenoids as light-absorbing chromophores. Photon energy absorbed by the light-harvesting antenna composed of Chls and carotenoids is transferred to the photosynthetic reaction center where photochemical conversion takes place. In high light conditions, the energy transfer from singled excited-state Chl (^{1}Chl*) of the light-harvesting antenna to the reaction center is saturated because the dark reactions of photosynthesis are much slower than the light reactions in high light. As a result, ^{1}Chl* is interconverted to triplet excited-state Chl (^{3}Chl*). In aerobic conditions, reaction of ^{3}Chl* with oxygen results in generation of singlet oxygen ($^1O_2$) that causes severe oxidative damage to the organism

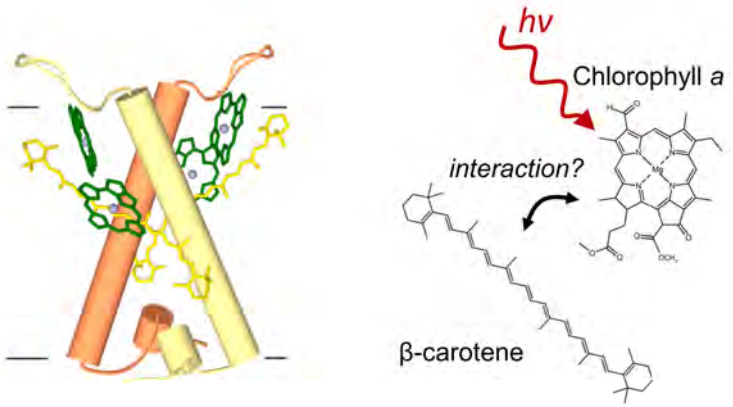

Figure 1.12. A structural model of HliC protein and carotenoid–chlorophyll interaction.

(photodamage)[120]. To prevent photodamage, photosynthetic organisms have evolved mechanisms to deplete ^{1}Chl* quickly (photoprotection). It is known that in LHCII, the major light harvesting complex of plants, Chls and carotenoids play a significant role in photoprotection, and the molecular mechanism has been controversially discussed: *e.g.* energy transfer[121-125], electron transfer[126-128], excitonic coupling[129,130], and Chl-Chl charge transfer[131].

HliC is a family of high-light inducible proteins (Hlips), which are found in cyanobacteria and ancestral to plant-like light-harvesting complexes (LHCs). HliC forms an oligomer, and bind 4 Chl *a* and 2 β-carotenes per a putative dimer[122,132] (**Fig. 1.12**). Since HliC is a much simpler system than plant LHCs and shows strong quenching of ^{1}Chl*, it is suitable for investigation of the photoprotection mechanisms. Making the most of femtosecond transient absorption and stimulated Raman spectroscopies, the Chl-carotenoid interaction on the photoprotection of HliC will be investigated (**Chapter 9**).

1.5. Time-resolved spectroscopy

To study photochemical dynamics of the photoreceptor proteins, time-resolved spectroscopies are used. In this section, transient absorption spectroscopy (TAS), transient stimulated Raman spectroscopy (TSRS) and time-resolved fluorescence spectroscopy are introduced. All time-resolved experiments were performed at room temperature.

1.5.1. fs-ms transient absorption spectroscopy (TAS)

Transient absorption spectroscopy (TAS), or pump-probe spectroscopy[124], is a technique to trace absorption spectral transitions in the excited states and photoproduct states. For TAS, two femtosecond laser pulses are used; a 'pump' pulse and a 'probe' pulse (**Fig. 1.13**). A pump pulse is irradiated to a sample and triggers its photoreaction, whereas a probe pulse passes though the sample and is projected on a detector with a certain time delay with respect to the pump pulse. The time delay from femtoseconds to nanoseconds is generated by an optical delay stage, which is composed of a translation stage and a pair of mirrors or a retroreflector. An optical chopper is often used in the pump line to modulate the pump pulse frequency; *e.g.* producing a 500 Hz pump and 1 kHz probe. The phase modulation enables sequential detection of probe lights with and without pump-light irradiation. For each time delay, the transient absorption signal (ΔOD) is calculated as:

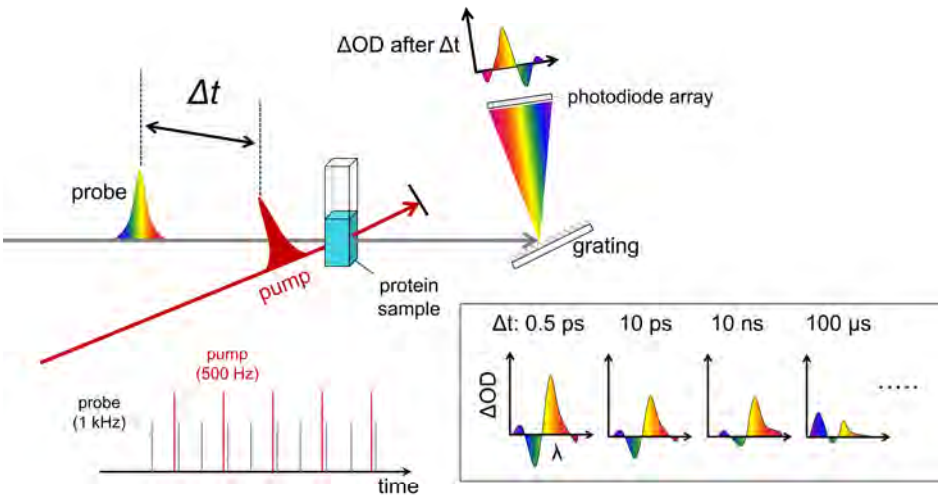

Figure. 1.13. Transient absorption spectroscopy (TAS). Two pulses are irradiated to a protein sample: pump and probe pulses. By varying the time delay (Δt) between the pump and probe pulses, transient absorption spectra are obtained.

$$\Delta OD = \log_{10} \frac{I_{unpumped} - I_{dark}}{I_{pumped} - I_{dark}} \qquad (2.1)$$

where I_{pumped} and $I_{unpumped}$ represents detected probe light signal intensities with and without the pump pulse, respectively, and I_{dark} indicates dark intensity without pump and probe lights. To achieve the desired S/N ratio, pump-probe signals at each delay time are accumulated typically for a few seconds. To generate a time delay between nanoseconds and milliseconds, an electronic delay is used, with a pair of electronically synchronized Ti:Sapphire amplifiers (1 kHz) sharing the same Ti:Sapphire oscillator (80 MHz)[133]. A seed pulse generated from the 80-MHz Ti:Sapphire oscillator is split to two lines, pump and probe, and amplified separately by each amplifier. The time gap between successive pulses from the oscillator is 12.5 ns at 80 MHz operation, and a synchronization and delay generator (SDG) selects which seed pulse is used for the pump-pulse amplification. When the pump pulse is amplified using the same seed pulse as the probe amplification, Δt is zero. When the seed

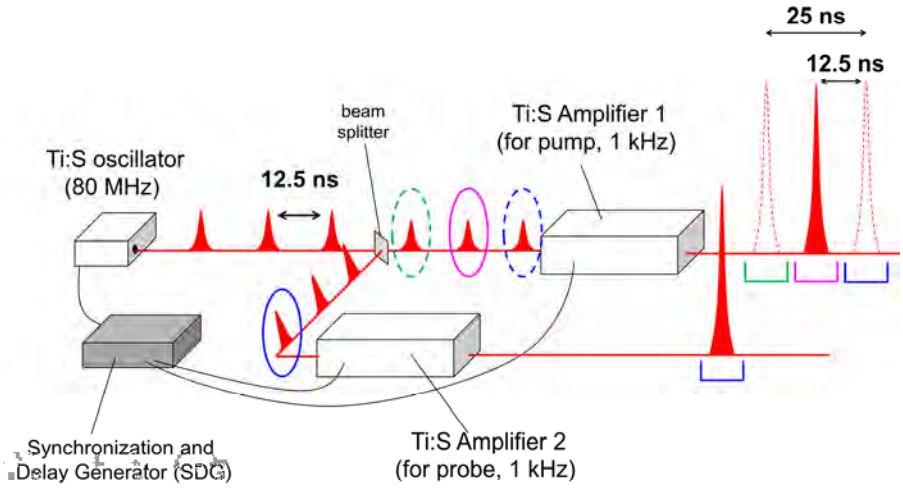

Figure. 1.14. Electronic delay generation. The two Ti:Sapphire amplifiers (1 kHz, output pulse every 1 ms) use seed pulses from the same Ti:Sapphire oscillator (80 MHz, seed pulse every 12.5 ns), and they are electronically synchronized by a synchronization and delay generator (SDG). The two amplifiers choose a specific seed pulse to amplify, which is electronically controlled by SDG and Pockels cells in the amplifiers. When both of the amplifiers choose the same seed pulse (blue circle in the figure), no electronic delay between the two output pulses is generated. When amplifier 1 selects the seed pulse one behind (magenta circle in the figure) with respect to the seed input to amplifier 2 (blue circle), a 12.5 ns delay is generated between the output pulses from the two amplifiers. In this way, electronic delays can be generated up to submillisecond with a shortest step of 12.5 ns.

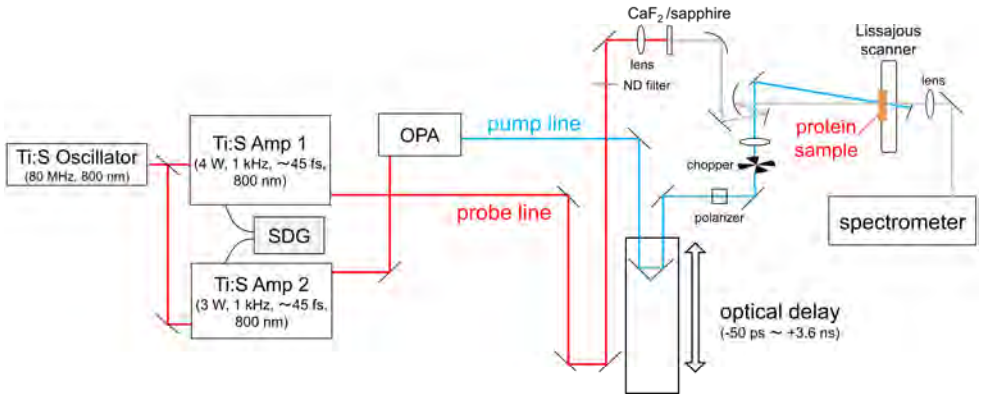

Figure 1.15. Transient absorption spectroscopy (TAS) setup. A pair of electronically synchronized Ti:Sapphire amplifiers (Amp 1 and Amp 2) are used: one for the pump pulses and the other for the probe pulses. The wavelength of the pump pulse is tuned by an optical parametric amplifier (OPA). Supercontinuum white light is generated by focusing 800-nm pulse onto a CaF_2 or sapphire plate and used as probe light. The optical delay generates a time delay up to 3.6 ns, and the electronic delay allows a time delay between 12.5 ns and 0.5 ms.

pulse one after is chosen for pump-pulse amplification, then Δt is 12.5 ns. Like this, Δt up to submillisecond with 12.5 ns steps can be generated (**Fig. 1.14**)[133]. Combination of optical delays and electronic delays enables continuous fs-ms pump-probe spectroscopy.

In **Fig. 1.15**, our fs–ms TAS setup is shown schematically[41,42,133]. A 80 MHz Ti:Sapphire oscillator (Vitesse, Coherent) is used as a seed laser for two 1 kHz Ti:Sapphire amplifiers (Legend and Libra, Coherent). The two amplifiers are electronically synchronized by two SDGs (SDG and SDG Elite, Coherent), and the electronic delay is controlled during experiments. The output powers of Legend and Libra are ~3 mJ and ~4.5 mJ, respectively, with a central wavelength at ~800 nm and pulse duration of ~45 fs for both. A femtosecond pulse from the Legend enters an OPA (OPerA Solo, Coherent) to convert its wavelength for sample excitation (pump pulse). After passing through an optical delay line and a 500 Hz optical chopper, the pump pulse is focused on a sample that is contained in a cuvette or a Lissajous scanner, which ensures sample refreshment after each laser shot with a time interval of 60 seconds between successive exposures to the laser pulses[134]. The pump beam power is attenuated to ~200–500 nJ with a beam diameter of ~200 μm (~0.6–1.6 mJ/cm^2). The number of molecules on the pump-light spot is ~10^{13}, while the number of photons on the spot is ~10^{12}. A femtosecond pulse from Libra is attenuated by a variable neutral density filter and used for supercontinuum generation (probe pulse). The beam

diameter of the probe pulse at the sample position is ~70 μm. The probe pulse passing through the sample cuvette is spectrally dispersed by a grating and detected by a 256-segment photodiode array with shot-to-shot detection. Typically, measurements are repeated for thousands of shots and the signals are averaged to achieve the desired signal-to-noise ratio. Transient absorption signals are processed with MATLAB (MathWorks) software following the eq. (2.1) for each wavelength. The instrument response function (IRF) is sub-100 fs, and so is the temporal resolution, even though the IRF is varied in different experiments. When only fs–ns delay is required, only a single Ti:Sapphire (Libra, Coherent) is used for both of pump and probe pulses, by installing a beam splitter.

In the electronic excited states and photoproduct states, typical transient absorption features are observed (**Fig. 1.16**). Positive ΔA signals are characterized as excited-state absorption (ESA) and/or photoproduct absorption. Negative ΔA signals are assigned as ground-state bleach (GSB) and/or stimulated emission (SE). GSB is seen with the depletion of the population of the initial ground state. SE is seen when the molecules are in the excited state, thus can be used as a marker of the excited-state population.

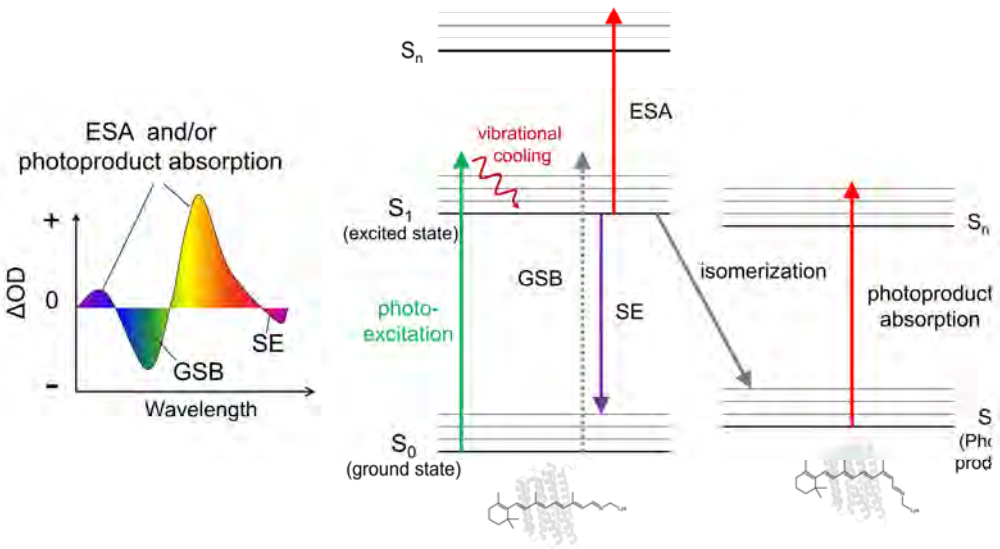

Figure 1.16. Diagram of transient absorption spectroscopy. Positive signals on the ΔOD spectrum show excited-state absorption (ESA) and/or photoproduct absorption. Positive signals on the ΔOD spectrum indicate ground-state bleach (GSB) and/or stimulated emission (SE).

1.5.2. fs-ms transient stimulated Raman spectroscopy (TSRS)

Stimulated Raman spectroscopy is a useful tool to gain molecular structural information from a chromophore specifically[135]. When photons are scattered by a molecule, most photons keep their energy after the scattering (Rayleigh scattering, **Fig. 1.17**). Some photons, however, gain or lose their energy by the scattering (Raman scattering, **Fig. 1.17**). The gain or loss of the energy is equivalent to vibrational energy of the molecule, thus the Raman scattering spectrum gives information on vibrational energy levels of the molecule, which offer direct information of the molecular structure. When two laser pulses with distinct energy; Raman pump (ω_R) and probe (ω_p), are induced to the molecule simultaneously, stimulated Raman amplification (Stokes Raman) is observed if the energy difference of ω_R and ω_p matches a vibrational mode of the molecule (**Fig. 1.17**). When a broad band probe is used, a wide-range Stokes Raman bands are obtained at single stimulated Raman detection event. Since stimulated Raman scattering is much stronger than spontaneous Raman scattering, stimulated Raman spectroscopy is more suitable for high-efficient detection of vibrational modes of molecules.

Femtosecond stimulated Raman spectroscopy (FSRS) combines the femtosecond pump-probe technique with stimulated Raman spectroscopy[135]. As in TAS, an excitation pump pulse (described as 'actinic pump' for differentiation from the Raman pump) is irradiated to the protein sample. After a time delay Δt, two pulses, Raman pump and probe, are focused on the sample simultaneously to detect a stimulated Raman spectrum at Δt (**Fig. 1.18**). The Raman pump is narrowband (~10 cm^{-1}) and of picosecond duration to confer

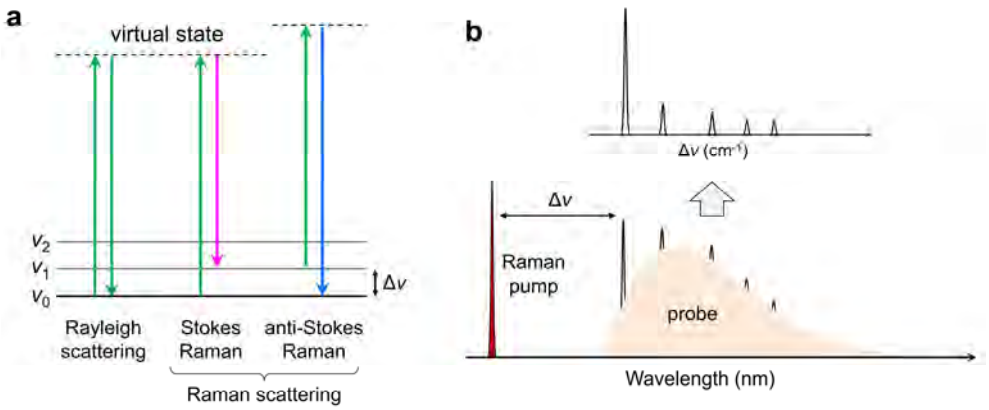

Figure 1.17. Scheme of Raman scattering. (**a**) Rayleigh and Raman scattering. (**b**) Stimulated Raman spectroscopy. The scheme is based on Kukura *et al.*, 2007[135]. Two pulses, Raman pump and probe, are induced simultaneously.

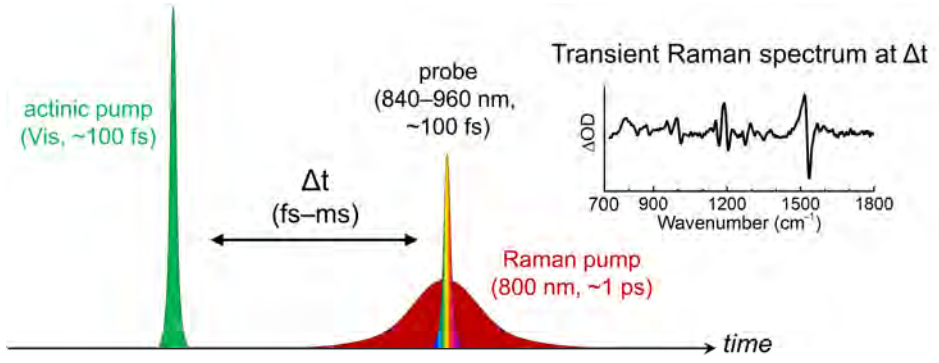

Figure 1.18. A time scheme of TSRS experiments.

spectral resolution to the method, while the probe is broadband and of <100 fs duration to achieve high time resolution. Through the 3rd order nonlinear polarizability of the sample, the probe light is amplified at Raman-active resonances and a stimulated Raman spectrum is obtained[135]. Our time-resolved setup can vary the time delay up to submillisecond, thus particularly we call the time-resolved Raman technique as transient stimulated Raman spectroscopy (TSRS)[41]. TSRS is a powerful technique to quest the molecular dynamics of chromophores in proteins in real time during the whole photocycle, as vibrational spectra give structural information and generally contain more spectral features..

In TSRS, a crucial problem is correction of the baseline which is strongly influenced by pump-probe (*e.g.* excited-state absorption and stimulated-emission), pump-dump-probe and pump-repump-probe signals, and coherent nonresonant signals by mixing of Raman pump and probe fields in the FSRS geometry. Note that in this technique, the baseline typically has amplitude that is an order of magnitude larger than the stimulated Raman signal[136]. Conventionally, a baseline is mostly corrected arbitrarily by eye and with an assumption of higher polynomials[137]. Yet, baseline correction with *ad hoc* estimation often cannot properly discriminate between baseline and genuine signals, and tends to overlook small stimulated Raman signals. Therefore, a more sophisticated way for baseline correction is required especially for detecting small TSRS signals. A useful approach for rational baseline correction is subtraction of signals that are taken with two different Raman pumps[137]. When the Raman pump wavelengths are slightly different, the detected Raman peak positions will be slightly shifted as well, while the intrinsic baseline from such as fluorescence appears at an identical position. Therefore, experiments with two different

Raman pump wavelengths enables baseline correction reasonably[137]. However, the subtraction method has mainly two difficulties in practical use. First, the wavelength gap of the two Raman pumps must be optimized very well. When the wavelength gap is too small, the subtracted signal becomes very weak, and when the gap is too large, the baseline correction cannot be performed properly[137]. Therefore, the experiments have to be repeated for several times with different wavelength gaps. Secondly, the intensities of the two Raman pumps need to be equal, otherwise recovery of signals from the subtracted signals becomes highly difficult.

In our TSRS setup, we use the 'watermarking' method for baseline correction[136]. 14 narrowband Raman pumps (λ~800 nm) with slightly different wavelengths are generated by a home-made pulse shaper in a folded geometry, comprising a compressor grating and a custom-built optical chopper[136] (**Fig. 1.19a**), thus 14 Raman datasets are obtained in which the Raman peaks appear at slightly different spectral positions. Strong Raman signals of the datasets are selected and used to produce a model watermark, which has a pseudorandom waveform (**Fig. 1.19b**). The 14-sequence Raman signals are multiplied by random numbers (n_1, n_2, ..., n_{14}), respectively, and a pseudorandom model watermark is created. Note that the sum of the random numbers is zero, ensuring cancellation of the baseline. **Fig. 1.19c** shows the baseline-canceling process by the watermarking approach. 14 Raman spectra with a certain background are collected, and multiplied by the same random numbers that were used to generate the model watermark. This process forms a watermarked Raman spectrum with a random waveform. The watermarked Raman spectrum is deconvoluted by using the model watermark, giving a baseline-free Raman spectrum. The watermarking process is repeated 2,000 times on the same data with different pseudorandom model watermarks. Details of the method are given in Kloz *et al.* 2016[136].

In **Fig. 1.20**, our TSRS setup is shown. The same Ti:Sapphire oscillator and amplifiers as the TAS setup are used, including the procedure to generate the actinic pump and fs–ms time delays. The process for the actinic pump is the same as the TAS setup. The output from Libra is separated in two beams by a beam splitter, one for Raman pump and one for probe. A pulse shaper composed of a grating and a chopper and an adjustable slit for the watermarking approach is installed in the Raman pump line. Supercontinuum probe light is generated by a sapphire plate, and the probe light is detected by a CCD detector after passing through the sample on the shot-to-shot basis. The Raman pump and probe pulses are overlapped spatiotemporally at the sample position. The Raman spectra are processed with MATLAB software.

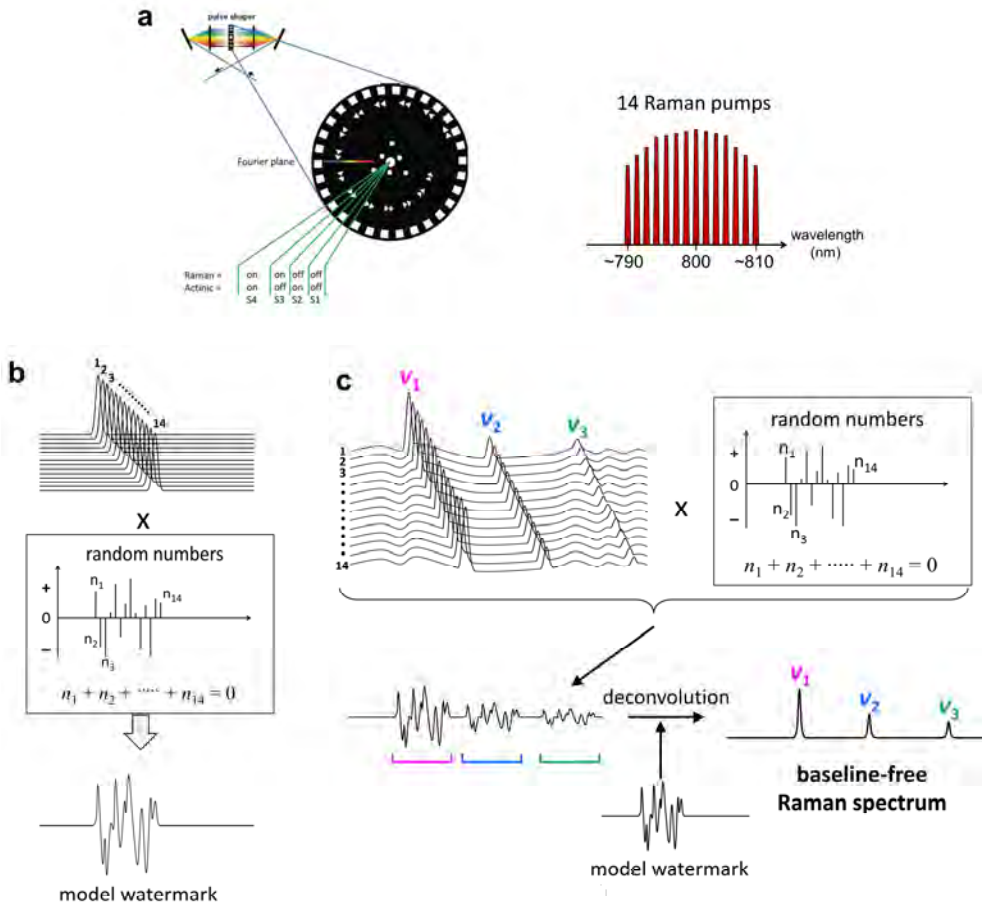

Figure 1.19. Baseline correction with watermarking approach. (**a**) Generation of 14 different Raman pumps with slightly different wavelengths, generated by a homemade optical chopper[136]. (**b,c**) The concept of baseline correction with the watermarking approach. 14 different Raman pumps are multiplied with a random number (n_1, n_2, ..., n_{14}, where $n_1 + n_2 + \ldots + n_{14} = 0$) to generate a model watermark (**b**). (**c**) Raw signals gained with the 14 different Raman pumps are convoluted with the random number, which results in canceling the baseline and giving watermarked signals. By deconvolution with the model watermark signal, a baseline-free Raman spectrum is obtained. The process of (**b**) and (**c**) is iterated for 2,000 times on the same data with different model watermarks to produce reliable datasets.

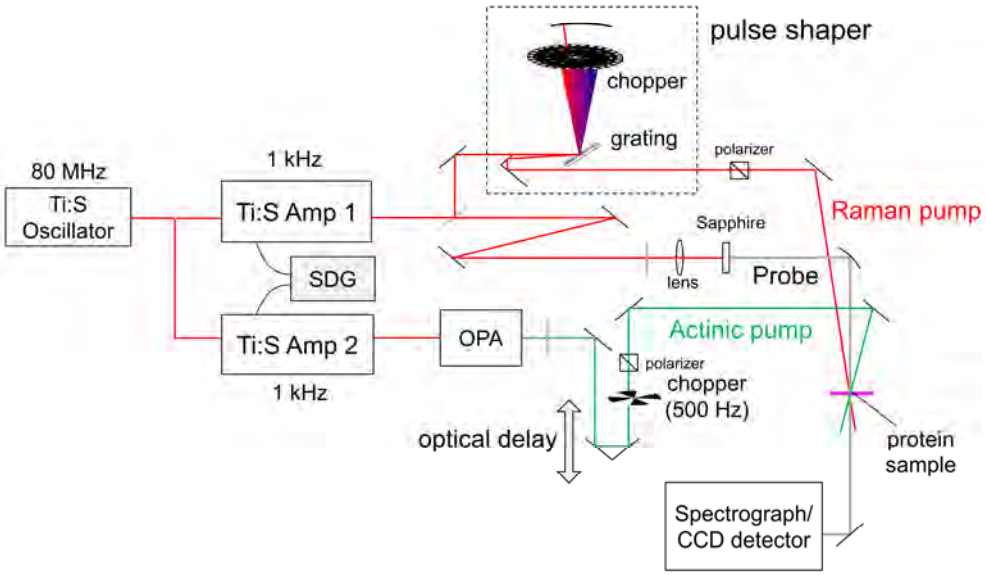

Figure 1.20. Transient stimulated Raman spectroscopy (TSRS) setup. Time delays are generated by the optical and electronical delay as same as TAS. Output from Amp 2 is used for excitation of the protein sample after wavelength conversion by OPA (actinic pump). Output from Amp 1 is split to two beams, Raman pump and probe. The pulse shaper in the Raman pump line is equipped for the watermarking background correction approach. Supercontinuum white light is generated by focusing 800-nm pulse onto a sapphire plate and used as probe light.

1.5.3. ps-ns fluorescence spectroscopy with streak camera

Pico- to nanosecond Time-resolved fluorescence measurements were carried out with a streak camera setup[138,139]. A streak camera is a device to measure ultrafast phenomena like fluorescence in real time (**Fig. 1.21**). In **Fig. 1.22**, our streak camera setup is shown[139]. The output from a femtosecond Ti:Sapphire amplifier (RegA 9000, Coherent) is converted to the desired wavelength by means of an optical parametric amplifier and used as an excitation pulse by focusing it on a sample cuvette. Perpendicularly emitted fluorescence is dispersed by a spectrograph (Chromex 250IS), and enters a streak camera (C5680, Hamamatsu) that is mounted with M5675 Synchroscan sweep unit. A photocathode in the streak camera setup converts the dispersed fluorescent light to photoelectrons, which enter the sweep circuit. In the sweep circuit, the electric field is increased linearly with time: *e.g.* early photoelectrons

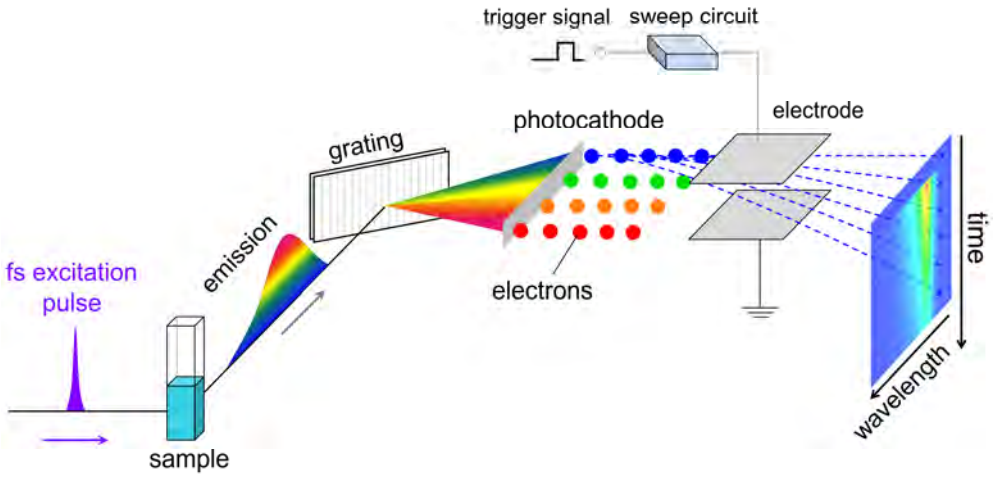

Figure 1.21. The principle of time-resolved fluorescence detection by a streak camera.

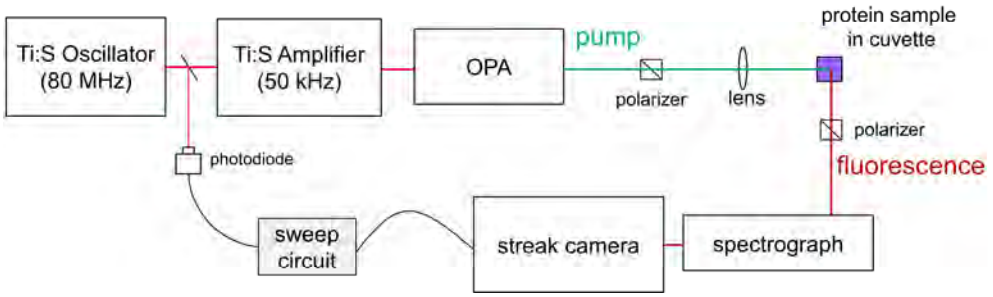

Figure 1.22. Streak camera setup for time-resolved fluorescence experiments.

are less deviated than late ones. The deviated photoelectrons are converted to photons by a phosphor screen and detected by a CCD detector, and three-dimensional signals (in wavelength, time and intensity) are obtained.

1.5.4. Global and target analysis for time-resolved spectra

Time-resolved spectra are obtained in three dimensions: time, wavelength (or wavenumber) and intensity. To fully extract the information about kinetics on the photochemistry from time-resolved spectra, a model-based analysis is necessary. Global analysis is powerful in model-based quantification of time-resolved spectroscopic data[140]. In the most basic form of global analysis, a parallel, sum-of-exponential scheme or a sequential reaction model is considered, and all wavelengths/wavenumbers are analyzed simultaneously with a set of common time constants[140]. Note that the parallel and sequential schemes are mathematically equivalent and yield identical time constants[89]. In a sequential analysis, Evolution-associated difference spectra (EADS) are produced, *i.e.* 1 → 2 → 3 →⋯ in which the arrows indicate successive mono-exponential decays of a time constant, which can be regarded as the lifetime of each EADS (**Fig. 1.23a**). For example the first EADS shows a ΔA spectrum immediately after photoexcitation, and evolves to the second EADS with a time constant τ_1, which in turn evolves to the third EADS with τ_2, and so on. As displayed in **Fig. 1.16**, positive signals

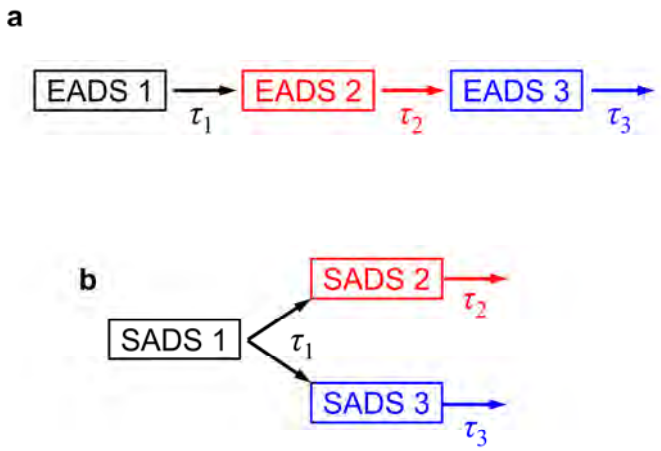

Figure 1.23. Reaction scheme of (a) global analysis and (b) target analysis. (**a**) In global analysis, a sequential model is considered. EADS1 evolves to EADS2 in τ_1, and so on. (**b**) In target analysis, a designated reaction model (a target model) is applied. In the case of panel **b**, SADS1 evolves to SADS2 and SADS3 in τ_1, and SADS2 and SADS3 evolve in τ_2 and τ_3, respectively.

in EADS show excited-state absorption (ESA) and/or photoproduct state, and negative signals in EADS are derived from ground-state bleach (GSB) and/or stimulated emission (SE). Decay-associated difference spectra (DADS) indicate the spectral change with parallel decay channels having the same time constants as EADS. When the DADS are positive and negative, the ΔA signal decreases and increased, respectively, with the time constant.

In some photoreactions of photoreceptor proteins, reaction branching exists or multi-exponential processes feed into the photoproduct generation process in which a simple sequential model is not sufficient for an adequate description in terms of physically distinct states. In target analysis, the data are described with a specific kinetic scheme (a target model), hence multiphasic decay and particular branching reactions can be taken into account to obtain the difference spectra of the pure molecular species involved in the reaction[140] (**Fig. 1.23b**). The difference spectra in the target analysis are called species-associated difference spectra (SADS)[140].

1.6. Scope of this thesis

In this thesis, new insights on reaction dynamics of various photoreceptor proteins are investigated utilizing fs–ms transient absorption spectroscopy (TAS), fs–ms transient stimulated Raman spectroscopy (TSRS) spectroscopy and ps–ns time-resolved fluorescence spectroscopy.

In **Chapter 2**, cation channelrhodopsin C1C2 is studied with TAS and multi-pulse spectroscopy combined with quantum mechanical calculations and target analysis.

In **Chapter 3**, anion channelrhodopsin *Ps*ACR1 is investigated with TAS.

In **Chapter 4**, a TSRS study on the light-driven Na^+ pump rhodopsin KR2 is described.

In **Chapter 5**, a near-infrared active H^+ pump proteorhodopsin is examined by TAS, stimulated Raman spectroscopy, and fluorescence spectroscopy.

In **Chapter 6**, unique excited-state dynamics of UV-absorbing histidine kinase rhodopsin HKR1 is reported with TSRS.

In **Chapter 7**, the photophysics of near-infrared fluorescent proteins is studied utilizing TAS and time-resolved fluorescence spectroscopy.

In **Chapter 8**, a BLUF domain photoreceptor is investigated with TSRS and quantum-chemical calculations.

In **Chapter 9**, the photoprotection mechanism of an LHC-like protein is studied with TSRS.

Chapter 2

Reaction dynamics of cation channelrhodopsin C1C2

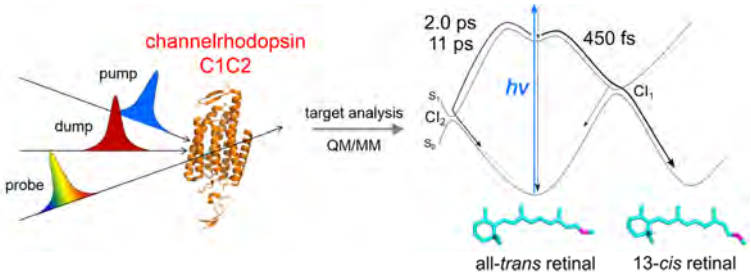

The excited-state reaction dynamics of the key optogenetic actuator channelrhodopsin was revealed by pump-dump-probe spectroscopy, QM/MM calculation and target analysis. Moreover, fs-s photocycle was investigated by transient absorption experiments.

Abstract

Channelrhodopsin (ChR) is a key protein of the optogenetic toolkit. C1C2, a functional chimeric protein of *Chlamydomonas reinhardtii* ChR1 and ChR2, is the only ChR whose crystal structure has been solved, and thus uniquely suitable for structure-based analysis. We report C1C2 photoreaction dynamics with ultrafast transient absorption and multi-pulse spectroscopy combined with target analysis and structure-based hybrid quantum mechanics/molecular mechanics calculations. Two relaxation pathways exist on the excited (S_1) state through two conical intersections CI_1 and CI_2, that are reached via clockwise and counter-clockwise rotations: (i) the C13=C14 isomerization path with 450 fs via CI_1 and (ii) a relaxation path to the initial ground state with 2.0 ps and 11 ps via CI_2, depending on the hydrogen-bonding network, hence indicating active-site structural heterogeneity. The presence of the additional conical intersection CI_2 rationalizes the relatively low quantum yield of photoisomerization (30±3%), reported here. Furthermore, we show the photoreaction dynamics from picoseconds to seconds, characterizing the complete photocycle of C1C2.

This chapter is based on the following publication:
Scientific Reports **7**, 7217 (2017),
collaborated with K. Stehfest and P. Hegemann for protein purification, M. Marazzi and M. Elstner for QM/MM calculation, and I. H. M. van Stokkum for target analysis.

2.1. Introduction

The discovery of channelrhodopsins (ChRs)[52,53] lead to a breakthrough in optogenetics[141], which became a key technology in current neuroscience to optically control neural activity with high spatio-temporal precision[26,28,142]. ChRs are light-gated cation channels (**Fig. 2.1a**) first discovered in *Chlamydomonas reinhardtii*[52,53], employing all-*trans* retinal as a chromophore. So far, diverse ChR variants have been engineered for customized optogenetic applications regarding excitability/color tuning[34,143], ion conductance[144-146] and modulation of the open state lifetime[36]. For rational design of further functional ChRs, clarification of the photoreaction mechanisms is highly required, yet the understanding of the molecular dynamics remains to a significant extent elusive. Photoisomerization from all-*trans* to 13-*cis* retinal, which is a key reaction to trigger the photocycle and also decides the quantum yield of the photoreaction, occurs in the femto- to picosecond time region. On the other hand, the channel pore is formed and opened (on-gating) in the microsecond/millisecond timescale following several photoinitiated intermediate states. Therefore, observation of the molecular dynamics from the femtosecond to millisecond time scales is essential for elucidation of the activation mechanisms of ChRs.

A combination of time-resolved information on photoactivation with structure-based calculations is a powerful approach to obtain a molecular picture of the photoinduced initial structural dynamics of ChRs. C1C2, a chimeric protein of *Chlamydomonas reinhardtii* ChR1 and *Chlamydomonas reinhardtii* ChR2, is the only channelrhodopsin whose crystal structures were solved up to now[16,147], providing the first direct molecular basis to understand the activation process of ChRs (**Fig. 2.1b**). C1C2 consists of five transmembrane helices (TM1–TM5) derived from ChR1 and two helices (TM6 and TM7) from ChR2. While

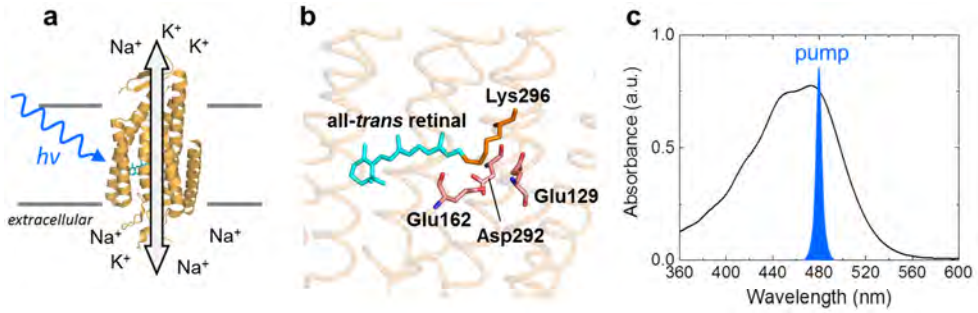

Figure 2.1. Three-dimensional structure and dark-state absorption spectrum of C1C2 (PDB ID: 3UG9[16]). (**a**) Function of C1C2 as light-driven cation channel. (**b**) Close-up of the retinal binding pocket. (**c**) Dark-state absorption spectrum. Excitation wavelength of pump-probe and pump-dump-probe experiments was 480 nm.

several ultrafast time-resolved spectroscopies of ChR2 were performed[148-150], no time-resolved spectroscopic data for C1C2 has been reported so far, which has restricted a systematic combination of experiments with computational calculation. Importantly, it has recently become clear that the dark-state structure in the vicinity of the retinal chromophore differs significantly between C1C2 and ChR2. In C1C2, the protonated retinal Schiff base forms a hydrogen-bond with Glu162, but not with Asp292[151]. On the other hand, in ChR2, the retinal Schiff base forms hydrogen-bonds to both of Glu123 (Glu162 in C1C2) and Asp253 (Asp292 in C1C2) and also to possibly water molecules[152]. The dark-state structural difference would result in different photoreaction dynamics in C1C2 and ChR2, thus the time-resolved experimental results of C1C2 are indispensable for direct access to theoretical approach based on the C1C2 structure.

Here we report a comprehensive femtosecond-to-second transient absorption study of C1C2. In combination with pump-dump-probe spectroscopy, target analysis and structure-based hybrid quantum mechanics/molecular mechanics calculations, we propose a multi-path excited-state dynamics model on C1C2 with two distinct conical intersections; a 450 fs isomerization path and a relaxation path with 2.0 ps and 11 ps. We further present a complete photocycle model of C1C2 from femtoseconds to seconds, which will be beneficial for further understanding of the activation mechanism of ChRs, and reveal striking kinetic differences on ground state dynamics between C1C2 and ChR2.

2.2. Results and Discussion

Femto- to microsecond transient absorption spectroscopy was performed for C1C2 at pH 8 with 480-nm excitation. **Fig. 2.2** shows the evolution-associated difference spectra (EADS) determined by global analysis of the transient absorption data of C1C2 in H_2O (**Fig. 2.2a**) and D_2O (**Fig. 2.2b**). Six spectral components were required to adequately represent the experimental data with the sequential time constants: 450 fs, 2.0 ps, 11 ps, 630 ps, 490 ns and infinity both in H_2O and D_2O. The top panels show the early time evolution up to 11 ps, the lower panels the later stages of the evolution from 11 ps onwards. No significant differences were observed between the transient absorption spectra in H_2O and D_2O up to 100 μs, *i.e.* H/D kinetics isotope effects are not significant in the reactions.

Primary photochemistry: ultrafast transient absorption spectroscopy

We first consider the primary reactions that take place on the femto- to picosecond timescale shown in the upper panel of **Fig. 2.2a**. The positive signals of the EADS consist of excited

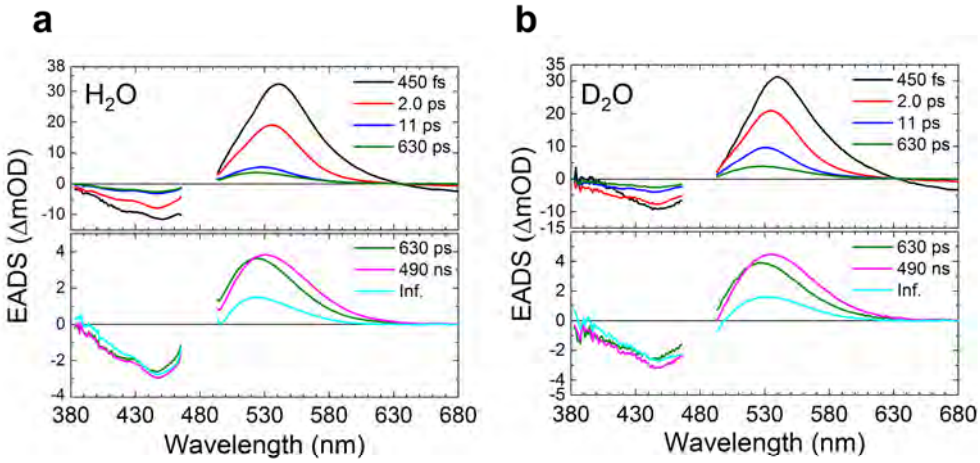

Figure 2.2. Globally fitted transient absorption spectra of C1C2 at pH 8 in H_2O and D_2O. EADS of transient absorption data of C1C2 in (**a**) H_2O and (**b**) D_2O. The spectra were fitted with six components. The spectral region of 465–495 nm is omitted because of the strong pump scattering. The 630 ps component is shown on both of the top and the bottom panels for reference.

state absorption (ESA) and/or absorption of early photoproducts. The negative signals at around 460 nm is due to ground state bleach. In the 450 fs EADS, the large positive band near 540 nm may be assigned to ESA, in line with earlier work on ChR2[148,149]. The negative signals at wavelengths > 630 nm occur in a region without ground state absorption and hence must be assigned to stimulated emission (SE), providing clear information on the excited state dynamics. The SE signals decayed with 450 fs, 2.0 ps and 11 ps, which implies that the excited-state decay occurs with those three time components. The excited-state absorption peaked at 541 nm immediately after the photon absorption (black line), and progressively blue-shifted to 535 nm in 450 fs (red line), and 528 nm in 2.0 ps (blue line), along with a spectral narrowing and a blue-shift of the isosbestic point. Such narrowing and blue-shifting is similar to that observed in protonated Schiff base retinal in solution, and may be assigned to vibrational relaxation and evolution on the excited-state potential energy surface[153]. Because the SE completely decayed in 11 ps, the 522-nm absorption that was left after the 11 ps evolution (green line) is only composed of the primary ground-state photoproduct, in addition to ground-state bleach of the reactant around 450 nm.

Primary photochemistry: pump-dump-probe spectroscopy

As seen in **Fig. 2.2**, the spectra of ESA and photoproduct absorption are strongly overlapped around 530 nm, which makes it difficult to distinguish multiphasic excited-state decay and vibrational relaxation from the primary product formation, and possible relaxation phenomena of the latter. This situation is similar to that observed in ChR2[148], but differs from bacteriorhodopsin, where the ESA is blue-shifted from the ground-state bleach[154] and the red-shifted primary photoproduct J/K is comparatively cleanly observed. To assess primary photodynamics in more detail, we applied pump-dump-probe spectroscopy to C1C2. Pump-dump-probe (**Fig. 2.3**), or multi-pulse spectroscopy, is a powerful technique to disentangle complex photoreaction dynamics[155-165]. This technique can be used to control and influence the course of reactions as they evolve, and its power lies in the ability to selectively remove or transfer the population of transient species with carefully timed laser pulses.

Fig. 2.4 shows the results of a pump-dump-probe experiment for C1C2 at pH 8, with pumping the ground state transition at 480 nm and dumping the SE at 720 nm at a time delay of 300 fs. **Fig. 2.4a** shows time traces of pump-probe and pump-dump-probe experiments probed at 530 nm, near the ESA and primary photoproduct absorption maxima. An 11% signal decrease was seen in the pump-dump-probe time trace immediately after application of the dump pulse, which indicates that 11% of the excited molecules were forcibly relaxed the ground state by the dump pulse, and therefore do not participate in product formation any longer. At 100 ps (**Fig. 2.4a**, inset) where the excited states had completely decayed and only photoproduct absorption is observed, the photoproduct

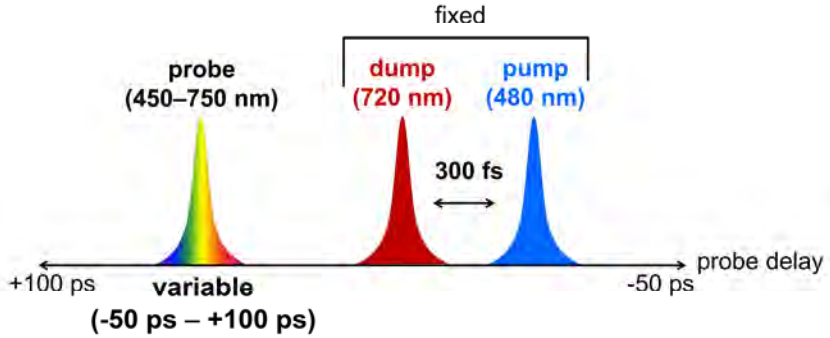

Figure 2.3. Scheme of pump-dump-probe experiments. Wavelengths of pump, dump and probe pulses were 480 nm, 720 nm and 450–750 nm, respectively. Time difference between the pump and dump pulses was fixed as 300 fs. Time difference between the pump and probe pulses was valuable from -50 ps to +100 ps.

absorption was decreased only by 6.5% by the dump pulse. This experiment shows that a large fraction of product states have already been formed prior to application of the dump pulse. Given the early time of the dump (300 fs), it is likely that the photoproduct is preferentially formed by the 450 fs component. Indeed, we can quantitatively describe the pump-dump-probe data with product formation from the 450 fs component only (*vide infra*). This means that branching of the excited-state dynamics occurs and that a sequential model is not adequate.

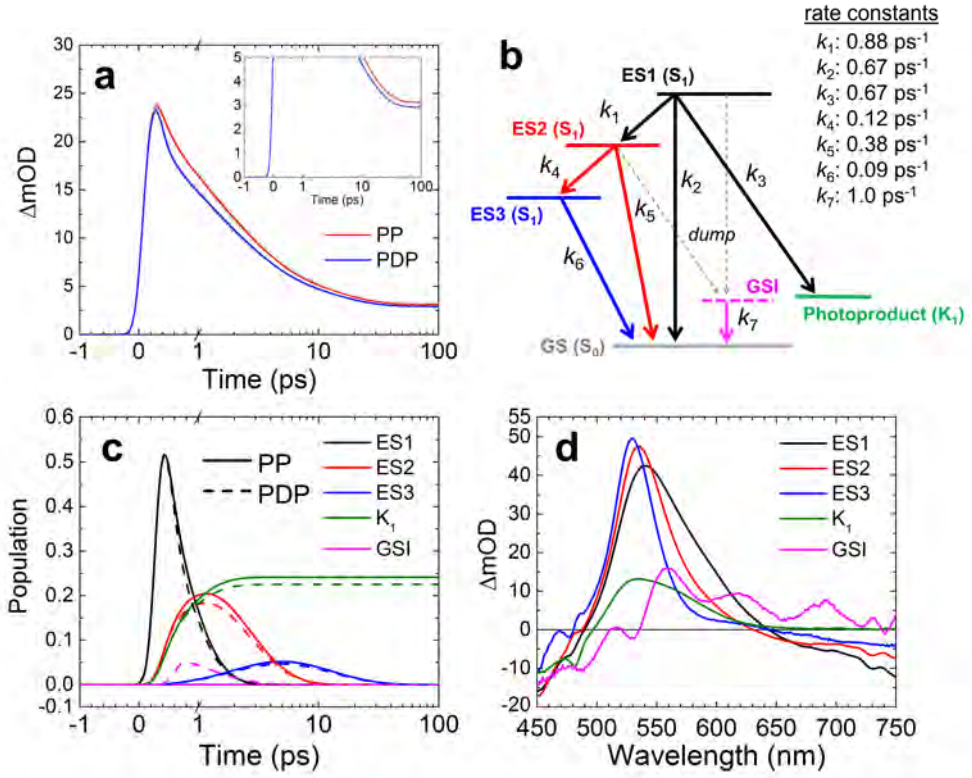

Figure 2.4. Pump-dump-probe data of C1C2 at pH 8 and target analysis results. (**a**) Time traces of pump probe (PP, open black dots with a red fitting line) and pump-dump-probe (PDP, closed gray dots with a blue fitting line) at 530 nm. In **a** and **c**, the time axis is linear until 1 ps, and logarithmic thereafter. (**b**) Kinetic scheme consisting of three excited states (ES1, ES2 and ES3), the first photoproduct state (K_1) and ground state intermediate (GSI). The dump pulse at 300 fs converts a fraction of the excited states to the GSI. It affects ES1 and ES2, which is indicated by the dashed gray arrows. (**c**) Time evolution of populations of ES1, ES2, ES3, K1 and GSI. The solid and dashed lines represent pump-probe (PP) and pump-dump-probe (PDP) data, respectively. (**d**) Species-associated difference spectra (SADS) of pump-dump-probe experiments.

Primary photochemistry: target analysis

The femtosecond transient absorption and pump-dump-probe data on C1C2 show that during the first few picoseconds, a mixture of excited states and photoproducts make up the transient spectra. To disentangle the contributions by the various molecular species, we performed a target analysis wherein the data are described in terms of a kinetic scheme, thereby identifying their spectral signatures, estimate their lifetimes and their connectivity and quantum yield. In a target analysis, reactive compartments are associated in an explicit kinetic model, thus multiphasic decay and specific branching can be taken into account to obtain the difference spectra of the 'pure' molecular species involved in the reaction, so-called species-associated difference spectra (SADS)[140].

To build the kinetic model, we need to consider the following aspects that become apparent from the transient absorption and pump-dump-probe experiments:

(i) We observe a progressive blue shifting and narrowing of the excited-state absorption on a sub-ps to ps timescale. Such phenomenology is indicative of vibrational relaxation processes in strongly vibronically coupled systems and/or evolution on the excited-state potential energy surface, as observed in protonated Schiff base retinal in solution[153].

(ii) We observe three decay components of the stimulated emission of 450 fs, 2 ps and 11 ps. Such heterogeneity may follow from branched reaction dynamics in the excited state and from heterogeneity in the ground state. We will show below that both aspects may contribute.

(iii) The pump-dump-probe experiments indicate that the fast, 450 fs excited-state decay component produces the primary photoproduct, and that the slower components may not contribute.

(iv) To estimate the relative amplitude of the SADS (and thereby the photoproduct quantum yield), we assume that the ground-state bleach amplitude of the three excited states and of the photoproduct state should be roughly the same.

(v) Dumping the excited state in rhodopsins is expected to give rise to intermediates on the ground state potential energy surface[162], which need to be included in the model.

The simplest adequate target model is shown in **Fig. 2.4b**. It includes three different excited states: ES1, ES2 and ES3 (on the S_1 excited state potential energy surface), to reflect the observed three excited-state lifetimes. In addition, ES1, ES2 and ES3 represent the excited state at various levels of vibrational relaxation and evolution on the potential

energy surface. ES1 is the initially populated shortest-lived excited state and branches to three other compartments: to ES2, the first photoproduct state K_1 and the original ground state GS (S_0). ES2 evolves to ES3 and GS, and ES3 evolves only to GS. A ground state intermediate (GSI) was populated only after application of a dump pulse, and evolves to GS. The target model was applied to transient absorption and pump-dump-probe datasets, of C1C2 at pH 8.

The target analysis results are shown in **Fig. 2.4c,d**. ES1 branches to three other compartments at a total rate constant of 2.2 ps^{-1}: to ES2 (40%), the first photoproduct state K_1 (30%) and the original ground state GS (30%). ES2 is blue-shifted and narrowed with respect to ES1, indicating that this state has undergone vibrational relaxation. K_1 is assigned as a well-known K-like state in microbial rhodopsins[7]. ES2 branches to ES3 and GS with rate constants of 0.12 and 0.38 ps^{-1}, respectively. ES3 has progressively blue-shifted and narrowed with respect to ES2, indicating that this state has further undergone vibrational relaxation and/or structural relaxation on S_1. ES3 evolved to GS with a rate constant of 0.09 ps^{-1}. The GSI decayed to the GS with a rate constant of 1.0 ps^{-1}. The GSI is characterized by a ground state bleach near 480 nm, and a broad absorption between 550 and 700 nm (**Fig. 2.4d**), indicating this species is red-shifted with respect to the steady-state ground state absorption of C1C2. Such GSI properties are similar to those observed previously in proteorhodopsin and PYP[158,162]. It is uncertain whether the somewhat oscillatory spectral shape of the GSI is real or spurious. In the latter case it may follow from its low transient concentration in the spectral evolution and limits in data quality.

Here we consider the possibility that the dump pulse, which is resonant with the stimulated emission, also induces re-pumping of the excited state given that the ESA may extend to 720 nm. Repumping would result in the production of distinct photoproducts. However, the transient absorption and pump-dump-probe data can be adequately described by the kinetic model and the molecular compartments of **Fig. 2.4b**. If any distinct photoproduct would have been formed due to repumping, such putative state should be visible in the spectral evolution. Such is clearly not the case, and we therefore conclude that no significant repumping of the excited state takes place.

Primary photochemistry: hybrid quantum mechanics/ molecular mechanics calculations

We performed CASPT2//CASSCF(12,12)/CHARMM calculations to study the excited-state photoisomerization of all-*trans* retinal in C1C2, in order to compare with the transient

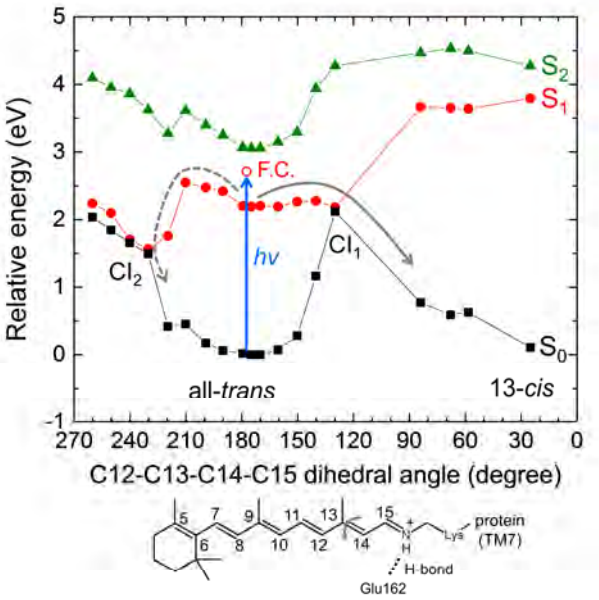

Figure 2.5. CASPT2//CASSCF(12,12) photoisomerization pathways from the all-*trans* retinal conformer, when the retinal Schiff base is hydrogen-bonded to Glu162. S_0 (black closed squires with black solid line), S_1 (red closed dots with red solid line) and S_2 (green closed triangles with green solid line) energy profiles are shown. The blue arrow shows light excitation of all-*trans* retinal as performed on our pump-probe and pump-dump-probe spectroscopic experiments. The open red dot shows the Franck–Condon state (F.C.). The solid gray arrow shows the isomerization path through energy barrier of 1.96 kcal/mol (0.09 eV) on S_1 via a conical intersection CI_1. The dashed gray arrow indicates a relaxation path through energy barrier of 7.42 kcal/mol (0.32 eV) on S_1 via another conical intersection CI_2.

absorption, the pump-dump-probe results and the target analysis scheme. The calculations of C1C2 including a direct hydrogen bond between the retinal Schiff base and the side chain of Glu162, indicate a two-step retinal isomerization mechanism (**Fig. 2.5**): After $S_0 \rightarrow S_1$ $^1(\pi,\pi^*)$ vertical excitation of all-*trans* retinal, the system relaxes from the Franck–Condon region to an S_1 energy-minimum geometry (excess energy of 12.0 kcal/mol), mainly driven by partial inversion of the bond length alternation. Indeed, the $S_0 \rightarrow S_1$ vertical excitation is optically much brighter than the eventual $S_0 \rightarrow S_2$ $^1(\pi,\pi^*)$ excitation, as evinced by the difference in their transition oscillator strengths: 1.4 and 0.1, respectively. It follows a transition to the photoproduct state via a conical intersection (CI_1). The C12–C13–C14–C15 dihedral angle of the retinal is *ca.* 180° on the ground state (S_0) and S_1 energy-minima,

indicating the retinal isomer as all-*trans*. At the CI_1, the dihedral angle evolved by a clockwise rotation to 130° (*i.e.* twisted by -50°) and finally relaxed to 24° (*i.e.* twisted by -156°), forming the 13-*cis* retinal isomer. Alternatively, CI_1 can also lead back to the initial all-*trans* isomer (*i.e.* internal conversion). A different pathway was also found via another conical intersection (CI_2), implying a counter-clockwise rotation after the initial vibrational relaxation to the S_1 energy-minimum. Along the path, the C12–C13–C14–C15 dihedral angle evolves to 230° (*i.e.* twisted by 50°) at CI_2, and relaxes back to 180° of the all-*trans* ground state. Starting from CI_2, no ground state pathway leading to photoproduct formation was found. The energy barriers in the S_1 state were calculated as 1.96 kcal/mol (0.09 eV) and 7.42 kcal/mol (0.32 eV) to reach CI_1 and CI_2, respectively. Those energy barriers are in agreement with previous CASPT2//CASSCF studies[166].

The calculations predict heterogeneous excited-state dynamics because of the presence of the two barriers leading to CI_1 and CI_2, as we observed experimentally and in the target analysis. The productive path through CI_1 can be assigned to the decay component of 450 fs, leading to the all-*trans* to 13-*cis* photoisomerization of the retinal and photoproduct K_1. The unproductive path through CI_2 likely involves the slower time components 2.0 ps and 11 ps, resulting in relaxation to the initial ground state. Nevertheless, the theoretical model predicts a single energy barrier to reach CI_2 (see **Fig. 2.5**). This was also found in a previous work using a similar computational approach to C1C2[166]. Hence, in the context of the theoretical model, to explain the presence of three different time components we postulate a variety of ground state active site retinal pockets, as was depicted in a recent study of ChR2[152]. Indeed, Guo *et al.* propose three hydrogen-bonded networks, involving a direct hydrogen bond to the Glu side chain, to the Asp side chain or to a water molecule. In C1C2, a hydrogen bond with Glu162, not with Asp292, was experimentally demonstrated[151]. Hence, we propose as alternative network a hydrogen bond between retinal and water. The differences between both active sites can be seen in **Fig. 2.6**, where both optimized all-*trans* and 13-*cis* conformations are shown: a water molecule (W2) can compete with Glu162 in the formation of the hydrogen bond with the retinal Schiff base. This alternative active site conformation is indeed related to different excited state energy barriers to reach CI_2, as recently discussed also in the study of a retinal-like biomimetic photoswitch[167]. In any case, as demonstrated by the single time constant involved in the photoproduct formation through CI_1, this ground state heterogeneity does not affect the clockwise rotation of the retinal in the excited state: the energy barriers in the S_1 state were calculated as 2.10 kcal/mol (0.09 eV) to reach CI_1 —*i.e.* almost the same as in **Fig. 2.5**— and 5.20 kcal/mol (0.23 eV) to reach

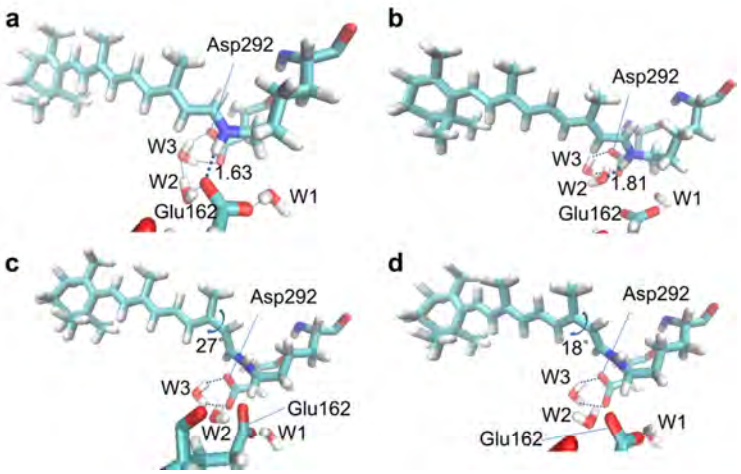

Figure 2.6. Calculated ground state minima structures. (**a,b**) all-*trans* and (**c,d**) 13-*cis* retinal-bound C1C2 active sites, including two possible hydrogen bonds to the retinal Schiff base for the all-*trans* conformations: to (**a**) Glu162 and to (**b**) a water molecule, W2.

CI_2 —*i.e.* 2.2 kcal/mol lower than in **Fig. 2.5**—, respectively, remaining almost unaltered the S_1 excess energy from the Franck-Condon to minimum region (12.2 kcal/mol) and the $S_0 \rightarrow S_{1,2}$ oscillator strengths. Thus, we conclude that the isomerization via CI_1 proceeds in 450 fs regardless of the hydrogen-bond network on the ground state, while the relaxation to the initial ground state via CI_2 occurs in 2.0 ps or 11 ps, depending on the ground-state hydrogen-bond network.

These conclusions highlight that, in spite of structural similarities between different rhodopsins, both electronic ground- and excited-states can result in different scenarios. Especially, rhodopsin (Rh) and bathorhodopsin (batho-Rh) have shown a single ground state conformation and a single excited state pathway, leading to the S_1/S_0 conical intersection in around 100 fs, hence without finding S_1 minima[168,169]. On the other hand, C1C2 is definitely a more complex system, where ground state heterogeneity and excited state minima should be considered for interpreting the experimental data.

The kinetic model of **Fig. 2.4b** assumes that the multiexponential excited-state decay arises exclusively from branching dynamics in the excited state. However, as argued above, dark state heterogeneity is likely present which will manifest itself as a biexponential, parallel excited-state decay that would be mixed in with the excited-state relaxation process, complicating the kinetic analysis. However, under the assumption that the spectral shape of the excited-state intermediates and the vibrational relaxation dynamics does not vary

appreciably between the two dark-state conformers, the model of **Fig. 2.4b** is equivalent to such extended parallel model.

Quantum yield of primary photoproduct K_1 formation

When comparing the ground state bleach amplitudes in the EADS of **Fig. 2.2**, the 630 ps EADS has an amplitude of about 25% of that of the 450 fs component, which indicates that about 25% of the initially excited molecules end up in the primary photoproduct K_1. However, estimations on the basis of such simple considerations may be problematic because of partly compensating bleach and absorption features in the transient absorption spectra. For a more systematic approach that takes into account the rich spectral and temporal evolution of the system, we applied the target analysis of **Fig. 2.4**, where the obtained SADS represent pure molecular states and hence have to conform to realistic spectral shapes. Here, we set the additional condition that the ground state bleach amplitudes should be similar. The kinetic modelling resulted in a quantum yield of 30±3%, which is similar to that estimated above from the sequential analysis.

The quantum yield of K_1 state formation as estimated from the target analysis, 30%, is low as compared to bacteriorhodopsin, where it is around 60%[170]. According to the target model, the losses have two causes: (i) the presence of nonproductive fractions in excited state decay, *i.e.* the 2.0 and 11 ps components which make up 40% of the excited-state decay, and

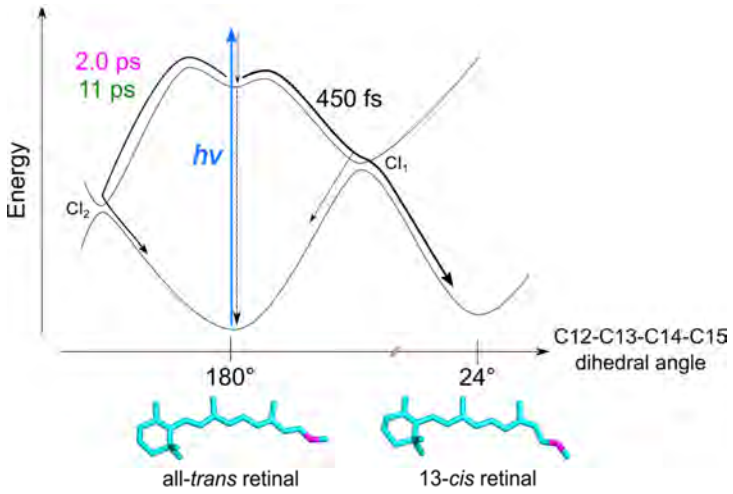

Figure 2.7. Energy diagram on excited-state dynamics of C1C2. After photon absorption, two distinct paths are suggested on the excited-state dynamics: isomerization path via CI_1 with 450 fs and relaxation path to the initial ground state via CI_2 with 2.0 ps and 11 ps.

(ii) a nonunity quantum yield of the 450 fs component. The 450 fs component constitutes 60% of excited-state decay, which means that half of those excited states proceed to the photoproduct K_1, and the other half relaxes to the original ground state through CI_1. Thus, the 450 fs component inherently has a 50% quantum yield, which is in line with bacteriorhodopsin that follows a single path on the potential energy surface. This is another indication that the 450 fs component does not follow the CI_2 reaction path. The schematic excited-state reaction diagram is shown in **Fig. 2.7**.

Isomeric composition of C1C2

A key question concerns the isomeric composition of C1C2 in the dark and in our experimental conditions. In the dark, C1C2 assumes an all-*trans* retinal chromophore, as evidenced from solid-state NMR[171] and the X-ray structure[16]. ChR2 also adopts an all-*trans* retinal chromophore in the dark[172]. There is evidence from resonant Raman spectroscopy that in ChR2/H134R, moderate illumination leads to a minority population of a 13-*cis*/15-*syn* conformer[171], but such has not been systematically investigated for C1C2. **Fig. 2.8a** shows the C1C2 absorption spectra and their 2nd derivatives of a dark-adapted sample and the same sample after two hours of 0.2 mW laser illumination in the Lissajous scanner, which is the same illumination condition as our transient absorption experiments. The

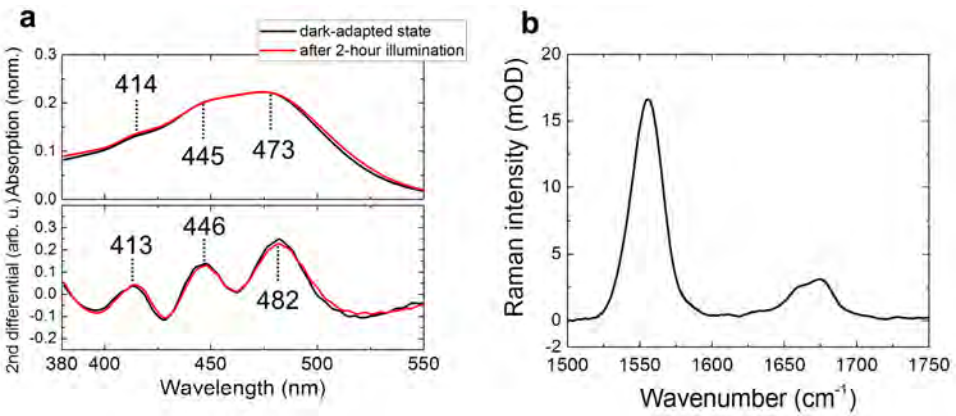

Figure 2.8. Steady-state absorption and stimulated Raman spectra of C1C2 at pH 8. (**a**) UV-Vis absorption spectra (top) and 2nd derivatives (bottom) of the absorption spectra (30-point Savitzky-Golay smoothing was applied) of C1C2 at pH 8, taken with the same experimental condition as transient absorption experiments on a Lissajous scanner. Spectra of dark-adapted state and after 2-hour illumination with 0.2 mW femtosecond laser (500 Hz, 480 nm, spot size: ~200 μm) are shown in black and red lines, respectively. (**b**) stimulated Raman spectra of dark-state C1C2 at pH 8 spectra (10-point Savitzky-Golay smoothing and baseline correction were applied).

spectra are virtually identical, with the same absorption maxima before and after illumination. **Fig. 2.8b** shows the stimulated Raman spectrum of the C1C2 dark state, with preresonant Raman pumping at 800 nm. It shows a C=C stretch band near 1560 cm^{-1} and a C=N stretch at 1660 cm^{-1}, which are indicative of an all-*trans* chromophore[65,171]. From these data, we conclude that under our experimental circumstances, C1C2 retains an all-*trans* retinal chromophore.

Comparison of the ultrafast reaction dynamics with other channelrhodopsins

Here we compare the excited-state dynamics of C1C2 with other channelrhodopsins: ChR2 from *Chlamydomonas reinhardtii*[148-150] and *Ca*ChR1[173-175], which is a channelrhodopsin found in *Chlamydomonas augustae*[176]. By visible pump-probe[148,149], visible-pump/IR-probe[150] and upconversion[148] experiments, it was concluded that the formation of the first photoproduct state occurs in ~400 fs in ChR2. As discussed above, the time constant of the retinal isomerization in C1C2 is 450 fs, which is close to that in ChR2. However, a clear difference was seen in the excited-state relaxation mechanisms to the initial ground state. In ChR2, the stimulated emission decays almost completely with ~400 fs[148,149], indicating relaxation to the ground state in this time frame. On the other hand, in C1C2, three components of 450 fs, 2.0 ps and 11 ps, of which the latter two make up 40% of the excited-state decay, are related to the relaxation to the ground state. Because five helices (TM1–TM5) among the seven transmembrane helices are originated from ChR1, the conformation of important residues for retinal dynamics such as Glu162 may be significantly different between C1C2 and ChR2 and should be similar to ChR1. Possibly, the conformational difference of residues such as Glu162 affects the relaxation process of the excited molecules. Further investigation *e.g.* with time-resolved vibrational spectroscopy in C1C2 would be helpful for deeper understanding of the relaxation process. In *Ca*ChR1, it was found that isomerization occurs much faster than ChR2 and C1C2, in 110 fs.[173-175] In that sense, C1C2 behaves more similar to ChR2 than *Ca*ChR1. However, *Ca*ChR1 has a red-shifted absorption (at ~520 nm) and different photocurrent kinetics from *Chlamydomonas reinhardtii* ChR1[176], thus the *Ca*ChR1 photoinduced kinetics may be significantly different from that of *Chlamydomonas reinhardtii* ChR1 and ChR2.

C1C2 pump–dump–probe spectroscopy: consequences for superresolution optogenetics

We have demonstrated that it is possible to dump the excited state of C1C2. This finding suggests that it might be possible to establish superresolution optogenetics based on

channelrhodopsin by means of STED/RESOLFT techniques: in such a case, a combination of blue activation and near-IR deactivation beams would be used to activate neurons with sub-diffraction resolution, particularly when optogenetics at the organelle level is considered[177]. However, the properties that we have determined for the excited-state reaction dynamics of C1C2 are not yet favorable for such applications. The excited-state lifetime is multiphasic, with lifetimes of 450 fs, 2.0 ps and 11 ps. We have shown that only the first, fast phase of 450 fs activates C1C2, which means that during this short time the excited states need to be dumped in a STED-like configuration. We find that dumping even at very early delays (300 fs) results in only partial effects on product formation (*i.e.* an 11% dumping of excited states leads to only 6.5% loss of photoproduct). For superresolution purposes, the proteins in the deactivation beam need to be deactivated by almost 100%, which is nearly impossible with the C1C2 short reactive lifetimes.

Slow photoproduct dynamics of C1C2

Next, we discuss the photoproduct dynamics after the K_1 state formation in C1C2. As discussed above, 450 fs, 2.0 ps and 11 ps lifetimes are involved in the excited-state dynamics, indicating that the slower components are related to the photoproduct ground state dynamics of C1C2 at pH 8 (**Fig. 2.2a**, bottom panel). The photoproduct absorption shows a red shift from 523 nm to 530 nm in 630 ps (**Fig. 2.2a**, green to magenta evolution), which can be assigned as a second K-like state formation as proposed for ChR2[149], hereafter referred to as K_2. In the 490 ns evolution (**Fig. 2.2a**, magenta to cyan evolution), a ~440-nm signal rises and the ~530-nm signal decreases to a lower amplitude. The ~440-nm signal rise can be assigned to formation of an L-like state, which is a blue-shifted intermediate widely seen in microbial rhodopsins[7,178]. In bacteriorhodopsin, it was suggested that the retinal Schiff base is located closer to the counterions in the L state than in the K state. As seen in **Fig. 2.2a**, the 530-nm absorption remains with the increase of the 440-nm absorption in 490 ns, implying the L-like state exists in equilibrium with the K-like state in C1C2. Furthermore, we performed flash photolysis experiments to investigate slow photoproduct dynamics from 1 μs to 10 s in C1C2 at pH 8. The counterplot, selected time traces, EADS and DADS are shown in **Fig. 2.9**. Three exponential components were seen for C1C2 at pH 8: 20 μs, 15 ms and 100 ms. In 20 μs, a near-UV absorption at <400 nm appeared, which is assigned to the M intermediate that has a deprotonated retinal.

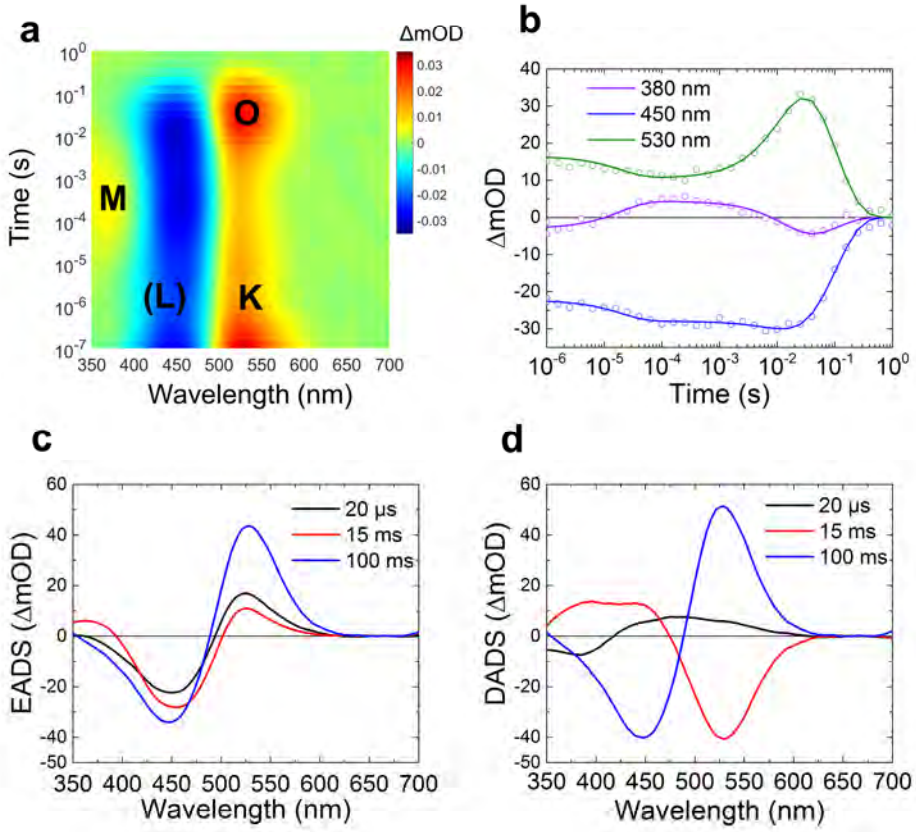

Figure 2.9. Transient absorption results for nanosecond-to-second kinetics of C1C2 at pH 8. (**a**) Counterplot of ns-s transient absorption spectra. (**b**) Selected time traces with fitting curves (solid lines) at 380 (purple), 450 (blue) and 530 nm (green). (**c**) EADS, (**d**) DADS fitted with three time components: 20 µs, 15 ms and 100 ms.

Notably, a decay of a broad peak at 430–600 nm was observed in 20 µs (**Fig. 2.9d**), which are probably derived from a mixture of the K and L intermediates, while a significant amount of the K state absorption (~530 nm) remained (**Fig. 2.9c**). Furthermore, an L-intermediate decay (at ~440 nm) is also seen in the 15-ms DADS component (**Fig. 2.9d**), which implies the L intermediate partially remains after 20 µs. These observations indicate that K/L/M equilibrium is formed after 20 µs, similarly to sodium ion pump rhodopsin KR2[41,62]. Significantly, the amplitude of the M state signal of C1C2 at pH 8 is ~3-fold less than that of ChR2 at pH 7.4[148], indicating that in C1C2 the K/L/M equilibrium is tilted towards K and L. In the pump-probe spectra shown in **Fig. 2.2a**, the M state absorption was

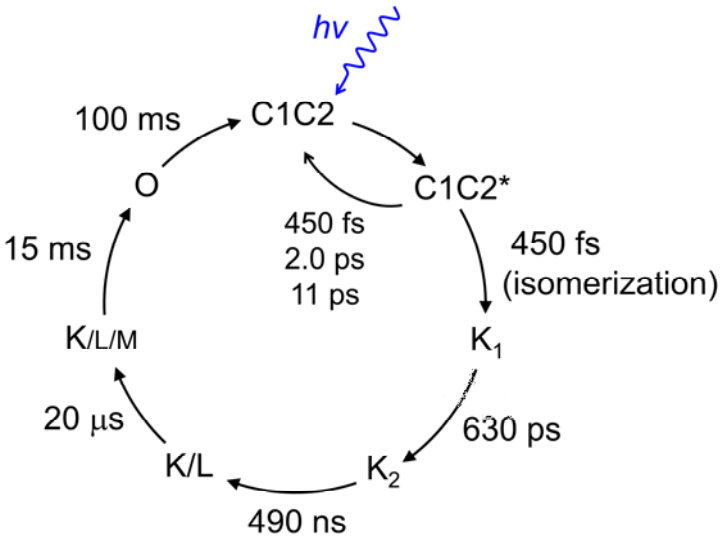

Figure 2.10. Photocycle model of C1C2 at pH 8.

not clearly visible and the ~20 µs component was not detected, which relate to noise issues in the near-UV that result from the decreased intensity of the white light continuum in this spectral region. In 15 ms, the L (~440 nm) and M (<400 nm) intermediates decayed, while another 530-nm absorbing component appeared, which is assigned as the ion-conducting O intermediate that has a reprotonated retinal. In 100 ms, the O state absorption disappeared with recovery of the GSB signal, which indicates the photocycle is completed in 100 ms. The photocycle model of C1C2 at pH 8 is shown in **Fig. 2.10**.

2.3. Conclusion

We investigated the excited-state and photoproduct-state dynamics of a functional chimeric channelrhodopsin C1C2, with known X-ray structure and which has properties similar to *Chlamydomonas reinhardtii* ChR1 and ChR2 with respect to absorbance, ion selectivity and photocurrent kinetics. With transient absorption and pump-dump-probe spectroscopy together with target analysis and QM/MM calculations, we demonstrated that the retinal isomerization in C1C2 occurs in 450 fs after photon absorption with an estimated quantum yield of 30% via a conical intersection CI_1 that is reached after clockwise rotation of the C13=C14 bond. Relaxation to the initial ground state, which is a competing process of the isomerization, proceeds with three time components: 450 fs (via CI_1), 2.0 ps and 11 ps via a

second conical intersection CI_2 that is reached after counterclockwise rotation of the C13=C14 bond. The presence of the additional conical intersection CI_2 lies at the basis of the low (30%) isomerization quantum yield determined in this study. Structural heterogeneity on the ground-state hydrogen-bond network around all-*trans* retinal possibly contributes to the distinct relaxation with 2.0 ps and 11 ps, but does not affect the isomerization with 450 fs. Furthermore, femtosecond to second photocycle of C1C2 has been determined. Strikingly, at pH 8 such M-like state is seen less significantly in C1C2 than in ChR2, while the C1C2 protein shows higher ion conducting. Thus, clear differences were observed in amplitude of the M-like state rise between C1C2 and ChR2, which indicates that the proton transfer mechanism and/or the transient equilibria between protonated and deprotonated forms of the retinal Schiff base is different in C1C2 and ChR2. Our findings can be considered a crucial step toward the elucidation of channelrhodopsin photoactivation.

Methods

Sample preparation: The C1C2 chimera (1-348 amino acids) was expressed and purified from *P. pastoris* according to previously described protocol[171]. Protein was concentrated to 520 μM in 20 mM Tris-HCl containing 150 mM NaCl and 0.03% β-D-maltoside (DDM) at pH 8.0. Buffers were exchanged by repeated dilution-concentration steps (Amicon Ultra 100000 MWCO, Millipore) to pH 10.0 (20 mM CAPS buffer with 150 mM NaCl) containing 0.03% DDM. Protein samples were placed between two CaF_2 plates separated by a 400 μm sample spacer. The sample holder was set on the Lissajous scanner as reported previously[65] to excite a fresh part of the samples in each pump-probe and pump-dump-probe data acquisition process[134].

Transient absorption spectroscopy: Femtosecond to sub-millisecond transient absorption measurements were performed by a pump-probe setup with synchronized 1 kHz Ti:Sapphire amplifiers as reported previously[38,39,133]. A CaF_2 plate was used for supercontinuum white light generation, and selected wavelength regions; 380–680 nm, were detected by the photodiode array. The time delay was varied up to 125 μs at 169 data points with the minimum temporal step of 50 fs. The diameters of the pump and the probe beams at the sample position were ~200 μm and ~70 μm, respectively. The wavelength of the pump beam was centered at 480 nm, and attenuated to ~400 nJ. The instrument response function was ~150 fs, estimated from global fitting. The flash photolysis experiments were performed as reported previously to observe transient absorption from 1 μs to 10 s[65].

Pump-dump-probe spectroscopy: Multi-pulse visible pump-dump-probe measurements were performed on a setup reported previously[161,163]. The central wavelength of the pump and dump pulses were set to 480 nm (~0.8 μJ/pulse) and 720 nm (~1.5 μJ/pulse), respectively. The pump and dump pulses were

modulated using choppers to 500 Hz and 250 Hz, respectively. On the probe line, an 800-nm pulse was focused on a 2-mm sapphire plate for supercontinuum white light generation. Two optical stages (IMS-6000, Newport) were installed on the pump and dump lines, and the temporal difference between the pump and dump pulses was fixed as 300 fs. The time delay between the pump and probe was covered from -50 ps to +100 ps with the shortest step of 20 fs. The pump-dump-probe spectra were globally fitted, and the instrumental response function was ~240 fs, estimated from the global fitting.

Computational methods: The monomer of C1C2 was built by using the crystal structure 3UG9 as template[16], where the retinal shows an all-*trans* conformation. A hybrid quantum mechanics/ molecular mechanics (QM/MM) model was set, by including the retinal chromophore in the QM region. More in detail, considering its successful results in describing quantitatively the energies and electronic structure of rhodopsin proteins[166,168,169] and retinal-based molecules[179-181], the MS-CASPT2//SA-CASSCF methodology[182] was applied, including the whole π system of the retinal in the active space (*i.e.* 12 electrons in 12 molecular orbitals). More in detail, the State Average-Complete Active Space Self Consistent Field (SA-CASSCF) method was applied to optimize the system, followed by MS-CASPT2 (Multi State-Complete Active Space Perturbation Theory to Second Order) energy calculation on top of the SA-CASSCF optimized geometries, performed to include the dynamic electron correlation by second-order perturbation theory. Indeed, the CASSCF method includes only the static electron correlation, hence allowing only a qualitative description of the system, while the inclusion of the dynamic electron correlation permits to reach a quantitative description of the ground and excited state energies.

CASSCF optimizations and CASPT2 single-point energy corrections were performed using 3 roots, *i.e.* the ground state (S_0) and the two lowest-lying singlet excited states (S_1 and S_2). Indeed, even if we are interested in the evolution of S_1 reaching S_0 through conical intersections, also S_2 was included for a better description of the system electronic structure. Moreover, CASPT2 calculations were performed using an imaginary shift of 0.2, as conventionally applied to avoid eventual problems of intruder states. The IPEA shift was set to 0.0.

The CHARMM22 classical force field[183] was applied to the rest of the protein, while the TIP3P model[184] was used to describe water molecules. Considering the high resolution of the X-ray data (2.3 Å)[16] and the aim to model the ultrafast photoinduced events after light absorption, all atom positions were kept to their crystal structure values, letting relax the active site, composed by the retinal and its nearby pocket (see below).

In order to correctly treat the frontier between the QM and the MM region, a hydrogen link atom was placed between the nitrogen atom of the Schiff base and the first carbon atom of the lysine residue, Cε. This allowed to include the whole chromophore in the QM region while keeping a reduced amount of atoms to be treated by the computationally expensive multiconfigurational quantum chemistry method MS-CASPT2//SA-CASSCF. During QM/MM optimizations, the Morokuma

scheme was used, *i.e.* the hydrogen link atoms was always kept along the line connecting the frontiers' QM and MM atoms.

The QM/MM (MS-CASPT2//SA-CASSCF/CHARMM) model applied ensures electrostatic and mechanical embedding through the Molcas/Tinker interface, *i.e.* the QM region is polarized by the MM point charges around. In order to avoid overpolarization of the QM wavefunction due to the presence of the hydrogen link atom, the charge of the Cε atom and of the two connected hydrogens was set to zero and redistributed on the rest of the atoms composing the lysine and the two neighboring amino acids.

During the QM/MM optimization, all atoms of the side chains and water molecules around the retinal – forming the retinal binding pocket – were allowed to move, following the micro-iterations scheme, that is converging the MM subsystem geometry every QM step. More in detail, the following residues were included: side chains of the lysine covalently bound to the retinal, Glu162, Trp163, Thr166, Cys167, Trp262, Ser295, Pro266, Trp299, Met294, Ile170, Cys298, Val125, Glu129, Asp292, Thr198, Leu221, Phe269, Phe217 and 6 water molecules. The rest of the protein and water molecules were kept at their crystallographic position, in order to keep the overall tertiary structure of the monomer. Indeed, the modeled retinal isomerization takes place in few hundreds of fs, a time which does not allow a full protein (including backbone) relaxation.

Both, all-*trans* and 13-*cis* retinal-bound C1C2, were optimized on the ground state, followed by a calculation of the S_1 minimum energy path from the all-*trans* Franck–Condon region to the S_1 minimum. Subsequently, it was performed an all-*trans*-to-13-*cis* relaxed scan on the optically bright state (S_1), along the photoisomerizable dihedral angle. The 6-31G(d) basis set was adopted for all optimizations, followed by energy calculations with the ANO-L-VDZP basis set. Different hydrogen-bonding patterns to the retinal Schiff base were considered, by CASSCF/MM optimization on the ground state: hydrogen bond (*i*) to deprotonated Glu162, as experimentally observed[151] and (*ii*) to a water molecule, as suggested computationally[185]. In the case (*i*) a S_1 CASSCF/MM excited state dynamics was additionally performed, considering the optimized ground state structure as initial geometry and without initial kinetic energy (*i.e.* temperature = 0 K). A time step of 1 fs was adopted for integration of the Velocity Verlet algorithm, keeping the total energy constant along the dynamics. This trajectory has the scope of giving more insights into the initial vibrational relaxation process upon light absorption, *i.e.* from the Franck–Condon to the S_1 minimum region. All calculations were performed with Molcas 7.8[186] interfaced to Tinker 5[187].

Chapter 3

The femtosecond-to-second photochemistry of red-shifted fast-closing anion channelrhodopsin PsACR1

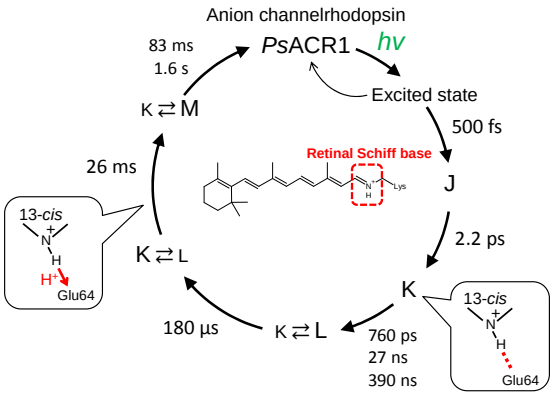

The complete photocycle of anion channelrhodopsin PsACR1 was determined by transient absorption spectroscopy. In addition, a hydrogen-bond switch with photoisomerization was proposed based on experiments with site-specific mutated proteins.

Abstract

Anion channelrhodopsins (ACRs) are of great interest due to their ability to inhibit electrical signaling in optogenetic experiments. The photochemistry of ACRs is currently only poorly understood and an improved understanding would be beneficial for rational design of ACRs with modified properties. Here we investigate the fs-s photocycle of an ACR from *Proteomonas sulcata* (*Ps*ACR1), which is valuable for optogenetic applications due to the red-shifted absorption/action spectra compared to the prototype, and the fast channel closing properties. We found that the photoisomerization occurs in ~500 fs independent of the protonation state of E64. Notably, E64 is involved in hydrogen-bond network rearrangement near the retinal Schiff base after photoisomerization. Furthermore, we suggest that E64 works as a primary proton acceptor during deprotonation of the retinal Schiff base.

This chapter is based on the following publication:
Physical Chemistry Chemical Physics **19**, 30402 (2017),
collaborated with M. Broser, A. Silapetere, B. S. Krause and P. Hegemann for protein purification, steady-state absorption and flash photolysis experiments.

3.1. Introduction

Microbial rhodopsins are photoactive sensory and ion-transporting proteins found in microorganisms, which are comprised of seven transmembrane helices with an all-*trans* retinal chromophore[7]. Importantly, microbial rhodopsins play an essential role in optogenetics as indispensable tools to activate or silence neural activities by light with unprecedented spatiotemporal precision[28]. Cation channelrhodopsins (CCRs)[52,53], which are light-gated cation channels, are the most widely used neural actuators. On the other hand, the light-driven chloride pump halorhodopsin is used to suppress neural activities[27,188]. However, the ion transport efficiency of ion pumps is much lower than that of ion channels generating a high demand of light-gated anion channels as neural silencers. In 2014, CCR-based artificial anion channels were reported[145,146]. More recently, native anion channelrhodopsins (ACRs) were found in cryptophyte algae as *Guillardia theta* (*Gt*ACR1 and *Gt*ACR2[54]), *Proteomonas sulcata* (*Ps*ACR1[55,56], also known as *Psu*ACR1) and relatives[57] (**Fig. 3.1a**). Some ACRs show much larger photocurrents than chloride pumps and CCR-based engineered anion channels[54] and were successfully used for neural inhibition in mouse[189] and *Drosophila*[58]. Among currently reported ACRs[55-57], *Ps*ACR1, despite of its smaller photocurrents relative to the *Gt*ACRs, exhibits two advantageous properties: (i) the absorption and action spectra are red-shifted (λ_{max} ~ 540 nm) compared to the other ACRs[57], which allows deeper and less harmful penetration in tissues; (ii) the channel closing is ~8-fold faster than *Gt*ACR1 and *Gt*ACR2[56], which is desirable for achieving higher temporal resolution.

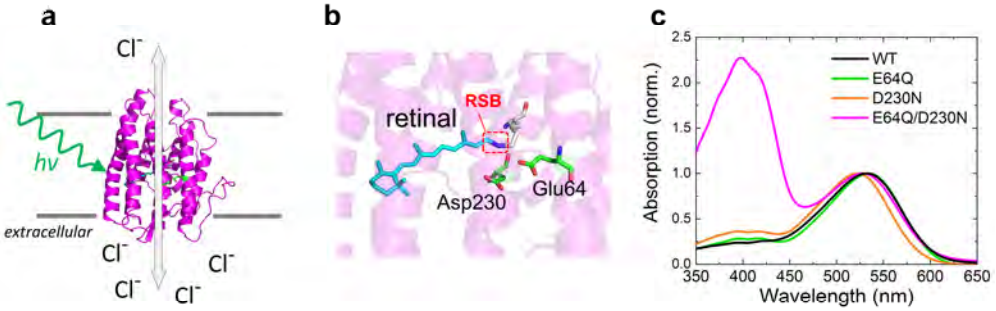

Figure 3.1. Three-dimensional structure model and dark-state absorption spectra of *Ps*ACR1. (**a**) Function of ACRs as light-driven anion channel. (**b**) Close-up of the retinal binding pocket of a homology model of *Ps*ACR1 based on the crystal structure of cation channelrhodopsin C1C2 (PDB ID: 3UG9) built by the Robetta server (robetta.bakerlab.org). (**c**) Normalized steady-state absorption spectra of wild-type (WT) *Ps*ACR1, the E64Q, D230N and E64Q/D230N mutants at pH 8.

In all microbial rhodopsins, protein function is closely linked to the molecular dynamics of the light-triggered cyclic reactions of the retinal chromophore, the so-called 'photocycle'. Thus, knowledge of the molecular mechanisms during the photocycle is crucial for a better understanding of the ACR functionality. The photocycle is comprised of a sequence of distinct spectral intermediates (J, K, L, M, N, O); first described for the prototypic proton pump bacteriorhodopsin (BR)[7,154,190]. Upon excitation, molecules undergo the excited-state dynamics within femto- to picoseconds and the photoproduct-state dynamics within picoseconds to seconds. The electronically excited-state reaction involves retinal photoisomerization as a subsequent trigger for sequential thermal ground state reactions, which drive activation and deactivation of microbial rhodopsins. Although the molecular mechanisms of the entire photocycle have been investigated in several microbial rhodopsins *e.g.* BR[7,191] and CCRs[6,192]; it is considered to be substantially different in ACRs[193]. Hence, elucidation of the whole photocycle of ACRs is of high importance. A general feature of ACRs is the absence of an acidic residue at the position homologous to the primary proton-acceptor D85 of bacteriorhodopsin (E123 in *Cr*ChR2) which is replaced by Ser (*Gt*ACR1 and *Gt*ACR2) or Ala (*Ps*ACR1)[57]. *Gt*ACR1 have been investigated in detail using single-turnover electrophysiology[194] and time-resolved spectroscopy within the ns–s time range[193]. These studies revealed a complex gating mechanism for *Gt*ACR1 and show that deprotonation of the retinal Schiff base (RSB) during M-state formation can be correlated with fast channel closure.

We have recently reported the photoreaction of *Ps*ACR1 on a ns–s timescale and we observed a late M-state formation (τ ~ 20 ms, ~500–1000 times slower than BR[195,196] and CCRs[42,197]) similar to *Gt*ACR1[193]. However, the detailed reaction dynamics of the early photocycle is still elusive for ACRs. In this chapter, the molecular properties of *Ps*ACR1 in the dark state, the excited state (fs-ps) and during formation of the photoproducts (ps-s) will be discussed; using transient absorption spectroscopy and point mutations of acidic residues near the RSB: E64 (E90 in *Chlamydomonas reinhardtii* channelrhodopsin-2, *Cr*ChR2) and D230 (D253 in *Cr*ChR2)[55], which may serve as the counterions of the protonated RSB, based on the sequence alignment (**Fig. 3.1b**)[55]. Notably, it is reported that E68 in *Gt*ACR1 (equivalent to E64 in *Ps*ACR1) plays a fundamental role in the gating mechanism[193,194]. Moreover, we found several differences of the photoreaction dynamics between *Ps*ACR1 and *Gt*ACR1.

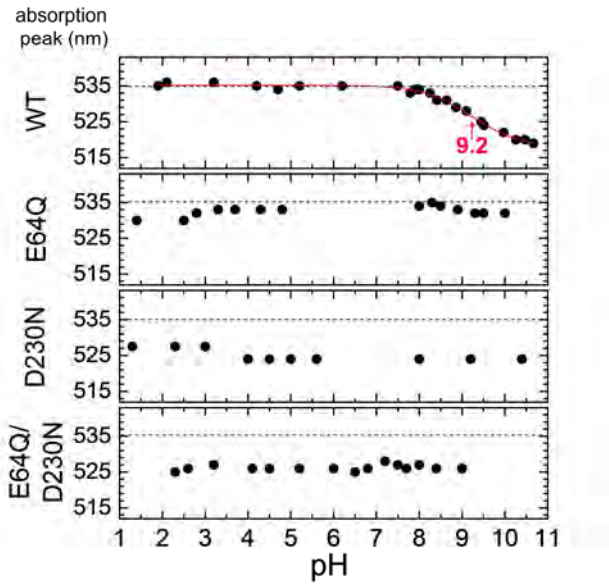

Figure 3.2. pH-titrated absorption maxima of *Ps*ACR1 and the mutants. The vertical axes show the absorption peak positions. Dashed lines indicate 535 nm. The pK_a value of a deprotonation reaction in the wild-type is shown (red line, fitted with Boltzmann sigmoid function).

3.2. Results and Discussion

Dark-state hydrogen-bond network near the protonated retinal Schiff base

Fig. 3.1c shows the dark-state UV/Vis absorption spectra of wild-type (WT) *Ps*ACR1 (λ_{max} ~ 534 nm), the E64Q (λ_{max} ~ 535 nm), the D230N (λ_{max} ~ 524 nm), and the E64Q/D230N (λ_{max} ~ 528 nm)
mutants at pH 8. The absorption maximum of the E64Q mutant is almost identical to that of the WT, while the D230N and E64Q/D230N mutants show blue-shifted spectra. In E64Q/D230N, the RSB chromophore is partially deprotonated seen from near-UV absorption (λ_{max} ~ 390 nm).In general, the electrostatic stabilization of the electronic ground state assures that the stronger the hydrogen bond interaction between the protonated RSB and a counterion is, the more blue-shifted the absorption, and *vice versa*[7,198]. The similarity of the E64Q and WT spectra implies that E64 is only weakly involved in the active site hydrogen-bond network at pH 8.0.

In WT, the absorption peak remained at ~534 nm at acidic and neutral pH, but the strong blue shift observed at high pH correlates with a pK_a value of a protonatable residue

near the RSB, possibly E64 or D230, around 9.2. (**Fig. 3.2**). This pH dependency is abolished by the E64Q mutation, which identifies E64 as the residue that deprotonates at high pH, as seen for the homolog substitution in *Gt*ACR1[193].

Dark-state absorption spectra were further recorded in different anion conditions (without salt or supplemented with either 150 mM NaCl or 100 mM Na_2SO_4) (**Fig. 3.3**) to probe for anion binding near the RSB. In WT, absorption maxima were weakly salt sensitive, with a minor increase of the deprotonated RSB fraction in the absence of salt. The E64Q spectrum slightly red-shifted (~3 nm) upon salt depletion suggesting that an anion is bound, although not close to the RSB. Large spectral red shifts under "salt-free" conditions were observed for the D230N (~7 nm) and E64Q/D230N (~10 nm) mutants, suggesting that chloride ions bind near N230 which is not possible in WT due to repulsion by the negatively charged D230. The larger SO_4^{2-} is not incorporated near the RSB in the E64Q and D230N mutants and subsequently no spectral shifts are observed.

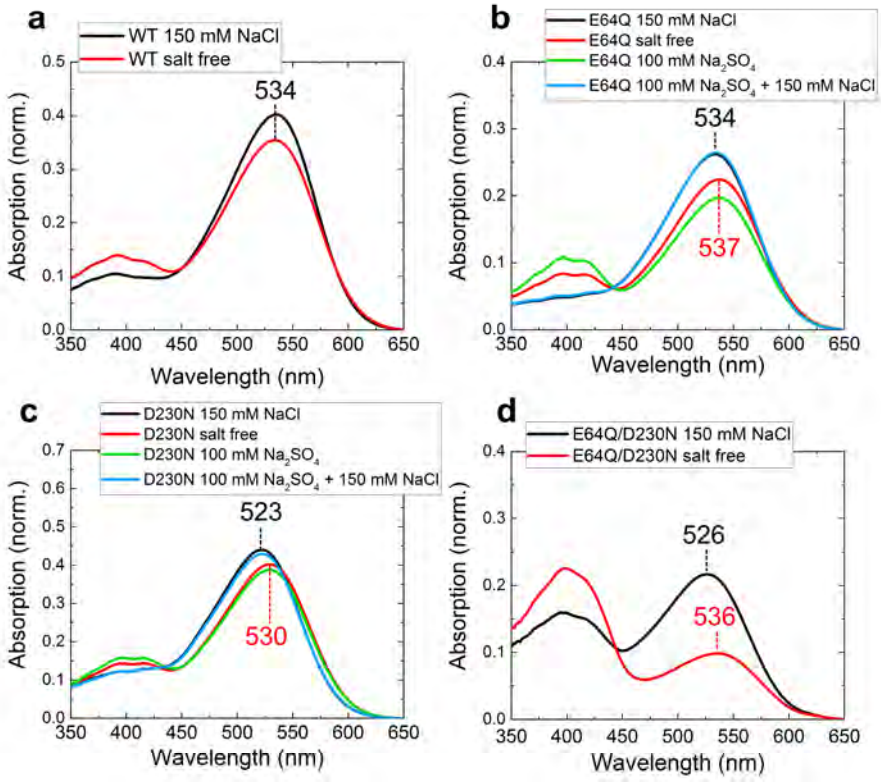

Figure 3.3. Dark-state absorption of *Ps*ACR1 and its mutants in different anion conditions at pH 7.

Excited-state dynamic and isomerization

We performed transient absorption spectroscopy on WT *Ps*ACR1 and the E64Q mutant (pH 8) with an electronically synchronized pair of Ti:Sapphire laser systems[42,133]. Selected fs-ps transient absorption spectra of WT *Ps*ACR1 are shown in **Fig. 3.4a**. At 100 fs, a positive band at ~480 nm and negative bands at ~560 nm and 720 nm are observed, which are assigned to excited-state absorption (ESA), ground-state bleach (GSB) and stimulated emission (SE), respectively. In the evolution up to 500 fs, an additional positive band appeared at ~610 nm, which was blue-shifted to ~600 nm after several picoseconds. Transient absorption spectra up to 400 μs were evaluated by global analysis to quantify the spectral evolution. Nine exponential components were required for adequate fitting: 100 fs, 500 fs, 2.2 ps, 14 ps, 760 ps, 27 ns, 390 ns, 180 μs and infinite (>400 μs). The evolution-associated difference spectra (EADS) of the first five components are shown in **Fig. 3.4b**, and selected time traces up to 10 ps are shown in **Fig. 3.4c**. The 1st EADS (dashed line) immediately formed after excitation exhibits ESA band around 550 nm and an SE band near 630 nm. Evolution to the 2nd EADS (red line) occurred within 100 fs and resulted in a blue shift of the ESA band to ~460 nm and red shift of the SE band to ~720-nm, indicating that the energy gap of S_1–S_n increases and S_1–S_0 decreases. Even though a cross-phase modulation artifact might contribute to the first spectrum, we assign the first 100 fs component to the relaxation from the Franck–Condon region. The population of the SE hardly changed in 100 fs, indicating that the excited-state population did not significantly decay in 100 fs.

In the 2nd EADS a negative peak emerged at ~560 nm and is assigned to GSB, resulting in a 160 nm gap between GSB and the SE (~720 nm). The observed Stokes shift of 160 nm is similar to the shift previously reported for bacteriorhodopsin[199]. Within 500 fs the formation of the first red-shifted photoproduct, assigned as the J intermediate in other microbial rhodopsins, is indicated by the rise at ~610 nm in the 3rd EADS (**Fig. 3.4b**; blue line). Since the formation of the J intermediate is characterized by the retinal isomerization from all-*trans* to 13-*cis* form, we conclude that the photoisomerization occurs in 500 fs in *Ps*ACR1. The isomerization time constant is similar to those of the chimeric channelrhodopsin C1C2 (~450 fs)[42], *Cr*ChR2 (~400 fs)[148,149] and also bacteriorhodopsin (~500 fs)[154], which is a model system for microbial rhodopsins. The ~10 nm blue shift of the ~610 nm absorbing species at 2.2 ps indicates the vibrational relaxation of the J intermediate, which converts into the K intermediate. The decays of the ESA (~460 nm), GSB (~560 nm)

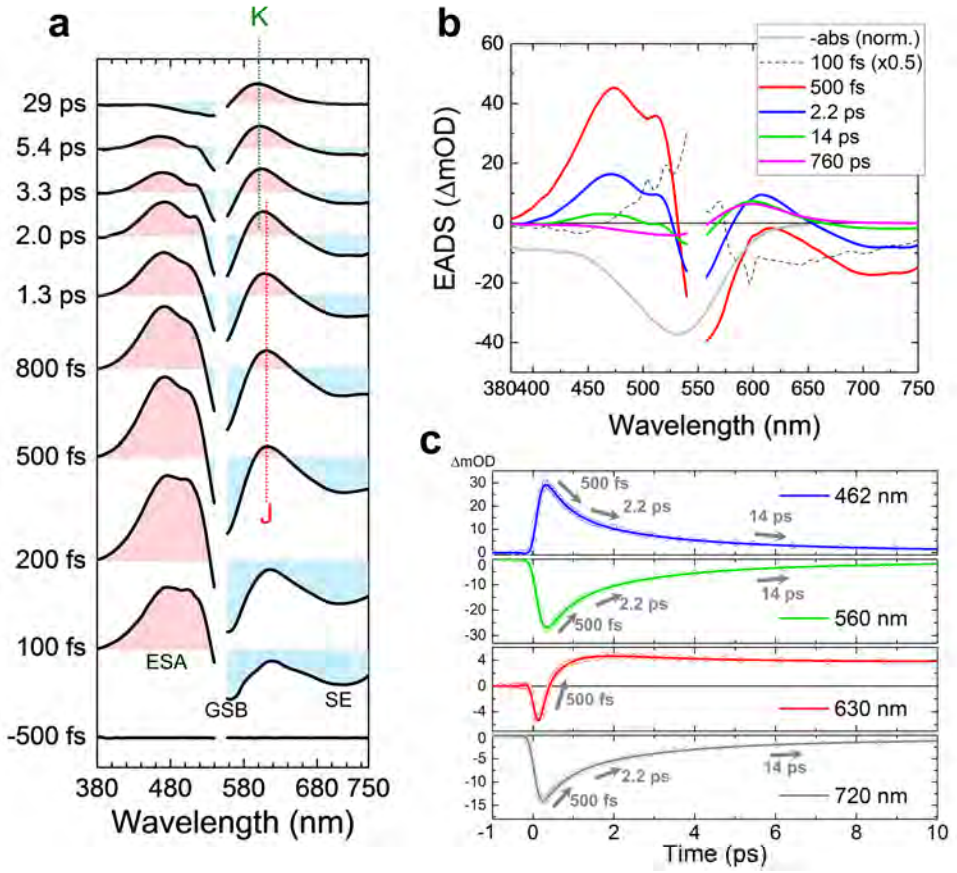

Figure 3.4. Femto-to-picosecond transient absorption spectra of wild-type PsACR1 at pH 8. (a) Selected transient absorption spectra up to 29 ps. The photointermediates 'J' and 'K' are indicated with positive bands at 610 nm and 600 nm, respectively. ESA, GSB and SE stand for excited-state absorption, ground-state bleach and stimulated emission, respectively. (b) Evolution-associated difference spectra (EADS) of fs–ps transient absorption spectra. The grey curve represents the inverted normalized dark-state absorption for comparison with the GSB. The spectral region of 540–560 nm is omitted due to the strong pump-light scattering in (a) and (b). (c) Time traces up to 10 ps at 462 nm (blue), 560 nm (green), 630 nm (red) and 720 nm (gray), which indicate ESA, GSB, photoproduct absorption and SE, respectively. Time constants (t) are depicted (grey arrows).

and SE (~720 nm) in 500 fs and 2.2 ps imply that relaxation from the excited state to the dark state proceeds simultaneously with photointermediate formation. However, in 14 ps, no signal development was seen in the photoproduct state, indicating a non-productive excited-state decay in *Ps*ACR1 similar to that observed in cation channelrhodopsin C1C2[42]. After the decay of the 14 ps component, the pure K-intermediate spectra appeared (magenta line, in **Fig. 3.4b**), which developed to the next photoproduct in 760 ps.

Properties of the E64 in the ultrafast reaction: a counterion switch?

The transient absorption spectra of the E64Q mutant at pH 8 were similarly fitted with nine exponential components, as the WT. The time constants of the first five time components were almost identical to the WT, while the signal amplitudes of the components were slightly different (**Fig. 3.5a**). This implies that E64 does not influence the isomerization rate. A significant red shift of 7 nm in the E64Q mutant was seen in the absorption maximum of the positive band near ~600 nm that represents the K state (**Fig. 3.6a**). This indicates that E64 influences the hydrogen bond network of the RSB in the K intermediate, but not in the dark state, in which the absorption of the E64Q is almost identical to the WT (**Fig. 3.1c**). Hence, the hydrogen bond network is rearranged upon photoisomerization involving E64 that either directly forms a hydrogen bond to the RSB or influences nearby water molecules.

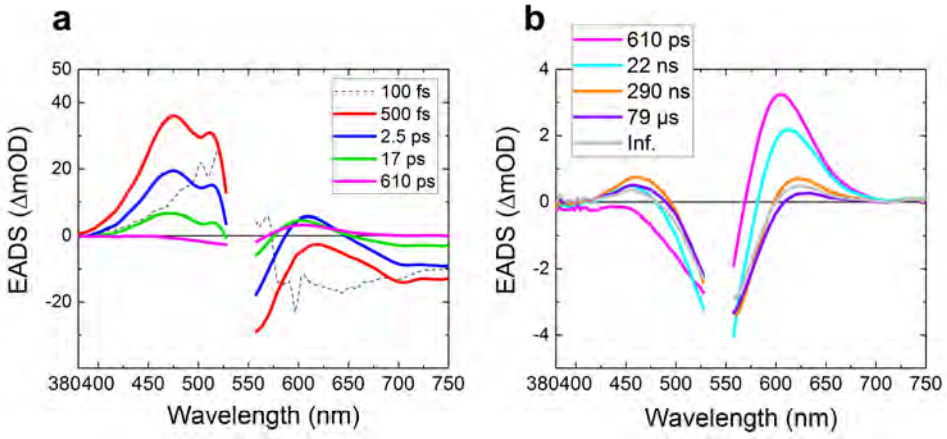

Figure 3.5. EADS of fs-µs transient absorption spectra of *Ps*ACR1/E64Q at pH 8. The spectral region of 540–560 nm is omitted because of the strong pump-light scattering.

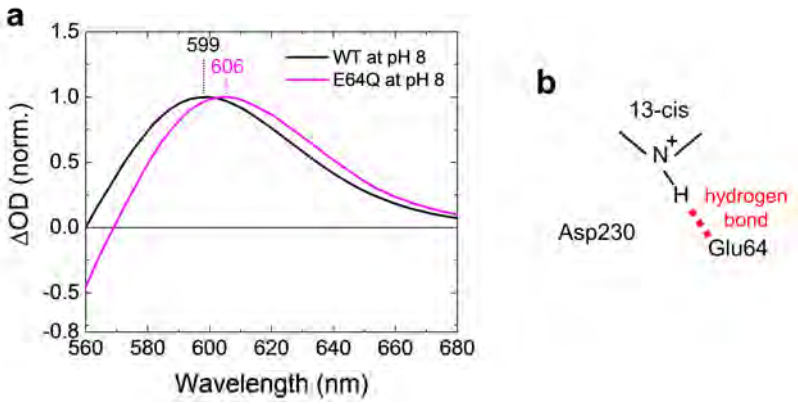

Figure 3.6. K-intermediate hydrogen bond model of the protonated retinal Schiff base in *Ps*ACR1. (**a**) Normalized spectra of the fifth EADS in **Fig. 3.4b** (for WT, decaying with 760 ps) and **Fig. 3.5** (for the E64Q mutant, decaying in 610 ps) are shown. (**b**) Hydrogen bond model of the retinal Schiff base in the K intermediate of wild-type *Ps*ACR1.

Nanosecond-to-second photoproduct dynamics

The combination of ultrafast transient absorption spectroscopy and flash photolysis overlapping four decades in time (40 ns to 400 µs) allows us to discuss the photoproduct dynamics quantitatively and in more detail than before[55]. Furthermore, all spectroscopic measurements have been performed using the same batch of purified protein to minimize the influence of possible batch to batch variation. **Fig. 3.7a** shows the last five components of the globally-fitted spectra of femto-to-submillisecond transient absorption spectra of WT *Ps*ACR1 at pH 8; involve spectral evolution with time constants of 760 ps, 27 ns, 390 ns, 180 µs and infinite (>400 µs). In **Fig. 3.7b**, selected time traces between 100 ps and 400 µs are shown. The positive peak at ~600-nm associated with the K intermediate decreased in 760 ps, 27 ns and 390 ns, while positive absorption at ~440–500 nm (assigned as an L intermediate[7]) increased simultaneously (**Fig. 3.7**). The K-state signal partially remained while the L intermediate was populated, indicating a K/L equilibrium state[41] that evolves in multiple steps, the 27 ns process being dominant. In *Gt*ACR1, a similar K/L equilibrium was reported at the room temparature[193] and at 80 K[200]. In 180 µs, the L positive absorption decreased, while the K absorption rose again, indicating that the K/L equilibrium was re-established in favor of K. The E64Q mutant showed a similar spectral evolution with time constants of 610 ps, 22 ns and 290 ns (**Fig. 3.5b**).

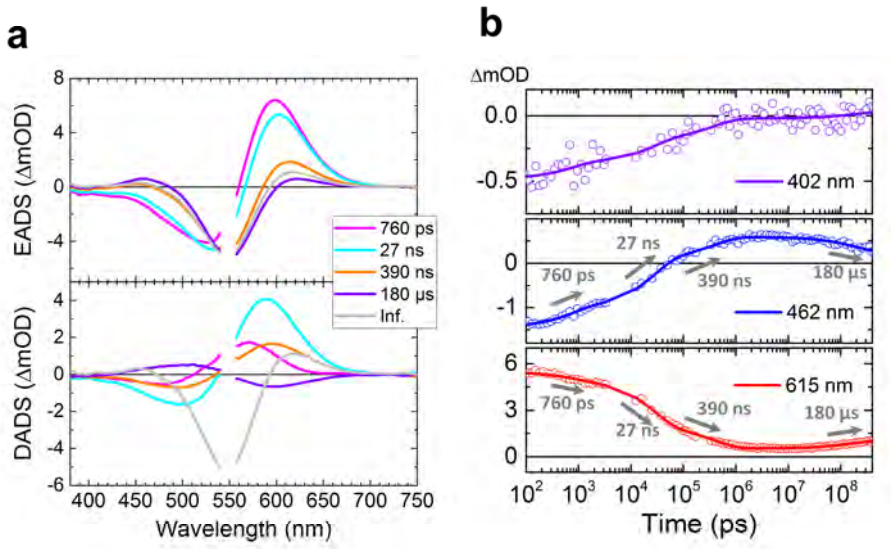

Figure 3.7. Globally-fitted picosecond-to-submillisecond transient absorption spectra of wild-type *Ps*ACR1 at pH 8. (**a**) EADS (top) and DADS (bottom) fitted with time constants of 760 ps, 27 ns, 390 ns, 180 µs and infinite (>400 µs). The spectral region of 540–560 nm is omitted because of the strong pump-light scattering. (**b**) Time traces from 100 ps to 400 µs at 402 nm (purple), 462 nm (blue) and 615 nm (red). The open dots show raw data, and the solid lines depict fitted curves. Time constants (τ) are depicted with grey arrows.

It is reported that the following M intermediate (an indicator of deprotonated RSB) appears in ~20 ms in WT *Ps*ACR1[55], which is out of the time range of the femto-to-submillisecond spectroscopy. To access the timescales up to seconds and investigate the deprotonation process in detail, flash photolysis experiments were performed for WT *Ps*ACR1, the E64Q, D230N and E64Q/D230N mutants at pH 8. The flash photolysis data were globally fitted, and the time traces normalized among datasets with fitting curves are shown in **Fig. 3.8**. In WT, the spectral evolution was essentially identical to the previous experiments[55]. In 26 ms, a substantial rise of the 400-nm peak was observed, accompanied by signal decrease at 460 nm (L state or P_{460}[55]) and 615 nm (named as K_2 state), which indicates formation of the deprotonated RSB (*i.e.*, M-intermediate formation)[7]. Significantly, the channel closing mainly proceeds in 4.8 and 41 ms in *Ps*ACR1 (-60 mV holding voltage) and in contrast to *Gt*ARC1 it was only weakly influenced by the membrane voltage[56]. Therefore it can be suggested that the M-intermediate formation is involved in the channel closing.

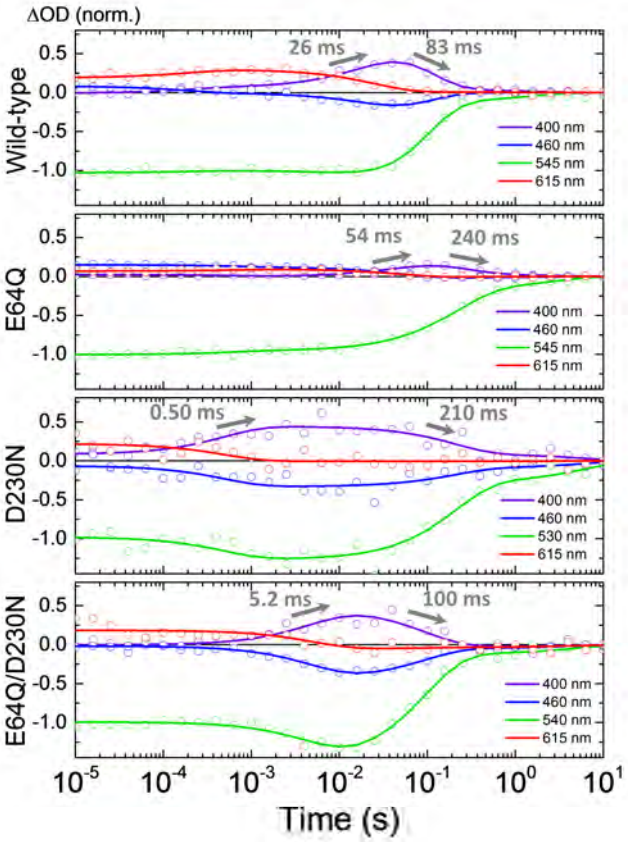

Figure 3.8. Normalized time traces of transient absorption of wild-type *Ps*ACR1 and the E64Q, D230N and E64Q/D230N mutants at pH 8 between 10 µs and 10 s. The open dots show raw data, and the solid lines depict fitted curves. Time constants (τ) of M rise and decay are illustrated (grey arrows).

The closing rate is similar to *Gt*ACR1 in which M formation is correlated to the fast channel closing (~20 ms) under absence of holding voltage[193]. In 83 ms, the positive signal at ~400 nm and the negative signal at 545 nm mostly decayed, implying that the RSB was reprotonated. In 1.6 s, the transient absorption components entirely decayed resulting in the completion of the photocycle.

The E64Q mutation significantly slowed down the formation of the M state compared to the WT. Notably, the relative signal intensity of the 400 nm signal in the E64Q mutant was ~3-fold weaker than the WT. These observations imply that E64 is

involved in the deprotonation of RSB and presumably works as a primary proton acceptor during the M-state formation in the WT. Regardless, deprotonation of the RSB is still present in the E64Q mutant, indicating that other residues, ions or water molecules may serve as alternative proton acceptors. In the D230N mutant, the M-state rise was accelerated relative to WT while the relative M-population was almost the same.

Significantly, deprotonation (5.2 ms; ~5-fold faster than WT) of the RSB proceeds even in the E64Q/D230N mutant lacking both protonable residues, which underlies the presence of alternative proton transfer routes. As noted above, the hydrogen bond network around the RSB is influenced by a Cl^- ion in the D230N and E64Q/D230N mutants, which may account for the fast M-state formation.

Comparison of PsACR1 and GtACR1

Substitution of E64 (E68 in *Gt*ACR1) by glutamine (Q64) only marginally influences the dark-state absorption spectrum of both *Ps*ACR1 (**Fig. 3.1c**) and *Gt*ACR1[193], but abolished the pH dependency of the chromophore absorption at high pH[193] (**Fig. 3.2**). Moreover, Sineshchekov *et al.* concluded that E68 in *Gt*ACR1 works as the primary counterion in *Gt*ACR1[193] corresponding to our interpretation of *Ps*ACR1 photodynamics measurements. There are several common characteristics of the photochemistry between *Ps*ACR1 and *Gt*ACR1: *e.g.* slower M-state formation (~20 ms) than other microbial rhodopsins (<100 µs)[42,62,195-197,201], formation of K/L equilibrium intermediate[193,200], and reduced M-intermediate formation upon mutation of E64Q (E68Q in *Gt*ACR1)[193].

A major difference is seen in the K-intermediate absorption: where a red shift is observed with the E64 → Q64 substitution in *Ps*ACR1, indicating that E64 plays a significant role in the hydrogen-bond network near the RSB in the K intermediate (**Fig. 3.6**). In contrast, low-temperature UV/Vis absorption and FT-IR spectroscopy showed no significant absorption-peak difference of the K intermediate between the WT and the E68Q mutant for *Gt*ACR1[200]. These observations indicate that the difference of the photochemistry between *Gt*ACR1 and *Ps*ACR1 already appears early after the photoisomerization on a fs-ps time scale

Notably, the mutation of D234 to asparagine (N234) in *Gt*ACR1 does not change the dark-state absorption[193], while a significant blue shift was observed for the D230N mutant of *Ps*ACR1 (**Fig. 3.1c**). Possibly, this difference derives from the altered Cl^- accessibility to the RSB introduced by the D230N substitution of *Ps*ACR1.

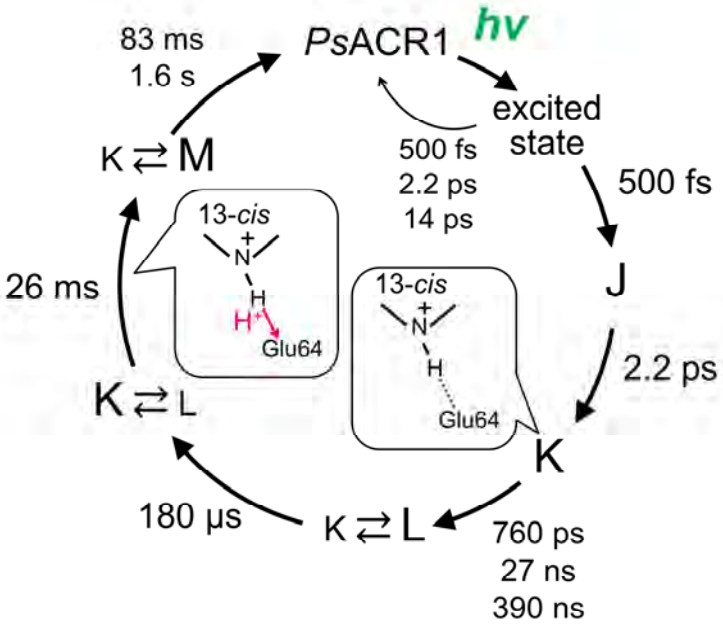

Figure 3.9. Complete photocycle model of wild-type *Ps*ACR1 at pH 8 from femtoseconds to seconds. Proposed hydrogen-bonding interaction near the retinal Schiff base in the K intermediate and a proton transfer reaction are shown (balloons).

3.3. Conclusion

In this chapter, the photochemistry of red-shifted fast-closing anion channelrhodopsin *Ps*ACR1 in the dark state and femtosecond-to-second transient states were investigated, utilizing femto-to-submillisecond transient absorption spectroscopy, flash photolysis and point mutations of acidic residues close to the RSB: E64 and D230. In the dark state, E64 does contribute to the RSB hydrogen-bond network of *Ps*ACR1 at neutral pH. We conclude that no interchangeable chloride ions are present close to the RSB. However, with substitution of D230 by N230, accessibility for Cl^- to the RSB is increased in the dark state. To summarize the femtosecond-to-second photoreactions of *Ps*ACR1, we propose a complete photocycle model with putative hydrogen-bonding interaction as well as proton transfer reaction in **Fig. 3.9**. The photoisomerization occurs in ~500 fs (J formation) and hydrogen-bond network near the RSB is rearranged in the K intermediate (evolved in 2.2 ps) with a strong involvement of E64. The following L intermediate appears with three time

constants: 760 ps, 27 ns and 390 ns; forming a K/L equilibrium. In 180 µs, the K/L equilibrium is shifted in favor of K. The M-intermediate is formed at 26 ms and decayed in 83 ms. The dark state recovers in 1.6 s. The observed time constants are similar to previously reported ones[55]. Furthermore, it is suggested that E64 works as the primary proton acceptor on the M-intermediate formation, although alternative proton acceptors likely exist in *Ps*ACR1.

Methods

Protein purification: For protein expression in *Pichia pastoris*, humanized *Ps*ACR1-encoding DNA sequence was cloned with C-terminal 6xHis-Tag into a pPICZ vector (Thermo Fisher Scientific, Waltham, MA, USA). Site-directed mutagenesis was performed according to the protocol from Agilent Technologies Inc., USA. Cell transformation, selection of recombinant clones, and expression have been performed mainly following the instruction of the manufacturer (Thermo Fisher Scientific, Waltham, MA, USA). Cells were harvested 24 h post-induction and lysed using a high pressure homogenizer (HTU Digi-French-Press, G. Heinemann, Germany). After preparation of the membrane fraction recombinant rhodopsin was solubilized with 1% (w/v) dodecylmaltoside (DDM, Glycon, Luckenwalde, Germany). The protein was purified by affinity-chromatography and gel-filtration (HisTrap FF Crude/HiLoad 16/600 Superdex 200 - all from GE Healthcare, Chalfont St. Giles, UK) and concentrated in 20 mM TRIS pH 8.0, 150 mM NaCl and 0.02% DDM using amicon ultra centrifugal filters with a molecular weight cutoff of 100 kDa (Merck Millipore Ltd., Ireland). For different salt conditions the buffer was changed by concentrators to 50 mM MOPS pH 7.0, 0.02% DDM either containing no salt, 150 mM NaCl or 100 mM Na_2SO_4.

Stationary UV-vis spectroscopy: Absorption spectra were recorded by a Cary 50 Bio spectrophotometer (Varian Inc., Palo Alto, USA) at 22°C. pH titration have been performed by adding small amounts of 1 M HCl or 1 M NaOH to samples buffered in equal molarity (20 mM) of citrate pH 5, Tris pH 8, CAPS pH 10, 150 mM NaCl, 0.02% DDM.

Femtosecond-to-submillisecond transient absorption spectroscopy: Transient absorption measurements were performed with a femtosecond-to-submillisecond pump-probe setup as reported previously[41,42,133]. A CaF_2 plate with a moving holder was used for supercontinuum white light generation, and a selected wavelength region: 380–750 nm, was detected by the photodiode array. The time delay was varied up to 430 µs at 163 data points with the minimum temporal step of 50 fs. The diameters of the pump and the probe beams at the sample position were ~200 µm and ~100 µm, respectively. The wavelength of the pump beam was centered at 550 nm, and the power was attenuated to ~300–400 nJ. The instrumental response function was ~100 fs, estimated from global analysis. The samples were filled in a homemade sample holder that has two 2-mm-thick CaF_2 plates[41]. The sample thickness was set as 400 µm with an appropriate sample spacer. The sample holder was set on the Lissajous scanner that

ensures sample refreshment after each laser shot with a time interval of 60 seconds between successive exposures to the laser pulses[41].

Flash photolysis: Microsecond-to-second transient absorption spectra were obtained with LKS.60 flash photolysis system (Applied Photophysics Ltd., Leatherhead, UK) as reported previously[65,202]. The aforementioned system is equipped with a tunable optical parametric oscillator (Rainbow, MagicPrism, Opotek Inc., Carlsbad, CA, USA), which was pumped by the third harmonic of a Nd:YAG laser (Brilliant B, Quantel, Les Ulis Cedex, France). Absorption changes between 350 and 700 nm were detected by an Andor iStar ICCD Camera (Andor Technology, Belfast, Northern Ireland). Samples were excited with a laser pulse adjusted to 530 nm with energy of 3 mJ/shot and pulse duration of 10 ns. A short-arc XBO Xenon lamp (150 W, Osram, München, Germany) was used as probe light. The transient spectra were recorded with intensified CCD camera at 46 time points between 10 ns and 10 s (5 data points/ decade, isologarithmically). Due to laser artifacts and scattering only spectra taken in time window of 1 μs–10 s were used for further analysis. The data sets were averaged over 15 cycles for each of the sample.

Chapter 4

The photochemistry of light-driven Na⁺ pump probed by transient stimulated Raman spectroscopy

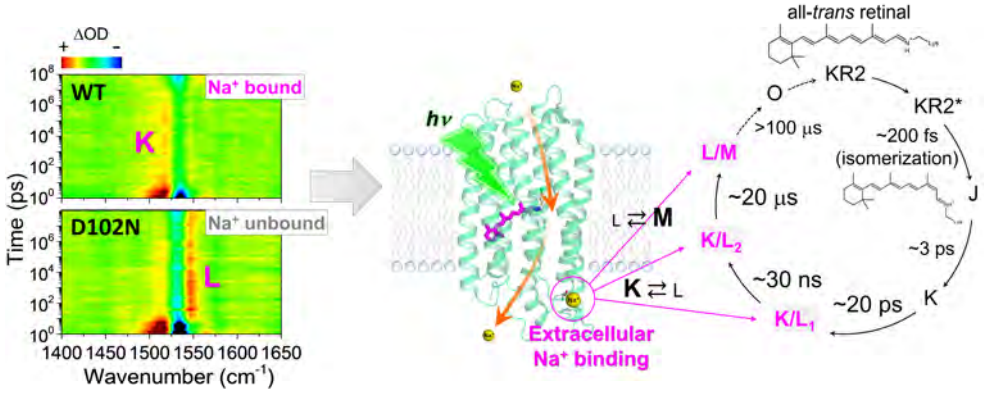

The femtosecond-to-submillisecond photocycle of Na⁺ pump rhodopsin KR2 was revealed through watermarked stimulated Raman spectroscopy.

Abstract

Krokinobacter rhodopsin 2 (KR2) is a recently discovered light-driven Na^+ pump that holds significant promise for application as a neural silencer in optogenetics. KR2 transports Na^+ (in NaCl solution) or H^+ (in larger cation solution, *e.g.* in CsCl) during its photocycle. In this chapter, the photochemistry of KR2 is described with femto- to submillisecond transient stimulated Raman spectroscopy (TSRS). A new photocycle from femtoseconds to submilliseconds is proposed: J (formed in ~200 fs) → K (~3 ps) → K/L_1 (~20 ps) → K/L_2 (~30 ns) → L/M (~20 µs). KR2 binds a Na^+ ion that is not transported on the extracellular side, of which the function is unclear. We demonstrate with TSRS that for the D102N mutant in NaCl (with Na^+ unbound, Na^+ transport) and for WT KR2 in CsCl (with Na^+ unbound, H^+ transport), the extracellular Na^+ binding significantly influences the intermediate K/L/M state equilibrium on the photocycle, while the identity of the transported ion, Na^+ or H^+, does not affect the photocycle.

This chapter is based on the following publication:
Physical Chemistry Chemical Physics **18**, 24729 (2016),
collaborated with K. Inoue, Y. Kato and H. Kandori for sample purification.

4.1. Introduction

Krokinobacter rhodopsin 2 (KR2) is the first identified outward sodium ion (Na^+) pump rhodopsin (NaR) reported in 2013[62]. KR2 is composed of seven trans-membrane helices (TM1–TM7), and covalently binds a common chromophore, all-*trans* retinal, which undergoes the isomerization to 13-*cis* form upon photon absorption. With the unique ability of the unidirectional Na^+ pump, KR2 is of great interest in optogenetic applications as a neural silencer[66,204]. The crystal structures of the pentameric state of KR2 were solved by Gushchin *et al.* in 2015[203], which showed that Na^+ binding exists on the extracellular side of the interfaces between two different protomers. This binding site consists of Tyr25 (on TM1), Thr87 and main chain carbonyl groups of Thr83 and Phe86 (on TM2) of the same protomer, Asp102 (on the loop between TM2 and TM3) of the neighboring protomer and two water molecules (**Fig. 4.1a**). Importantly, the Na^+ ions on this binding site are not the ones that are transported[62,203]. Moreover, it was reported that the D102N mutant of KR2

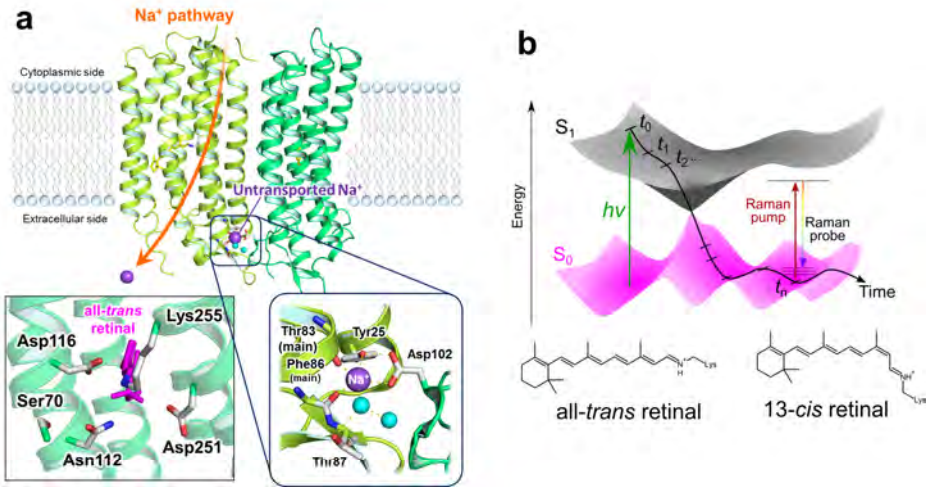

Figure 4.1. The extracellular Na^+ binding site of KR2 and a schematic diagram of transient stimulated Raman spectroscopy. (**a**), **A** crystal structure of KR2[203] (PDB ID: 4XTN) and close-up of the retinal binding pocket and the Na^+ binding site on the extracellular side. The Na^+ binding site consists of Tyr25 (on TM1), Thr87 and main chain carbonyl groups of Thr83 and Phe86 (on TM2) of the same protomer, Asp102 (on the loop between TM2 and TM3) of the neighboring protomer and two water molecules. (**b**) A schematic diagram of transient stimulated Raman spectroscopy. A narrowband Raman pump (~800 nm) and a broadband Raman probe (~840–960 nm) are applied simultaneously after a time delay. The time delay was varied from -50 ps to 110 μs with the shortest step of 50 fs.

does not bind Na^+ on the extracellular binding site, but still pumps Na^+ as well as WT KR2[66]. KR2 also pumps Li^+, but transports only H^+ in the absence of Na^+ and Li^+, *e.g.* in solution containing only larger cations such as K^+, Rb^+ and Cs^+ [62,66]. Attenuated total reflection-Fourier transform infrared (ATR-FTIR) studies showed K^+, Rb^+ and Cs^+ do not bind to the ion binding site on the extracellular side of KR2[62,66].

A femtosecond transient absorption study indicated that KR2 has a J intermediate, which is a vibrationally excited state of the primary photoproduct[154,205], and a K intermediate, which is the vibrationally relaxed primary photoproduct[205,206], as other microbial rhodopsins[207]. Furthermore, flash photolysis experiments showed that an L/M intermediate, which is an equilibrium of L and M states, is formed in ~20 μs[62]. According to the crystal structure of the L intermediate of bacteriorhodopsin, the retinal Schiff base is located closer to the counterions in the L intermediate than in the K intermediate[208,209]. The M state is a typical intermediate that appears after proton transfer from the retinal Schiff base to a counterion[7]. Subsequently, an O intermediate, in which a proton is reconstituted to the 13-*cis* retinal[7], is formed in ~1 ms, and goes back to the initial ground state in a few tens of milliseconds[62]. According to the crystal structures reported by Kato *et al.* in 2015[66], it is suggested that Asp116 flips in the M-like intermediate with the proton transfer from the retinal Schiff base to Asp116, resulting in opening the pathway of Na^+ transport near the retinal Schiff base. Thus, it is considered that the retinal plays important roles not only in triggering the photoreaction, but also in the Na^+ pump function. Therefore, observation of the retinal dynamics in earlier time regions than the L/M formation is essential to clarify the molecular mechanism of KR2.

Femtosecond stimulated Raman spectroscopy (FSRS) is a time-resolved vibrational spectroscopy that features high temporal (~100 fs) and spectral (<10 cm^{-1}) resolutions (**Fig. 4.1b**)[135] and broadband spectral detection. When the wavelength of the Raman pump is tuned resonant or pre-resonant for the chromophore, chromophore-specific observation is possible without disturbance by signals from the protein backbone and side chains. As a major drawback of FSRS, it suffers from notorious problems that arise from unpredictable high-amplitude baselines[137]. Recently, we solved these baseline problems with a spectral watermarking approach, involving shaping of the Raman pump in combination with wavelet transform of pseudorandomly generated watermarks, which enables us to automatically eliminate the baseline and minimize the fixed-pattern noise of the CCD detectors. Furthermore, we have extended the FSRS technique with wide-range continuous time delays from ~10^{-14} s to ~10^{-4} s utilizing synchronized ultrafast Ti:Sapphire amplifiers[133], which

enables us to investigate chromophore dynamics from femtoseconds to submilliseconds in detail in a single experiment. We call this technique Transient Stimulated Raman Spectroscopy (TSRS).

Here we present femto- to submillisecond TSRS results on WT KR2 in NaCl (Na^+ bound, Na^+ transport), the D102N mutant in NaCl (Na^+ unbound, Na^+ transport) and WT KR2 in CsCl (Na^+ unbound, H^+ transport). With the spectral data, we will discuss the retinal dynamics on the excited state and the photoproduct states up to the L/M intermediate formation. Moreover, we will show that the extracellular Na^+ binding significantly affects the ps-μs retinal chromophore dynamics, and that the identity of the transported ion, H^+ or Na^+, does not affect the ps-μs reaction.

4.2. Results

Femto- to submillisecond transient absorption spectroscopy

For reference, we first applied femto- to submillisecond UV-vis transient absorption spectroscopy to KR2. The time-resolved data were globally analyzed in terms of a kinetic model of sequentially interconverting species with increasing time constants[140], **Fig. 4.2** shows steady state absorption spectra and globally fitted transient absorption spectra (evolution-associated difference spectra, EADS, and decay-associated difference spectra, DADS) of WT KR2 in NaCl up to 150 μs. Nine components were required to adequately represent the transient absorption data with the following time constants: 20 fs, 170 fs, 420 fs, 2.4 ps, 29 ps, 6.5 ns, 370 ns, 18 μs and infinity. The decay components up to 100 ps are consistent with recently reported femtosecond pump-probe spectroscopy of KR2[207], and the 18-μs decay component corresponds to the ~26-μs component in the flash photolysis experiment[62]. The first component of the global fitting was created immediately after photon absorption, possibly mixed as a precursor state and a coherent artifact from overlapping of pump and probe pulses. On the second component, typical peaks assigned as exited state absorption (ESA, at ~480 nm and at ~630 nm), ground state bleach (GSB, at ~550 nm) and stimulated emission (SE, at > ~680 nm) were seen. Those peaks apparently overlap each other, influencing the intensity and the peak positions. The positive signals on the EADS consist of ESA and/or photoproducts. Transient absorption spectra of KR2/D102N in NaCl and WT KR2 in CsCl were also globally fitted with nine exponential components as well as WT KR2 in NaCl. No significant difference was seen on the transient absorption spectra of the three different sample conditions within the spectral resolution. The time constants of the transient absorption spectra are shown in **Table 4.1**.

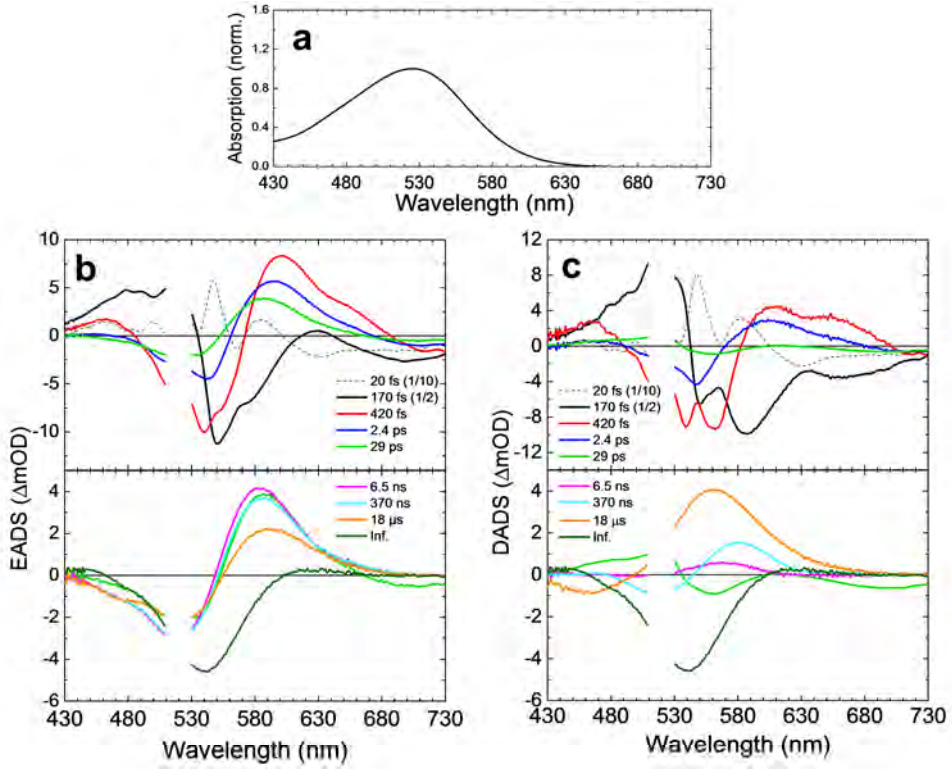

Figure 4.2. Steady state and transient absorption spectra of WT KR2 in NaCl. (**a**) Steady state absorption of WT KR2 in NaCl. Globally fitted transient absorption spectra ((**b**) EADS and (**c**) DADS) of WT KR2 in NaCl. The first five (top) and the following four (bottom) time components are shown separately. Spectra at 510–530 nm on transient absorption spectra are cut because of the strong pump light scattering. The components of 20 fs and 170 fs are scaled down by a factor of 10 and 2, respectively. The 29-ps component is shown on both of the top and the bottom figures for reference.

Femto- to submillisecond transient stimulated Raman spectroscopy

Fig. 4.3a shows baseline-free stimulated Raman spectra on the ground state with all-*trans* retinal in WT KR2 in NaCl, KR2/D102N in NaCl and WT KR2 in CsCl. The ground state Raman spectra were almost identical between WT KR2 in NaCl and CsCl, and KR2/D102N mutant. The 1532 cm^{-1} band is assigned as the C=C ethylenic stretching mode[210,211], The 1169 cm^{-1} and 1201 cm^{-1} bands are assigned as C–C stretching mode[211,212]. Typical hydrogen out-of-plane (HOOP) vibrational modes were seen at 831 and 884 cm^{-1},

Table 4.1. Time constants of global fitting on transient absorption spectra in WT KR2 in NaCl, KR2/D102N in NaCl and WT KR2 in CsCl.

Transient absorption	τ_1	τ_2	τ_3	τ_4	τ_5	τ_6	τ_7	τ_8	τ_9
WT KR2 in NaCl	20 fs	170 fs	420 fs	2.4 ps	29 ps	6.5 ns	370 ns	18 μs	inf.
KR2/D102N in NaCl	20 fs	190 fs	570 fs	3.0 ps	28 ps	6.5 ns	450 ns	19 μs	inf.
WT KR2 in CsCl	20 fs	180 fs	500 fs	4.0 ps	34 ps	6.5 ns	320 ns	20 μs	inf.

and methyl rocking mode was observed at 1009 cm^{-1} [211,212]. In **Fig. 4.3b**, transient stimulated Raman spectra of WT KR2 in NaCl at selected time delays are shown, represented as the difference stimulated Raman spectrum between actinic pulse on minus actinic pulse off. We prefer to show the TSRS spectra as such difference spectra instead of conventional reconstructed all-positive Raman spectra, because for the latter a certain amplitude of the ground-state stimulated Raman spectrum has to be added, which requires visual inspection and therefore introduces a bias. In total, TSRS spectra at 96 delays were recorded. Positive and negative transient Raman signals were seen in the HOOP (~800–1000 cm^{-1}), the C–C stretching (~1150–1250 cm^{-1}) and the C=C stretching (~1510–1560 cm^{-1}) regions, whose evolution will be shown with globally fitted data in detail.

The transient stimulated Raman spectra of WT KR2 were globally fitted with seven time components: 20 fs, 260 fs, 3.4 ps, 22 ps, 25 ns, 21 μs and infinity. The 20 fs component is probably a coherent artifact with the three-pulse mixing and is not further considered. **Fig. 4.4** shows EADS of the transient Raman spectra including HOOP, the C–C stretching and the C=C stretching regions. The negative signals show GSB, and the positive signals show Raman spectra on the excited state and/or photoproduct states. In the transient absorption measurement, SE was seen at a near-infrared region at very early delay times in KR2, so Raman initiated by nonlinear emission (RINE)[213] signals that decayed mostly with 260 fs were observed on the excited state because of the 800-nm Raman pump pulses. The difference in number of fitting components in the transient Raman (seven) and the transient absorption (nine) spectra probably results from a lower signal-to-noise ratio in the former. Significant spectral shifts on transient Raman signals were seen in C–C stretching region (**Fig. 4.4b**). Positive signals at 1156 and 1185 cm^{-1} appeared in 260 fs[212], while ground state

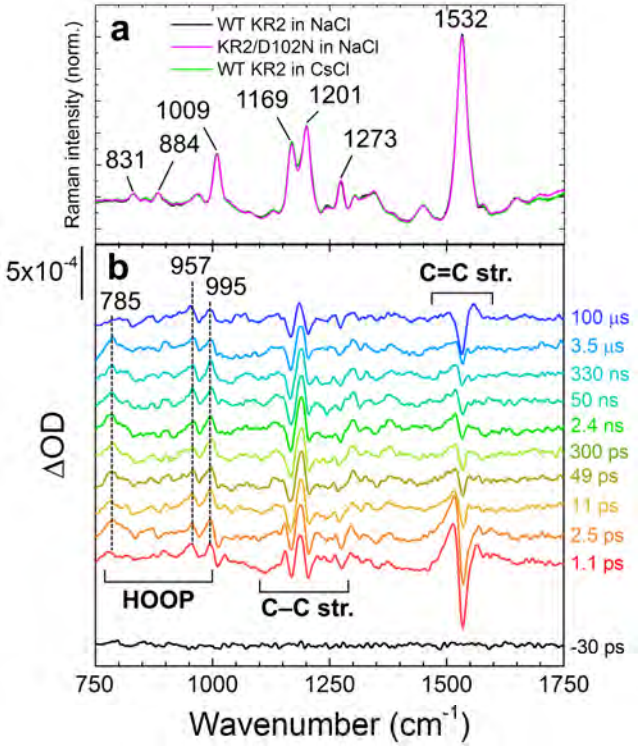

Figure 4.3. Baseline-free stimulated Raman spectra of WT KR2 in NaCl. (**a**) Ground state stimulated Raman spectra of WT KR2 in NaCl (black), KR2/D102N in NaCl (magenta) and WT KR2 in CsCl (light green). (**b**) Selected transient stimulated Raman spectra in WT KR2 in NaCl.

bleach signals at 1169 cm^{-1} and 1205 cm^{-1} were seen. Similar peaks at 1194 cm^{-1} (positive), 1167 and 1201 cm^{-1} (negative) reported in 77 K FT-IR experiments[212], indicating those peaks are derived from the 13-*cis* retinal isomer in the K intermediate.

In the C=C stretching region, a negative signal at around 1535 cm^{-1} was seen in the transient Raman spectra after 260 fs, which was continuous up to 100 μs (**Fig. 4.4c**). On the other hand, a positive signal at 1513 cm^{-1} appeared in 260 fs. Importantly, in 3.4 ps, the peak at 1513 cm^{-1} was blue-shifted to 1519 cm^{-1}. The third spectrum has a lifetime of 22 ps (blue spectra in **Fig. 4.4**) and is almost identical to the 77 K FT-IR experiments[212]. In 22 ps, the peak intensity at 1519 cm^{-1} decreased by a factor of 2, while a peak at 1547 cm^{-1} appeared. In 25 ns, the peak intensity at 1519 cm^{-1} was slightly increased, and that at 1547 cm^{-1} was decreased. In 21 μs, a positive peak at ~1560 cm^{-1} appeared. Simultaneously with the 1560

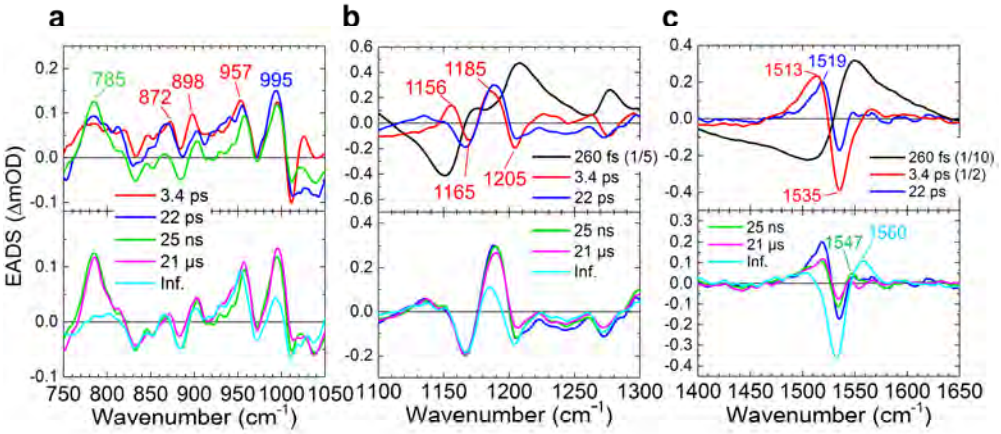

Figure 4.4. Globally fitted stimulated Raman spectra (EADS) of WT KR2 in NaCl. The signal evolves as 260 fs (black), 3.4 ps (red), 22 ps (blue), 25 ns (green), 21 μs (magenta) and an infinite time constant (cyan) in order. (**a**) EADS at 750–1050 cm^{-1} including the HOOP region. The 260-fs component is not shown. The first three (top) and the following two (bottom) time components are shown separately. The 25-ns component is shown on both of the top and the bottom figures for reference. EADS at (**b**) 1100–1300 cm^{-1} including the C–C stretching region and (**c**) 1400–1650 cm^{-1} including the C=C stretching region. The 260-fs (in **b** and **c**) and 3.4-ps (in **c**) components are scaled down. The first three (top) and the following three (bottom) time components are shown separately. The 22-ps component is shown on both of the top and the bottom figures for reference.

cm^{-1} signal appearance, the positive peak at 1519 cm^{-1} completely decayed while the signal at 1547 cm^{-1} remained.

Clearly, positive difference Raman signals were seen in the HOOP region (~800–1000 cm^{-1}); *e.g.* at 785, 872, 898, 957 and 995 cm^{-1} after 260 fs, while no clear negative bands appeared in the HOOP region. In 22 ps, HOOP signals at ~830–930 cm^{-1} dropped, while some strong positive signals remained up to 25 ns. Significant signal decrease of other peaks such as at 785 and 995 cm^{-1} was seen in 21 μs.

Similarly to WT KR2 in NaCl, transient Raman spectra of KR2/D102N in NaCl and KR2 WT in CsCl were globally fitted with seven exponential components. Transient Raman spectra from 1.0 ps to 100 μs are shown in **Fig. 4.5a–c. Fig. 4.5d** shows transient Raman spectra of WT KR2 in NaCl, KR2/D102N in NaCl and WT KR2 in CsCl at 4.5 ps, 50 ps, 480 ns and 100 μs. The spectra at 4.5 ps were similar between the three different samples. However, different features were seen at 50 ps and at 480 ns between WT KR2 in NaCl and the other two samples in the C=C stretching mode region; the ~1547 cm^{-1} peak gained amplitude as compared to the ~1519 cm^{-1} peak in KR2/D102N in NaCl and WT

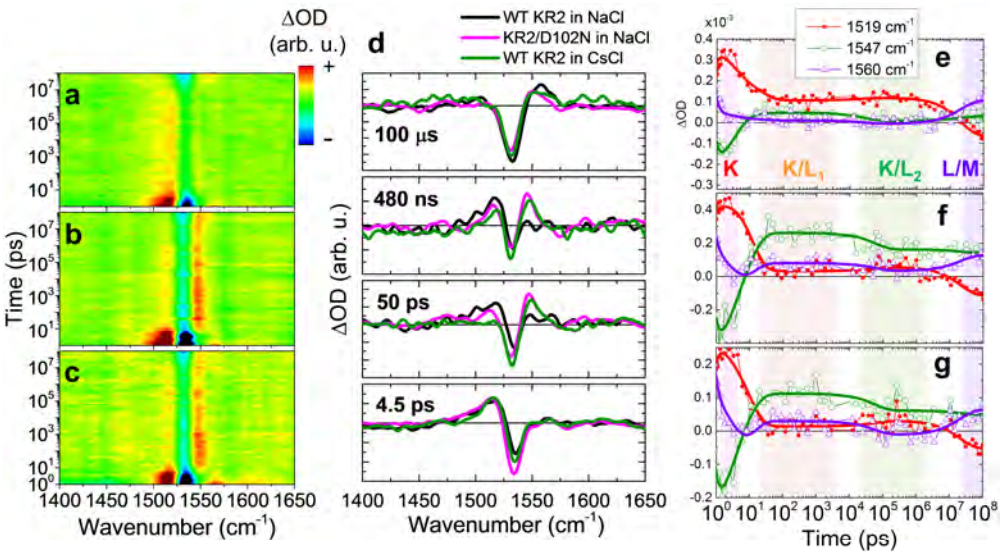

Figure 4.5. Transient stimulated Raman spectra in the C=C stretching region in WT KR2 in NaCl, KR2/D102N in NaCl and WT KR2 in CsCl. Two-dimensional false color representation of transient stimulated Raman spectra of (**a**) WT KR2 in NaCl, (**b**) KR2/D102N in NaCl and (**c**) WT KR2 in CsCl in the spectral region of 1400–1650 cm^{-1}. The difference Raman signals are color-coded as red for positive, green for zero and blue for negative. **d,** Normalized transient Raman spectra of WT KR2 in NaCl (black), KR2/D102N in NaCl (magenta) and WT KR2 in CsCl (light green) at 4.5 ps, 50 ps, 480 ns and 100 μs. Time traces of stimulated Raman signals at 1519 cm^{-1} (red closed dots with a red fitting line), 1547 cm^{-1} (open green dots with a green fitting line) and 1560 cm^{-1} (open purple triangles with a purple fitting line) in (**e**) WT KR2 in NaCl, (**f**) KR2/D102N in NaCl and (**g**) WT KR2 in CsCl.

KR2 in CsCl, while the ~1519 cm^{-1} peak was more significant in WT KR2 in NaCl. At 100 μs, the ~1560 cm^{-1} signal appeared in all of the three samples while the ~1547 cm^{-1} signal remained in KR2/D102N in NaCl and WT KR2 in CsCl. Notably, the characteristics of the transient Raman spectra of KR2/D102N in NaCl and WT KR2 in CsCl were very similar up to 100 μs. In **Fig. 4.5e–f**, the evolution of signals at 1519 cm^{-1}, 1547 cm^{-1} and 1560 cm^{-1} are shown. In ~20 ps, the 1547 cm^{-1} signal rose above that of 1519 cm^{-1} in KR2/D102N in NaCl and WT KR2 in CsCl, differently from WT KR2 in NaCl. In ~60 ns, the signal at 1519 cm^{-1} slightly rose again, while the 1547 cm^{-1} signal decayed in the three different samples. In ~20 μs, a blue-shifted peak appeared at 1560 cm^{-1} as in WT KR2 in NaCl, but the 1547 cm^{-1} signal remained at a higher amplitude in KR2/D102N in NaCl and WT KR2 in CsCl than in WT KR2 in NaCl.

4.3. Discussion

With femtosecond-to-picosecond time resolved stimulated Raman spectra, we discuss the excited-state dynamics and the retinal isomerization. The 260-fs decay of the RINE signals, which result from non-linear emission on the excited state[213], implies excited-state population decays mostly in 260 fs. Since typical vibrational peaks from 13-*cis* retinal (1185 cm^{-1})[212] appeared in 260 fs with the ground state bleach at 1165 and 1205 cm^{-1}, it is clearly shown that the first isomerized J intermediate is formed in 260 fs. The ~200-fs J-intermediate formation can be also characterized by transient absorption spectra (**Fig. 4.2b**); in ~200 fs, the red-shifted species at 602 nm appeared with the significant decay of the stimulated emission (**Fig. 4.2b**), which indicates the first photoproduct J intermediate is formed in ~200 fs[207]. Because the frequency of the C=C stretching mode is correlated with the retinal absorption energy, it is considered that the red-shifted C=C stretching mode (1513 cm^{-1}) corresponds to the J-intermediate (**Fig. 4.4c**). Notably, the appearance of the positive HOOP signals after the J-intermediate formation indicates the 13-*cis* retinal is markedly distorted compared to the all-*trans* retinal, as previously shown in bacteriorhodopsin[214].

Here we discuss the J-to-K state transition, which is interpreted as a vibrational cooling on the primary photoproduct state. When the system relaxes to the bottom of the potential energy well, the energy gap for the electronic transition to higher electronic states becomes larger, which results in the blue shift of the absorption. Thus, observation of the blue shift is useful to identify the time scale of the J-to-K transition. On the transient absorption spectra in **Fig. 4.2**, the blue shift was observed in two time constants: 420 fs and 2.4 ps. However, owing to the broad photoproduct absorption peaks and the overlap with the negative signals from the ground state bleach and the stimulated emission, it is difficult to decide which time component is involved in the J-to-K transition. On the other hand, the Raman spectra have narrower peaks, which make it easier to identify the time scale of the K-intermediate formation. We observe a 6 cm^{-1} blue shift on the C=C stretching region with ~3 ps in EADS (**Fig. 4.4c**), indicating that the J-to-K transition occurs on that timescale. A similar blue-shifted C=C stretching mode in J-to-K transition was seen in bacteriorhodopsin[214].

Next, we discuss the retinal dynamics of KR2 on the photoproduct intermediates after the K-intermediate formation. The EADS of the transient Raman spectra at the C=C stretching region (1510–1560 cm^{-1}) indicate that there are four different intermediate photoproduct states up to 100 μs: evolving with 22 ps, 25 ns, 21 μs and longer than 100 μs

(infinity) (**Fig. 4.4**). The blue-shifted C=C Raman signal at ~1547 cm^{-1} that rose in 22 ps is assigned as the L state, which is a typical blue-shifted absorption species in microbial rhodopsins[7,178,208]. With the L-state formation, the HOOP signals at ~830–930 cm^{-1} dropped (**Fig. 4.4a**), which suggests that the retinal chromophore structurally relaxes, but this may also result from slightly reduced resonance conditions of L with respect to K. In channelrhodopsin, the L state showed significant HOOP intensity in time-resolved infrared spectroscopy[215]. Significantly, the L-state signal (1547 cm^{-1}) rose in 22 ps while the K-state signal (1519 cm^{-1}) did not completely disappear (**Fig. 4.4c**, green line and **Fig. 4.5e**). The coexistence of the positive peaks at 1519 cm^{-1} and 1547 cm^{-1} indicates that KR2 forms distinct K/L equilibrium states between ~20 ps and ~20 μs. The two distinct newly found K/L equilibrium intermediates are described as K/L_1 (formed in 22 ps, **Fig. 4.4c**, green line) and K/L_2 (formed in 25 ns, **Fig. 4.4c**, magenta line) intermediates. In 25 ns, the 1519 cm^{-1} signal slightly rose again while the peak intensity at 1547 cm^{-1} decreased (**Fig. 4.4c**), which implies the equilibrium of K/L shifts back to K in the K/L_2 intermediate before the formation of the following L/M intermediate. Even though the L-state structure of KR2 is unsolved, it can be suggested that the retinal Schiff base is oriented to the counterions with a closer distance on the L state, similar to bacteriorhodopsin[208,209]. Because the K/L equilibrium slightly shifts back to K again in ~30 ns, the distance between the retinal Schiff base and the counterions might become longer before the M-state formation.

The blue-shifted 1560 cm^{-1} band, which forms in ~20 μs can be assigned as the M state (**Fig. 4.4c**, cyan line). The mixture of the positive peaks at 1547 cm^{-1} and 1560 cm^{-1} indicates the L state coexists with the M state, forming an L/M intermediate in ~20 μs as seen in the flash photolysis experiments[62] and our transient absorption experiments (**Fig. 4.2**). Significant decrease of the HOOP signals at 785 and 995 cm^{-1} in 21 μs implies that the twist of the retinal is relaxed with the formation of the M state as seen in bacteriorhodopsin[216]. From the overall discussion above, a new photocycle model from femtoseconds to submilliseconds is proposed in **Fig. 4.6**.

We now compare the retinal dynamics of WT KR2 in NaCl (Na^+ bound, Na^+ transport), KR2/D102N in NaCl (Na^+ unbound, Na^+ transport) and WT KR2 in CsCl (Na^+ unbound, H^+ transport). A similar photocycle up to 100 μs in **Fig. 4.6** can be applied to the three different sample conditions, albeit with important differences as outlined below. At 4.5 ps, 50 ps, 480 ns and 100 μs, the retinal of KR2 is in the K, K/L_1, K/L_2 and L/M intermediate, respectively (**Fig. 4.5d**). The ground state stimulated Raman spectra of WT KR2 in NaCl, KR2/D102N in NaCl and WT KR2 in CsCl were almost identical as seen in

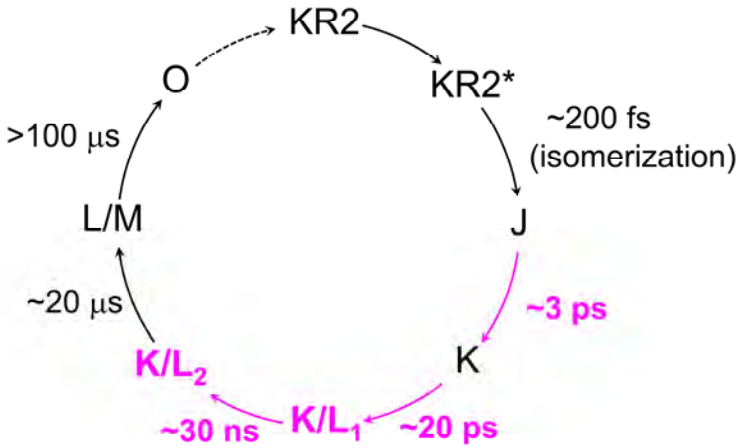

Figure 4.6. A new photocycle model of WT KR2 in NaCl. The newly identified intermediates and time components by this work are high-lighted as magenta. The O-intermediate formation and decay are previously proposed[62,207].

Fig. 4.3a. Moreover, no significant difference was seen in transient Raman spectra at 4.5 ps in the three different conditions as seen in 77 K FT-IR experiments[212]. These results imply that the molecular structure of the all-*trans* retinal and the 13-*cis* retinal in the K intermediate is identical regardless of the Na^+ binding on the extracellular side and whether Na^+ or H^+ is transported.

In the K/L_1 intermediate, clear differences between the three different samples were observed in the TSRS experiments: the L state signal (1547 cm^{-1}) is dominant as compared to the K state signal (1519 cm^{-1}) in KR2/D102N in NaCl and WT KR2 in CsCl, while the K state is more significant than the L state in WT KR2 in NaCl, as clearly seen in the false color time-wavenumber plots of **Fig. 4.5a–c**, and the time-resolved Raman spectra of **Fig. 4.5d**. These observations imply that the equilibrium in the K/L_1 intermediate shifts to L in the absence of Na^+ binding at the extracellular side. In the K/L_2 intermediate, the equilibrium slightly shifts to K as compared to in K/L_1 intermediate, although the L state is still dominant in the absence of Na^+ binding on the extracellular side. The shift of the K/L equilibrium is clearly seen in the time traces of 1519 cm^{-1} and 1547 cm^{-1} signals in **Fig. 4.5e–g**. Furthermore, in the L/M intermediate at 100 µs, the M-state peak at 1560 cm^{-1} has lower amplitude in the D102N mutant and WT KR2 in CsCl (**Fig. 4.5d**). This indicates that the equilibrium shifts to L in the L/M intermediate in the absence of the extracellular Na^+

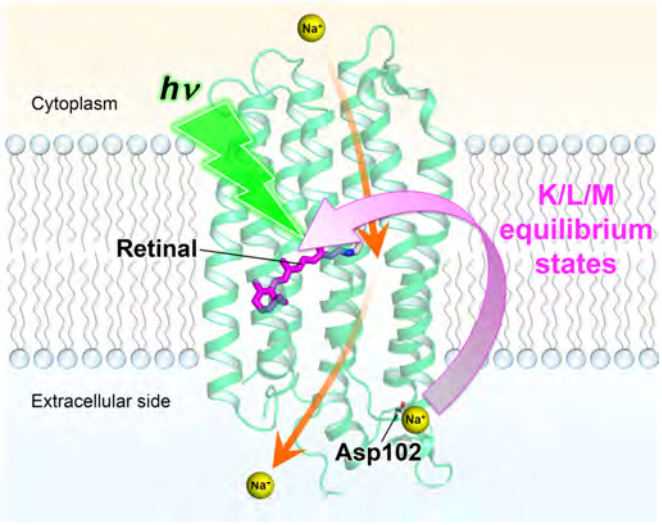

Figure 4.7. Proposed model of the extracellular Na^+ binding that affects the primary dynamics of retinal between picoseconds and microseconds. The Na^+ ion bound on the extracellular side affects the K/L and L/M equilibrium states of the retinal. The protein structure is based on Gushchin *et al.* (PDB ID: 4XTN). The proposed Na^+ pumping pathway[62] is drawn with orange arrows.

binding. Possibly, the distance between the retinal Schiff base and the counterions is different with and without the extracellular Na^+ binding, which makes the difference in the K/L/M equilibrium (**Fig. 4.7**). Notably, in the case where Na^+ is unbound to KR2, the K/L/M equilibrium state is very similar regardless of which ion, Na^+ or H^+, is transported.

A protomer of the pentameric KR2 has two different Na^+ binding sites; (i) bound to Tyr25 (on TM1) and Thr87 main chain carbonyl groups of Thr83 and Phe86 (on TM2), and (ii) bound to Asp102 (on TM2–TM3 loop) (**Fig. 4.1a**)[203]. On the other hand, monomeric KR2 has only a Na^+ binding site (i), near Tyr25 and Thr87, lacking the Na^+ binding to Asp102 on the TM2–TM3 loop[203]. Between the monomeric and pentameric forms, significant structural differences were seen in the first half of TM3, while no notable difference was observed in other regions (**Fig. 4.8**)[203]. Possibly, Na^+ binding to Asp102 affects the structure of the half of TM3 even though the structural difference might be just from difference of the oligomeric states. The structural difference on the half of TM3 is perhaps involved in the K/L/M equilibrium states, although it does not affect the retinal structure on the steady state and the K intermediate. However, to fully understand how Na^+

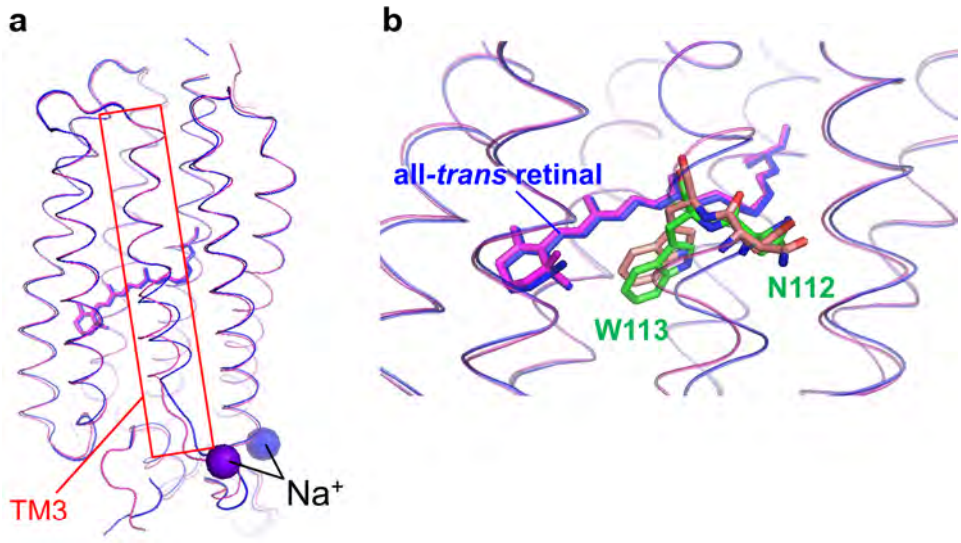

Figure 4.8. Structural difference with/without Na^+ binding to $Asp102^{203}$ (PDB ID: 4XTL and 4XTN). (**a**) Overlapping structures of the monomeric form (blue) at pH 4.3 and the pentameric form (magenta) at pH 4.9. (**b**), Close-up crystal structures near all-*trans* retinal. Asn112, Trp113 (green in monomeric form and orange in pentameric form) and all-*trans* retinal are shown.

influences the ps-μs retinal dynamics in K/L_1, K/L_2 and L/M intermediates, tracing backbone transitions in those time scales with further time-resolved experiments is required.

4.4 Conclusion

We investigated the photocycle of sodium ion pump rhodopsin KR2 by applying the watermarked femto- to submillisecond transient stimulated Raman spectroscopy technique. By considering the transient Raman spectra on the hydrogen-out-of-plane (HOOP), the C–C stretching and the C=C stretching modes, we propose a new photocycle model of KR2, evolving to J (formed in ~ 200 fs) → K (~3 ps) → K/L_1 (~20 ps) → K/L_2 (~30 ns) → L/M (~20 μs). We also observed that the retinal conformation and the dynamics in the three probed conditions were almost identical in the ground state and the K intermediate. However, significant differences were observed in K/L_1, K/L_2 and L/M intermediates, as the K/L and L/M equilibrium shifts to L in the absence of extracellular bound Na^+. By our research, it was revealed for the first time that the extracellular Na^+ binding plays an important role on the primary photoreactions from picoseconds to microseconds, while the identity of the transported ion, Na^+ or H^+, does not affect the photocycle.

Methods

Protein expression and purification: The protein samples of WT KR2 and D102N mutant were expressed in *E. coli* (C41(DE3) strain) and purified as previously reported[66]. The purified proteins were solubilized in 1.0% n-dodecyl-β-D-maltoside (DDM), 100 mM NaCl, 50 mM Tris-HCl (pH 8.0). For the spectroscopic measurement in CsCl solution, the solvent was exchanged to that containing 100 mM CsCl instead of NaCl. The proteins were concentrated to 200 μM (5.0 mg/mL) for transient absorption experiments, and to 2.0 mM (50 mg/mL) for stimulated Raman experiments, with using a centrifugal filter device (Millipore 30 kDa Mw cutoff). The samples were filled in a homemade sample holder that has two 2-mm-thick CaF_2 plates. The sample thickness was set as 400 μm for transient absorption experiments and 200 μm for stimulated Raman experiments with an appropriate sample spacer. The sample holder was set on a Lissajous scanner that ensures sample refreshment after each laser shot with a time interval of 60 seconds between successive exposures to the laser pulses[134].

Transient absorption spectroscopy: Transient absorption measurements were performed with a femtosecond-to-submillisecond pump-probe setup as reported previously[133]. A sapphire plate was used for supercontinuum white light generation, and a selected wavelength region; 430–730 nm or 720–940 nm, was detected by the photodiode array. The time delay was varied up to 150 μs at 164 data points with the minimum temporal step of 50 fs. The diameters of the pump and the probe beams at the sample position were ~200 μm and ~70 μm, respectively. The wavelength of the pump beam was centered at 520 nm, and the power was attenuated to ~500 nJ. The instrumental response function was ~80 fs, estimated from global analysis.

Baseline-free Transient stimulated Raman spectroscopy: Femtosecond to submillisecond time-resolved stimulated Raman experiments were performed with the watermarked baseline-free stimulated Raman setup reported previously[136]. Raman pump (800 nm, ~20 μJ) and Raman probe (~840–960 nm) were spatiotemporally overlapped at the sample position with the diameter of ~100 μm. Actinic pump (~520 nm, ~600 nJ) was focused on the protein sample to the diameter of ~150 μm with a time delay from -50 ps to 110 μs at 96 data points (logarithmically spaces after 2 ps), generated by an optical delay and an electronic delay as reported previously[133]. The sample exposure time to the beams was ~1 hour in total for each time-resolved stimulated Raman experiment.

Chapter 5

The electronic structure and dynamics of a near-infrared active microbial rhodopsin analogue disclosing intense pH-dependent fluorescence

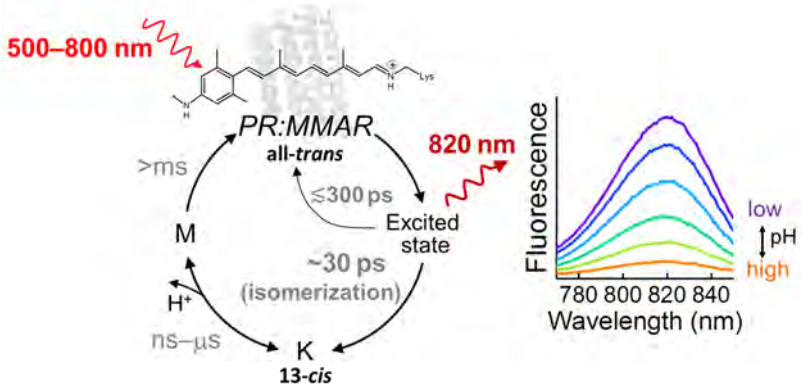

The photocycle of NIR active H⁺ pump rhodopsin was determined, disclosing highly pH-dependent fluorescence.

Abstract

Near-infrared (NIR)-driven ion transporters are of great interest in optogenetics and other optobiotechnological developments such as artificial photosynthesis. Recently, NIR-driven proton pumps generated by incorporation of retinal analogues in proteorhodopsin (PR) were described. Severe lack of understanding of the electronic properties and photochemical dynamics of such systems limits further rational design and development of cutting-edge applications. In this chapter, a mechanistic study of PR reconstituted with analogue pigments is reported using stimulated Raman and fs-µs transient absorption spectroscopy. The most remarkable results were obtained with the PR:MMAR analogue, which shows the most red-shifted absorption profile. The photoisomerization proceeded significantly slower in PR:MMAR than in native PR, but Schiff base deprotonation rates were comparable. Strikingly, PR:MMAR showed one unusually long-lasting lifetime (τ~300 ps), resulting in strong NIR fluorescence at 130 times higher quantum yield than the native PR. The NIR fluorescence was strongly pH dependent in the range pH 6–8.5, suggesting potential application of MMAR-binding proteins as ultrasensitive NIR-emitting voltage sensors.

This chapter is based on a submitted paper:
collaborated with S. Ganapathy and W. J. de Grip for sample purification.

5.1. Introduction

Rhodopsins are essential photoreceptor proteins detected in many organisms and displaying a variety of functionalities[5,7]. These proteins harbor the widespread seven-transmembrane-α-helical structural motif, and are generally classified in two groups: microbial and animal rhodopsins. For their functional and spectral properties they depend on a chromophore, namely retinal, which is incorporated in the binding pocket under formation of a covalent Schiff base linkage with a lysine residue of the apoprotein, opsin. Microbial rhodopsins, in particular the light-driven ion transporters, are of great interest in optobiotechnology, engineered or artificial photosynthesis[217,218] as well as physiological applications like voltage sensing[219-221] optogenetics[58,66,141,222,223] which is a fundamental technique to control neural and cellular activities by light with high spatial and temporal precision[28]. Spectral tuning, functional conversion and enhancing fluorescent properties of diverse microbial rhodopsins have been addressed to engineer derivatives with special properties to suit various practical optobiotechnological applications[34-37,143-146,219].

A recent challenge in microbial rhodopsin research is to red-shift the absorption spectra into the deep-red to near-infrared (NIR) range of the electromagnetic spectrum (> 650 nm)[34,224,225]. In particular absorption in the NIR region (> 700 nm) will strongly improve non-invasive and deeper-tissue optogenetic applications because the 'optical transparence window' of mammalian tissues lies in the range 650–900 nm, where hemoglobin, melanin and water absorption are minimal[75], and interference by light scattering in tissue is much less severe for NIR radiation than for visual radiation. Moreover, proton transporters activated by NIR-light have great potential in complementing natural light-harvesting systems, since NIR is hardly used in oxygenic photosynthesis. There are several strategies for accessing red-shifted absorbance bands, *e.g.* by directed or random mutagenesis techniques[28], designing chimaeric proteins[226] and screening algal genomes[224]. However, so far, NIR-absorbing species that sufficiently maintain their ion transporting activity have not yet been achieved with those approaches.

Recently, NIR-activated proton pumping proteorhodopsin (PR) and *Gloeobacter* rhodopsin (GR) were generated by incorporating retinal analogues, resulting in red shifts of the absorption maxima from 20–200 nm[227,228]. With some combinations significant proton pumping activity was preserved upon illumination up to 730-nm, the most red-shifted light source tested. Ca 20–40 nm red shifts in the absorption maxima were achieved also with retinal analogues in other microbial rhodopsins such as channelrhodopsin-2 (ChR2, cation channel) and archaerhodopsin-3 (Arch3, outward proton pump), which are key proteins in

optogenetic applications[229]. Thus, retinal analogue strategies seem to be broadly applicable for tuning action spectra of rhodopsins into the NIR region.

For the rational design of retinal-analogue based functional rhodopsins, understanding their electronic structure and photochemistry is essential. In spite of this, the photochemistry of most microbial rhodopsins is poorly understood in detail, while analogue pigments have hardly been investigated at all. The electronic structure of retinal in rhodopsins is largely dictated by protonation of its Schiff base and direct interactions with the opsin[230]. The well-accepted common denominator in the photoreaction of microbial rhodopsins is the first event, involving all-*trans* to 13-*cis* isomerization of the chromophore, which occurs in the femtosecond time scale[7]. After the isomerization, several intermediate states become populated and ion transport is triggered in the microsecond to millisecond time range. Therefore, comprehensive studies of on the one hand the electronic structure and on the other hand the photoreaction from femtoseconds to milliseconds are indispensable to clarify and schematize the red-shift and the activation mechanism, and understand the protein-chromophore interplay in microbial rhodopsins equipped with retinal analogues. Here we report the first analyses of the electronic structure and photochemistry of red-shifted analogues of the proton pump PR utilizing stimulated Raman spectroscopy and femto- to submillisecond transient absorption spectroscopy.

5.2. Results and Discussion

Previously we described red-shifted analogue pigments of PR equipped with the retinal analogues 3-methylamino-16-nor-1,2,3,4-didehydroretinal (MMAR), 3,4-

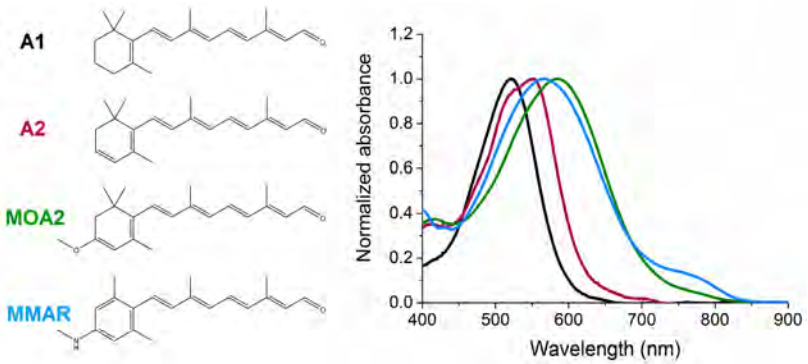

Figure 5.1. Structure of the retinal analogues studied in this chapter (left panel) and the main absorbance band of the corresponding analogue pigments generated with PR, recorded at pH 8 (right panel). Data are based upon Ganapathy *et al.* 2017[228].

dehydroretinal (A2) and 3-methoxy-3,4-dehydroretinal (MOA2) (**Fig. 5.1**), resulting in the analogue pigments PR:MMAR, PR:A2, and PR:MOA2[228]. These retinal analogues induce red shifts in the λ_{max} of their analogue pigment from 32 to 65 nm relative to A1 (the native retinal as chromophore), and in addition generate strongly broadened absorbance bands, extending beyond 700 nm (**Fig. 5.1**). However, large differences were observed in proton pump activity[228]. While the maximally attained activity of PR:A2 was close to that of PR:A1, for PR:MOA2 and PR:MMAR it was only about 20% of that of PR:A1. Strikingly, PR:MOA2 exhibited hardly any activity in red light, and PR:MMAR was the only pigment still active in near-infrared light.

Ground-state conformation and electronic structure of PR:A2, PR:MOA2 and PR:MMAR

To investigate the ground-state retinal configuration and its electronic structure, pre-resonance stimulated Raman spectroscopy with an 800-nm Raman pump was applied to PR:A2, PR:MOA2 and PR:MMAR. Upon dark adaptation of BR about half of the all-*trans*/15-*anti* chromophore thermally isomerizes into the 13-*cis*/15-*syn* configuration. In contrast, PR:A1 maintains an all-*trans*/15-*anti* chromophore also during dark adaptation[231-234]. The ground-state Raman spectrum of PR:A2 at pH 7.0 is shown in **Fig. 5.2a,b**. This spectrum shows a peak distribution, which is quite similar to PR:A1[231,232], except for a strong additional band at 1512-cm^{-1}. In the C–C stretching region, peaks are observed at 1171,

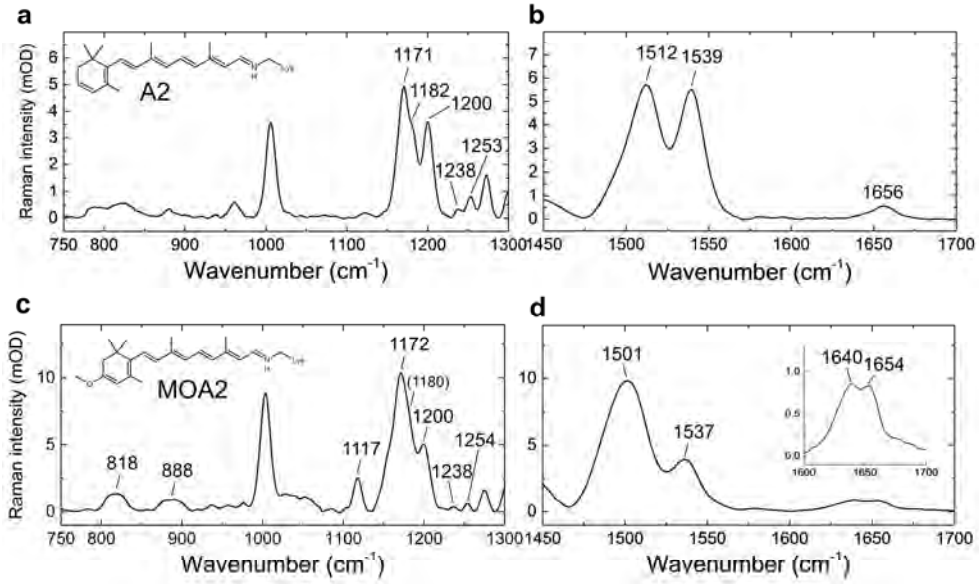

Figure 5.2. Ground-state Raman spectrum of (a,b) PR:A2 and (c,d) PR:MOA2 at pH 7.0.

1182, 1200, 1238 and 1253 cm^{-1}. These peaks correspond to Raman peaks of the all-*trans* A1 chromophore in BR and PR (1170/1172, 1187/1185, 1201/1198, 1234 and 1255/1253 cm^{-1})[211,231,232,235]. The single peak at 1656 cm^{-1}, which is assigned to the protonated retinylidene Schiff base (RSB), and the absence of a strong peak near 800 $cm^{-1,}$ which is characteristic for the 13-*cis* configuration[236], also agrees with an all-*trans* configuration of the A2 chromophore. Although a minor amount of 13-*cis* species may be present, represented by the small 1185 peak[233,236], there is general consensus that in the ground state PR:A1 contains an all-*trans* chromophore, and we conclude that the same is true for PR:A2. In the C=C stretching region of PR:A2, two large peaks at 1512 and 1539 cm^{-1} are present. These are attributed to the main C=C stretching modes of the two PR:A2 sub-states with absorbance peaks at ~552 and ~515 nm, respectively (c.f. **Fig. 5.1**).

The ground-state Raman spectrum of PR:MOA2 at pH 7.0 is shown in **Fig. 5.2c,d**. Again C–C stretching peaks were observed at 1172, 1180 (weak), 1200, 1238, and 1254 cm^{-1}, but two C=NH stretching peaks were seen at 1640 and 1654 cm^{-1}. The most straightforward explanation is that MOA2 forms heterogeneous all-*trans* and 13-*cis* conformers in the dark state[211,236]. The stronger peak at 1117 cm^{-1} would also support the presence of a 13-*cis* chromophore. In addition, significant peaks of hydrogen out-of-plane (HOOP) modes were observed around 818 and 888 cm^{-1}, probably reflecting structurally distorted 13-*cis* conformers as observed in microbial rhodopsins containing 13-*cis* chromophores[171,236]. The two strong C=C stretching peaks at 1501 and 1537 cm^{-1} further suggest that heterogeneous species exist in the dark state of MOA2, which could also explain the broad absorbance peak (**Fig. 5.1**).

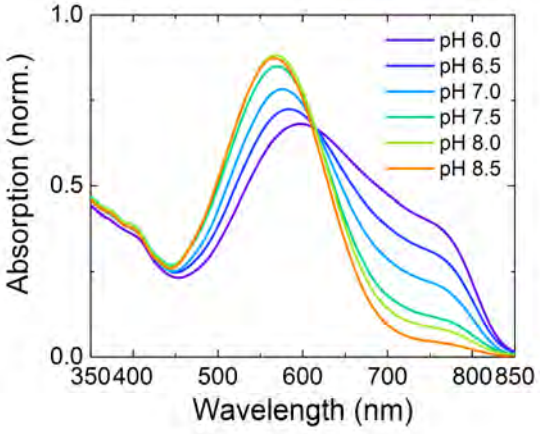

Figure 5.3. Normalized pH-dependent absorption spectra of PR:MMAR. Modified from Ganapathy *et al*[228].

Similar to PR:A1, PR:A2 and PR:MOA2 also exhibit only a small red-shift in the main absorbance band upon acidification from pH 9 to pH 6[228]. This most likely reflects protonation of the counterion Asp97[201,237,238]. In spite of this, it has been shown that the resonance Raman spectrum of PR:A1 is very similar at pH 5 and pH 9, except for a small shift in the C=C stretching vibration[231,232]. We therefore refrained from Raman measurements of PR:A2 and PR:MOA2 at pH 9. In contrast, PR:MMAR shows very complex UV-Vis absorbance band changes upon acidification from pH 8.5 to pH 6.0 (**Fig. 5.3**). Next to a red-shift of the main band, strong enhancement of lower energy bands around 700 and 750 nm was observed. Therefore, we decided to record pre-resonance Raman spectra of PR:MMAR over the pH range 6 to 9.

Fig. 5.4a shows the ground state Raman spectrum of PR:MMAR at pH 7.0 between 750 and 1300 cm^{-1}. Various C–C stretching modes are seen (1169, 1191, and 1216 cm^{-1}), corresponding to C–C stretching modes in all-*trans* A1 in BR and PR (1170/1172, 1201/1198, 1214/1211 cm^{-1}, respectively). Further, a strong HOOP around 800 cm^{-1} is not observed, implying that at pH 7.0 MMAR is also largely bound in the all-*trans* configuration in PR. **Fig. 5.4c** shows this vibrational region in the normalized ground-state Raman spectra of PR:MMAR at pH values between 6.0 and 9.0. The overall band distribution in the region 1100-1220 cm^{-1}, hardly varies over this pH range, except for a slight shift in frequencies, an increase in the intensity of the 1191 cm^{-1} mode (C14–C15 stretch[211]) with increasing pH, and concomitantly a more pronounced shoulder at ca 1150 cm^{-1}, possibly reflecting deprotonation of the Asp97 counterion[231]. We conclude that the all-*trans* configuration persists in the chromophore of PR:MMAR over the entire pH range of 6-9.

In the C=C stretching region (~1500–1600 cm^{-1}) of PR:MMAR at pH 7.0 (**Fig. 5.4b**) several Raman peaks can be observed at 1482, 1501, 1528, 1580 and 1605 cm^{-1}. These peaks are very strongly pH dependent (**Fig. 5.4d**). Those at 1482, 1501, 1580 and 1605 cm^{-1} are very small at pH 8.5 and 9.0, and strongly increase upon acidification, while the single very strong peak at 1532 cm^{-1} slightly downshifts to 1528 cm^{-1} and substantially decreases upon acidification. This pH-dependence reflects that of the absorbance spectrum (**Fig. 5.3**). The bands between 1450 and 1550 cm^{-1} should represent C=C stretching modes[211,236]. The C=C stretching frequency is correlated with the degree of electron delocalization in the chromophore, hence inversely correlated with the λmax[239]. According to the latter correlation, the 1532 cm^{-1} mode would correspond to an absorbance band around 560 nm, and the 1501 and 1482 cm^{-1} modes to bands around 690 and 750 nm, respectively, in excellent agreement with the absorbance spectra in **Fig. 5.3**.

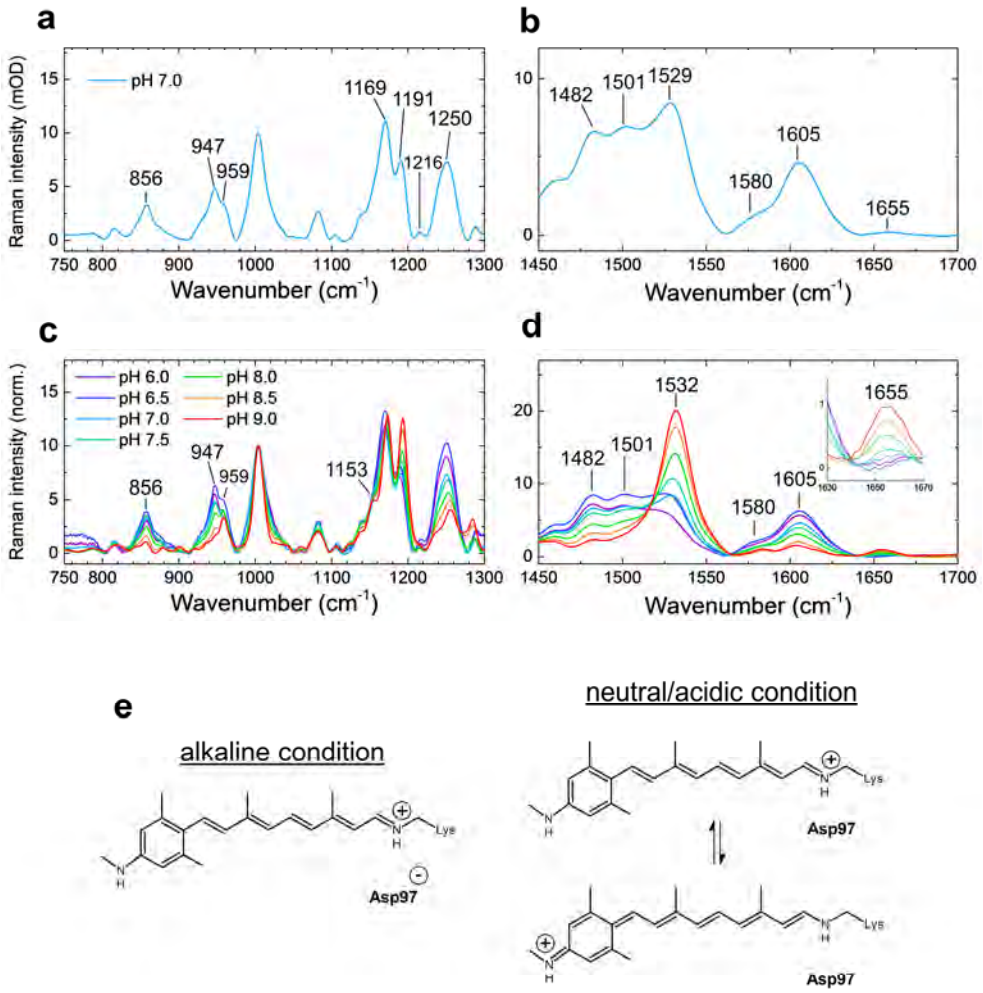

Figure 5.4. pH dependent ground-state Raman spectra of PR:MMAR and proposed MMAR boundary structures. Raman spectra at pH 7.0 over the range (**a**) 750–1300 cm^{-1} and (**b**) 1450–1700 cm^{-1}. (**c,d**) Family of Raman spectra over the same vibrational ranges, in dependence of the pH. The spectra were normalized at the 1000 cm^{-1} peak. (**e**) Boundary structures of MMAR in PR under alkaline and neutral/acidic conditions.

The 1655-cm^{-1} signal is assigned to the C=NH stretching mode, which is an indicator for the protonated RSB widely seen in native rhodopsin pigments (A1)[171,211]. Remarkably, the 1655-cm^{-1} mode was replaced upon acidification by two peaks at ~1580-cm^{-1} and ~1605-cm^{-1}. If those peaks would represent a C=C stretching mode, we would expect high-frequency (blue-shifted below 400 nm) absorption species to appear at a lower pH, but this is not observed in the absorption spectra (**Fig. 5.3**). Therefore, we do not assign the 1580 and 1605 cm^{-1} peaks to C=C stretching modes, but rather consider the possibility of formation of resonance species upon protonation of the Asp97 counterion, resulting in extensive electron delocalization involving both –N-C- elements (**Fig. 5.4e**). Since the p*K*a of the primary counterion (D97) of the protonated RSB in PR pigments varies between 6.5 to 7.7[201,228,240-242], the counterion is largely protonated at acidic pH, resulting in a weakened hydrogen bond between the RSB and the counterion and less effective charge stabilization at the protonated RSB. But, importantly, in MMAR the charge can effectively delocalize towards the other methyl-N-C group on the aromatic ring at the other end of the chromophore, allowing a boundary structure with another protonated Schiff base (**Fig. 5.4e**, bottom). This would lead to a strong reduction in bond-length alteration over the conjugated double bond system, which agrees with a lower stretch vibration frequency for both Schiff bases (**Fig. 5.4**) as well as the strong increase of the bands around 1250 cm^{-1} in the ground state Raman spectrum upon protonation (**Fig. 5.4**), which could reflect an aromatic secondary amine stretch[211]. Presumably, the two boundary structures shown in **Fig. 5.4e** are in a pH-dependent equilibrium, resulting in a complex system of resonance states, yielding the heterogeneous absorbance and vibrational profiles of PR:MMAR under alkaline and acidic conditions. We assume that the charge delocalization induced upon protonation will result in further hybridization of molecular orbitals leading to the lower energy broad absorbance bands at 690 and 750 nm. Notably, the HOOP signals at 850–960 cm^{-1} become substantially more significant at lower pH (**Fig. 5.4c**). This observation implies that under neutral and acidic condition the MMAR moiety is significantly distorted in the ground state, possibly because of the skeletal changes accompanying the alteration in bond length distribution (**Fig. 5.4e**).

Photochemistry of PR:A2

The pump activity of rhodopsins at least partly depends on their photodynamics[7]. Hence, in search for an explanation of the substantial differences in their activity, we set out to investigate the early photokinetics of these analog pigments by femtosecond to

(sub)millisecond spectroscopy. We also included PR:A1 as a reference. The latter data corroborated earlier literature reports (see below), and are not discussed here. The pump activities of these PR pigments were assayed at pH 7[228], hence we recorded most spectroscopic data also at pH 7. According to the literature, excitation at a higher pH yields a similar sequel of early photointermediates, but at several fold higher rates[162,238,242-244]. We therefore also collected some data at pH 9. PR:MOA2 was only studied at pH 9, as outlined below.

Because PR:A2 most resembles the native PR:A1 with respect to ground state chromophore structure and pump activity[228], we first discuss our time-resolved spectroscopic analysis of PR:A2 (**Fig. 5.5**). Femto- to submillisecond transient absorption spectroscopy

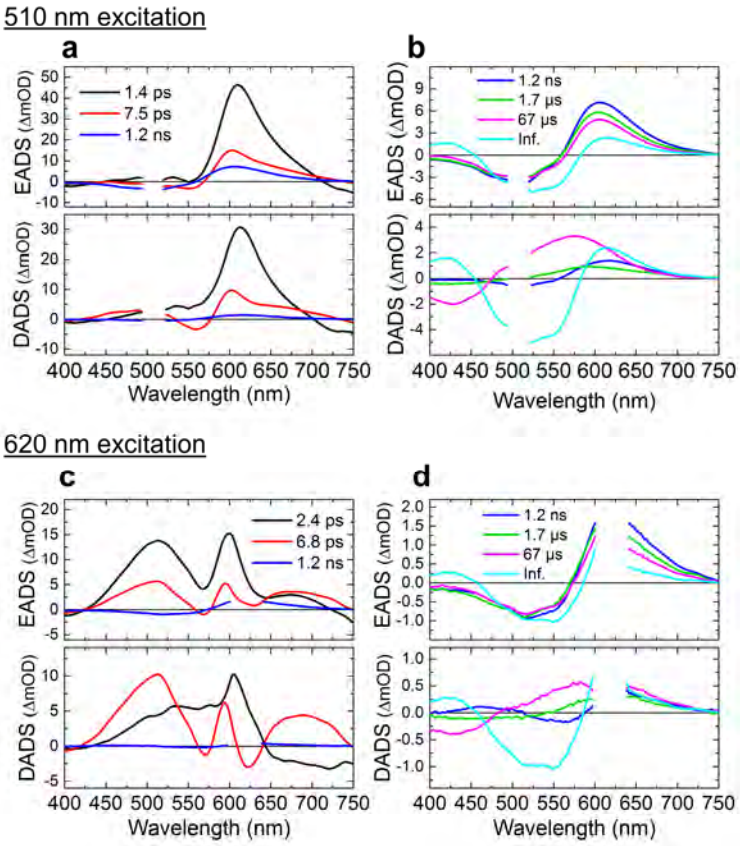

Figure 5.5. Global-fitted transient absorption spectra of PR:A2 at pH 7.0 with (a,b) 510-nm and (c,d) 620-nm excitation. EADS (top) and DADS (bottom) of (**a,c**) the first three component and (**b,d**) the last five components. The wavelength region of 500–520 nm of **a,b** is omitted because of the strong scattering.

was applied to PR:A2 at pH 7.0 with 510-nm excitation. The transient absorption spectra were globally fitted with six time components: 1.4 ps, 7.5 ps, 1.2 ns, 1.7 μs, 67 μs and infinite. The evolution-associated difference spectra (EADS) and decay-associated difference spectra (DADS) are shown in **Fig. 5.5a,b**, and selected time traces are shown in **Fig. 5.6**. Immediately after the photoexcitation, the 1st EADS (black in **Fig. 5.5a**) appeared, which has excited-state absorption (ESA) bands at ~510 (weak) and ~620 nm (strong). The negative signal at >700 nm is assigned to stimulated emission (SE), confirming that the molecules are in the excited states. In 1.4 ps, development to the 2nd EADS (red in **Fig. 5.5a**) was observed, involving a large decay in the SE and ESA signals, while a small SE component still remained. In 7.5 ps, the signal develops to the 3rd EADS (blue in **Fig. 5.5a**), which does no longer show a SE band, indicating that the excited states were no longer populated after the 7.5-ps decay. Hence, it can be considered that the 3rd EADS, which has an absorption peak at ~610 nm, shows the first K-like photoproduct state. The ESA at ~620 nm strongly overlaps with the K-like absorptions at ~610 nm. Thus from the current transient absorption data, it is difficult to decide which one of the time components (1.4 ps and/or 7.5 ps) is involved in the all-*trans* to 13-*cis* isomerization in PR:A2. Using single-pulse or multi-pulse spectroscopy, it was reported that at acidic to neutral pH multiphasic isomerization in PR:A1 proceeds with three components (0.2-0.7 ps, 6-10 ps and 20-30 ps)[162,238,243]. Therefore, it seems like the photoisomerization of A2 in PR proceeds in a time frame similar to A1.

According to the DADS in **Fig. 5.5b** (bottom panel), in 1.2 ns the absorbance of K at 610 nm is decaying with a concomitant rise around 500 nm. The ~500-nm absorbance band can be assigned to an L-like intermediate. The K-like absorption largely persists after the 1.2-ns signal development, implying that a K/L equilibrium is formed in 1.2 ns. In 1.7 μs and 67 μs an absorbance band around 420-nm appears, which is assigned to an M-like intermediate, in which the RSB is deprotonated. It may be concluded that proton transfer from the RSB of A2 proceeds with 1.7 μs and 67 μs time components. From the DADS in **Fig. 5.5b**, the rise of the M-like intermediate appears to be ~5-fold larger in amplitude in 67 μs than in 1.7 μs, which implies that the 67-μs component is dominant for the proton transfer process. The K-intermediate absorption still persists after 67 μs, indicating that a K/L/M equilibrium is formed in 67 μs. For PR:A1 it was reported that at acidic to neutral pH the M-like intermediate is formed with components of 2-4 μs and several tens of μs[162,242]. Hence the dominant M formation in PR:A2 (67 μs) seems to be somewhat slower than in PR:A1, while the minor M formation proceeds at almost the same rate in both pigments.

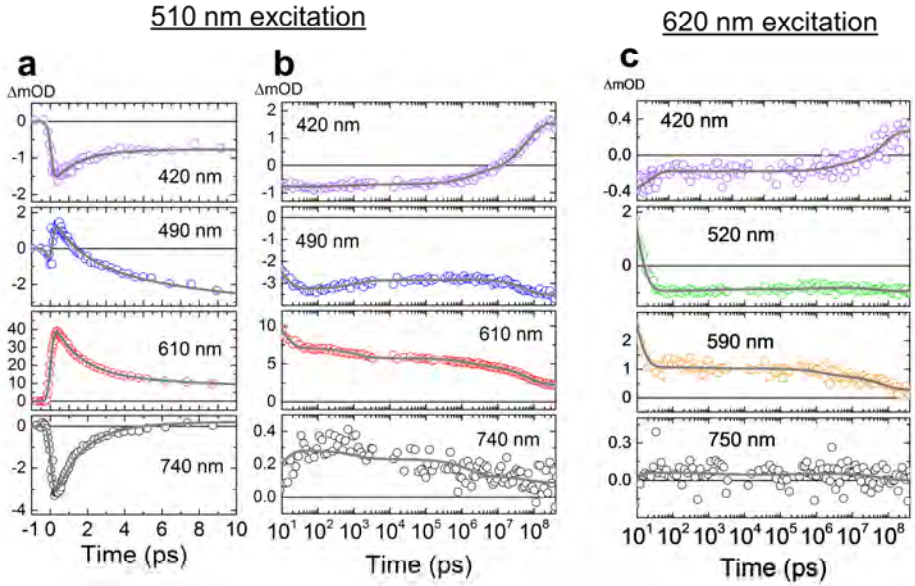

Figure 5.6. Selected time traces of transient absorption of PR:A2 at pH 7.0. Selected time traces between (**a**) -1 ps and 10 ps, (**b**) 10 ps and 400 μs upon 510 nm excitation. (**c**) Selected time traces between 10 ps and 400 μs upon 620 nm excitation. Open dots show the raw data, and the solid lines show fitting curves.

It was recently reported that the excitation wavelength may affect the intensity and sequel of photoproducts in PR:A1[242]. Therefore, we also applied 620-nm excitation and observed a different set of excited-state species peaking at ~500, 600 and 670 nm (**Fig. 5.5c**), but a similar set of photoproducts (**Fig. 5.5d**). Possibly, different excited states were populated, which are derived from heterogeneous ground or excited state species of PR:A2. The signal development of the photoproducts was almost identical for 620-nm and 510-nm excitation, but the signal intensity was significantly larger with 510 nm excitation. The molar absorption coefficient of PR:A2 at 510 nm is about 5.6-fold higher than at 620 nm (**Fig. 5.1**), the excitation power at 620 nm was 1.5 times that at 510 nm (see the Methods section), and with the same power the photon flux at 620 nm is higher by a factor 1.2. Therefore, we estimate that the ratio of the number of excited molecules is about 3.1:1 for 510- and 620-nm excitation, respectively. However, the M-intermediate population was about 4.8-fold stronger with 510-nm excitation (**Fig. 5.6b,c**). Hence this would indicate that 510-nm light can trigger the photocycle somewhat more efficiently than 620-nm light, which would imply that the hypochromic ground-state species is somewhat more dominant in producing a functional photocycle in PR:A2. On the other hand, higher production of the M

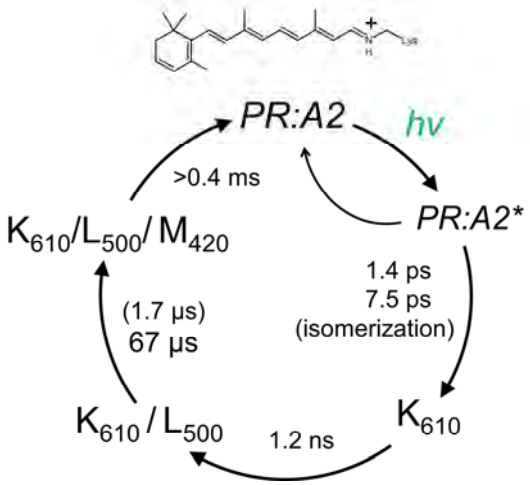

Figure 5.7. Suggested photocycle of PR:A2 at pH 7.0 upon 510-nm excitation.

intermediate with blue light under acidic conditions was also reported for PR:A1[242], and hence could simply be the result of populating higher energy vibronic states on the excited state surface. In **Fig. 5.7**, the photocycle of PR:A2 upon 520-nm excitation is shown.

Photochemistry of PR:MOA2

The photochemistry of PR:MOA2 was studied at pH 9.0 with 520-nm excitation. Remarkably, only femtosecond and picosecond components were required in the global analysis, yielding time components of 120 fs, 2.0 ps and 4.2 ps (**Fig. 5.8a,b**). In 120 fs, a slight rise in a signal at ~610 nm was observed. In the 2.0-ps and 4.2-ps components (red and blue lines in **Fig. 5.8a**, respectively), strong positive signals were seen, but no negative peaks were detected. The multiple positive peaks are assigned to ESA bands with maxima at ~520 nm, ~560 nm, ~610 nm and ~700 nm. Probably, the ground-state bleach (GSB) and SE signals strongly overlap with the ESA, explaining the absence of clear negative signals in the red and blue spectra in **Fig. 5.8a**. Concomitantly with the decay of the 4.2-ps component, all ΔA signals decayed completely, implying that all excited molecules returned to the initial ground state in 4.2 ps. This observation indicates that under the applied conditions PR:MOA2 does not generate detectable photoproducts, *i.e.* photoisomerization does not seem to occur. Furthermore, the absence of an M-like absorption in the near-UV region suggests that proton transfer from the protonated RSB in PR:MOA2 does not occur either. This would explain why hardly any pump activity is obtained upon illumination with a 617

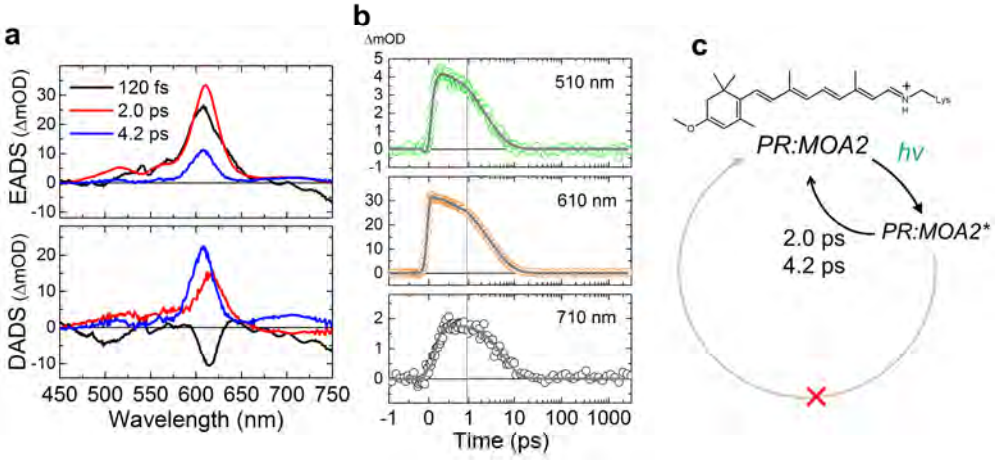

Figure 5.8. Global-fitted transient absorption spectra of PR:MOA2 at pH 9.0 upon 520-nm excitation. (**a**) EADS (top) and DADS (bottom). (**b**) Selected time traces at 510 nm, 610 nm and 710 nm. Open dots show the raw data, and the solid lines show fitting curves. The time axis is linear until 1 ps, and logarithmic thereafter. (**c**) Suggested photocycle of PR:MOA2 at pH 9.0 upon 520-nm excitation.

nm LED source[228]. However, continuous white light illumination does produce significant proton pump activity[228]. These observations are not easily reconciled. Our ground-state Raman data indicate heterogeneity in the Schiff-base region, possibly due to the presence of all-*trans* as well as 13-*cis* conformers in the chromophore. We cannot exclude that this complex system reacts differently to continuous white light illumination than to femtosecond laser light excitation. In **Fig. 5.8c**, the photocycle of PR:MOA2 upon 520-nm excitation is shown.

Excited-state dynamics of PR:MMAR

Femto- to submillisecond transient absorption spectroscopy was applied to PR:MMAR at pH 7.0 with excitation at 510, 620, 670, and 730 nm. In **Fig. 5.9**, globally fitted transient absorption spectra (EADS and DADS) and selected time traces of PR:MMAR with 620-nm excitation are shown. Global fitting required seven exponential components: 260 fs, 6.4 ps, 34 ps, 290 ps, 540 ns, 12 µs and infinite. With 510- and 670-nm excitation, again seven components were required (**Fig. 5.10**), while only three components were required for adequate fitting for 730-nm excitation (**Fig. 5.10**). In the global-fitted spectra obtained with 620 nm excitation (**Fig. 5.9**), a mixture of signals from negative peaks representing GSB and SE, and positive signals from ESA and photoproduct absorption, are observed. The negative

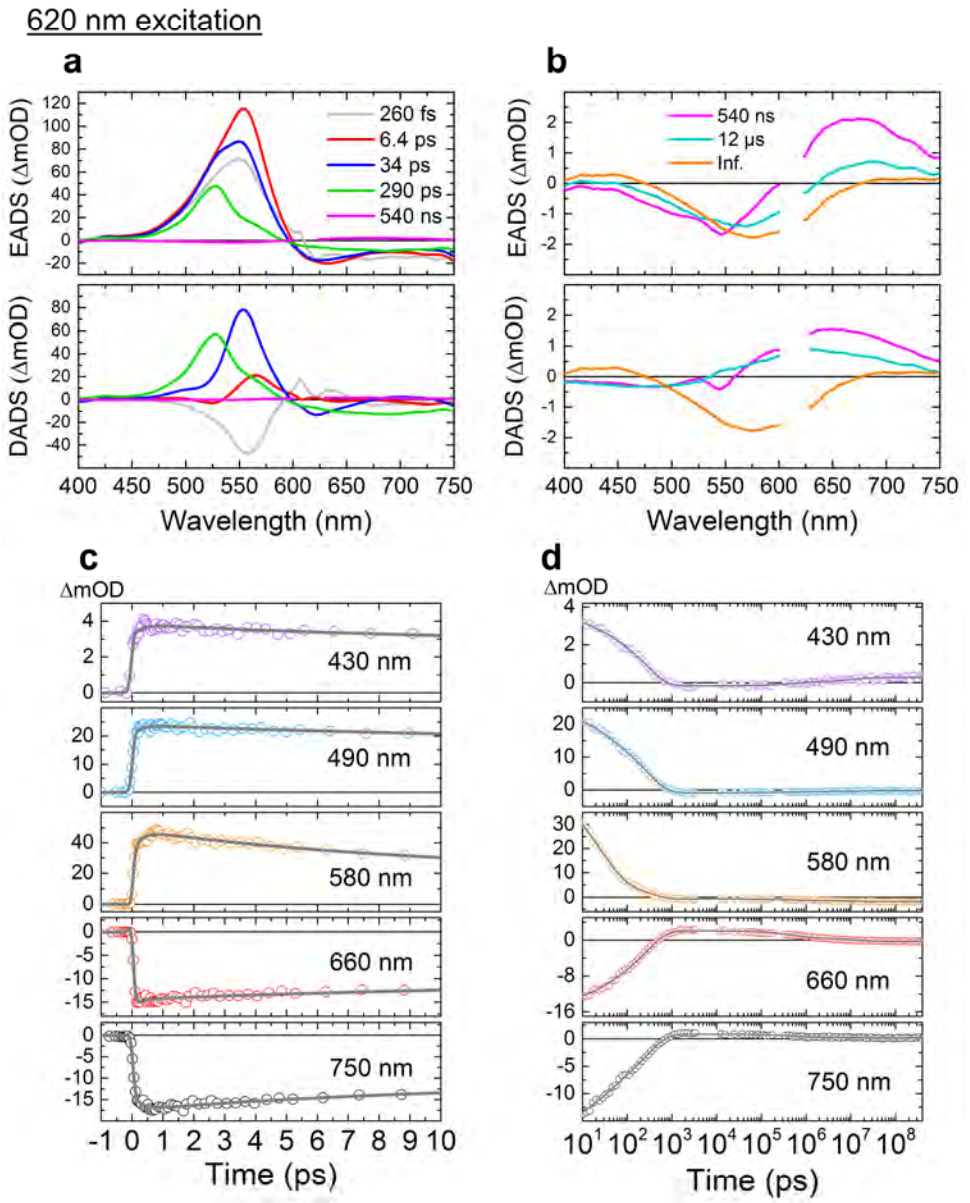

Figure 5.9. Global-fitted transient absorption spectra of PR:MMAR at pH 7.0 with 620-nm excitation. Evolution-associated difference spectra (EADS) and decay-associated difference spectra (DADS) of the (**a**) first five and (**b**) the last three components. In **b**, the wavelength region of 610–630 nm is omitted because of the strong scattering. Selected time traces (**c**) between -1 ps and 10 ps and (**d**) between 10 ps and 400 µs. Open dots show the raw data, and the solid lines show fitting curves.

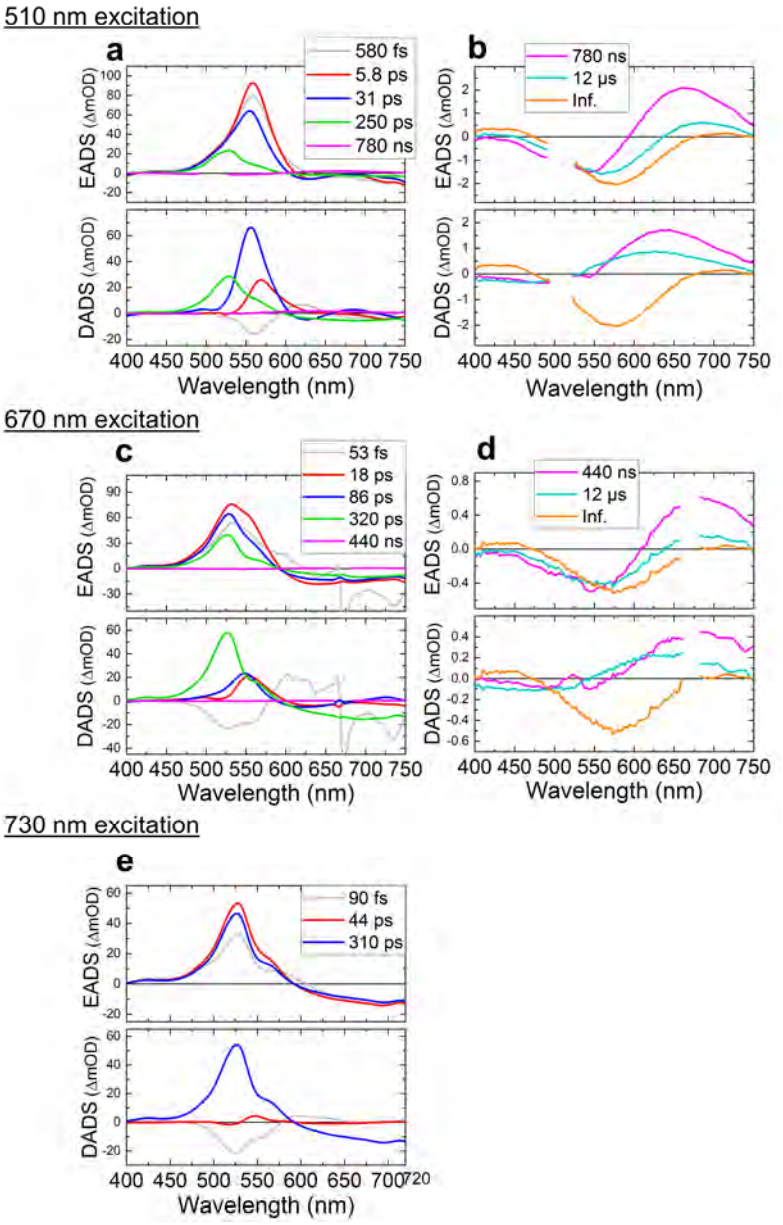

Figure 5.10. Global-fitted transient absorption spectra of PR:MMAR at pH 7.0. EADS and DADS upon excitation at (**a,b**) 510 nm, (**c,d**) 670 nm and (**e**) 730 nm.

bands in the near-infrared (NIR) region (≳700 nm) are assigned primarily to SE, which is an indicator for molecules in the excited-state, but probably also contain a contribution from the GSB of the 760 band (**Fig. 5.10**). The negative signals at >~700 nm were also observed at pH 9.0 (**Fig. 5.11**), where PR:MMAR has very low ground-state absorption at wavelengths >720 nm (**Fig. 5.3**), indicating that the negative signals in the NIR region at least partly derive from SE. The SE decayed with four time constants: 260 fs, 6.4 ps, 34 ps and 290 ps, which indicates that four time components are involved in the excited-state dynamics. The positive signals at 460–600 nm are assigned to ESA, which overlaps with the GSB. As obvious from the DADS (**Fig. 5.9**, lower panel), the signal at 600–650 nm slightly decreased in 260 fs, while the signal at ~560 nm rose (grey curve). The blue shift of the ESA possibly indicates relaxation from the Franck–Condon region to the energy minima on the excited state surface. Significantly, three distinct ESA components exist on the picosecond excited-state dynamics, namely at ~560 nm (ESA1, decaying in 6.4 ps, red curve), ~550 nm (ESA2, decaying in 34 ps, blue curve) and ~530 nm (ESA3, decaying in 290 ps, green curve). In 290 ps, the first photoproduct appeared at ~660 nm at low amplitude (green to magenta evolution) which is assigned to a K-like intermediate that is quite common to microbial rhodopsins[7].

The ESA1, ESA2 and ESA3 components of the DADS obtained with 510-, 620-, 670- and 730-nm excitation are shown in **Fig. 5.12**. Quite notably, with 730-nm excitation

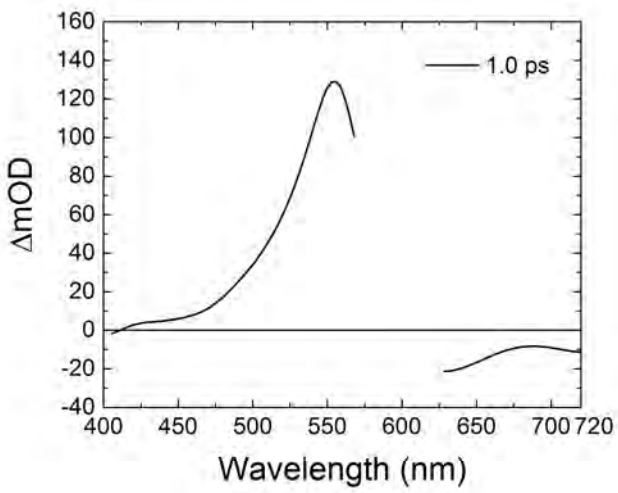

Figure 5.11. Transient absorption spectrum at 1.0 ps in PR:MMAR at pH 9.0 with 600-nm excitation. The wavelength region of 570–625 nm is omitted because of the strong scattering.

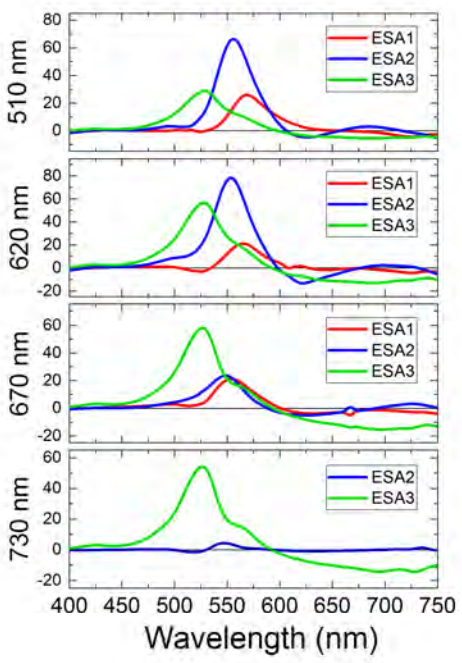

Figure 5.12. DADS of the three excited-state components of PR:MMAR at pH 7.0 with excitation at 510, 620, 670 and 730 nm.

the ESA1 component was not detectable and the ESA2 signal was very small, while still a large ESA3 signal was observed. Equally significant is that no photoproduct was detected upon 730-nm excitation. These observations imply that under our experimental conditions the 750-nm ground-state absorbing species (**Fig. 5.3**) is involved almost solely with ESA3, which does not generate a photoproduct and hence does not result in photo-isomerization and/or proton transfer. We conclude that relaxation to the ground state dominates the 290 ps component (ESA3). This observation is consistent with the charge delocalization and bond leveling for the 750-nm ground-state absorbing species that we proposed on the basis of the stimulated Raman results (**Fig. 5.4e**, right panel), which will decrease the C13=C14 double bond character, thereby impairing isomerization and hence significantly extending the excited-state lifetime.

With excitation at 510 nm, 620 nm and 670 nm, ESA1, ESA2, ESA3 as well as the K-like intermediate were detected. In **Table 5.1**, the measured peak values of the ESA1, ESA2, ESA3 and the K-like intermediate signals on the DADS with different excitation

Table 5.1. Comparison of the peak intensities of the excited-state absorption species and the K-like state of PR:MMAR with different excitation wavelengths. The unit of the values is ΔmOD.

Excitation wavelength	ESA1	ESA2	ESA3	K-like state
510 nm	26	**66**	29	**2.1**
620 nm	21	**78**	56	**2.1**
670 nm	21	**24**	58	**0.6**
730 nm	—	4	54	—

wavelengths are shown. The populations of ESA1 were almost identical with excitation at 510, 620 and 670 nm, while those of ESA2 are about 3-fold smaller with 670-nm excitation than with 510- and 620-nm excitation. Strikingly, the K-like state population is also ~3-fold smaller with 670-nm excitation than with 510- and 620-nm excitation; which is suggestive of a positive correlation between the population of ESA2 and that of the K-like photoproduct. These observations indicate that ESA2 is the productive excited-state species, and ESA1 is a non-productive state. Overall, we tentatively conclude that the ESA2 is the dominant state in producing the K-like intermediate in ~30 ps, and the ESA1 and ESA3 are excited-state species returning to the initial ground state.

Photoproduct dynamics of PR:MMAR

Deprotonation of the RSB, *i.e.* M-like intermediate formation, is generally considered to be an essential step in the proton transfer mechanism[245]. **Fig. 5.9b** shows that the absorbance at 400–500 nm was rising in 540 ns (magenta to cyan evolution) and 12 μs (cyan to orange evolution) whereby the K-like signal (~650 nm) was decreasing. This signal rise at 400–500 nm reflects formation of a M-like intermediate[7], which shows that proton transfer also occurs during the photocycle PR:MMAR, similarly to PR:A1 and PR:A2. It is noteworthy that the K-like signal partially persisted after 540 ns (cyan line in the upper panel of **Fig. 5.9b**), indicating that the M-like and K-like intermediates are in equilibrium on that timescale. On the other hand, after 12 μs (orange line in the upper panel of **Fig. 5.9b**), the K-like absorption has disappeared almost completely, implying that a pure M-like intermediate is formed in 12 μs. Similar signal developments were observed with 510-nm

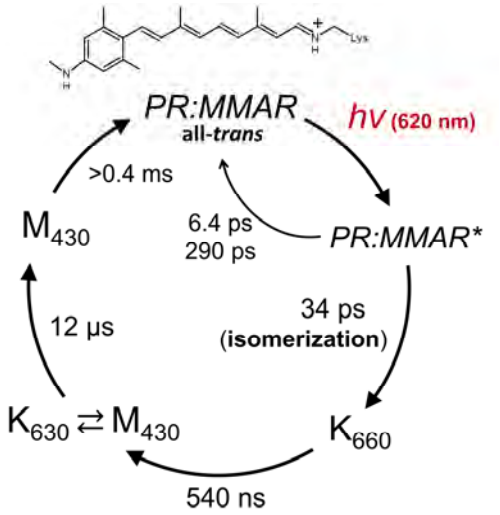

Figure 5.13. Proposed photocycle model of PR:MMAR at pH 7.0 with 620-nm excitation.

and 670-nm excitation (**Fig. 5.10**). Moreover, the time constants of M-formation are similar to PR:A1[201,242,246] and other microbial rhodopsins [7], which implies that the proton transfer mechanism might be similar in PR:MMAR and PR:A1. A schematic of the overall photocycle of PR:MMAR based upon our data at pH 7.0 with 620-nm excitation is shown in **Fig. 5.13**. This shows good resemblance to that of PR:A1[201,242,243].

It should be noted that it is not clear whether proton transfer from the protonated RSB in PR:MMAR is essential for its proton pumping function. Significant proton pumping activity was observed at pH 7 with 617-, 660- and 730-nm continuous LED illumination[228]. As shown above, M formation was enhanced upon femtosecond 620-nm relative to 670-nm laser excitation, and in fact no photocycle was detected upon femtosecond 730-nm laser excitation, *i.e.* no evidence for proton transfer from the protonated RSB. To estimate how effective the different LEDs are in inducing proton pumping in PR:MMAR, we normalized the reported molecular pumping activity[228] by correcting for pigment molar absorbance, LED emission cross section and LED photon flux. The outcome uncovers that the resulting net molecular pumping rates with 617 nm, 660 nm or 730 nm LED illumination (1.0 ± 0.2 , 0.7 ± 0.2 and 0.8 ± 0.2 protons/sec, respectively, per normalized quantity of photons) are not significantly different. We have to conclude that factually over this wavelength range the pump activity of PR:MMAR is constant under continuous illumination, and is not correlated with photoproduct formation upon femtosecond laser

excitation. Although the micro-environment is different under either condition (DDM micelles for the photodynamics, *E. coli* membranes for proton pumping), this should not make a fundamental difference for the photocycle[201,231,232]. A possible explanation would be that proton transfer from the protonated RSB is not absolutely essential for proton pumping[245]. On the other hand, ultrarapid transient-grating spectroscopic studies on visual rhodopsin[247,248] may suggest that narrow-band femtosecond excitation would not uncover the full photodynamic theatre of retinal proteins. This might also underlie the discrepancy between the PR:MOA2 pumping ability and the measured lack of a photocycle, discussed above.

Fluorescence properties of PR:MMAR: potential usage as a voltage sensor

As discussed above, PR:MMAR has a long-lived excited state (ESA3, τ = 290 ps). Because fluorescence quantum yield is determined by the excited-state lifetime, we surmised that PR:MMAR would have a much higher fluorescence quantum yield than native PR:A1, which has a very low fluorescence quantum yield Φ_{FL} of 0.026%[243]. The D97N mutant of PR:A1 (PR-D97N:A1, also known as PROPS), cannot pump protons, has a higher fluorescence yield (Φ_{FL}~1.0%) and was demonstrated to be a suitable membrane voltage sensor in *E. coli*[219]. Since then, various voltage sensors have been designed based on microbial rhodopsins and applied to visualization of action potentials of neurons[220,221,249]. For an ideal pH or voltage sensor, a high fluorescence quantum yield and strong pH dependence of the emission intensity around physiological pH are required. Moreover, NIR absorption/emission will be beneficial for deeper tissue imaging[84,249]. We recorded the fluorescence properties of PR:MMAR to investigate potential application of MMAR-based microbial rhodopsins as a pH and/or voltage sensor.

Fig. 5.14a shows pH-dependent emission spectra of PR:MMAR at pH 6.0–8.5 with 760-nm excitation. Independent of the pH value, the emission peak was centered at 820 nm, which is about 120-nm red-shifted from the native PR:A1[243]. The excitation spectrum of the 820-nm emission at pH 7.0 overlaps with the 1-T (1-transmittance) spectrum as shown in **Fig. 5.14b**, clearly indicating that the far-red (>750-nm) absorbing species is the major emissive species. A quantum yield of 3.3 % was measured with 760-nm excitation at pH 7.0, which is 130-fold higher than that of PR:A1[243] and 3.3-fold higher than PROPS[219]. Importantly, a strong pH-dependence was observed for the fluorescence intensity over the pH range 6.0–8.5 (**Fig. 5.14c**), which clearly corresponds with the pH-dependent absorbance band at 760 nm. Considering this combination of properties of

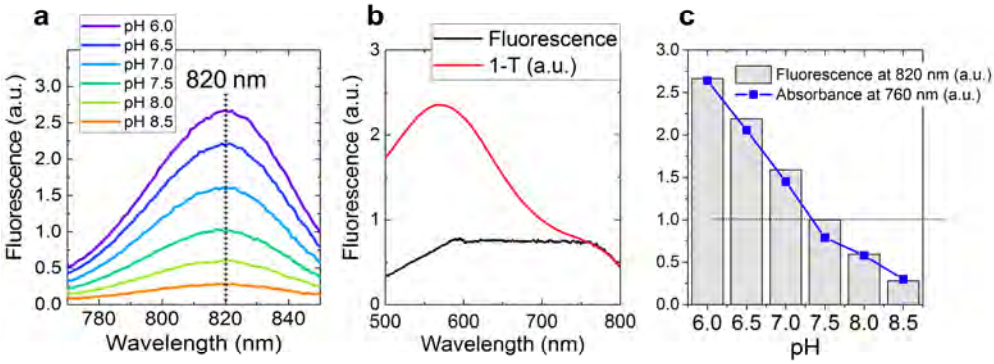

Figure 5.14. Fluorescence of PR:MMAR at pH 6.0–8.5, with 760-nm excitation. The sample concentration was uniformed for different pH samples. (**a**) pH dependent fluorescence spectra. (**b**) Excitation spectrum of 820-nm fluorescence of PR:MMAR at pH 7.0 overlapped with 1-transmittance (1-T) spectrum. (**c**) Comparison of the fluorescence at 820 nm (gray bars) and the absorbance at 760 nm (blue plots).

PR:MMAR: high fluorescent quantum yield, NIR absorption/emission and strong pH dependence in the pH range 6.0–8.5, we would advocate MMAR-binding proteins as very promising candidates for ultrasensitive NIR pH and/or voltage sensors.

5.3. Conclusion

We report a comprehensive study of PR pigments containing the retinal analogues: A2, MMAR, or MOA2 through stimulated Raman spectroscopy of their ground states and a femtosecond-to-submillisecond transient absorption spectroscopy of their photodynamics. In PR:A2, photo-isomerization and the ensuing thermal reactions proceed largely similar as in native PR, albeit overall slower. In PR:MOA2, all excited molecules relaxed to the initial ground state on the picosecond timescale without detectable photoproduct formation.

PR:MMAR has the most red-shifted absorption profile among these three analogue pigments presenting a main absorption band with λ_{max}~580 nm and a satellite NIR band around 760 nm, the latter of which dramatically increases its intensity upon acidification. Based upon the pH-dependent stimulated Raman spectroscopy results, we propose that the MMAR chromophore's charge delocalizes towards the secondary methyl-N-C group on the aromatic ring at the other end of the chromophore, essentially creating a second protonated Schiff base boundary structure (**Fig. 5.4e**, bottom). The two boundary

structures shown in **Fig. 5.4e** are in a pH-dependent equilibrium, resulting in a complex system of resonance states, yielding the heterogeneous absorbance and vibrational profiles of PR:MMAR under alkaline and acidic conditions, of which those geared most towards the boundary structure of **Fig. 5.4e** (bottom) represent the longest-wavelength NIR absorption and emission bands at 760 and 820 nm, respectively.

Our transient photochemical analyses of PR:MMAR indicate that the photoisomerization proceeds in ~30 ps, which is substantially slower than in PR:A1. Similar to PR:A1 and PR:A2, subsequent to photo-isomerization PR:MMAR proceeds to formation of an M-like intermediate, reflecting proton transfer from the protonated RSB, in 540 ns and 12 μs. Strikingly, the population of photoproducts was highly dependent on the excitation wavelength, being ca 3-fold higher with 510- and 620-nm excitation than with 670-nm excitation, and undetectable with 730-nm excitation.

Crucially, with 730-nm excitation, an unusually long excited-state decay time constant (τ~300 ps) was observed along with absence of any detectable isomerized photoproduct, implying strong fluorescence emanating from the longest-wavelength PR:MMAR species absorbing at 760 nm. Indeed, we observed NIR emission at 820 nm at a high fluorescence quantum yield (~3.3%) for PR:MMAR with 720-nm excitation, which is 140 times higher than of native PR:A1 and 3.3 times higher than that of the PR-D97N:A1 (PROPS) voltage sensor. We further show a remarkable pH dependence of the fluorescence intensity in the range 6.0–8.5, suggesting potential application of MMAR-based proteins as ultrasensitive NIR-absorptive/emissive voltage and/or pH sensors.

The above observations can all be rationalized by partial formation of the second protonated Schiff base at the aromatic side of the MMAR molecule in a pH-dependent counterion protonation equilibrium: the long-wavelength NIR absorption and emission follows from bond leveling and charge delocalization towards the secondary amine, whereas the resulting decrease of the C13=C14 double bond character impairs isomerization at that site and significantly extends the excited-state lifetime, in turn leading to a strongly increased pH-dependent fluorescence. Hence, we conclude that careful design of retinal analogue molecules in combination with advanced mechanistic spectroscopic assessment has resulted in a crucial understanding of newly engineered, valuable qualities of microbial rhodopsins.

Methods

Cell culturing: E. coli strain UT5600 transformed with the pKJ900 plasmid was used to express recombinant PR with a C-terminal 6-His tag. The cells were grown in LB medium, harvested, lysed and regenerated with the appropriate retinal as per protocols described previously[227,228].

Protein purification: The lysed cell suspension was incubated with 4% DDM (w/v) overnight at 4°C and centrifuged to remove the insoluble cellular debris. The His-tagged proteorhodopsins were purified by immobilized-metal affinity chromatography (IMAC), as reported previously[228]. 10 ml Ni^{2+}-NTA resin was used per 2000 mL original culture volume. The purified proteorhodopsin was eluted in 5 ml fractions containing 20 mM bis-tris propane, 500 mM imidazole, 0.5 M NaCl, 0.1% DDM, pH 8 at RT. The fractions were combined and. concentrated using a 10 kDa cut-off column (Amicon) to OD~10 at the absorption maxima for steady-state Raman and transient absorption experiments or OD~0.05 for fluorescence experiments. Buffer solutions for pH-dependent experiments contained 150 mM NaCl and 2.5% DDM, with 20 mM bis-trispropane (for pH 6.0–7.0) or 20 mM Tris-HCl (for pH 7.5–9.0),.

Steady-state stimulated Raman spectroscopy: Steady-state stimulated Raman experiments were performed as reported previously[41,42,136], using a 2-mm pathlength quartz cuvette (100-QS, Hellma Analytics).

Femto- to submillisecond transient absorption spectroscopy: Transient absorption measurements were performed with a femtosecond-to-submillisecond pump-probe setup as reported previously[41,42,133]. The samples were filled in a homemade sample holder that has two 2-mm-thick CaF_2 plates. The sample thickness was set at 400 μm for transient absorption experiments with an appropriate sample spacer. The sample holder was set on a Lissajous scanner that ensures sample refreshment after each laser shot with a time interval of 60 seconds between successive exposures to the laser pulses[134]. A CaF_2 plate on a moving stage was used for supercontinuum white light generation, and a selected wavelength region; 400–750 nm, was detected by the photodiode array. The time delay was varied up to 430 μs at 163 data points with the minimum temporal step of 50 fs. The diameters of the pump and the probe beams at the sample position were ~200 μm and ~50 μm, respectively. The central wavelength and the power of the pump beam were set at 510 nm (~400 nJ) and 620 nm (~600 nJ) for PR:A2, at 520 nm (~500 nJ) for PR:MOA2, and at 510 nm (~400 nJ), 620 nm (~400 nJ), 670 nm (~400 nJ), and 730 nm (~600 nJ) for PR:MMAR. The instrumental response function was ~100 fs, as estimated from global analysis.

Fluorescence spectroscopy:

Fluorescence spectra of PR:MMAR at pH 6.0, 6.5, 7.0, 7.5, 8.0 and 8.5 were taken with a Vis/NIR fluorescence spectrometer (Fluoromax, Horiba) at 20°C, as reported previously[250]. For the data acquisition process, the excitation light intensity was monitored by a photodiode and the fluorescence intensity was corrected for the photon flux of the excitation light. The samples were diluted to an OD< 0.05 (per cm) at 760 nm to prevent reabsorption. The pigment concentration was the same for the different pH conditions. The fluorescence quantum yield of PR:MMAR at pH 7.0 with 760-nm excitation was measured using a near-infrared laser dye (HITCI, Φ_{FL} = 28.3%[251]) dissolved in ethanol as a standard. The samples were contained in a quartz cuvette (104F-QS, Hellma Analytics) with 10-

mm pathlength in the excitation direction and 4-mm pathlength in the detection direction. The fluorescence spectra were obtained for the PR:MMAR and HITCI between 700–850 nm, and multi-Gaussian fitting was applied to calculate the total area of emission counts. The fluorescence quantum yield of PR:MAMR ($\Phi_{FL,PR}$) was calculated with the following formula[251]:

$$\Phi_{FL,PR} = \Phi_{FL,dye} \times f_{dye}(\lambda_{ex})/f_{PR}(\lambda_{ex}) \times F_{PR}/F_{dye} \times n_{water}^2/n_{ethanol}^2$$

Here f_x , F_x and n_x represent 1–transmittance, total area of emission and refractive index, respectively.

Chapter 6

Unique excited-state dynamics of unprotonated retinal in UV-absorbing histidine kinase rhodopsin HKR1

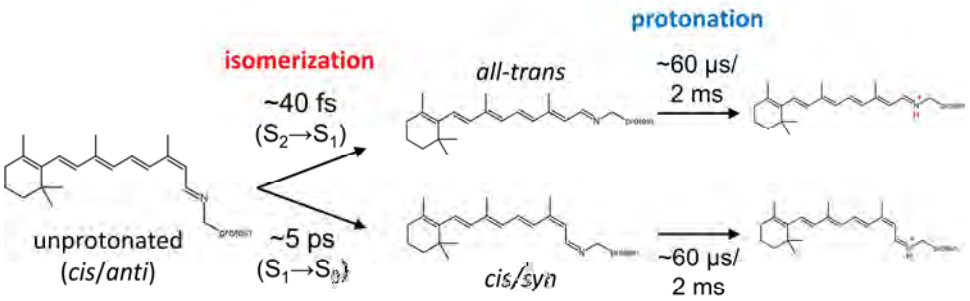

Double-isomerization on distinct potential energy surfaces and protonation of unprotonated retinal in HKR1 were observed by TSRS.

Abstract

Histidine kinase rhodopsin 1 (HKR1) is a unique microbial rhodopsin having bistable ground states: UV-absorbing (Rh-UV, unprotonated retinal incorporated) and blue-absorbing (Rh-Bl, protonated retinal incorporated). Photoreaction dynamics of unprotonated retinal is of great interest for deeper understanding of Rh-UV in HKR1 and other UV-absorbing animal rhodopsins, but is poorly understood. We report the excited-state dynamics of Rh-UV in HKR1 probed by transient stimulated-Raman spectroscopy, a powerful technique for real-time observation of pigment dynamics. An unusually upshifted Raman signal was detected at ~1720 cm^{-1}, which is assigned to the C=C stretch in optically forbidden S_1 ($2Ag^-$) state that is widely seen in carotenoids. Simultaneously, Raman bands of isomerized states were observed in the S_1 state, indicating that isomerization proceeds in S_2–S_1 relaxation, which is an extraordinary reaction pathway in animal and microbial rhodopsins equipped with protonated retinal. Moreover, the isomerization rate was <50 fs, which is much faster than any reported isomerization of protonated retinal in proteins. Notably, two distinct isomerization coordinates can be proposed: 13-*cis* to 13-*trans* isomerization and 15-*anti* to 15-*syn* isomerization.

This chapter is in preparation for publication:
collaborated with M. Broser, M. Luck and P. Hegemann for sample preparation.

6.1 Introduction

Rhodopsin proteins are fundamental light sensors widely seen in various organisms belonging to Eukaryota, Bactaria and Archaea domains[7]. Most of animal and microbial rhodopsins have a protonated retinal to absorb a wide range of visible light from blue to red[7]. Some animal rhodopsins equip an unprotonated retinal in the dark state, which enables UV-light sensing[252,253]. Histidine kinase rhodopsin 1 (HKR1) is a unique microbial rhodopsin having photochromic bistable dark states: blue absorbing state (Rh-Bl, λ_{max} ~ 485 nm) and UV-absorbing state (Rh-UV, λ_{max} ~ 380 nm), incorporating a protonated retinal and an unprotonated retinal, respectively[65] (**Fig. 6.1**). Similar bistable rhodopsins with blue- and UV- absorbing species have been found in animals recently[254,255]. Notably, resonant Raman spectroscopy has revealed that the Rh-Bl state has heterogeneous retinal components (all-*trans* and 13-*cis*/15-*syn*), whereas Rh-UV state has only a single retinal conformer (13-*cis*/15-*anti*)[65] (**Fig. 6.1a**).

In photoactive proteins, excited-state dynamics that proceed in the fs–ps timescale play a significant role in triggering their function, *e.g.* photoisomerization in rhodopsin proteins. So far, various studies have been conducted for elucidating excited-state dynamics of protonated retinal in animal and microbial rhodopsins, showing S_0–S_1 photoexcitation and following ultrafast photoisomerization via a conical intersection between S_1 and S_0 (photoproduct) states[42,148,154,168,207,214,243,256,257]. An early theoretical study reported that retinal Schiff base (RSB) protonation leads to Bu^+/Ag^- excited-state energy level inversion, *i.e.* in protonated RSB, the optically allowed Bu^+ state is the lowest-lying excited state, whereas in unprotonated RSB, the optically forbidden Ag^- state is the lowest, as it is in linear polyenes[258]. Thus, in rhodopsins equipped with an unprotonated retinal, it was proposed that photoexcitation occurs to the optically-allowed S_2 state but not to optically-forbidden S_1

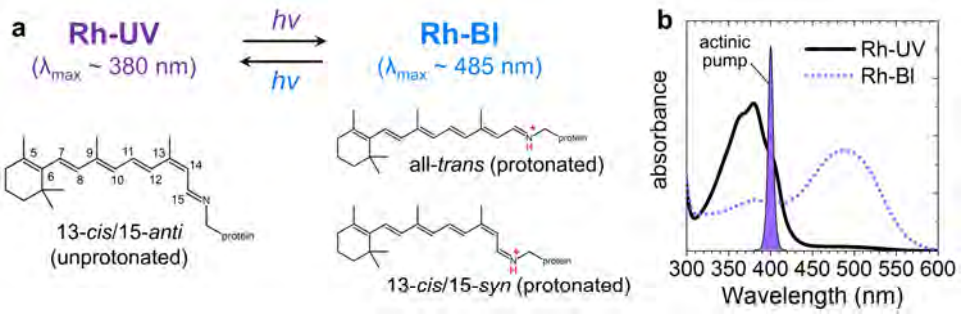

Figure 6.1. Retinal conformers in HKR1. (**a**) UV-absorbing (Rh-UV) and blue-absorbing (Rh-Bl) states of HKR1. (**b**) Steady-state absorption spectra of Rh-UV (black solid line) and Rh-Bl (blue dotted line) states.

state, with steady-state spectroscopy[259] and quantum mechanical calculations[260]. Therefore, the excited-state dynamics of Rh-UV state of HKR1 is expected to be fundamentally different from that of other rhodopsin proteins that have a protonated RSB. Ultrafast transient absorption spectroscopy was applied previously to Rh-UV in HKR1, showing that the excited state decays in ~5 and ~60 ps, although clear photoproduct species were not detected after those decays[65]. In addition, it was shown that protonation that results in Rh-Bl formation occurs very slowly in 2.3 ms by flash photolysis. However, it is still unclear whether and when the isomerization happens, and when the heterogeneous retinal conformers of the Rh-Bl state are formed, while these information is critical to understand the photoreaction.

Transient stimulated Raman spectroscopy (TSRS) is a powerful method to obtain detailed molecular information with high spectrotemporal resolution[41,135]. In this work, we show the excited-state and ground state photoproduct dynamics of Rh-UV in HKR1 with a combination of femto-to submillisecond transient absorption (TA) and TSRS, discussing double photoisomerization on distinct potential energy surfaces. Our work will constitute an important standard for photochemistry on UV-absorbing rhodopsins.

6.2 Results

Excited-state dynamics: femtoseconds to picoseconds

Femto- to submillisecond TA spectroscopy and TSRS were performed on the Rh-UV state of HKR1 with 400-nm excitation. Globally fitted spectra (EADS: evolution-associated difference spectra, and DADS: decay-associated difference spectra) are shown in **Fig. 6.2a**, while selected kinetic traces are shown in **Fig. 6.2b**. For the global analysis, six components were needed; 40 fs, 370 fs, 4.8 ps and 62 ps, 58 μs and infinite. The time constants and spectral features of the 370 fs, 4.8 ps and 62 ps components correspond to the previously reported TA spectra[65]. However, an additional 40 fs component was necessary in the TA data, which was not considered in the previous experiment[65]. The 40 fs EADS shows a stimulated emission band at ~450 nm and a pronounced excited-state absorption at >470 nm. It evolves to the second EADS in 40 fs (blue line, **Fig. 6.2a**) that has two positive peaks at ~470 nm and ~590 nm. In 370 fs, the EADS becomes sharpened, while its peak positions do not significantly change (magenta line, **Fig. 6.2a**). In 4.8 ps and 62 ps, the positive signals decayed almost completely (red line, **Fig. 6.2a**). In 58 μs, a positive peak at ~480 nm appeared (cyan line, EADS on **Fig. 6.2a**). A negative band at ~400 nm is observed in all time components, which is considered as ground state bleach of the Rh-UV state.

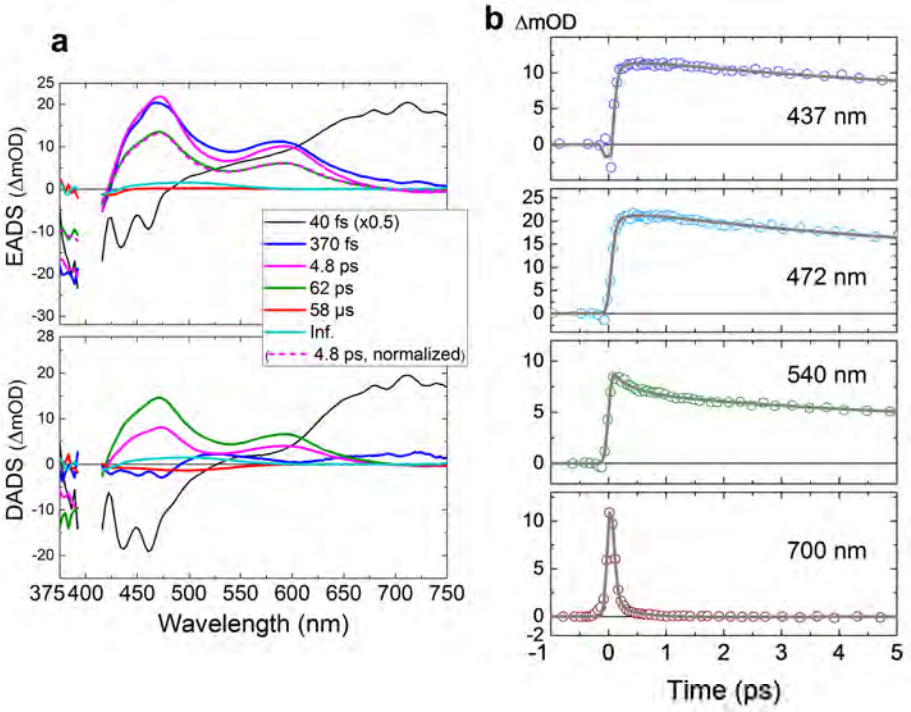

Figure 6.2. Global-fitted transient absorption spectra of Rh-UV state of HKR1 upon 400 nm excitation. (a) Evolution-associated difference spectra (EADS, top) and decay-associated difference spectra (DADS, bottom) of the transient absorption signals. Normalized EADS of the 4.8 ps component is shown in dashed magenta line. (B) Open dots and gray solid lines show the raw data and fitting curves, respectively.

Fig. 6.3a shows selected transient Raman spectra at 1500–1900 cm^{-1}, obtained with pre-resonant ~800-nm Raman pump upon actinic excitation of Rh-UV at 400 nm. In the previous resonance Raman study, a strong C=C stretching peak was observed at 1566 cm^{-1} on the ground state of Rh-UV[65]. Negative signals at ~1570 cm^{-1} were observed in the entire time-resolved spectra, which are considered as ground state bleach of the Rh-UV state. Within hundreds of femtoseconds after excitation, a positive band at ~1712 cm^{-1} appeared, which upshifted to 1716 cm^{-1} in several picoseconds. To quantify its dynamics, global analysis was performed to the transient stimulated Raman spectra, applying the same time components as for the TA experiments; 40 fs, 370 fs, 4.8 ps and 62 ps, 58 μs and infinite (**Fig. 6.3b**). Notably, all of the six components were required for adequate fitting. From the EADS and DADS (**Fig. 6.3b**), it is obvious that the ~1712-cm^{-1} band appeared in 370 fs. Moreover, two positive decay components peaking at 1696 and 1716 cm^{-1} were observed in

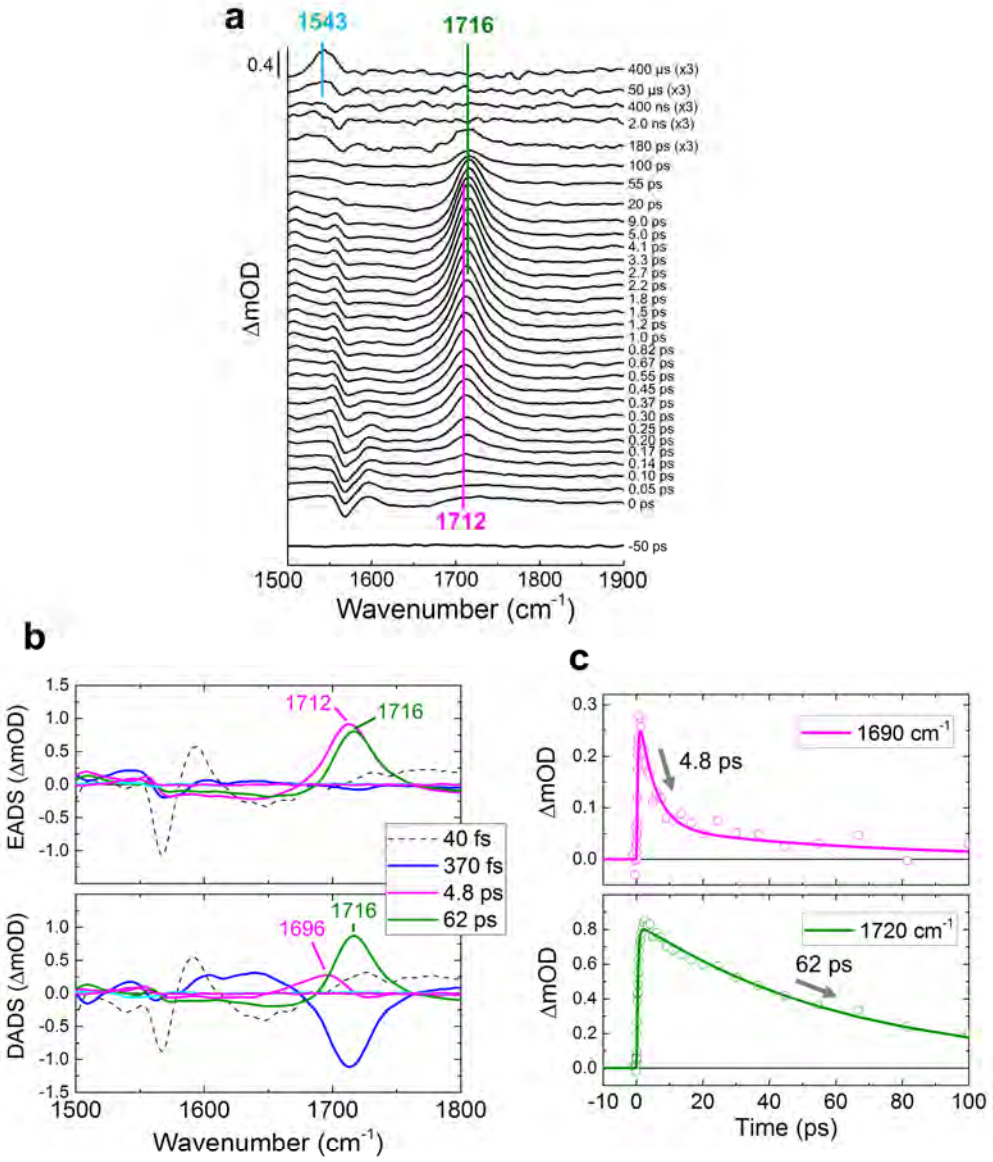

Figure 6.3. Transient stimulated Raman spectra of Rh-UV state of HKR1 with 400 nm excitation. (**a**) Selected transient Raman spectra. (**b**) Evolution-associated difference spectra (EADS, top) and decay-associated difference spectra (DADS, bottom) of the transient Raman signals. (**c**) Time traces at 1690 cm^{-1} (top panel) and 1720 cm^{-1} (bottom panel). Open dots and solid lines show the raw data and fitting, respectively.

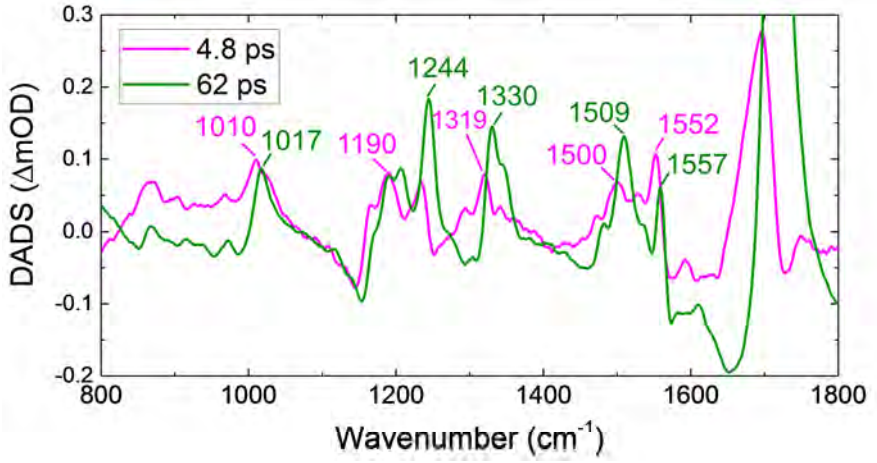

Figure 6.4. DADS of 4.8 ps and 62 ps components of transient Raman data.

the DADS, which decayed in 4.8 ps and 62 ps, respectively (**Fig. 6.3b**). In **Fig. 6.3c**, the kinetic traces at 1690 cm^{-1} (top) and 1720 cm^{-1} (bottom) are demonstrated with fitted curves as they result from the global analysis. **Fig. 6.4** shows the third (decaying with 4.8 ps) and fourth (decaying with 62 ps) DADS of the TSRS experiments on the spectral window between 800 and 1800 cm^{-1}. The 4.8 ps component (magenta line) has additional positive bands at 1010, 1190, 1319, 1500 and 1552 cm^{-1}, and the 62 ps component (green line) shows positive bands at 1017, 1244, 1330, 1509 and 1557 cm^{-1}. Note that the 4.8 ps and 62 ps EADS show a broad negative baseline in the region between 1600 and 1800 cm^{-1}. This is a consequence of the watermarking approach, which causes broad negative features to appear on either side of strong positive bands (the 'Mexican hat' effect), and should be interpreted as an incomplete baseline removal rather than genuine negative signals[136].

Ground-state dynamics: picoseconds to microseconds

In **Figs. 6.5a** and **5b**, EADS of the two last components of 58 µs (red line) and non-decaying (cyan line) of transient absorption and a ns-µs time trace at 500 nm are shown, respectively. The 58 µs component appears upon decay of the 62 ps component (**Fig. 6.2b**, green line), and evolves to the non-decaying EADS in 58 µs. In the TA data, the EADS is almost zero between 450 and 600 nm in the 58 µs species (red line, **Fig. 6.5a**), while a band at ~500 nm appeared in the evolution to the non-decaying species in 58 µs (cyan line in **Fig. 6.5a,b**). In **Fig. 6.5c**, EADS of the two last components of the transient Raman experiments are shown. A relatively weak positive band at 1529 cm^{-1} is observed in the 58 µs component, along with

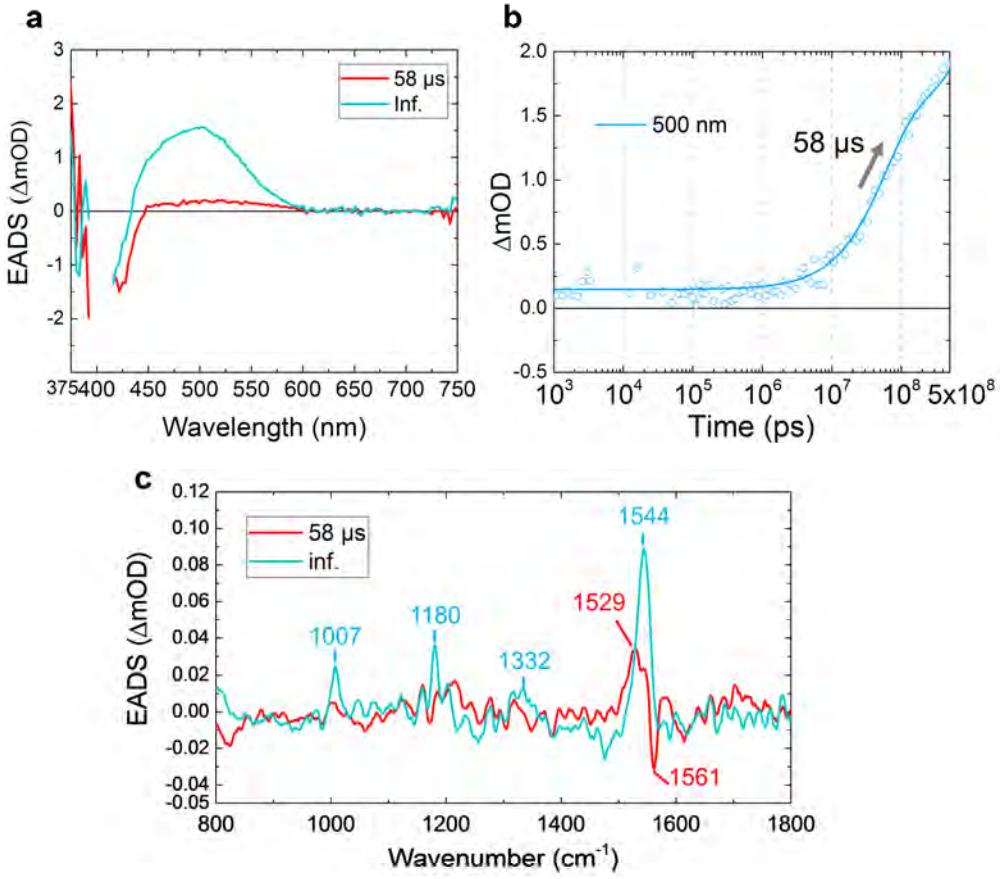

Figure 6.5. EADS of the 58 μs and infinite components of the transient Raman and absorption experiments. (**a**) EADS of the transient absorption signals. (**b**) A ns-μs time trace at 500 nm of the transient absorption experiments. The open dots and the solid line show raw data and a fitting curve, respectively. (**c**) EADS of the transient Raman signals.

a negative signal at 1561 cm^{-1} that corresponds to ground state bleach of the Rh-UV state (red line, **Fig. 6.5c**). In the infinite component, clear peaks at 1007, 1180, 1332 and 1554 cm^{-1} are seen in the Raman spectrum (cyan line, **Fig. 6.5c**). Most likely, the increase of the Raman signal intensity in 58 μs is due to increased preresonance with the 800-nm Raman pump upon formation of the 500 nm absorbing species (**Fig. 6.5a,b**).

6.3. Discussion

Excited-state ordering, interconversions and relaxation in HKR1

First, the dynamics on the ~40 fs component will be discussed. The first EADS of TA in **Fig. 6.2b** show stimulated emission (SE) at ~450 nm and ground-state bleach signals, indicating that the molecules are on the excited state. Significantly, this EADS has quite comparable features to the optically allowed S_2 ($1Bu^+$) state TA spectrum of carotenoids[261-263]. Early theoretical studies have indicated that RSB protonation/deprotonation leads to Bu^+/Ag^- level inversion[258]. Here, we experimentally confirm that this simple picture is essentially correct, *i.e.* the optically allowed $1Bu^+$ is located higher than the optically forbidden $2Ag^-$ state, resulting in S_0–S_2 photoexcitation in Rh-UV HKR1. The 40-fs decay of the carotenoid-like S_2 signal implies that the S_2 ($1Bu^+$)→S_1 ($2Ag^-$) transition proceeds in 40 fs. The spectral sharpening of TA spectra (**Fig. 6.2b**) in 370 fs is likely due to vibrational cooling of the S_1 ($2Ag^-$) state, as has been well established for carotenoids with regard to timescale and spectral signature[263-265], thus no electronic state transition occurs with that time constant. Spectral evolutions in 4.8 ps and 62 ps are likely derived from S_1 ($2Ag^-$)→ S_0 ($1Ag^-$) relaxation, forming ground-state photoproduct state(s).

Next, the origin of the upshifted 1710 cm^{-1} transient Raman peak (**Fig. 6.3**) will be discussed. This upshifted band at ~1710 cm^{-1} has not been observed in the excited state of rhodopsins having a protonated RSB[41,173,214]. Importantly, similar upshifted C=C stretching bands are generally observed in the optically forbidden S_1 ($2Ag^-$) state of linear polyenes such as carotenoids: *e.g.* at ~1778 cm^{-1} for β-carotene and ~1743 cm^{-1} for spirilloxanthin[136,266,267], and result from strong vibronic coupling between the S_1 ($2Ag^-$) and S_0 ($1Ag^-$) states[268]. In carotenoids, photoexcitation occurs to an optically allowed S_2 ($1Bu^+$) state, followed by internal conversion from S_2 to the optically forbidden S_1 ($2Ag^-$) state in ~200 fs[264]. Correspondingly, we assign the unusually upshifted band at ~1712 cm^{-1} in HKR1 that appears within 370 fs as a C=C stretching band of the optically forbidden S_1 ($2Ag^-$) state. Following the discussion above with TSRS, we conclude that S_1 state was formed at least within 370 fs. Since TA data indicates that the 370 fs, 4.8 ps and 62 ps components originate from the same electronic state (*i.e.* $2Ag^-$ S_1), the S_1 state is formed in the former timescale, 40 fs. Those TSRS observations sufficiently support our TA results. In TSRS, the S_1 C=C stretching modes appeared in 370 fs, not in 40 fs, even though the S_1 state is formed with 40 fs. Most likely, intramolecular vibrational energy redistribution is required prior to the occurrence of strong S_1–S_0 vibronic coupling, as previously observed in carotenoids[267].

The positive DADS at 1696 and 1716 cm^{-1} in **Fig. 6.3b** demonstrate that there are two distinct S_1 decay species. Because the 4.8 ps DADS is essentially all-positive (magenta line), the 4.8 ps spectral evolution does not represent a band shift of the S_1 C=C stretch but rather a decay component of the S_1 state, as we observed in the TA data (**Fig. 6.2a**). Moreover, another S_1 decay was observed in 62 ps (green line). These observations indicate that the S_1 state decays both in 4.8 ps and 62 ps, consistent with the observations of TA spectroscopy. It might be considered that the 4.8 ps component belongs to vibrational cooling. However, in addition to the nearly all-positive DADS of TSRS in the ~1710 cm^{-1} region (**Fig. 6.3b**), the 4.8 ps EADS in TA displays nearly identical features to that of the 62 ps EADS (**Fig. 6.2b**, see normalized 4.8 ps EADS). Indeed, the TA experiments clearly indicated vibrational cooling in 370 fs, as evidenced from the sharpening of the S_1 excited-state absorption with that time constant (**Fig. 6.2a**). Therefore, we conclude that vibrational cooling is completed in 370 fs, and eliminate the possibility that vibrational cooling occurs in 4.8 ps.

The significant difference on the S_1 C=C stretching (1696 and 1716 cm^{-1}) decays implies that structurally heterogeneous S_1 states are formed following population of the optically allowed S_2 state by the 400 nm excitation. Note that the retinal conformer of the Rh-UV state is homogeneous in the dark state, having only one C=C stretching peak at 1566 cm^{-1} [65]. From the substantial difference in the 4.8 ps and 62 ps DADS at the 800–1600 cm^{-1} spectral window (**Fig. 6.4**), we arrive at the important conclusion that two distinct retinal conformers are formed in the two S_1 states, and hence that retinal isomerization has taken place.

Deprotonated ground state species and protonation dynamics

Next, the nature of the photoproducts and their dynamics on the reaction from the Rh-UV state will be discussed. In the TA spectra (**Figs. 6.2b** and **6.5a**), a nearly zero absorption was observed after the decay of the S_1 state, giving no clear-cut indication of photoproducts after excited-state decay. In contrast, in TSRS (**Fig. 6.5c,** red line), a clear photoproduct was observed upon S_1 state decay involving a positive C=C stretching mode at 1529 cm^{-1}. We conclude that a photoproduct is formed thus has a distinct vibrational signature but lacks an obvious UV-vis signature. Most likely, the photoproduct corresponds to a deprotonated RSB species with a UV-vis spectrum that significantly overlaps with that of Rh-UV, causing their intrinsic positive and negative signals to cancel out. In bacteriorhodopsin, upon illumination

of the cryotrapped M state, a deprotonated photoproduct was formed that was red-shifted by only 3 nm, consistent with our observations[269].

The stimulated Raman signal from the deprotonated RSB photoproduct has a rather low amplitude, which is likely caused by lack of (pre)resonance with the 800 nm Raman pump and, possibly, a low quantum yield[259]. Closer inspection of its stimulated Raman signature reveals that besides the obvious positive product band at 1529 cm^{-1}, its ground state bleach of the parent Rh-UV state is located at 1561 cm^{-1}. Given that the C=C stretch of the Rh-UV state is located at 1566 cm^{-1} [65], this finding suggests that another positive product absorption is present at the high-frequency side of the ground-state bleach band that partly overlaps with the bleach and shifts its apparent peak wavenumber down. We therefore tentatively propose that a second photoproduct species is formed with a C=C stretch frequency near 1580 cm^{-1}. Interestingly, such species has been observed for the all-*trans* deprotonated Meta-II RSB species of rhodopsin[239]. However, more accurate experiments will be required to settle this issue.

No signal development was observed in the TSRS and TA spectra between subnanosecond and a few microseconds, implying no or only minor conformational changes occur on this time scale. The first reaction for the ground-state photoproduct proceeds in 58 μs, as observed in the TSRS (**Fig. 6.5c**) and TA spectra (**Fig. 6.5a**). The ~480-nm absorption appeared in 58 μs (cyan line, **Fig. 6.5a**) clearly indicating formation of the Rh-Bl state[65] (**Fig. 6.1**), *i.e.* RSB protonation occurs in 58 μs. In the previous flash photolysis experiments, the Rh-Bl state was reported to form in 2.3 ms[65], which is out of the temporal range of our TA spectroscopy. Therefore, we conclude that two protonation channels exist that proceed in 58 μs and 2.3 ms and results in completion of Rh-Bl state formation. Such protonation dynamics are much slower than that reported for the photoactive M state of bacteriorhodopsin[270] and proteorhodopsin[271], which proceed on the ns to 100s of ns timescales. Importantly, because the Rh-Bl state has heterogeneous retinal conformers (all-*trans* and 13-*cis*/15-*syn*), it is reasonable to consider that protonation of the two distinct retinal species occurs with distinct time constants, 58 μs and 2.3 ms. Since no significant transitions in the TSRS and TA spectra were observed until 58 μs after the first photoproduct formation, a possibility of thermal isomerization of unprotonated retinal can be excluded. Hence, we conclude that the two distinct deprotonated retinal conformers (all-*trans* and 13-*cis*/15-*syn*) in the ground state appear upon electronic relaxation from the S_1 states in 4.8 ps and 62 ps, with C=C stretch frequencies at 1580 and 1529 cm^{-1}, respectively.

Accordingly, two isomerization reactions from 13-*cis*/15-*anti* to all-*trans* and 13-*cis*/15-*syn* seemingly occur on the excited states or with decays of the excited states.

Double isomerization on distinct potential energy surfaces: rates and pathways

As discussed already, we observed heterogeneous retinal conformers in the S_1 state, and concluded that at least one isomerization occurs with the decay of S_2. Furthermore, an isomerization process involved in the S_2–S_1 evolution may be implied from the very fast S_2 decay in ~40 fs: in carotenoids the S_2–S_1 internal conversion occurs in ~200 fs, and in fact the shorter the C=C conjugated chain, the slower the internal conversion is expected to occur[264]. Therefore, it is expected that the intrinsic S_2–S_1 internal conversion rate is slower in unprotonated RSB, which has only six conjugated double bonds, than in carotenoids. In addition, very short S_2 lifetimes of ~50 fs in carotenoids were observed only when S_2 depopulates via additional depopulation channels such as energy transfer to chlorophyll[272,273]. Most likely, in the case of Rh-UV HKR1, the photoisomerization process constitutes an additional decay channel that accelerates the S_2 dissipation.

An open question here is which isomerization occurs with which electronic energy state transition, given that RSB in the parent Rh-UV state assumes a single 13-*cis*/15-*anti* conformation. In general, photoisomerization occurs via a conical intersection[274], and there are three possibilities:

(i) Isomerization to all-*trans* with S_2–S_1 transition; isomerization to 13-*cis*/15-*syn* with S_1–S_0 transition.

(ii) Isomerization to 13-*cis*/15-*syn* with S_2–S_1 transition; isomerization to all-*trans* with S_1–S_0 transition.

(iii) Double isomerization to all-*trans* and 13-*cis*/15-*syn* with S_2–S_1 transition.

It can be reasonably considered that 40 fs is too short for a system to proceed through two conical intersections. Therefore, we may assume only one conical intersection between the S_2 and S_1 states, resulting in one isomerization reaction. Accordingly, we consider option (iii) unlikely. In protonated RSB in microbial rhodopsins, the $1Bu^+$ state drives C13=C14 isomerization on femtosecond timescales[42,154,173,207,243,257]. Consequently, we suggest that the first photoisomerization in 50 fs involves in C13=C14 *cis*/*trans* isomerization similarly to protonated RSB.

As discussed in the previous section, both all-*trans* and 13-*cis*/15-*syn* isomers are likely formed on the electronic ground-state potential energy surface, indicating that *anti*/*syn* isomerization (C=N isomerization) must occur upon S_1–S_0 relaxation in 4.8 or 62 ps,

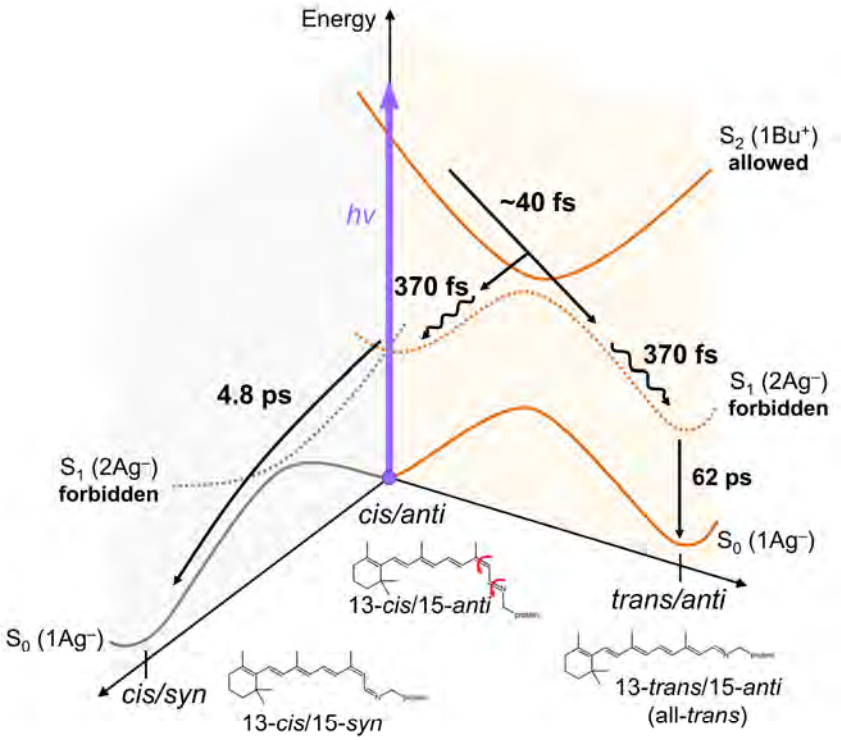

Figure 6.6. An excited-state reaction model of Rh-UV HKR1.

probably via another conical intersection. We now discuss which of the two time constants may correspond to 15 *anti-syn* isomerization. For linear polyenes like carotenoids, it is known that S_1–S_0 internal conversion rates through strong vibronic coupling (maintaining the same isomeric state) depend on the number of double bonds in their conjugated system, *i.e.*, the longer the conjugation, the larger the S_1–S_0 internal conversion rate[264].

In unprotonated RSB in organic solvent, lifetimes up to 200 ps were reported[275]. Such 200 ps lifetime is consistent with S_1–S_0 internal conversion for a polyene with 6 conjugated double bonds[264]. Internal conversion rates may differ by a factor of ~3 even when conformers have the same number of conjugated double bonds, depending on their conformations. Therefore, the observed S_1 lifetime of 62 ps may be assigned to internal conversion to the S_0 ground state while maintaining the isomeric state. However, the observed 4.8 ps lifetime is more than an order of magnitude shorter than the estimation for internal conversion, implying that the 4.8 ps decay must follow from other deactivation processes, possibly relaxation via a conical intersection which causes a change of its isomeric

state. Therefore, we suggest that the C15=N16 *anti/syn* isomerization proceeds in 4.8 ps, via a conical intersection between S_1 and S_0. In principle, one would expect positive signals, especially in the C=C region, from the ground-state unprotonated photoproduct upon decay of the S_1 4.8 ps fraction. However, because the remaining 62 ps S_1 component is much more preresonant with the 800 nm Raman pump than the unprotonated photoproduct, it will dominate the signals on this timescale and overwhelm any ground state photoproduct absorption. Therefore, the deprotonated ground-state photoproducts only become apparent after full decay of the S_1 states.

Overall, we consider model (i) most probable, even though the possibility of the other models is not fully excluded. A suggested reaction model based on our time-resolved experiments is shown in **Fig. 6.6**. The thus formed deprotonated RSB species subsequently each protonate with a distinct time constant of 58 μs or 2.3 ms to result in the two Rh-Bl RSB *all-trans/15-anti* and *13-cis/15-syn* conformers.

6.4. Conclusion

We investigated the unique photoreaction dynamics of HKR1 from the UV-absorbing state (Rh-UV, unprotonated 13-*cis*/15-*anti* retinal) to blue-absorbing state (Rh-Bl, mixture of protonated all-*trans* and 13-*cis*/15-*syn* retinal), utilizing transient absorption (TA) and transient stimulated Raman spectroscopy (TSRS). A typical TA signal for optically allowed S_2 ($1Bu^+$) state, which is widely seen in linear polyenes such as carotenoids, was seen right after photoexcitation and decayed in ~50 fs. Moreover, unusually upshifted Raman signals at ~1710 cm^{-1} appeared, which are assigned as the C=C stretching in the optically forbidden S_1 ($2Ag^-$) state. These observations indicate that unprotonated retinal is excited to optically allowed S_2 state, and relaxed to optically forbidden S_1 state in ~50 fs. Importantly, a heterogeneous spectral signature and decay of the S_1 state were observed, at 1696 cm^{-1} decaying in 4.8 ps and at 1716 cm^{-1} decaying in 62 ps, implying that two distinct unprotonated retinal conformers exists in the S_1 state. After the first photoproduct formation on the picosecond timescale, no spectral development was seen up to the tens of μs timescale. In 58 μs, a TA signal at 480 nm appeared that is assigned to Rh-Bl formation. Since another protonation stage was reported in 2.3 ms[65], we arrive at the conclusion that there are two protonation channels; in 58 μs and 2.3 ms, resulting in completion of Rh-Bl formation. The two protonation processes can be understood as protonation of all-*trans* and 13-*cis*/15-*syn*. Accordingly, it can be considered that two ground-state deprotonated retinal conformers are already formed after 4.8 and 62 ps. Comprehensively, we propose an excited-state reaction

model in which C13=C14 isomerization (13-*cis*/*trans* isomerization) proceeds in ~50 fs on S_2–S_1 relaxation, and the C15=N16 isomerization (15-*anti*/*syn* isomerization) occurs in 4.8 ps on S_1–S_0 relaxation. Possibly, similar excited-state dynamics are applied to other UV-absorbing rhodopsins, and our work will be a benchmark of them.

Methods

Sample preparation: The protein samples were expressed and purified as reported previously[65]. The samples were solubilized in 20 mM Tris buffer at pH 8.0 containing 150 mM NaCl and 0.03% β-D-maltoside (DDM), and concentrated to OD (/cm) ~10 and ~30 at 380 nm for transient absorption and trainset Raman experiments, respectively. The samples were filled in a homemade sample holder that has two 2-mm-thick CaF_2 plates, and the sample thickness was set as 400 μm with an appropriate sample spacer. The sample holder was set on a Lissajous scanner that ensures sample refreshment after each laser shot with a time interval of 60 seconds between successive exposures to the laser pulses[134,276].

Transient absorption spectroscopy: Transient absorption measurements were performed with a femtosecond-to-submillisecond pump-probe setup as reported previously[42,133]. A CaF_2 plate was used for supercontinuum white light generation, and a selected wavelength region; 370–730 nm was detected by a photodiode array. The time delay was varied up to 500 μs at 167 data points with the minimum temporal step of 50 fs. The diameters of the pump and the probe beams at the sample position were ~200 μm and ~70 μm, respectively. The wavelength of the pump beam was centered at 400 nm, and the power was attenuated to ~300 nJ. The instrumental response function was ~50 fs, estimated from global analysis. The sample was illuminated with a ~100 mW LED (λ_{max} ~ 470 nm) during the experiments.

Watermarked Transient stimulated Raman spectroscopy: Femtosecond to submillisecond time-resolved stimulated Raman experiments were performed with the watermarked, nearly baseline-free stimulated Raman setup reported previously[41,136]. The Raman pump (~800 nm, ~12 μJ) and Raman probe (~840–960 nm) were spatiotemporally overlapped at the sample position with the diameter of ~100 μm. Actinic pump (~400 nm, ~400 nJ) was focused on the protein sample to the diameter of ~150 μm with a time delay from -500 ps to 400 μs at 72 data points, generated by an optical delay and an electronic delay as reported previously[133]. The sample was illuminated with a ~100 mW LED (λ_{max} ~ 470 nm) during the experiments. Raman pumps pass through a specially-designed chopper blade for watermarking approach[136], which produces 14 Raman pump sequences whose wavelengths are slightly shifted each other[136]. As a result, 14 different stimulated Raman experiments are effectively performed simultaneously, which makes the baseline-free watermarking approach possible. The sample exposure time to the beams was ~1.5 hour in total for the time-resolved stimulated Raman experiment.

Chapter 7

Bright near-infrared fluorescent bacterial phytochromes: fluorescence mechanisms and excited-state dynamics

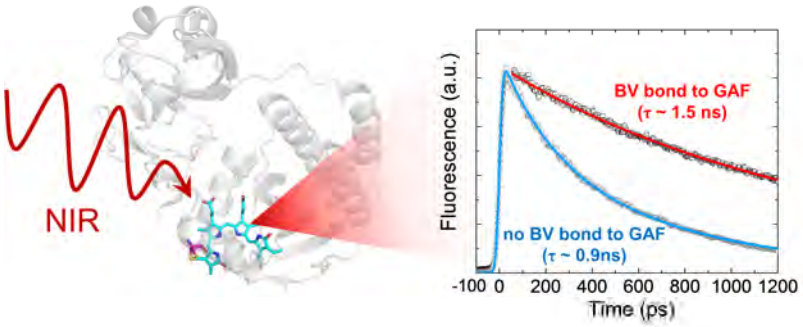

Excited-state properties of near-infrared fluorescent proteins were investigated. A chromophore binding to the GAF domain results in a spectral blue-shift and a longer fluorescence lifetime.

Abstract

Near-infrared fluorescent proteins (NIR FPs) engineered from bacterial phytochromes (BphPs) are of great interest for *in vivo* imaging of mammalian tissues. These NIR FPs utilize biliverdin (BV) as a chromophore, which is a heme degradation product and therefore they are readily genetically encodable. Here, we report on fluorescence properties of NIR FPs with key alterations in their BV binding sites. BphP1-FP, iRFP670 and iRFP682 have Cys residues in both PAS and GAF domains, rather than in the PAS domain alone as in wild-type BphPs. We found that NIR FPs with Cys in GAF domain or with Cys in both PAS and GAF domains show blue-shifted emission with long fluorescence lifetimes. In contrast, mutants with Cys in the PAS domain only or no Cys residues at all exhibit red-shifted emission with shorter lifetimes. Combining the time-resolved spectroscopic results with previous biochemical and BphP1-FP structural data, we conclude that the BV adducts bound to Cys in the GAF domain are the origin of bright blue-shifted fluorescence.

This chapter is based on the following publication:
Scientific Reports 6, 37362 (2016),
collaborated with D. M. Shcherbakova, M. Baloban and V. V. Verkhusha for protein purification.

7.1. Introduction

Near-infrared (NIR) fluorescent proteins (FPs) are of great interest for *in vivo* imaging of mammals. Because an optical transparency window of mammalian tissues exists in the NIR region, 650–900 nm, where water, hemoglobin and melanin absorptions are minimal[74,75], noninvasive deep-tissue imaging can be realized with NIR FPs. So far, many kinds of GFP-based FPs have been engineered and applied to real-time optical imaging in life sciences[277]. However, probably due to the limitation of the extent of the conjugated π-electron system, the absorption in engineered GFP-like proteins is limited at around 610 nm[76,77] and fluorescence emission at around 675 nm[78].

Phytochromes are red-light absorbing photoreceptors using bilin chromophores[278-280]. The first fluorescent phytochrome, derived from the cyanobacterial phytochrome Cph1 was reported by Fischer and Lagarias[281]. Subsequently, NIR FPs have been engineered from bacterial phytochromes (BphPs), derived from *Deinococcus radiodurans Dr*BphP[282,283] and *Rhodopseudomonas palustris Rp*BphP[74,80,81,83,84]. BphPs bind a biliverdin (BV) tetrapyrrole compound, which is a heme degradation product. Therefore BV is endogenously present in all mammalian tissues[282,284], which allows use of BphP-derived NIR FPs as easy as GFP-like proteins without adding chromophore exogenously. The photosensory core of phytochromes comprises three domains: PAS, GAF and PHY (**Fig. 7.1**). The PAS-GAF fragment, which has a molecular weight of 35 kDa in the monomeric form[81], is adequate for chromophore binding. BphPs have a Cys residue in the PAS domain that covalently binds to BV via the

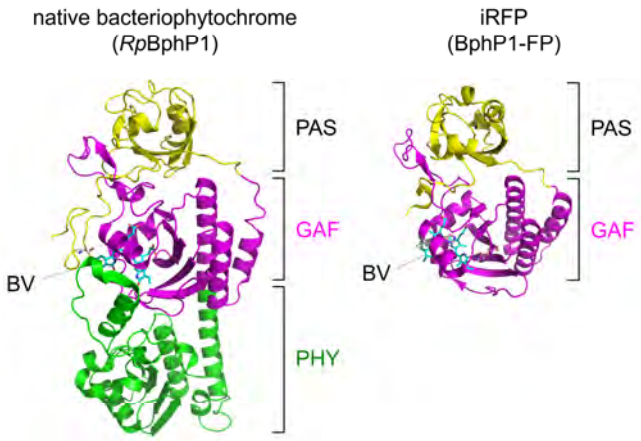

Figure 7.1. 3D structures of native bacteriophytochrome (*Rp*BphP1, PDB ID: 4GW9) and iRFP (BphP1-FP/C20S, PDB ID: 4XTQ). Native bacteriophytochromes are composed of PAS, GAF and PHY domains, and iRFPs are composed of PAS and GAF domains.

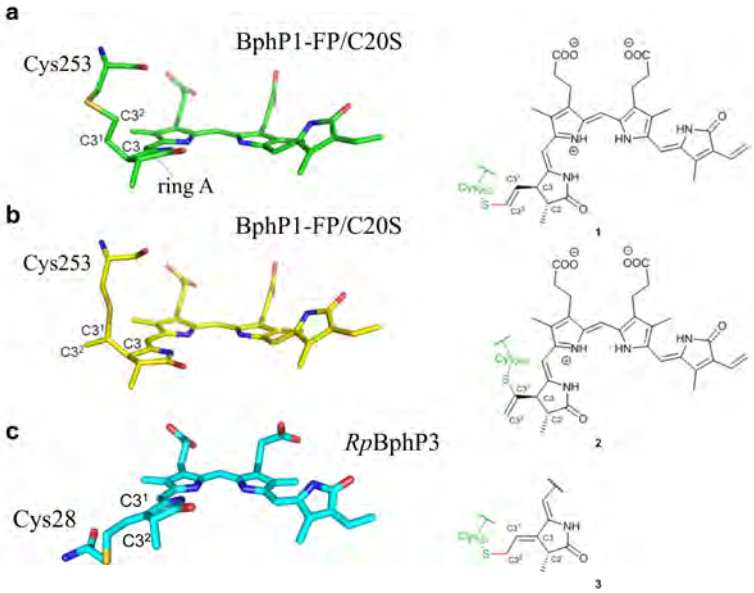

Figure 7.2. Structures of the BV adducts in engineered fluorescent bacterial phytochromes and in native bacterial phytochrome. (**a**,**b**) the engineered BphP1-FP/C20S (PDB ID: 4XTQ) and (**c**) native *Rp*BphP3 (Rhodopseudomonas palustris, PDB ID: 2OOL)

$C3^2$ atom in ring A[285,286] (**Fig. 7.2c**). In the dark, canonical BphPs adopt a 670–690 nm absorbing state known as the P_r state. Upon irradiation at these wavelengths, BphPs undergo photoisomerization in C15=C16[287,288], resulting in a photoproduct Lumi-R[88,289-296], which then thermally relaxes to a 740–760 nm absorbing state termed Pfr[297].

In recent years, several blue-shifted bright NIR FPs have been engineered from wild-type *Rp*BphP1, *Rp*BphP2, and *Rp*BphP6[84], such as BphP1-FP (the brightest FP among current BphP-derived NIR FPs)[81], iRFP682[80] and iRFP670[80], respectively. In these NIR FPs, the PHY domain was truncated (**Fig. 7.1**), and photoisomerization was blocked through mutation of key residues. Furthermore, a Cys residue was introduced in the GAF domain: Cys253 in BphP1-FP, Cys244 in iRFP670 and Cys249 in iRFP682, enabling BV to covalently bind to cysteine residues in the PAS and GAF domains[80,84]. These Cys residues in the GAF domain of BphP1-FP, iRFP670 and iRFP682 were introduced at the same position as the conserved Cys residues in plant and cyanobacterial phytochromes, which bind phycocyanobilin (PCB) or phytochromobilin (PΦB)[278]. The blue-shifted NIR FPs have been

successfully used in deep-tissue imaging and, moreover, allowed multicolor *in vivo* imaging[80,298,299].

More recently, a crystal structure of BphP1-FP/C20S variant has been determined[81]. BV binds to Cys253 in the GAF domain in two ways, either via the $C3^1$ atom or via the $C3^2$ atom in an approximate 1:1 stoichiometry (**Fig. 7.2).** The unique chromophore species that result from this binding appears to be responsible for the spectral blue shift and the high fluorescence quantum yield. Yet, real-time investigation of the picosecond dynamics on the excited states is essential to understand the molecular mechanisms of fluorescence more deeply.

Here we report the ultrafast photodynamics in BphP1-FP, iRFP670 and iRFP682 with femtosecond transient absorption and picosecond fluorescence spectroscopy. Furthermore, we analyze the ultrafast dynamics in their mutants that have a Cys residue in the GAF or PAS domains, or no Cys at all. We aim to gain insights into the molecular origin of the blue-shifted and bright BphP1-FP fluorescence, combining ultrafast spectroscopic results with previous biochemical and structural analyses. Elucidation of molecular mechanisms of fluorescence emission should give insight into rational design of further enhanced NIR-FPs with higher quantum yield and various absorption and emission wavelengths.

7.2. Results

Steady-state absorption and fluorescence spectroscopy

Fig. 7.3a,b show steady-state absorption and fluorescence spectra of BphP1-FP and its C20S, C253I, C20S/C253I mutants. The absorption of BphP1-FP and BphP1-FP/C20S peaks around 640 nm, while the other two mutants have maximum absorption around 670 nm. Fluorescence spectra of BphP1-FP and BphP1-FP/C20S have a maximum around 670 nm, while fluorescence of mutants BphP1-FP/C253I and BphP1-FP/C20S/C253I have a maximum around 700 nm. Compared to the wild-type *Rp*BphPs, which absorb at around 700 nm and fluoresce around 720 nm[89,286,300-302], both of the absorptions and fluorescence of BphP1-FP and BphP1-FP/C20S has been strongly blue-shifted by about 60 nm. For mutants BphP1-FP/C253I and BphP1-FP/C20S/C253I, only moderate blue-shifts of absorption and fluorescence by ~20–30 nm were observed. In BphP1-FP and BphP1-FP/C20S, broader absorption was observed on the red edge compared to BphP1-FP/C253I and BphP1-FP/C20S/C253I. Similar observations were made in iRFP670 and iRFP682 and their corresponding mutants[250]. These results are consistent with previous work[80,81,303].

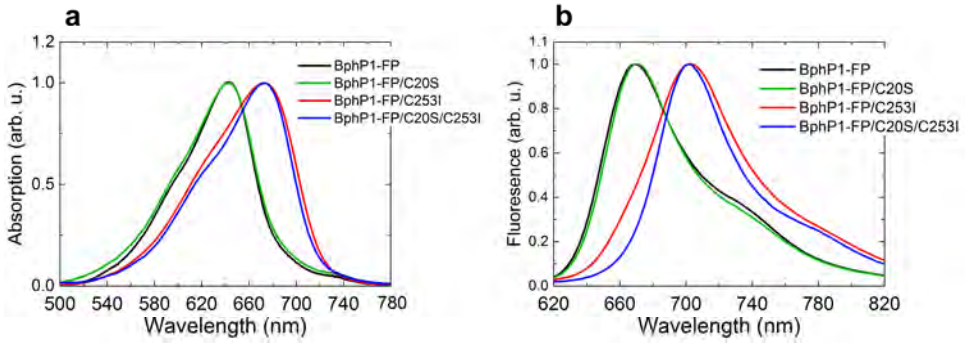

Figure 7.3. Steady-state absorption and fluorescence of BphP1-FP variants. (**a**) Absorption spectra and (**b**) fluorescence emission spectra of BphP1-FP and its C20S, C253I and C20S/C253I mutants are shown.

Time-resolved fluorescence spectroscopy

Picosecond time-resolved and spectrally resolved fluorescence spectroscopy was conducted to investigate the emission processes on BphP1-FPs, iRFP670 and iRFP682. Selected time-resolved emission spectra and decay associated spectra (DAS) on BphP1-FP are shown in **Fig. 7.4**. The excitation wavelength was 640 nm. Two exponential decay components were required for the fitting: τ_{f2} (1.56 ns) with a DAS peaking around 670 nm and τ_{f1} (0.35 ns) with its DAS peaking around 700 nm. The blue component τ_{f2} was dominant on the emission process, with amplitude of about 93% of the initially excited molecules.

Experiments on the BphP1-FP/C20S mutant gave very similar results to BphP1-FP, with a minor short-lifetime emission component τ_{f1} (0.34 ns) at around 700 nm, and a dominant long-lifetime component τ_{f2} (1.47 ns) at 670 nm (**Fig. 7.5a**). On the other hand, for the BphP1-FP/C253I and BphP1-FP/C20S/C253I mutants, no 670 nm emission was observed (**Fig. 7.5b,c**). In BphP1-FP/C253I, two emission components decaying with 0.26 ns (centered at 700 nm) and 0.88 ns (centered at 710 nm) were observed. Meanwhile, in BphP1-FP/C20S/C253I, two emission components centered at 700 nm decaying with 0.26 ns and 0.93 ns were observed.

Results for iRFP670 and iRFP682 are presented in **Fig. 7.6**, with global fitted time constants and DAS. Blue-shifted and long-lifetime components were observed only in iRFP670, iRFP670/C10A, iRFP682 and iRFP682/C15S. On the other hand, in the iRFP670/C244S, iRFP670/C10A/C244S, iRFP682/C15S and iRFP682/C15S/C249S mutants, only red-shifted and shorter-lifetime components were found, similar to the corresponding BphP1-FP mutants[250].

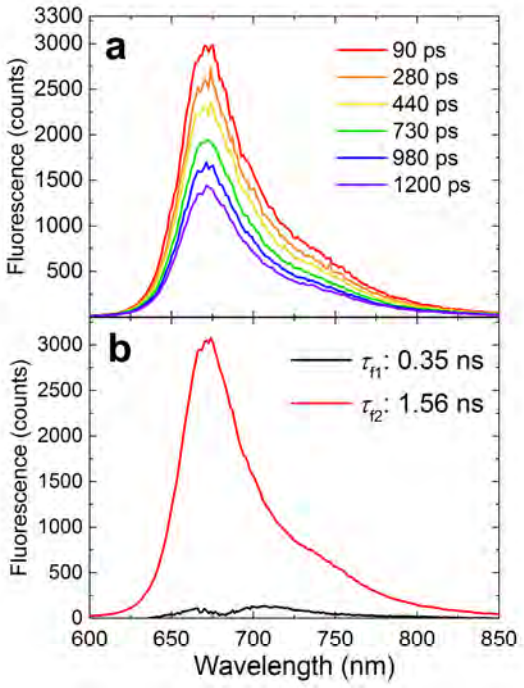

Figure 7.4. Picosecond time-resolved fluorescence spectra of BphP1-FP. (**a**) Selected time-resolved emission spectra and (**b**) decay-associated spectra (DAS) with 640 nm excitation.

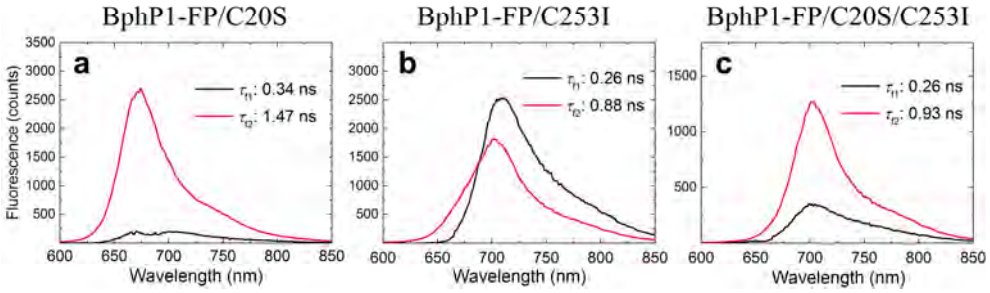

Figure 7.5. DAS of picosecond time-resolved fluorescence. (**a**) BphP1-FP/C20S with 640 nm excitation, (**b**) BphP1-FP/C253I with 640 nm excitation and (**c**) BphP1-FP/C20S/C253I with 640 nm excitation.

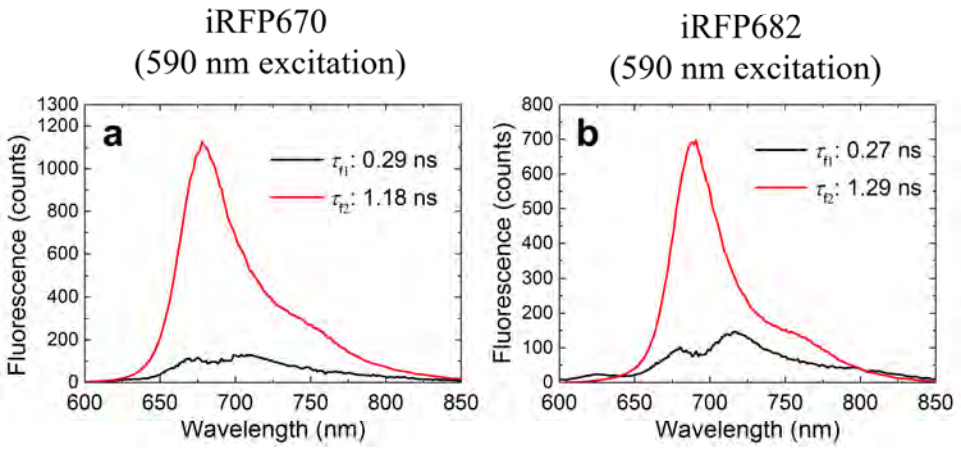

Figure 7.6. DAS of picosecond time-resolved fluorescence in (a) iRFP670 and (b) iRFP682 with 590 nm excitation.

The time-resolved emission spectra shown in **Figs. 7.4** and **7.5** demonstrate that BphP1-FP, which has Cys253 in the GAF domain and Cys20 in the PAS domain, has a dominant fluorescence component (>90% amplitude) with a blue-shifted emission at 670 nm and long fluorescence lifetime of 1.56 ns. The experiments on the cysteine mutants clearly demonstrate that this blue-shifted, long-lived emission arises from BV bound to Cys253 in the GAF domain: upon deletion of Cys20 in the PAS domain, the emission wavelength and lifetime remains essentially the same. Upon deletion of Cys253 in the GAF domain, only shorter-lived emission components around 700–710 nm are observed. For iRFP670 and iRFP682 and their cysteine mutants, similar results were obtained although their fluorescence lifetimes were somewhat shorter than in BphP1-FP.

The BphP1-FP/C20S/C253I mutant shows weak fluorescence at 700 nm (decay with 0.26 ns and 0.93 ns, **Fig. 7.5c**) even though it does not have a covalent bond with a cysteine according to the zinc staining[81]. This observation implies that BV has been incorporated non-covalently into the GAF domain pocket[285], and has a red-shifted fluorescence component at 700 nm. The two fluorescence species of BphP1-FP/C253I at 710 nm and 700 nm are assigned to a BV covalently bound to Cys20 and a BV that non-covalently incorporated into the protein, respectively. In the corresponding Cys mutants of iRFP670 and iRFP682, the same characteristics were observed[250].

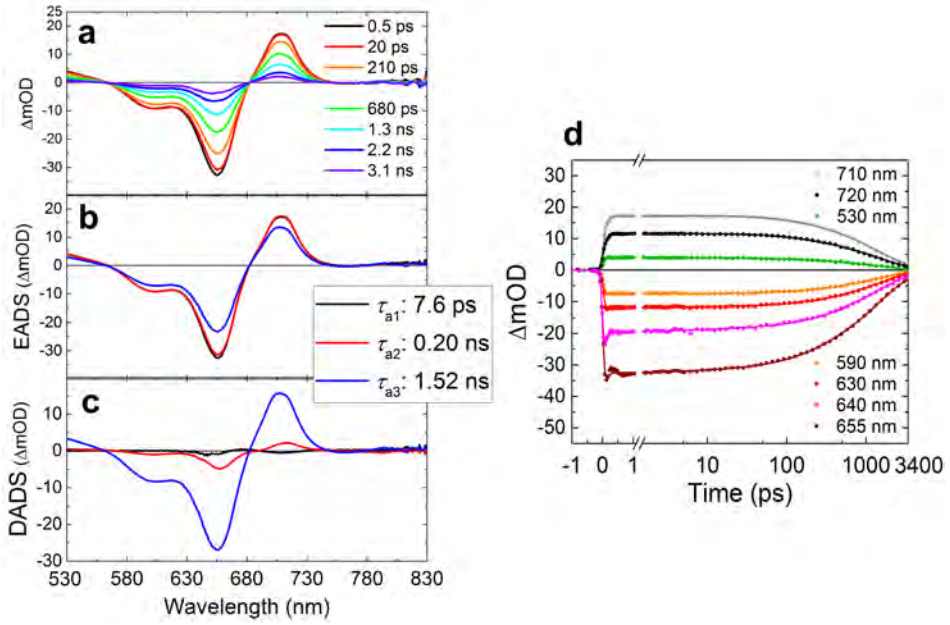

Figure 7.7. Femtosecond transient absorption spectra in BphP1-FP with 640 nm excitation. (**a**) Selected transient absorption spectra. (**b**) Evolution-associated difference spectra (EADS). (**c**) Decay-associated difference spectra (DADS). (**d**) Time traces of selected wavelengths.

Transient absorption spectroscopy

Femtosecond transient absorption spectroscopy was performed to characterize the primary photoreactions in BphP1-FP, iRFP670, iRFP682 and their mutants. **Fig. 7.7a** shows raw transient absorption spectra in BphP1-FP at selected delay times with excitation at 640 nm. These data were globally fitted with three components, with lifetimes of τ_{a1} (7.6 ps), τ_{a2} (0.20 ns) and τ_{a3} (1.52 ns), and the resulting EADS and DADS are shown in **Fig. 7.7b** and **7.7c**, respectively. For the BphP1-FP mutants, transient absorption spectra were fitted with three components as well[250]. The negative ΔA signal in **Fig. 7.7b** at 570–670 nm originates from ground state bleaching (GSB), and the positive ΔA signals around 530 nm and 700 nm indicate excited state absorption (ESA). As it can be seen from the EADS and DADS in **Fig. 7.7c**, the 1.52 ns component was clearly dominant and indicates loss of excited states, in agreement with the streak camera results. The 0.20 ns component denotes a minor excited-state decay component and corresponds to the minor 0.35 ns component from the streak camera experiments (**Fig. 7.4b**). In the early time range, transient absorption spectra only slightly changed with a time constant of 7.6 ps, which is interpreted as a relaxation process in the excited state[88].

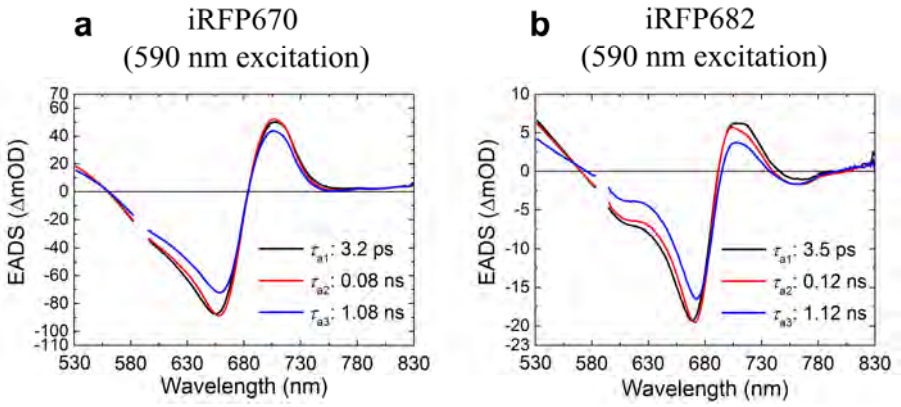

Figure 7.8. EADS of femtosecond transient absorption in (a) iRFP670 and (b) iRFP682 with 590 nm excitation. Spectra region at 585–595 nm are omitted because of the strong pump light scattering.

The global analysis indicates that no long-lived species are formed in the BphP1-FP (**Fig. 7.7b,c)** in contrast to wild-type *Rp*BphPs that form the photoproduct Lumi-R[88,89]. In agreement, time traces at selected wavelengths on transient absorption spectra of BphP1-FP are shown in **Fig. 7.7d**, clearly showing that the transient absorption signal almost completely decayed in 3 ns. These observations indicate that the BV C15=C16 photoisomerization that in native BphPs results in Lumi-R formation has been successfully impeded.

Similarly to BphP1-FP, three time constants were required to adequately describe the transient absorption data of iRFP670 and iRFP682, with 3.2 ps, 0.08 ns and 1.08 ns in iRFP670, and with 3.5 ps, 0.12 ns and 1.12 ns in iRFP682 (**Fig. 7.8**). Furthermore, three components were required to fit iRFP670/C10A, iRFP670/C10A/C244S, iRFP682/C15S, iRFP682/C249S as were the mutants of BphP1-FP[250].

The shape of the transient absorption spectra reported here merits some discussion. A pronounced excited-state absorption (ESA) band near 700 nm that is red-shifted with respect to the ground state absorption is observed in BphP1-FP (**Fig. 7.7**) and iRFP670 (**Fig. 7.8a**) and their cysteine mutants, and iRFP682 (**Fig. 7.8b**), while in the cysteine mutants of iRFP682 no or very little of such absorption is observed. The time evolution of the DA signal at 700 nm is indistinguishable from the ESA at 530 nm, which solidifies the assignment of this signal to ESA. Almost all biliproteins show such a structured ESA at varying intensities, in phytochromes[88,89,290,294,304] as well as biliprotein light harvesting

antennae[305]. Such ESA may either be red-shifted, blue-shifted, or overlap with respect to the ground state absorption. In previous work it was demonstrated for *Rp*BphP2 and *Rp*BphP3 that the spectral position of this ESA is highly sensitive to the protein matrix, involving interactions between BV ring D with charged and hydrogen-bonding amino acid side chains[88]. In the case of the iRFP682 cysteine mutants, the ESA either has a low amplitude or absorbs near the P_r absorption maximum, and is therefore entirely compensated by the ground state bleach and stimulated emission. Note that in plant phytochrome, such apparent absence of ESA was also observed[289].

One has to realize that because of the aforementioned variability of excited-state absorption in the transient absorption spectra, which compensates the ground state bleach and stimulated emission in an unpredictable manner, one cannot reliably associate the minima, maxima and zero crossings in the transient absorption spectra of **Figs. 7.7** and **7.8** with the distinct spectral forms as observed in time-resolved fluorescence. For this reason, we make such assignments exclusively on the basis of the time-resolved fluorescence streak camera results. Given that the short-lived minor decay components in the transient absorption data have similar time constants as those derived from the streak camera, we conclude that they probably arise from the red-shifted population.

Furthermore, one may consider the possibility that the strong absorption near 700 nm could be due to a primary ground-state photoproduct, given that 15Ea product Lumi-R is expected to absorb near such wavelengths. We will show here that this is not the case. First, we note that the transient absorption and the streak camera experiments agree on the measured lifetimes, so we can assign the time constants in the transient absorption clearly to excited-state decay, and not ground-state product decay. Thus, if a transient product would be formed it would need to coexist with the singlet excited state during the fluorescence lifetime. With these conditions, the idea that the positive band arises from a primary photoproduct is highly unlikely, given that the 700 nm absorption rises within the instrument response of 100 fs. If it were a primary photoproduct, it would have to be formed in less than ~50 fs, which is highly unlikely: it is well-established that in wild type phytochromes, the isomerized Lumi-R product rises on a timescale of tens to hundreds of picoseconds from the P_r state[88,89,289-291,295]. Even if this were to happen, this putative product would then fortuitously need to have a lifetime that is exactly the same as the singlet excited state lifetime. We note that the biliprotein light harvesting antenna PC645 from cryptophyte algae shows a similar transient absorption signal red-shifted with respect to the ground state[305], very similar to that of BphP1-FP. These type of light harvesting antennae have

evolved for optimal light harvesting and show no transient photoproducts of their bilin chromophores whatsoever. Thus, we may safely conclude that the 700 nm transient absorption band corresponds to excited-state absorption, and not to a ground-state photoproduct.

Kinetic isotope effects on the fluorescent lifetime

To investigate the fluorescence deactivation mechanisms in the presently studied NIR FPs, time-resolved fluorescence experiments in H_2O and D_2O solutions were conducted. **Fig. 7.9** shows DAS and time traces on BphP1-FP in H_2O and D_2O with 640 nm excitation. The DAS in H_2O and D_2O are almost identical, but the time constants are significantly different: 0.35 ns and 1.56 ns in H_2O, and 0.48 ns and 2.89 ns in D_2O. The H/D kinetic isotope effects (KIEs), defined as the fluorescence lifetime in D_2O divided by the lifetime in H_2O, on τ_{a1} and τ_{a2} on BphP1-FP were 1.4 and 1.9, respectively. For the BphP1-FP/C20S, C253I and C20S/C253I mutants, significant KIEs were observed as well (**Table 7.1**). Moreover, significant H/D KIEs were observed in iRFP670, iRFP682 and their mutants (**Table 7.1**). In the time region shorter than ~0.8 ns, a longer lifetime carries a larger KIE as in other iRFPs[304] and wild-type BphPs[88,89]. On the other hand, a KIE of ~1.8 was observed for all lifetimes longer than ~0.8 ns (**Fig. 7.10**). The values of the large KIEs correspond to those of other red-shifted NIR FPs: iRFP702, iRFP713 and iRFP720[304]. The transient absorption data showed similar KIEs (**Table 7.1**). Significant KIEs were detected in fluorescence decays

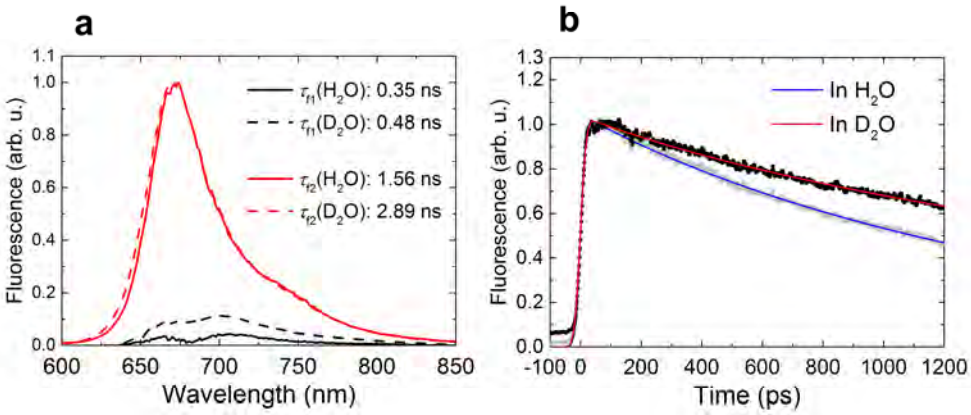

Figure 7.9. Time-resolved fluorescence spectra of BphP1-FP in H_2O and D_2O upon 640 nm excitation. (**a**) DAS in H_2O (solid lines) and D_2O (dashed lines). (**b**) Time traces of time-resolved emission at 670 nm in H_2O and D_2O with global fitted curves

Table 7.1. Time constants of transient absorption and fluorescent spectra of BphP1-FP and its cysteine mutants. Populations and H/D kinetic isotope effect (KIE) of each decay are shown in the brackets.

	Time-resolved fluorescence			Time-resolved absorption		
	Excitation wavelength	τ_{f1}	τ_{f2}	Excitation wavelength	τ_{a2}	τ_{a3}
BphP1-FP	640 nm	0.35 ns (5%) **(KIE: 1.4)**	1.56 ns (95%) **(1.9)**	640 nm	0.20 ns (amp. of GSB: -4.7) **(KIE: 1.2)**	1.52 ns (-27.0) **(1.5)**
BphP1-FP/ C20S	640 nm	0.34 ns (10%) **(1.3)**	1.47 ns (90%) **(1.9)**	640 nm	0.16 ns (-2.7) **(1.9)**	1.33 ns (-15.5) **(1.7)**
BphP1-FP/ C253I	640 nm	0.26 ns (59%) **(1.5)**	0.88 ns (41%) **(1.7)**	640 nm	0.23 ns (-6.0) **(1.7)**	0.90 ns (-2.3) **(1.7)**
BphP1-FP/ C20S/C253I	640 nm	0.26 ns (29%) **(1.4)**	0.93 ns (71%) **(1.9)**	640 nm	0.20 ns (-3.1) **(1.5)**	0.88 ns (-4.8) **(1.6)**

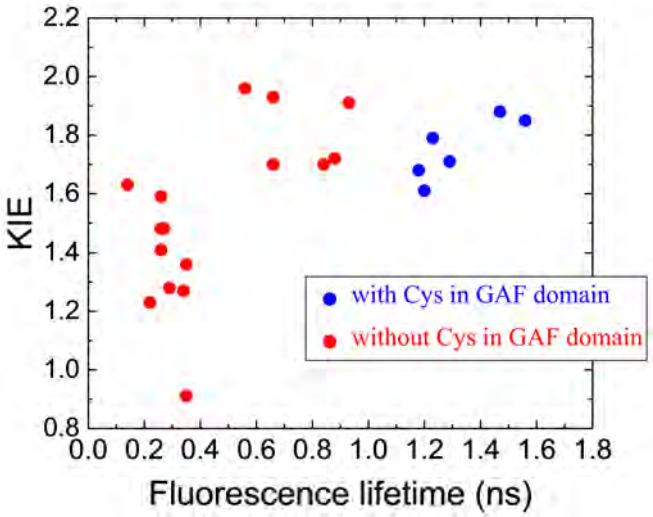

Figure 7.10. H/D kinetic isotope effects (KIEs) of BphP1-FP, iRFP670, iRFP682 and their Cys mutants. Blue dots show KIEs of NIR FPs that have Cys in the GAF domain, and red dots show KIEs of NIR FPs without Cys in the GAF domain.

(**Fig. 7.9**) consistent with those of other iRFPs[304], wild-type BphPs and their point mutants[88,89], indicating that excited state proton transfer (ESPT) may constitute a significant non-radiative decay process, as discussed before[88,89,304,306]. Furthermore, KIEs in blue-shifted BphP1-FP (KIE: 1.9), iRFP670 (1.7) and iRFP682 (1.7) are as large as red-shifted iRFP702 (1.8), iRFP713 (1.8) and iRFP720 (1.9) while lifetimes of the blue-shifted NIR FPs are approximately twice larger[304], which could imply that that the deactivation mechanism of the blue-shifted NIR FPs is similar to that of the red-shifted NIR FPs.

7.3. Discussion

Molecular basis for blue-shifted long-lived fluorescence in engineered bacterial phytochromes

Our results have shown that the fluorescence of BphP1-FP is blue-shifted, bright and long-lived as compared to that of other native and engineered BphPs, which confers important advantages on this type of fluorescent proteins for *in vivo* multicolor imaging. We now discuss the molecular basis of these key properties. In previous work on BphP1-FP/C20S, its high-resolution X-ray structure was reported[81]. In that work, two distinct models of BV binding to Cys253 in the GAF domain were proposed, *i.e.* via the BV $C3^2$ atom (**1, Fig. 7.2a**) and via the BV $C3^1$ atom (**2, Fig. 7.2b**) in a ~1:1 stoichiometric ratio[81]. In contrast, the native BV adduct of the similar RpBphP3 protein (**3**, **Fig. 7.2c**) binds BV to Cys28 in the PAS domain. In both BV adducts of BphP1-FP/C20S, the C3 atom is sp^3 hybridized resulting in an upward orientation of its substituent toward Cys253, and hence does not form the double bond with $C3^1$ or C2 that is present in native bacterial phytochromes[286,300,302]. This molecular structure implies that the π-conjugated system of both BV adducts becomes shorter by one double bond as compared to BV bound to native bacterial phytochrome (cf. **1** and **2** vs. **3**, **Fig. 7.2**) and consequently, their absorption is 30–40 nm blue-shifted. In fact, the proposed conjugated π-electron system is identical to that of PCB or PΦB bound to plant or cyanobacterial phytochromes[307,308], and accordingly their absorption and emission maxima are nearly identical[281,289]. Recent work on the terminal phycobilisome emitter L_{CM} demonstrated a ZZZssa conformation for its PCB chromophore, like that in phytochrome, with its absorption and emission wavelength maxima very similar to that of BphP1-FP, plant and cyanobacterial phytochrome[309]. This indicates that the conjugated π-electron system of the chromophore constitutes the main determinant of absorption (~640–650 nm) and emission maxima (~670 nm), with a minor contribution from the specific protein environment.

In principle, there should be two distinct blue-shifted emissions from BV binding to Cys253 via $C3^1$ and $C3^2$, whereas only one component is observed. Apparently, the two fluorescent species have emission spectra and lifetime too close to each other to be resolved in the time resolved measurements. This is likely the case because (i) the emission wavelength is mainly determined by the π-electron conjugation, which identical in both cases and to a lesser extent by pigment-protein interactions, which are highly similar for both cases, and (ii) the lifetime is mainly determined by pigment-protein interactions in the binding pocket to rings B, C and D, which is highly similar in both cases. We further note that in BphP1-FP and its C20S mutant, the steady-state absorption spectra (**Fig. 7.3**), transient fluorescence spectra (**Figs. 7.4b** and **7.5a**) and transient absorption spectra (**Fig. 7.7b**) are almost identical. These spectra reflect structures of BV adducts in the protein, suggesting that BV in BphP1-FP forms almost the same adducts as in BphP1-FP/C20S. In other words, BphP1-FP has BV that forms a covalent bond with Cys253 in GAF in two ways via $C3^1$ and via $C3^2$, but hardly binds Cys20 in the PAS domain. Possibly, the minor red-shifted species of BphP1-FP and its C20S mutant with weak 700-nm fluorescence originated from non-covalent BV-protein complex, like in the C20S/C253I mutant. Similar conclusions apply to iRFP670 and iRFP682 (**Fig. 7.8**).

Taken together, the static and time-resolved spectroscopic data on BphP1-FP and its mutants and the 3D X-ray structural data indicate that the blue-shifted species of BphP1-FP are derived from the BV adducts covalently bound to Cys253 in the GAF domain via $C3^1$ and via $C3^2$.

Fluorescence lifetime, quantum yield and protein design opportunities

The BphP1-FP fluorescence lifetime of 1.56 ns is by far the longest reported on BV-binding bacterial phytochromes[88,89,304,310], and, in fact, is almost identical to that of allophycocyanin (APC)[311,312], a cyanobacterial photosynthetic light harvesting complex that binds PCB in a ZZZasa configuration[313]. This notion is interesting because APC has been optimized through natural evolution for optimal resonant energy transfer, and the same molecular parameters need to be optimized for resonant energy transfer and fluorescence. The phycobilisome terminal emitter L_{CM}, which transfers energy to the chlorophylls in the photosynthetic membrane, binds PCB in a ZZZssa configuration as in phytochromes[309] and has a fluorescence lifetime of 1.2 ns[314]. The BphP1-FP fluorescence lifetime is almost as long as that of the intensely fluorescent Y176F mutant of cyanobacterial phytochrome Cph1 (1.8 ns)[281,315], which binds PCB.

The blue-shifted fluorescence components of BphP1-FP, iRFP670 and iRFP682 have a higher quantum yield than red-shifted NIR FPs[80,282]. BphP1-FP has the highest quantum yield (~13%)[81] and corresponding long fluorescence lifetime (1.56 ns) among the blue-shifted NIR FPs, which is twice higher than *e.g.* iRFP713 (~6.3%)[80]. The blue-shifted NIR FPs have a Cys residue in GAF domain, while the red-shifted NIR FPs have a Cys only in PAS domain, which clearly indicates that covalent binding of BV to the Cys in GAF (via $C3^1$ and $C3^2$) is a key condition to achieve the high fluorescence quantum yield. Theoretical studies have indicated that ring A and ring D rotation followed by internal conversion constitute major causes of excited-state deactivation in bilin chromophores[316], that will form an effective channel to deactivate fluorescence in NIR FPs and wild-type BphPs. Considering the above, two plausible factors may contribute to the higher fluorescence quantum yield of the proteins studied here: (i) the BV $C3^1/C3^2$–Cys adduct in GAF domain is sterically more constrained and leaves less mobility for ring A and by extension, the A-B methine bridge than in BphPs with the BV–Cys adduct in PAS domain; (ii) differently from the red-shifted NIR FPs and wild-type BphPs, the π-electron conjugated system does not extend on the ring A in BphP1-FP (**Fig. 7.2**). Consequently, any ring A rotation will affect the π-electron conjugated system to a lesser extent than in traditional BphPs.

So far, most efforts to optimize the fluorescence quantum yield of BphP-based NIR FPs have been focused on restricting the motion of the BV D ring[80,83,317]; here, we find that restricting ring A motion and/or locking out ring A from the conjugated system increases the fluorescence quantum yield. This result suggests that in general, restricting ring A mobility in red-shifted fluorescent BphP derivatives may prove beneficial for achieving higher brightness. This proposal seems to contradict an earlier study on BphPs with locked BV chromophores[318], where restricting the motion of ring A did not have a significant effect on the fluorescence quantum yield. However, in those studies, the quantum yields were comparably low (<0.01), which implies that other pathways including ring D motion contributed to the fluorescence decay. It suggests that for a BphP with a low fluorescence quantum yield, ring D motion and/or ESPT[88,89,304] is limiting the fluorescence, and as ring D is locked down by genetic engineering with a resulting higher fluorescence quantum yield, ring A motion becomes limiting for the fluorescence.

7.4. Conclusion

We have systematically characterized the excited state dynamics and fluorescence deactivation mechanisms in the *Rp*BphP-derived NIR FPs: BphP1-FP, iRFP670, iRFP682, and their Cys mutants in the PAS and GAF domains. Significantly prolonged lifetimes and enhancement of fluorescence were identified in the blue-shifted NIR FPs, while isomerization processes were found to be completely blocked. In the time-resolved fluorescence spectra, a distinct blue-shifted emission with a long lifetime was identified. Combining the results from ultrafast spectroscopy with the crystal structure of BphP1-FP/C20S variant, mutational analysis of relevant cysteine residues we assign the bright blue-shifted fluorescent species to BV adducts covalently bound to the Cys residue in the GAF domain. Our studies also suggest the explanation for the origin of high fluorescence quantum yield and blue-shifted spectra in protein with these BV adducts. Our findings provide significant insights for rational design of brighter and multicolor NIR FPs from a variety of wild-type BphPs.

Methods

Protein expression and purification: The BphP1-FP, iRFP670 and iRFP682 genes were cloned into the pBAD/His-B vector (Invitrogen). Site-specific mutagenesis was performed using QuikChange kit (Stratagene). The proteins with polyhistidine tags on the N-termini were expressed in LMG194 bacterial cells (Invitrogen) bearing the pWA23h plasmid encoding heme oxygenase under the rhamnose promoter[80]. To initiate protein expression, bacterial cells were grown in RM medium supplemented with ampicillin, kanamycin and 0.02% rhamnose for 5 h at 37°C. Then 0.002% arabinose was added and bacterial culture was incubated for additional 12 h at 37°C followed by 24 h at 18°C. Proteins were purified using Ni-NTA agarose (Qiagen). Ni-NTA elution buffer contained no imidazole and 100 mM EDTA. The elution buffer was substituted with PBS buffer using PD-10 desalting columns (GE Healthcare). For spectroscopic experiments, the samples were diluted in PBS buffer composed of 137 mM NaCl, 2.7 mM KCl, 10 mM Na_2HPO_4 and 2 mM KH_2PO_4 at pH 7.4.

Steady state absorption and fluorescence spectroscopy: Steady-state absorption spectra were recorded using a UV/Vis spectrometer (Cary 4000, Agilent) at room temperature (~20°C). The samples were diluted with PBS buffer (pH 7.4) and measured in a 1 mm pathlength quartz cuvette (100-QS, Hellma Analytics). Steady-state fluorescence spectra were measured with a Vis/Near-IR spectrometer (FluoroMax, Horiba) at the room temperature (~20°C). The samples were diluted to an absorbance of 0.1 per cm to prevent reabsorption and measured in a 10 mm pathlength PMMA cuvette (759150, Brand). The excitation wavelength was 600 nm for the fluorescence measurements.

Femtosecond transient absorption spectroscopy: Femtosecond transient absorption measurements were performed with a femtosecond pump-probe setup described previously[124,133] at room temperature (~20°C). The excitation wavelengths were selected as 590 nm, 630 nm, 640 nm or 660 nm depending on the sample. Narrow band interference filters (Δλ ~10 nm) for the excitation wavelengths were inserted on the pump path. On the probe path, the beam was attenuated and focused on a 2 mm sapphire plate to generate white light for probing. A spectral range of 530-830 nm of the white light probe pulse was detected by a 256-segment photodiode array[97]. The polarization of pump and probe was set at the magic angle (54.7°). The samples in 1-mm cuvettes (100-QS, Hellma Analytics) with an absorbance of 1.5 per cm at the absorption maximum were set on a home-built vibrating sample holder in order to avoid damage to the samples.

Picosecond time-resolved fluorescence spectroscopy: Time-resolved fluorescence measurements were carried out with a streak camera setup, as described previously[138] at room temperature (~20°C). The excitation pulse was focused on a 3 mm pathlength quartz cuvette (102.251-QS, Hellma Analytics). The samples had an absorbance of 0.25 per cm at their absorbance maximum. The samples were excited at 590 nm, 630 nm, 640 nm or 660 nm. A narrowband interference filter (Δλ~10 nm) for respective excitation wavelength was located on the pump path. The applied excitation pulse energy was ~4 nJ, and the polarization between the excitation beam and emission was set at the magic angle (54.7°).

Chapter 8

Excited-state structure and dynamics of a BLUF photoreceptor

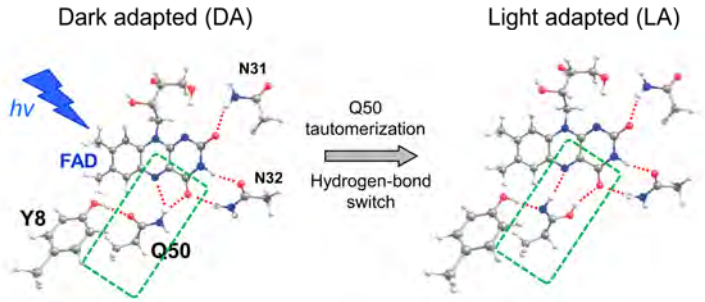

Photoinduced H-bond switch of FAD in the BLUF photoreceptor was proposed by FSRS and quantum-chemical calculations.

Abstract

Blue-light using flavin (BLUF) photoreceptors that are incorporated with flavin adenine dinucleotide (FAD) chromophore are a key protein family in optogenetics applications. The chemical environment and its photodynamics of FAD and its adjacent amino acid residues are essential for deeper understanding of the activation mechanisms, but still controversial. Femtosecond stimulated Raman spectroscopy, which is a powerful technique to study excited-state molecular structures, is applied to Slr1694 BLUF photoreceptor. The excited state of the dark-adapted (DA) state molecules were relaxed with three time constants; 340 fs, 14 ps and 130 ps, whereas almost no spectral peak shifts were observed, indicating that the excited-state structure is homogeneous and decays with the three time constants. Vibrational modes of the excited-state Raman spectra of DA and light-adapted (LA) states were further assigned by computational simulation for the S_1 state based on the CIS-D3/6-31(d,p) method. From the consistency of the experimental and calculated Raman spectra, it is proposed that the amino group of Q50 is oriented toward the C4=O group of the FAD in the DA state, while tautomerized Q50 is more likely adapted for the LA state.

This chapter is in preparation for publication:
collaborated with T. Domratcheva for quantum-chemical calculations, and J. Mehlhorn and P. Hegemann for sample purification.

8.1. Introduction

Blue-light using flavin (BLUF) photoreceptors are blue-light sensing proteins having a flavin chromophore. BLUF photoreceptors are involved in various functions *e.g.* photosynthetic gene regulation[91,92], phototaxis[93] and enzymes[94,95], and also are of great interest in optogenetics[95,96]. BLUF photoreceptors are incorporated with a flavin adenine dinucleotide (FAD) chromophore, which absorbs near-UV and blue light. Photoactivation leads to a red-shifted FAD absorption by 10–15 nm[97,100], indicating that the FAD remains oxidized, and a hydrogen bond rearrangement around the FAD likely constitutes the photoactivation mechanism[99,104,319]. Since the FAD plays crucial roles on the activation/deactivation of the protein, understanding the static state chemical and the reaction dynamics of FAD is essential to understand the photoreaction of BLUF domains, which will also lead rational design of functional optogenetic proteins.

In a representative BLUF photoreceptor, Slr1694 BLUF domain from *Synechocystis sp.* PCC 6803 (also known as SyPixD), Y8 and Q50 are involved in the hydrogen bond network near the FAD in the dark-adapted (DA) state (**Fig. 8.1**)[19]. Upon blue-light illumination to the DA state, the singlet excited (FAD_{DA}*) state is populated, and sequential electron and proton transfer occurs from Y8 to the FAD. First, $FAD^{\bullet-}$ is formed in 7, 40 and 180 ps[19,101] (**Fig. 8.S1**) upon Try–FAD electron transfer[101,118]. Subsequently, proton transfer proceeds in 6 ps (formation of $FADH^{\bullet}$), and reoxidation of FAD and a hydrogen bond rearrangement are completed in 65 ps[19,101]. Due to the presence of long-lived FAD* states and the short-lived nature of the transient FAD radicals, global and target analysis techniques had to be used to extract the radical spectral signatures[101,102,118]. As a result of the hydrogen-bond switch reaction, conformational changes occur in the BLUF fold on longer timescales[45] that may involve a slide of the β5 strand[320], as recently demonstrated for SyPixD[98]. This photoactivated, or light-adapted (LA) state thermally recovers to the DA state in ~6 s[97]. When blue-light is irradiated to the LA state, the excited (FAD_{LA}*) state is formed, which induces concerted electron and proton transfer from Y8 to FAD in 1 ps, resulting in formation of $FADH^{\bullet}$. The molecules return to the initial LA state in 66 ps[19,100] (**Fig. 8.S1**).

The hydrogen-bond patterns that connect the FAD to its neighbouring residues and their relation to the photodynamics in BLUF photoreceptors are still controversial, despite many studies with X-ray crystallography[103-106], NMR[107-110], FT-IR[111-113], computational calculations[111,114-116] and time-resolved spectroscopies[97,100,101,117-119]. Several static hydrogen-bonding models have been put forward[321,322], among which Model 1 and 2

(**Fig. 8.1d**) for DA and LA[101,104], or Model 2 and 3 for DA and LA[111], respectively, where the latter corresponds to the imidic tautomerized form of Q50. To deeper understand the static and dynamic structures of the FAD and its adjacent protein side chains, further studies are required. Femtosecond stimulated Raman spectroscopy (FSRS) is a strong method to investigate the reaction dynamics of biological chromophores[135]. We recently developed watermarked FSRS to eliminate the notorious baseline problems that have afflicted FSRS since its inception more than a decade ago[41,136]. Since vibrational spectra from molecules resonant with the Raman pump are selectively measured in FSRS, specific vibrational spectra from FAD can be obtained. The vibrational modes obtained by FSRS can be directly compared with excited-state quantum chemical calculations, giving significant insights into structures of the FAD and its adjacent residues in the static and excited states. Combining watermarked FSRS with quantum mechanical calculation by the CIS-D3/6-31(d,p) method, we investigate the excited-state structures of FAD and its dynamics on the Slr1694 BLUF domain.

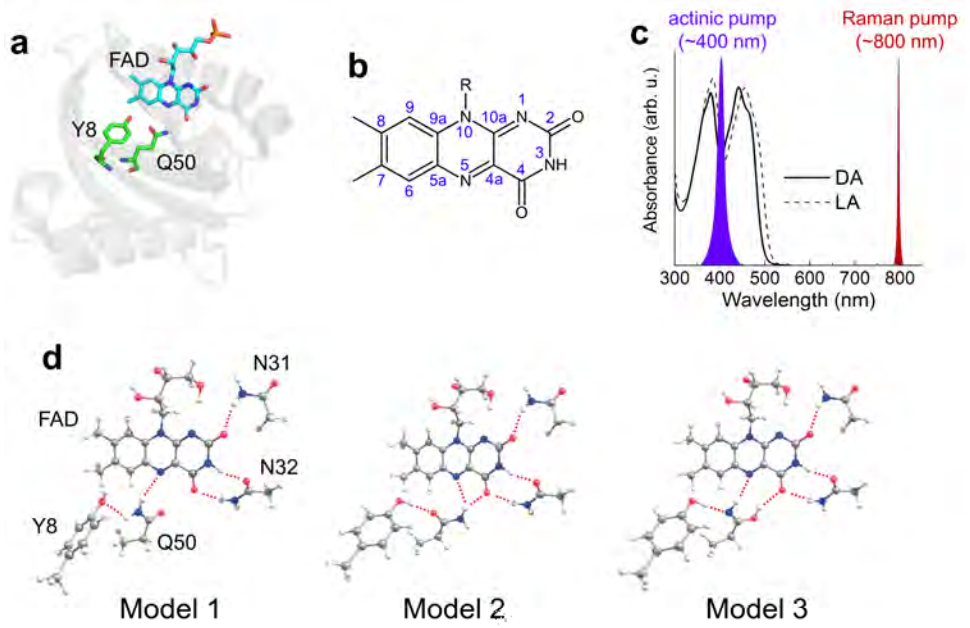

Figure 8.1. FAD structures and the dark-state absorption spectrum of Slr1694. (**a**) X-ray structure of Slr1694 (PDB: 2HFN)[105]. (**b**) A chemical structure of FAD. (**c**) Absorption spectrum of the dark-adapted (DA) state. 400-nm actinic pump and 800-nm Raman pump were selected for the transient Raman experiments. (**d**) Proposed structural models near the FAD. The red dashed lines show hydrogen bonds.

8.2. Results and Discussion

Fig. 8.2a shows selected transient stimulated Raman spectra of WT Slr1694 BLUF domain in H_2O buffer of the reaction from the DA state, obtained with a 400-nm actinic pump and an 800-nm Raman pump (see Supporting information for the experimental procedures). The transient Raman spectra in H_2O and D_2O were globally fitted (see Supporting information for procedures of global fitting) with three time components: 340 fs, 14 ps and 130 ps in H_2O, and 390 fs, 12 ps and 150 ps in D_2O (**Fig. 8.2b**). **Fig. 8.2c** shows kinetic traces at selected wavenumbers. Immediately after photoexcitation (**Fig. 8.2b**, black line), strong peaks appeared at 1204, 1258, 1284, 1386, 1415, 1505 and 1576 cm^{-1} in H_2O, similarly to FSRS of FAD in solution[323] and the AppA BLUF domain[324]. These positive peaks decayed with the three time constants, without any significant spectral shifting. The absence of peak shifts indicates that the tri-exponential decays all originate from the same molecular state, *i.e.* the lowest FAD singlet excited state of DA BLUF, denoted FAD_{DA}*. In transient absorption (TA) and time-resolved fluorescence spectroscopy of WT Slr1694 BLUF domain, decays of the FAD_{DA}* were observed with three time constants fitted by target analysis: 7 ps, 40 ps and 180 ps[101,118]. With the exception of the 310 fs component, the lifetimes of FAD_{DA}* observed with FSRS are comparable with the TA results. Strikingly, in

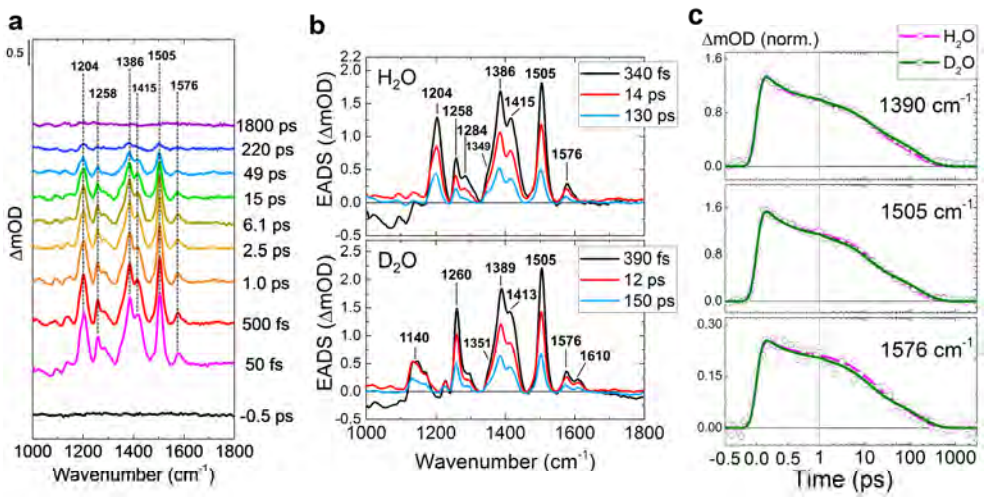

Figure 8.2. Transient Raman spectra of dark-adapted WT Slr1694. (**a**) Selected transient Raman spectra. (**b**) Global-fitted evolution-associated difference spectra (EADS) in H_2O (top) and D_2O (bottom). (**c**) Selected time traces with fitting curves. Green and magenta open dots show the raw data in H_2O and D_2O, respectively, and the green and magenta lines show the fitting curves in H_2O and D_2O.

contrast to the earlier TA results[97,101,102], no signature of the radical intermediates was observed in the FSRS data. Notably, FAD_{DA}* has a strong excited-state absorption at wavelengths >700 nm, whereas only weak or almost no absorption was observed in that region for the $FAD^{\bullet-}$ and $FADH^{\bullet}$ intermediate states[101]. Probably, the high resonance enhancement with the 800-nm Raman pump of the FAD_{DA}* state overwhelms the signals from the radical intermediate states, and the presence of a long-lived FAD_{DA}* additionally precludes their detection. No H/D kinetic isotope effect (KIE) was observed in the decay of FAD_{DA}* state (**Fig. 8.2b,c**), as in TA[101] and time-resolved fluorescence[118]; the absence of H/D KIE implies that proton transfer is not involved in the decay of FAD_{DA}* state, supporting the sequential electron-proton reaction model that was proposed by Gauden *et al.*[101].

The tri-exponential decay of the FAD_{DA}* state with no significant peak shifts indicates that only a single FAD species is excited by the actinic pump. Recently, it was suggested by structure-based free-energy calculations that a heterogeneous hydrogen-bond network near the FAD may exist in the ground DA state, which may result in heterogeneous decay of the excited state through distinct electron transfer pathways[116]. If this were the case, distinct FAD excited-state Raman features would be expected for the different FAD* decay fractions, resulting from the different hydrogen-bond pattern realizations. However, our FSRS results show that a single FAD species decays in multi-exponential fashion, which indicates that a single realization of the hydrogen-bond pattern between FAD and Y8-Q50 underlies the dynamics, and that the multiple phases in the FAD* decay are caused by varying donor-acceptor distances in the initial electron transfer.

To investigate the BLUF photoreaction from the LA state, we used the Slr1694-W91F mutant, which exhibits a ~50-fold longer-lived LA state than WT (223 s vs 6 s, for the W91F mutant and WT, respectively)[97], but fully retains the hydrogen-bond switch reaction of the WT[97] The LA state was prepared with backlight blue LED (λ_{max}~475 nm) illumination. The Raman spectra of the FAD_{DA}* were very similar between WT and the W91F mutant (**Fig. 8.S2**), indicating that the W91F mutation does not affect the conformation of the FAD_{DA}*. **Fig. 8.3a** shows selected transient Raman spectra of the W91F mutant in H_2O buffer on the reaction from the LA state. The FSRS spectra were globally fitted with three exponential components: 730 fs, 4.7 ps and 300 ps in H_2O (**Fig. 8.3b**), and 470 fs, 3.0 ps and 230 ps in D_2O (**Fig. 8.S3**). The 1st EADS (black line, **Fig. 8.3b**) which can be assigned to the FAD singlet excited state of LA BLUF , denoted FAD_{LA}*, shows positive peaks at 1210, 1264, 1398, 1511 and 1582 cm^{-1}. These peak positions are similar to

the FAD_{DA}*, while slight (~6 cm^{-1}) upshifts were observed for some bands. The 2nd EADS (red line, **Fig. 8.3b**) shows the Raman spectrum after the first 730-fs decay; the peak intensity at 1398, 1511 and 1582 cm^{-1} significantly dropped, while the 1356-cm^{-1} peak was only slightly weakened. The 3rd EADS (blue line, **Fig. 8.3b**) shows Raman spectra after the 4.7-ps decay; signals at 1210, 1398, 1511 cm^{-1} decayed, while peak intensity at 1356 and 1530 cm^{-1} only slightly dropped. The differences of the spectral features are clear in the DADS (lower panel, **Fig. 8.3b**) and normalized EADS (**Fig. 8.S4**). In 300 ps, all Raman peaks decayed, implying full decay of the molecules that are resonant to the 800-nm Raman pump.

The significant dynamic Raman band shifts of FSRS spectra in the LA state implies that an intermediate state was formed with a distinct Raman spectrum and was in preresonance with the 800-nm Raman pump. With TA and femto-IR spectroscopy and target analysis, it was shown that FAD_{LA}* evolves to $FADH^{\bullet}$ through concerted proton-coupled electron transfer (PCET) in 1 ps, with a minor fraction of FAD_{LA}* decaying to the initial ground state in 5 ps[100]. The 730-fs and 4.7-ps components of the FSRS likely correspond to the 1-ps and 5-ps decays in TA spectra, respectively. With this assumption, we propose that $FADH^{\bullet}$ Raman spectrum is mixed in the second EADS formed in 730 fs

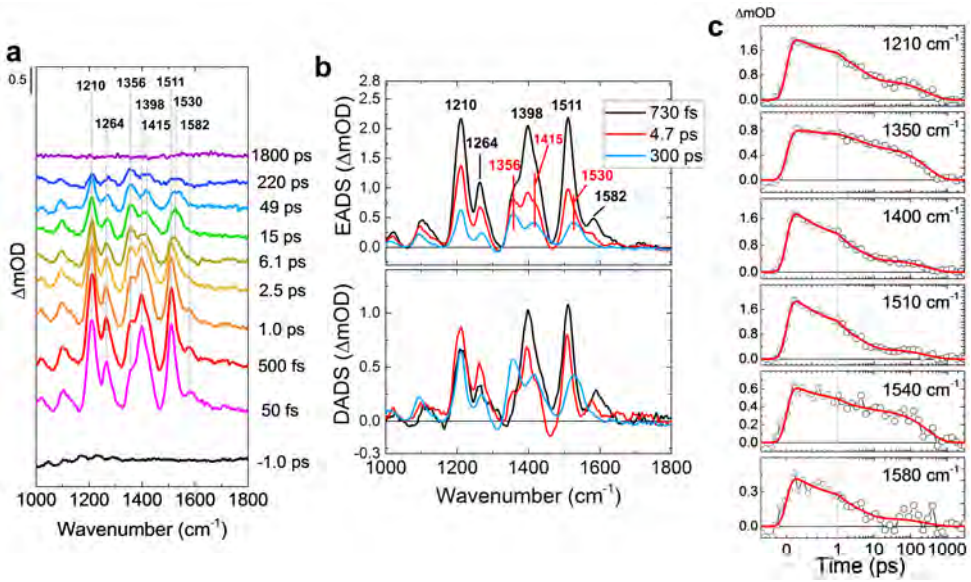

Figure 8.3. Transient Raman spectra of light-adapted Slr1694-W91F mutant in H_2O. (**a**) Selected transient Raman spectra. (**b**) Global-fitted evolution-associated difference spectra (EADS, top) and decay-associated difference spectra (DADS, bottom). (**c**) Selected time traces with fitting curves. Open dots show the raw data, and red lines show the fitting curves.

(red line, **Fig. 8.3b**), and largely constitutes the 300 ps EADS (blue line, **Fig. 8.3c**). The question arises why such radical FSRS spectral features would arise in the LA state, but not in the DA state (**Fig. 8.2**) given that in the latter case, flavin radicals are clearly involved in the reaction[100,101,118]. TA data showed that $FADH^{\bullet}$ transiently formed in the DA state does not absorb light at wavelengths >650 nm[101], while $FADH^{\bullet}$ from the LA state has a significant absorption tail at >700 nm[100], and hence has better preresonance with the 800 nm Raman pump. Thus, the long-lived (τ~300 ps) FSRS species (blue line, **Fig. 8.3b**) likely corresponds to the stimulated Raman spectrum of $FADH^{\bullet}$ that is formed from the photoexcited LA state in 730 fs. Yet, its properties are not entirely clear-cut: its decay time is ~4-fold longer than previously observed in TA (300 ps vs. 65 ps), and the Raman spectral signature only partly agrees with that of previously reported $FADH^{\bullet}$ resonant Raman spectra[325], with the 1530 and 1356 cm^{-1} bands assignable to $FADH^{\bullet}$. The reasons for these discrepancies are not clear, but possibly a small fraction of long-lived FAD excited states exists that distorts the spectral signature and lifetime of this component.

To assign the experimentally observed vibrational bands, we built minimal models of the BLUF active site involving the FAD, Q50, Y8, N31 and N32, as shown in **Fig. 8.1d**. Model 1 corresponds to the 'Anderson' model for the DA state[101,104], with the amino group of Q50 oriented towards Y8. Model 2 corresponds to the 'Kita/Jung' model for the DA state[103,106,326], and the 'Anderson' model for the LA state[101,104], with the carbonyl of Q50 oriented towards Y8. Model 3 represents the imidic tautomerized form of Q50 that was proposed as LA state by Domratcheva and co-workers[111,114,327]. We conducted quantum chemical calculations utilizing the CIS/6-31(dp)-D3 method to determine the Raman-active normal modes in the S_1 excited state. **Tables 8.S1–S3** summarize the calculated frequencies and Raman intensities for model 1 – 3 in H_2O and D_2O, whereas **Figs. 8.S5-S7** show the atomic motions that constitute the most Raman-active normal modes.

Fig. 8.4 aims to test the 'Domratcheva' model[114] to the observed and calculated S_1 Raman spectra. **Fig. 8.4a** shows the calculated spectrum for model 2 (upper panel, black line) convoluted with a spectral width (FWHM) of 30 cm^{-1} and the experimental FAD_{DA}* state (lower panel, magenta line), with main bands correlated through vertical lines. There is reasonably fair agreement between the experimental and calculated spectra, both in frequency as in Raman intensity. Only the Raman intensity of the experimental band at 1580 cm^{-1} appears to be overestimated in the calculations. The calculated band is composed of two normal modes at 1561 and 1545cm^{-1}, which correspond to N5-C4a/C10a-N1/N3-H and ring I C8-C9/C9-H normal modes, respectively (**Fig. 8.S6**). In D_2O, the 1580 cm^{-1} band

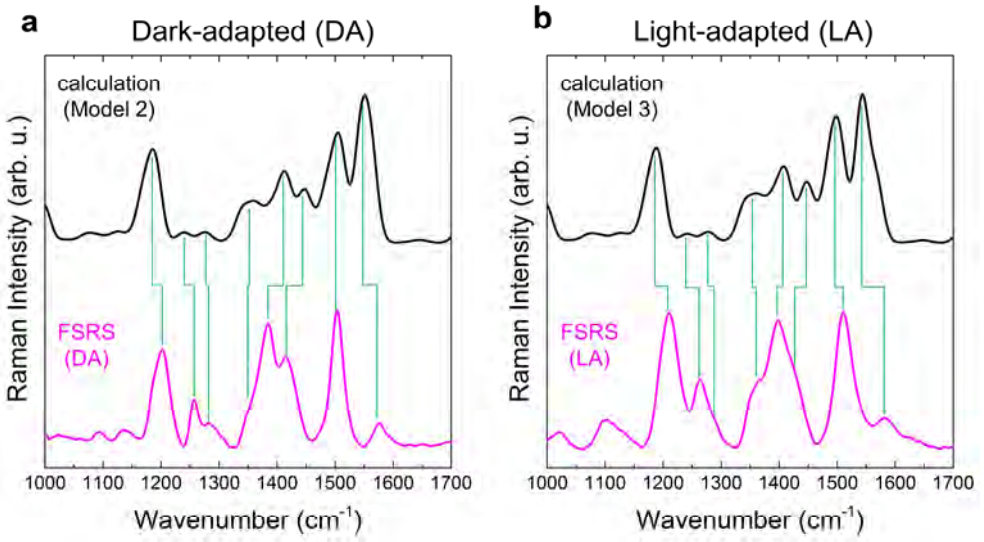

Figure 8.4. Comparison of calculated and experimental S_1 Raman spectra in H_2O. (**a**) Calculated Raman signals based on Model 2 (on **Fig. 8.1d**) (black line) and the second EADS of the DA state (on the upper panel of **Fig. 8.2b**) (magenta line). (**b**) Calculated Raman signals based on Model 3 (on **Fig. 8.1d**) (black line) and the first EADS of the LA state (on the upper panel of **Fig. 8.3b**) (magenta line). Green lines show tentative assignments of the FSRS peaks.

splits in the experimental spectrum (**Fig. 8.2b**, lower panel), while in the calculated spectrum the vibrational frequencies move further apart in D_2O as well (to 1540 and 1561 cm^{-1}, respectively), which supports the assignment of the experimental 1580 cm^{-1} band to these particular modes.

Fig. 8.4b furthermore shows the calculated spectrum for model 3 (upper panel, black line) and the experimental FAD_{LA}^* state (lower panel, magenta line). As mentioned previously, the overall pattern of the experimental LA state spectrum is similar to that of the DA state, with only minor upshifts of a few bands. Likewise, Model 3 shows an overall pattern that is very similar to that of Model 2, with only minor shifts. However, Model 3 shows small downshifts with respect to Model 2, whereas the LA state shows slight upshifts with respect to the DA state.

In a similar fashion, **Fig. 8.5a** examines the 'Anderson' model[101,104]. It shows the calculated spectrum for Model 1 (upper panel, black line) and the experimental FAD_{DA}^* state (lower panel, magenta line). Notably, the overall calculated Raman intensity for Model 1 is lower than for Model 2 and 3 and shows an overall different pattern of Raman band intensities and frequencies. As a consequence, the agreement between the Model 1

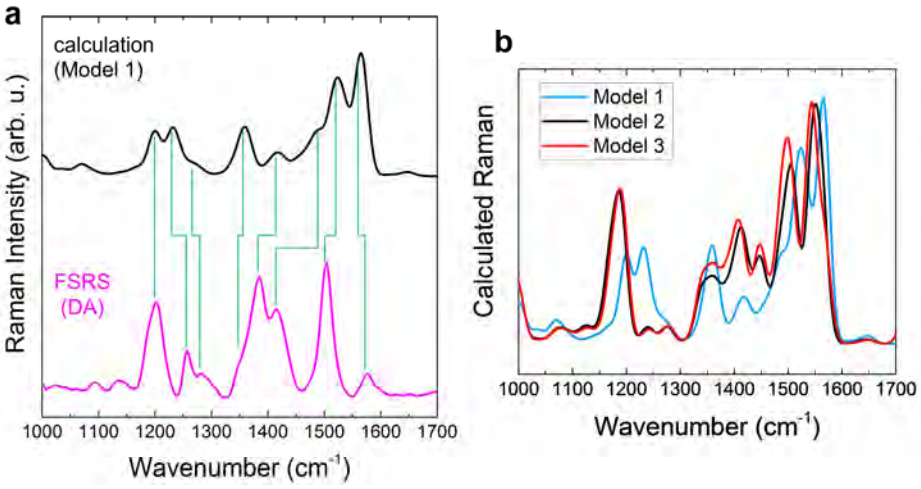

Figure 8.5. Comparison of calculated Raman spectrum of Model 1 and experimental FSRS of the DA state in H_2O. (**a**) Calculated Raman signals based on Model 1 (on **Fig. 8.1d**) (black line) and the second EADS of the DA state (on the upper panel of **Fig. 8.2b**) (magenta line) are shown. (**b**) Overlap of calculated Raman spectra of Model 1–3.

calculated and the experimental Raman intensities and frequencies is rather poor. The experimental BLUF FAD_{LA}* state (lower panel, red line) agrees quite well with Model 2 (upper panel, black line), as we showed above in **Fig. 8.4**.

Based on the considerations above, we may relate the agreement, or lack thereof, between experimental and calculated S_1 state Raman spectra to the hydrogen-bond patterns and tautomeric states in the BLUF active site of Model 1–3. The initially proposed 'Anderson' model, which features Model 1 for the DA and Model 2 for the LA state shows large discrepancies: the calculated spectra would predict large differences between the DA and LA states (**Fig. 8.5b**), which are not experimentally observed. In addition, the agreement between Model 1 and the experimental DA spectrum is rather poor. On the other hand, the 'Domratcheva' model, which features Model 2 for the DA state and Model 3 for the light state shows overall fair agreement, in calculated Raman intensity as well as frequencies. Although Model 3 predicts overall slightly downshifted bands with respect to Model 2, contrary to experimental observation (**Fig. 8.4**), in absolute terms the 'Domratcheva' model is clearly superior to the 'Anderson' model. Hence, we tentatively conclude, within the accuracy of our computational approach, that FSRS spectroscopy of the PixD BLUF domain reveals that the Domratcheva model likely represents the most correct model for BLUF photoactivation.

8.3. Conclusion

In this chapter, excited-state chemical structures of/near the FAD and its excited-state dynamics of the DA and LA states were investigated by FSRS combined with computational calculation based on the CIS-D3/6-31(d,p) method. In the DA state, the excited FAD_{DA}* state decayed in 340 fs, 14 ps and 130 ps. Since the resonance with the 800-nm Raman pump was weak in other states than the FAD_{DA}* state, FSRS only showed pure FAD_{DA}* state signals. No significant band shifts were observed during the FAD_{DA}* decays, implying that the FAD_{DA}* state is homogeneous with regard to hydrogen-bond pattern. On the reaction from the LA state, which was studied with the W91F mutant, overall similar excited FAD_{LA}* state Raman features as compared to FAD_{DA}* were observed, with slight but significant differences from the FAD_{DA}* state. The FAD_{LA}* state mostly decayed in 730 fs, and a distinct spectral evolution was observed. The shifted bands that appear in 730 fs likely derive from $FADH^{\bullet}$ state, which is probably well in preresonance with the 800-nm Raman pump. The FAD_{LA}* and $FADH^{\bullet}$ states completely decayed in 4.7 ps and 300 ps. We assigned the FSRS spectra of the FAD excited state in DA and LA utilizing quantum chemical calculations. The experimental excited-state Raman spectra of DA and LA BLUF can be assigned correspondingly to Model 2 and Model 3 (**Fig. 8.1d**), respectively, but not to Model 1. This observation implies that the 'Domratcheva' model, which involves tautomerization of Q50 to the imidic form in the LA state[114] is more likely to apply to the Slr1694 BLUF photoreceptor.

Methods

Sample preparation: WT Slr1694 BLUF photoreceptor and the W91F mutant samples were prepared as reported previously[97,100,101]. The samples were filled in a homemade sample holder that has two 2-mm-thick CaF_2 plates. The sample thickness was set as 400 μm for transient absorption experiments and 200 μm for stimulated Raman experiments with an appropriate sample spacer. The sample holder was set on a Lissajous scanner that ensures sample refreshment after each laser shot with a time interval of 60 seconds between successive exposures to the laser pulses[134].

Femtosecond stimulated Raman spectroscopy (FSRS): Femtosecond time-resolved stimulated Raman experiments were performed with the watermarked stimulated Raman setup reported previously[41]. Raman pump (800 nm, ~10 μJ) and Raman probe (~840–960 nm) were spatiotemporally overlapped at the sample position with the diameter of ~100 μm. Actinic pump (~400nm, ~2 μJ) was focused on the protein sample to the diameter of ~150 μm with a time delay from -50 ps to 1800 ps at 63 data points (logarithmically spaces after 2 ps), generated by an optical delay. Raman pumps pass through a

specially-designed chopper blade for watermarking approach[136], which produces 14 Raman pump sequences whose wavelengths are slightly shifted each other[136]. As a result, 14 different stimulated Raman experiments are effectively performed simultaneously, which makes the nearly baseline-free watermarking approach possible. The sample exposure time to the beams was ~1 hour in total for each time-resolved stimulated Raman experiment. For experiments of the LA state of Slr1694-W91F mutant, 475-nm LED (~10 mW/cm^2) was continuously irradiated to the sample during the experiments. Residual baselines of FSRS were manually corrected before global analysis.

Computational methods: Molecular complexes mimicking hydrogen-bonding interactions of the flavin cofactor with residues of the active site (Tyr8, Gln50, Asn34, and Asn35) were computationally characterized to facilitate the assignment of the Raman spectra. Starting atomic coordinates of the models were assigned according to the PDB model 2HFN (molecule A). Geometry optimization, vibrational analysis in harmonic approximation and calculations of Raman intensities were performed using the CIS-D3/6-31(d,p) method in the S_1 state dominated by the HOMO-LUMO $\pi\pi^*$ excitation of the isoalloxazine chromophore; the harmonic vibrational frequencies were scaled by 0.91. In order to model the D_2O effect, the computations of the Raman spectra were re-computed for models in which the hydrogen atoms of the OH and NH/NH_2 groups were substituted by deuterium atoms. The calculations were performed using the Firefly quantum-chemistry program, version 8.2[328] which is partially based on the US GAMESS source code[329].

Supplemental Figures and Tables

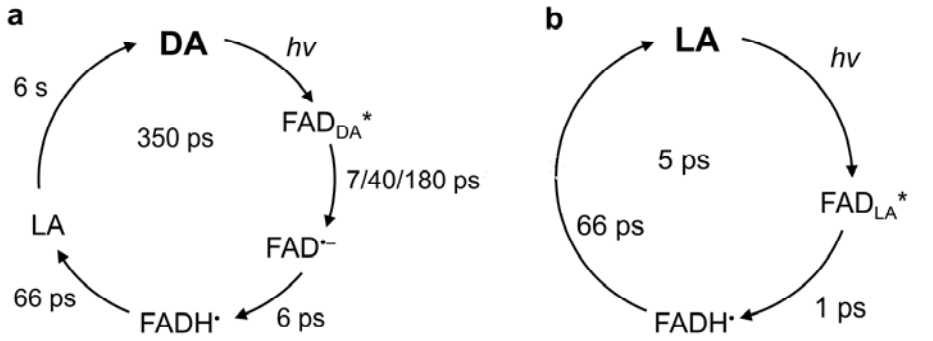

Figure 8.S1. Previously proposed reaction models of Slr1694 BLUF photoreceptor. Photoreaction models of (**a**) dark-adapted (DA) state proposed by Gauden *et al.*[101] and (**b**) light-adapted (LA) state proposed by Mathes *et al.*[100].

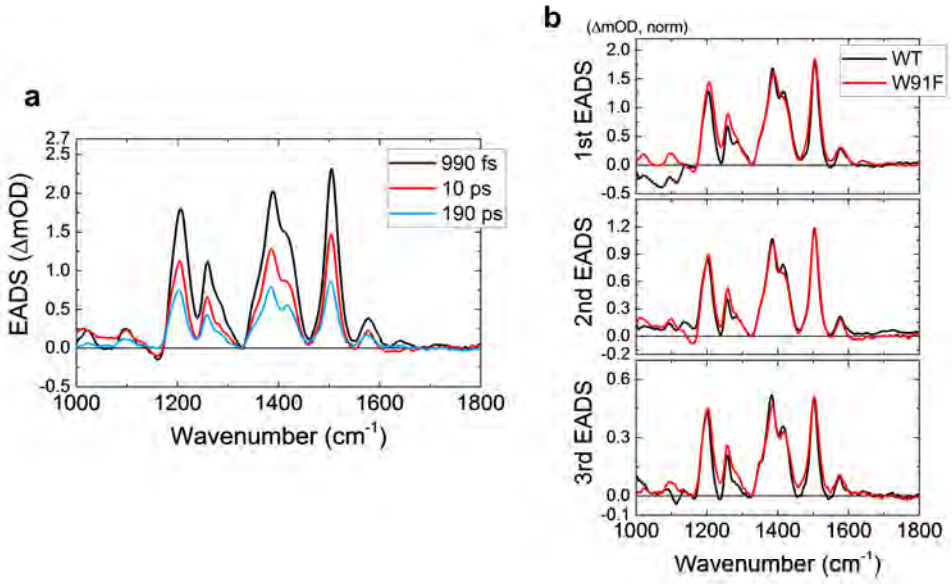

Fig. 8.S2. Comparison of FSRS of the DA state between WT Slr1694 BLUF photoreceptor and its W91F mutant. (**a**) EADS of the DA FSRS of the W91F mutant. (**b**) Comparison of normalized EADS of WT (black lines) and the W91F mutant (red lines) proteins. 1st (top), 2nd (middle) and 3rd (bottom) EADS are compared.

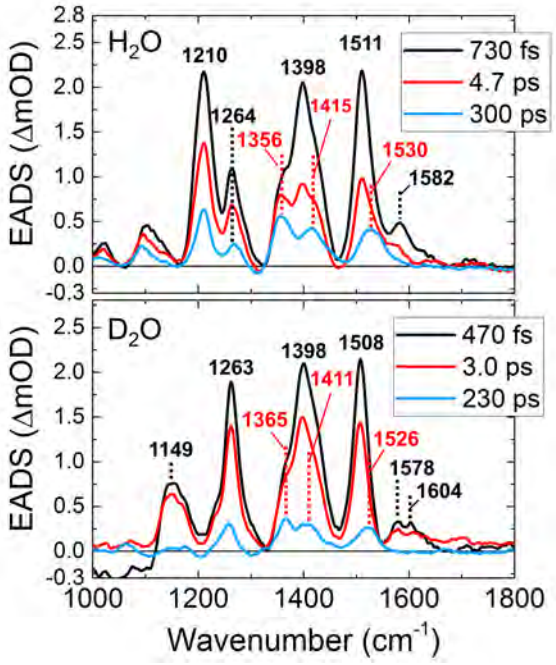

Fig. 8.S3. EADS of FSRS of the LA state on the W91F mutant in H_2O (top) and D_2O (bottom). The top figure is the same as the top panel on **Fig. 8.3b**.

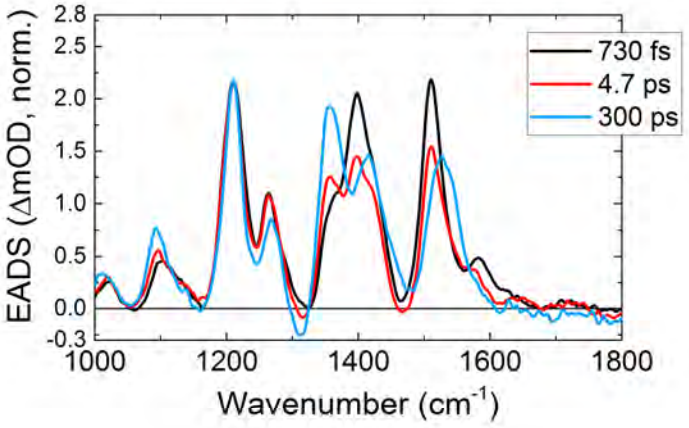

Fig. 8.S4. Normalized EADS of FSRS of the LA state on the W91F mutant in H_2O.

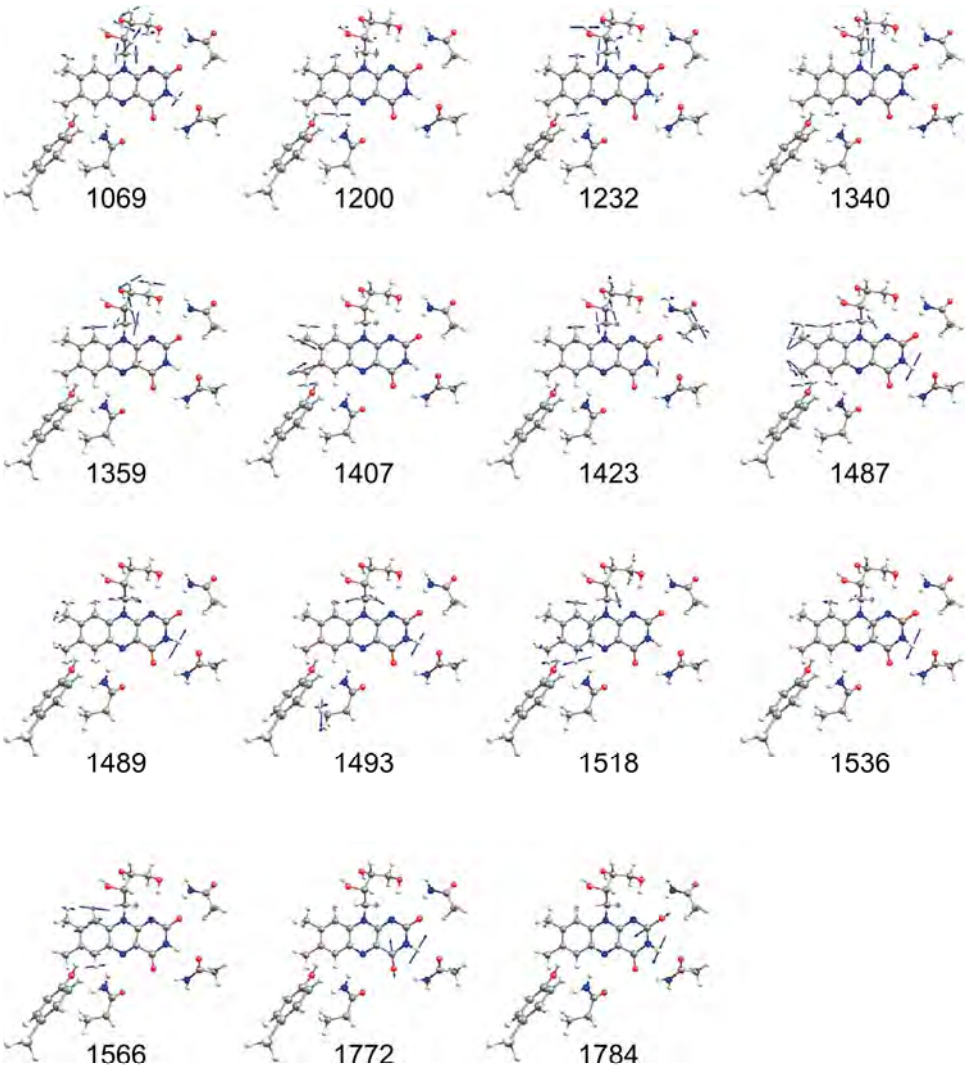

Fig. 8.S5. Selected vibrational modes of computational model on Model 1 FAD configuration. The values in the figure show wavenumbers (cm^{-1}).

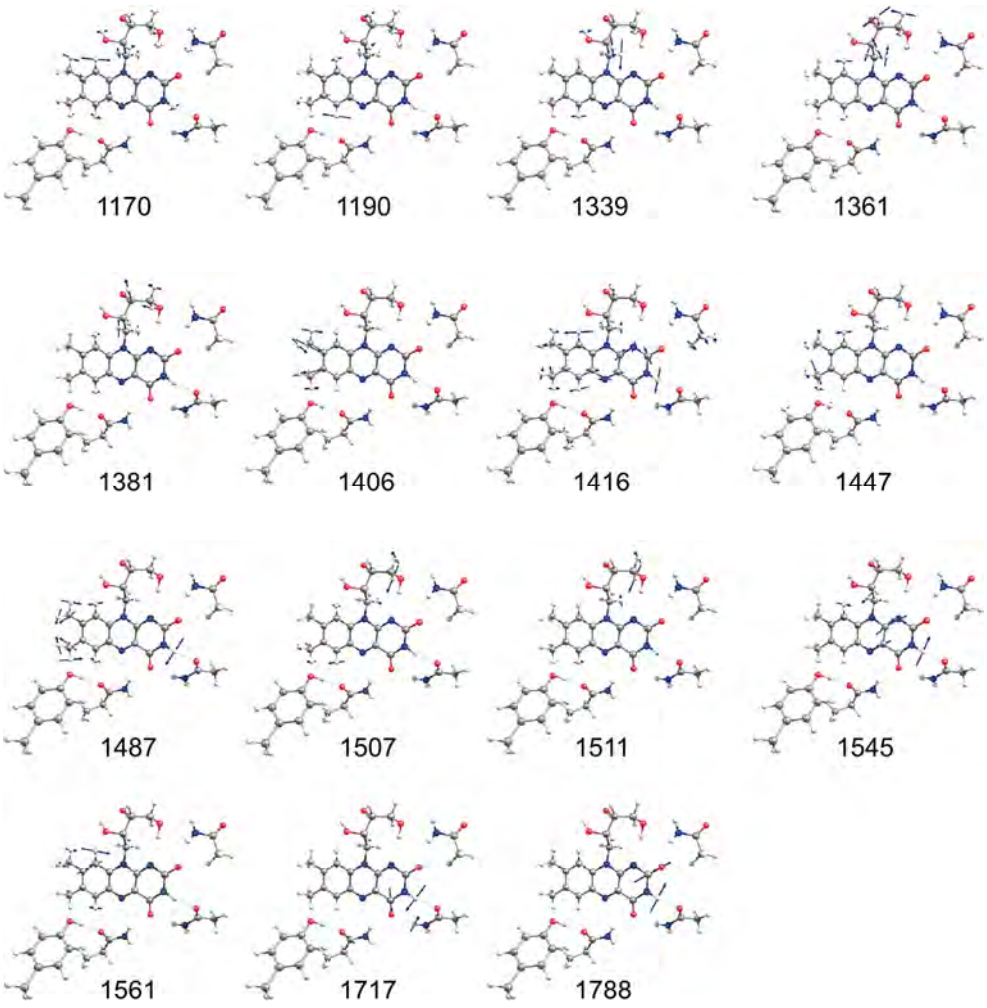

Fig. 8.S6. Selected vibrational modes of computational model on Model 2 FAD configuration. The values in the figure show wavenumbers (cm^{-1}).

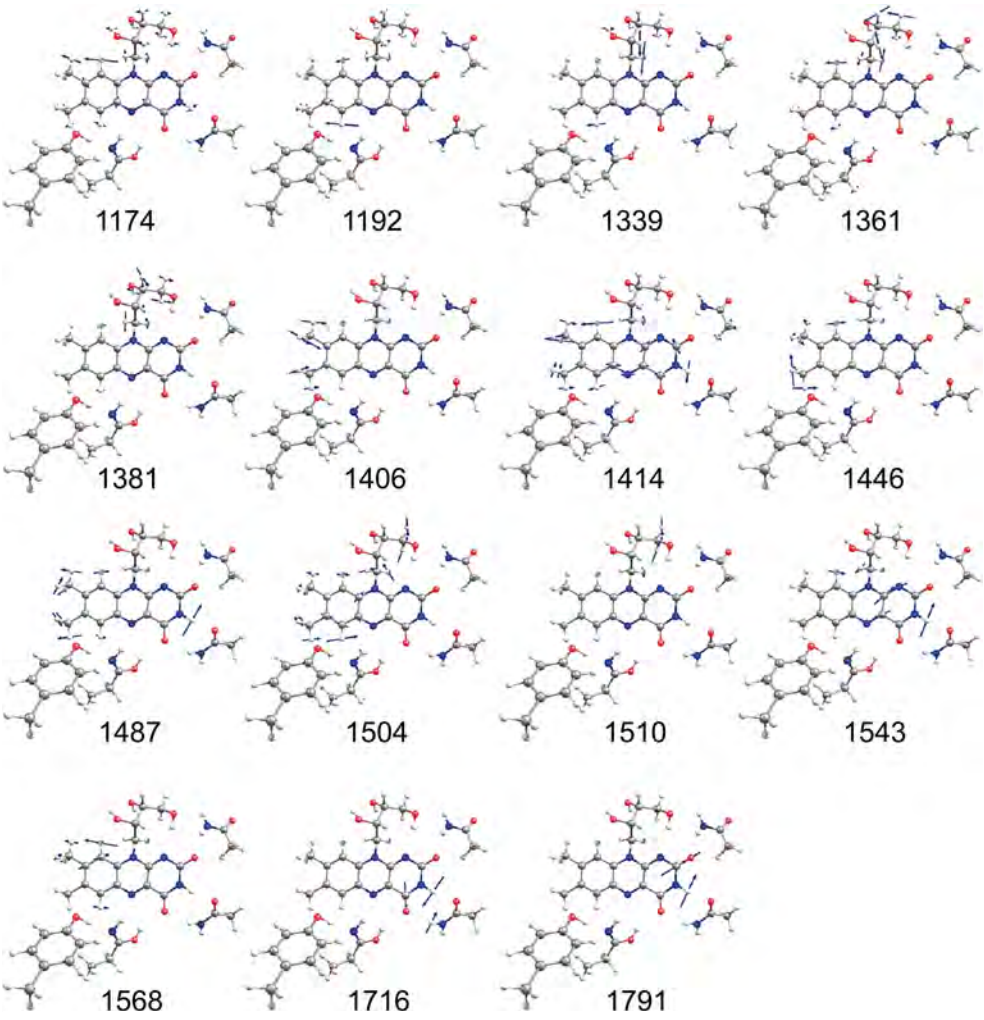

Fig. 8.S7. Selected vibrational modes of computational model on Model 3 FAD configuration. The values in the figure show wavenumbers (cm^{-1}).

Table 8.S1. Frequency and Raman activity of computational model on Model 1.

Model 1			
H_2O		D_2O	
Freq., cm^{-1}	Raman Act., $Å^4$/AMU	Freq., cm^{-1}	Raman Act., $Å^4$/AMU
		1056	193
1069	**124**		
1089	41		
		1093	13
1104	16		
		1111	10
1114	5		
		1115	19
1125	3		
		1130	41
		1144	13
1146	33		
		1158	6
1169	91		
		1175	6
1183	8		
		1181	14
		1187	25
		1187	15
1200	**537**		
0		1205	849
1232	**539**		
1245	78	1245	375
1247	19		
1263	94		
1277	77	1275	80
		1285	12
		1290	20
1292	11		
		1308	67
1314	24		
		1321	71
		1328	102
1340	**119**		
		1347	111

Model 1			
H_2O		D_2O	
Freq., cm^{-1}	Raman Act., $Å^4$/AMU	Freq., cm^{-1}	Raman Act., $Å^4$/AMU
1359	**497**	1359	460
1367	92	1367	4
1382	18	1383	75
1387	10		
1396	17		
1397	6	1397	11
1407	**119**	1407	125
		1417	4
1423	**113**	1423	80
1426	36	1427	78
		1428	53
1430	2		
1439	8		
1450	62	1449	45
		1450	46
1453	24	1453	26
1454	24	1455	29
1456	22		
1472	27	1472	56
1473	76	1473	53
1487	**151**	1487	57
1489	**107**		
		1491	22
1493	**140**		
1510	54	1509	43
1518	**881**	1518	774
		1528	1087
1536	**675**		
1566	**1520**	1566	1510
		1719	69
		1753	185
1772	**190**		
		1778	407
1784	**404**		

Table 8.S2. Frequency and Raman activity of computational model on Model 2.

Model 2			
H_2O		D_2O	
Freq., cm^{-1}	Raman Act., $Å^4$/AMU	Freq., cm^{-1}	Raman Act., $Å^4$/AMU
		1133	297
		1144	370
		1158	6
1170	**1191**		
		1175	157
		1181	205
1183	121		
		1187	366
1190	**2032**		
		1192	2249
1236	136		
1241	111		
1247	38		
		1250	85
1266	33		
		1270	264
1276	243		
		1286	35
		1291	7
1292	2		
		1307	106
1316	47		
		1320	67
		1335	128
1339	**720**		
		1346	796
1361	**710**	1360	780
1368	134	1368	3
1381	**366**	1382	461
1387	152		
1395	208		
1396	253	1396	81

Model 2			
H_2O		D_2O	
Freq., cm^{-1}	Raman Act., $Å^4$/AMU	Freq., cm^{-1}	Raman Act., $Å^4$/AMU
1406	**398**	1406	435
1416	**1285**	1416	395
		1417	597
		1419	739
1425	67	1424	218
		1428	56
1430	2		
1438	111		
1447	**831**	1447	890
1452	145	1452	115
		1456	193
1457	132		
1470	16	1470	17
1473	134	1472	118
1485	153		
1487	**1066**	1486	468
1493	42		
		1495	44
1507	**1727**	1506	1859
1511	**900**	1510	821
		1540	3421
1545	**2868**		
1561	**2235**	1561	2148
		1696	350
1717	**439**		
		1778	1025
1788	**835**		

Table 8.S3. Frequency and Raman activity of computational model on Model 3.

Model 3			
H_2O		D_2O	
Freq., cm^{-1}	Raman Act., $Å^4$/AMU	Freq., cm^{-1}	Raman Act., $Å^4$/AMU
		1133	225
		1145	357
		1159	9
1174	**1139**	1175	141
		1182	85
1183	19		
		1188	434
1192	**2129**		
		1194	2289
1237	99		
1243	99		
1248	45		
		1251	51
1267	34		
		1272	277
1279	261		
		1286	45
		1291	12
1292	2		
		1308	108
1316	51		
		1320	80
		1336	113
1339	**824**		
		1346	958
1361	**835**	1360	897
1368	140	1368	5
1381	**478**	1382	592
1386	222		
1395	327		
1396	215	1396	64

Model 3			
H_2O		D_2O	
Freq., cm^{-1}	Raman Act., $Å^4$/AMU	Freq., cm^{-1}	Raman Act., $Å^4$/AMU
1406	**632**	1406	752
1414	**1063**	1414	1399
		1416	202
1425	57	1424	137
		1428	52
1430	6		
1438	114		
1446	**1008**	1446	987
1451	260	1451	250
		1454	210
1455	83	1455	11
1468	94	1468	102
1470	48	1470	29
1485	43		
1487	**1467**	1486	818
		1491	47
1492	187		
1504	**1968**	1504	2210
1510	**347**	1510	307
		1535	265
		1538	4266
1543	**3750**		
1568	**1604**	1568	1569
		1695	327
1716	**401**		
		1780	1092
1791	**896**		

Chapter 9

Molecular Origin of Photoprotection in Oxygenic Photosynthesis Probed by Femtosecond Raman Spectroscopy

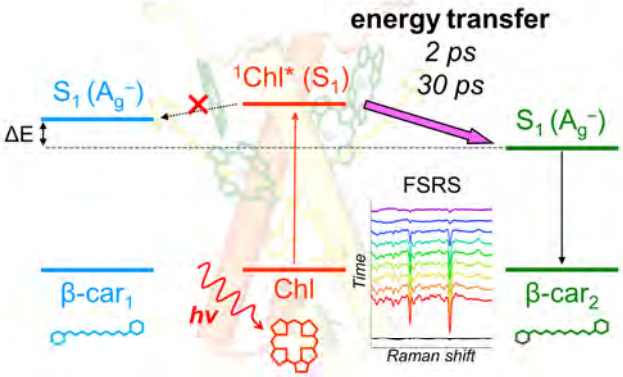

Chlorophyll-carotenoid excited-state energy transfer quenching was captured by FSRS.

Abstract

Photoprotection is fundamental in photosynthesis to avoid oxidative photodamage upon excess light exposure. Excited chlorophylls (Chl) are quenched by carotenoids, but the precise molecular origin remains controversial. The cyanobacterial HliC protein belongs to the Hlip family ancestral to plant light-harvesting complexes, and binds Chl *a* and β-carotene in 2:1 ratio. We analysed HliC by watermarked femtosecond stimulated Raman spectroscopy to follow the time evolution of its vibrational modes. We observed a 2-ps rise of the C=C stretch band of the $2A_g^-$ (S_1) state of β-carotene upon Chl *a* excitation, demonstrating energy transfer quenching and fast excess-energy dissipation. We detected two distinct β-carotene conformers by the C=C stretch frequency of the $2A_g^-$ (S_1) state, but only the β-carotene whose $2A_g^-$ energy level is significantly lowered and has a lower C=C stretch frequency is involved in quenching. It implies that the low carotenoid S_1 energy that results from specific pigment-protein or pigment-pigment interactions is the key property for creating a dissipative energy channel.

This chapter is based on the following publication:
The Journal of Physical Chemistry Letters **9**, 1788–1792 (2018),
collaborated with T. Polívka, M. K. Shukla and R. Sobotka for sample purification.

9.1. Introduction

Oxygenic photosynthetic organisms need to protect themselves from the consequences of excess sunlight, as the photosynthetic machinery easily gets overloaded even at moderate light intensities. To this end, elaborate photoprotection mechanisms have evolved, collectively known as nonphotochemical quenching (NPQ)[120,330]. NPQ involves the active dissipation (quenching) of singlet excited states in the light harvesting antenna before they reach the reaction centers for photochemical conversion, and manifests itself in distinct ways in various oxygenic photosynthetic organisms. In plants and algae, NPQ involves specific interactions between carotenoids and chlorophylls in the light-harvesting complex (LHC) family, where the lifetime of Chl singlet excited states is quenched to hundreds of ps. The mechanism by which this process occurs has been controversially discussed in the literature[331]:energy transfer[121-125], electron transfer[126-128], excitonic coupling[129,130], and Chl-Chl charge transfer interactions[131] have been proposed.

Cyanobacterial photosynthesis is ancestral to that of plants and algae and although cyanobacteria do not use the plant-like LHC antenna system for light harvesting, they contain so called high light-inducible proteins (Hlips) that are homologues to 1st and 3rd helices of plant LHC proteins. Hlips are small single-helix polypeptides (5-7 kDa) ubiquitous in cyanobacteria, which play an important role during assembly and repair of photosystem II, particularly under stress conditions[332]. So far, only two members of the Hlip family, HliC and HliD, have been isolated and biochemically characterized[122,132]. Both these proteins, isolated from the cyanobacterium *Synechocystis* 6803, form oligomers and bind 4 Chl *a* (HliC) or 6 Chl *a* (HliD) and 2 β-carotenes per a putative dimer[122,132].

Fig. 9.1 shows the absorption spectrum and a structural model of HliC[122]. Despite the apparent two-fold symmetry in the proposed structure, resonance Raman spectroscopy demonstrated that two distinct β-carotene conformers exist in HliC and also in HliD[333]: β-car$_1$ absorbs at higher energy and exhibits a higher C=C stretch frequency at 1525 cm^{-1}, whereas β-car$_2$ absorbs at lower energy and has a lower C=C stretch frequency at 1515 cm^{-1}. Strikingly, ultrafast transient absorption spectroscopy showed that the HliD protein was highly quenched, with dominant Chl *a* lifetimes of only 2 and 30 ps, and a minor unquenched fraction[122]. Moreover, it was shown that the quenching of the Chl *a* excited state proceeded via energy transfer to the optically forbidden S_1 (A_g^-) state of β-carotene[122]. This observation posed an important conundrum: close Chl-carotenoid positioning that is a common motif in light-harvesting proteins is necessary to promote triplet-triplet transfer from Chl to carotenoid upon Chl intersystem crossing. Yet, in most antenna complexes the

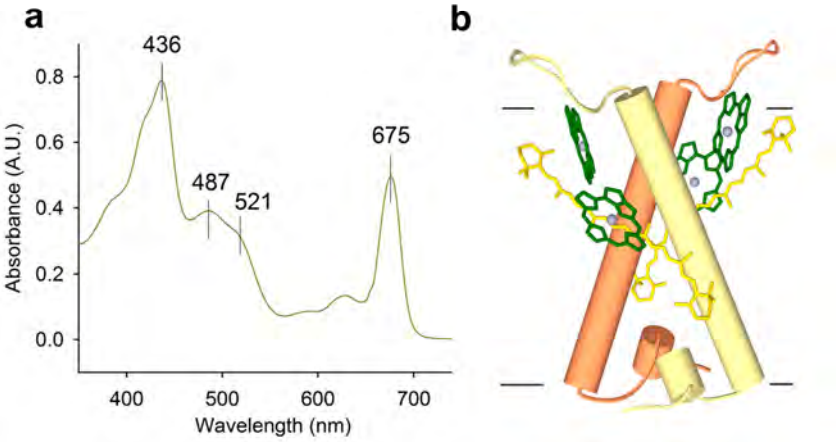

Figure 9.1. Steady-state absorption and a structural model of HliC. (**a**) Room-temperature absorbance spectrum of the purified HliC protein. (**b**) A structural model of the putative HliC dimer depicted as a side view along the membrane plane (modified from[132]).

Chl singlet excited state is not quenched at all. Hence, unresolved questions remain about the quenching mechanisms in photosynthetic light harvesting complexes with regard to electronic coupling to optically forbidden states and the energetics of the states involved[334]. The latter is especially pressing because the energy level of the optically forbidden S_1 state of carotenoids is largely insensitive to polarity and polarizability of the environment[264].

Femtosecond stimulated Raman spectroscopy (FSRS) is a powerful method to gain detailed molecular information through transient vibrational spectra[135]. It features a high temporal resolution of <100 fs, high spectral resolution and high sensitivity with respect to time-resolved resonance Raman methods. Recently, we have developed a watermarked FSRS method involving shot-to-shot Raman pump wavelength modulation and wavelet transformation to successfully suppress the large and unpredictable baseline fluctuations that have dogged the FSRS method since its inception more than a decade ago[41,136,137]. Through this method, baseline issues due to nonresonant nonlinear contributions, transient absorption, pump-dump-probe and pump-repump probe signals are successfully suppressed without any biased human intervention. Watermarked FSRS seems particularly suited to study pigment-protein complexes of oxygenic photosynthesis since its Raman pump at 800 nm is conveniently preresonant with the main pigment absorption bands. In this work, we make use of the ability of FSRS to follow specific molecular vibrations with sub-100 fs time resolution to assess the mechanism, pathways and energetics of excited-state energy

quenching in HliC. To our knowledge, this work represents the first demonstration of energy transfer processes in a photosynthetic light harvesting complex probed with FSRS and lays the groundwork for general application of the watermarked FSRS method in photosynthesis research.

9.2. Results and Discussion

Fig. 9.2a shows the stimulated Raman spectrum of the HliC ground state with preresonant 800 nm pump. The two strongest bands at 1517 and 1156 cm^{-1} are due to the β-carotene C=C (ν_1) and C-C stretches (ν_2), respectively[132,333]. The bands at 1002 and 920 cm^{-1} belong to the ν_3 (methyl in-plane rocking) and ν_4 (hydrogen-out-of-plane rocking) vibrations of β-carotene, respectively[132,333]. It furthermore features a shoulder near 1550 cm^{-1} and a band at 1671 cm^{-1}, which are both due to Chl *a*[132]. The amplitude of the β-carotene bands is much higher than those of Chl *a* even though the 800 nm Raman pump is more preresonant with the Chl *a* Q_y band than the β-carotene S_2 band, which relates to the higher Raman cross section of the latter pigment. The bands at 1466, 1051 and 851 cm^{-1} are due to glycerol, which was added to stabilize the sample and are conveniently used as an internal marker for the FSRS experiments. The spectral width of the HliC stimulated Raman bands is approximately 20 cm^{-1}, which is larger than the bandwidth expected from convolution with the spectral width of the Raman pump (~10 cm^{-1}). Hence, the observed bandwidths do not result from the experimental conditions but are inherent to the HliC protein at room temperature.

Fig. 9.2b shows FSRS spectra at selected delays upon Chl *a* excitation at 675 nm. At very short delays (300 fs), large bleaches of the β-carotene C=C stretch at 1515 cm^{-1} and C-C stretch at 1156 cm^{-1} are observed, as well as a bleach of the Chl *a* band at 1668 cm^{-1}. Importantly, the glycerol solvent bands at 1465, 1047 and 851 cm^{-1} are bleached as well, which indicates that these are likely spurious signals caused by partial absorption of the 800 nm Raman pump by Chl *a* excited-state absorption (ESA)[335,336], *i.e.* an inner filter effect that diminishes the Raman pump intensity and hence results in a lower signal[337]. Thus, the bleaching signals associated with β -carotene stretches at early delay times do not imply population of β -carotene excited states. This was confirmed by a FSRS experiment on a Chl *a* – β-carotene mixture in organic solvent, where no close interactions exist between the pigments. Here, selective Chl *a* excitation and population also lead to bleach of Chl *a*, β-carotene and solvent modes (**Fig. 9.3**), confirming the inner filter effect. We did not observe any positive bands that arise from the Chl *a* excited state, which may seem surprising given

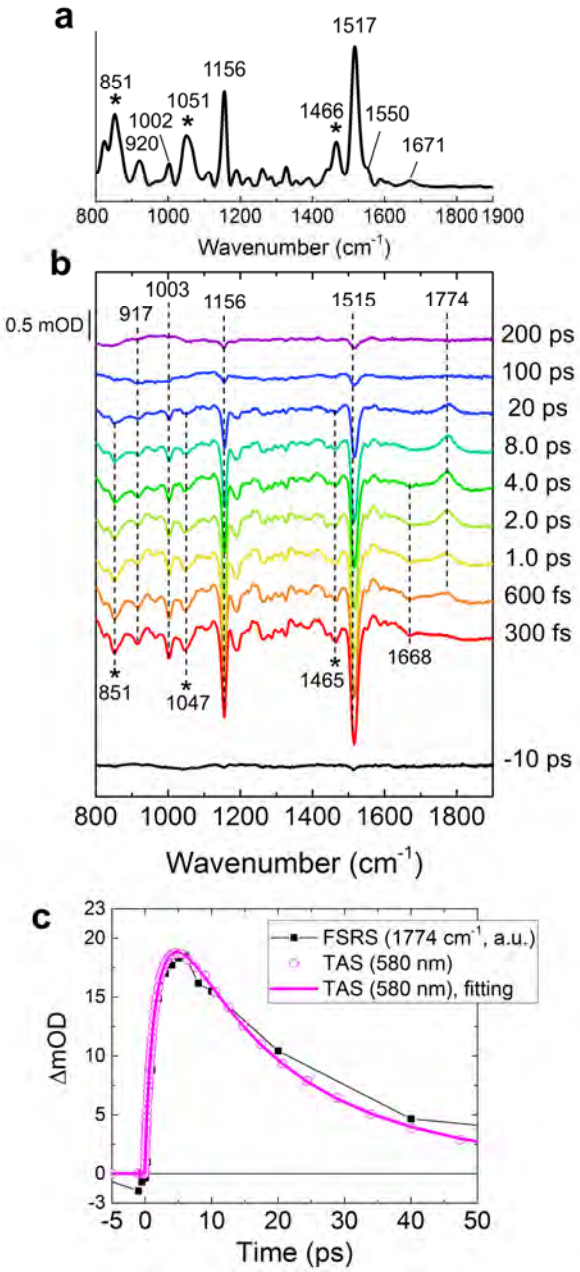

Figure 9.2. FSRS of HliC upon 675 nm excitation. (**a**) Ground-state Raman spectrum of HliC. (**b**) Selected time traces of difference spectra of FSRS. Asterisks (*) indicate signals originated from glycerol. (**c**) Transient absorption kinetic trace at 580 nm (magenta open dots) with a fitting curve (magenta line) overlapped with FSRS data at 1774 cm^{-1} (black closed squares).

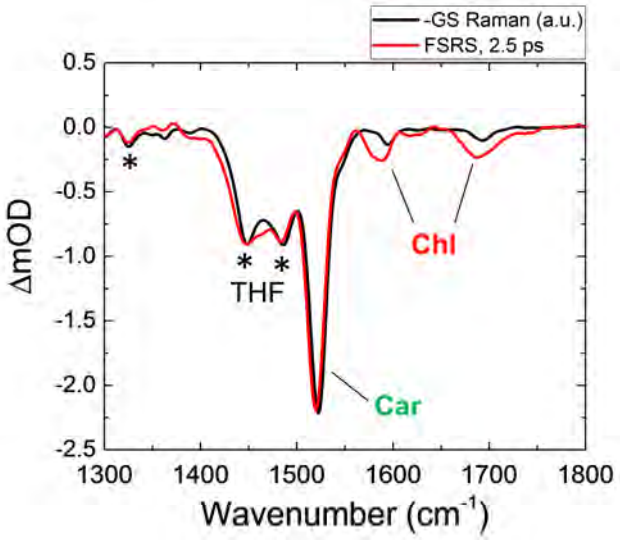

Figure 9.3. FSRS of a Chl *a* – β-carotene mixture in tetrahydrofuran (THF). Red line: FSRS spectrum at 2.5 ps upon excitation at 675 nm. Black line: ground state stimulated Raman spectrum, inverted and scaled to the red line on the 1520 cm^{-1} β-carotene C=C stretch. The bands at 1580 and 1690 cm^{-1} arise from Chl *a*, whereas the bands at 1430 and 1480 cm^{-1} arise from the THF solvent.

the resonance of the Raman pump with the Chl *a* ESA. However, the Chl a ESA has a rather low amplitude and the strong electronic transition to the Q_y state at 670 nm, which is preresonant with the Raman pump in the ground state, entirely disappears in the excited state. At the same time, β-carotene has a very high Raman cross section. Apparently, these combined effects result in Chl *a* excited-state Raman bands that are unobservably weak with respect to those of the β-carotene ground state.

In the ensuing evolution on the picosecond timescale, we observe the rise of a positive band at 1774 cm^{-1}. This band is a unique marker of the optically forbidden S_1 ($2A_g^-$) state of carotenoids, as it represents an upshifted C=C stretch frequency that results from strong vibronic coupling between the S_0 ($1A_g^-$) and S_1 ($2A_g^-$) states[268]. Thus, FSRS data gives direct evidence of energy transfer from the excited Chl *a* to the optically forbidden S_1 state of β-carotene in 2 ps, consistent with transient absorption measurements (**Figs. 9.2c** and **9.4**) where the β-carotene S_1 state has a prominent absorption at 560 nm. The same quenching pathway has also been earlier reported by ultrafast transient absorption experiments on HliD[122]. The 1774 cm^{-1} band disappears on a timescale of 10 ps, which is assigned to the S_1–S_0 internal conversion (IC) of β-carotene[264]. In addition, a minor slow phase of 30 ps is observed in the β-carotene S_1 decay (1774 cm^{-1}) in transient absorption as well as in

stimulated Raman. The Chl *a* bleach signal mainly decayed in 2.5 and 20 ps (**Fig. 9.4**). Given that the IC time constant of β-carotene can hardly be longer than 15 ps due to the properties of its conjugated π-electron system[264], we interpret this to result from a slow 30 ps phase in the energy transfer process from Chl *a* to β-carotene, which through inverted kinetics (*i.e.*, when a state is populated slower than it is depopulated, it rises with its decay time, and decays with its risetime[124]) shows up as a 30 ps lifetime component of the β-carotene S_1 state. A nondecaying phase in the Chl *a* transient absorption is assigned to a minor fraction of loosely bound or unbound Chl *a* (**Fig. 9.4b**, magenta line).

Given the (low) Chl *a* ESA around 800 nm, it might be anticipated that Chl *a* could be promoted to a higher-up excited state due to the combined actions of actinic and Raman pumps. However, the FSRS time evolution closely follows that of the TA experiments (**Figs. 9.2c** and **9.4**), indicating that such processes, if they occur at all, do not affect the FSRS experiment in any appreciable way.

To gain additional information about the energy transfer processes and pathways, we performed FSRS experiments with direct excitation of β-carotene at 488 and 532 nm (**Fig. 9.5**). Here, the two β-carotene conformers, β-car$_1$ and β-car$_2$, are to a certain extent selectively excited. We observe that for both datasets upon 488- and 532-nm excitation, the

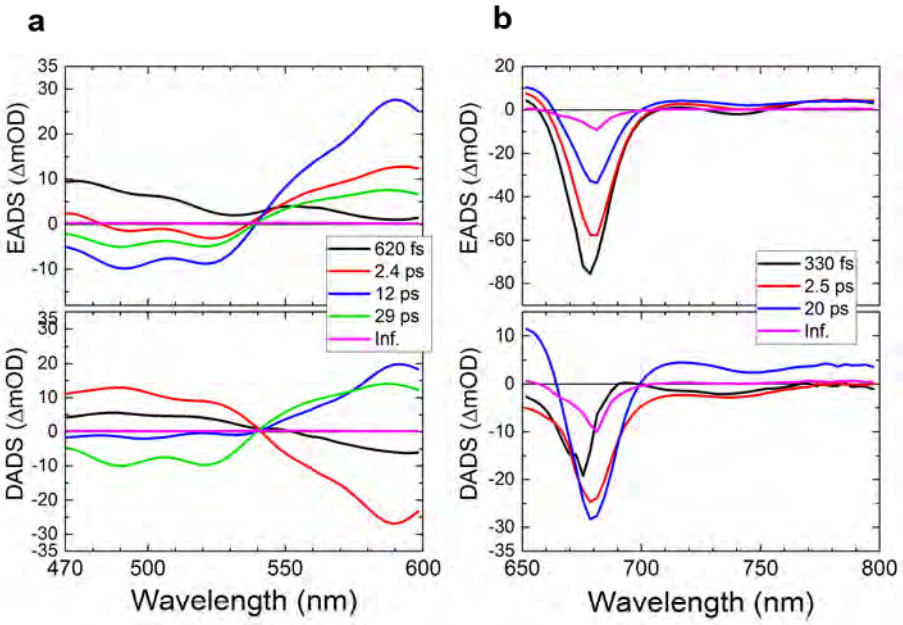

Figure 9.4. Transient absorption spectrum of HliC upon 675-nm excitation. EADS and DADS of (**a**) 470–600 nm and (**b**) 650–800 nm spectral regions.

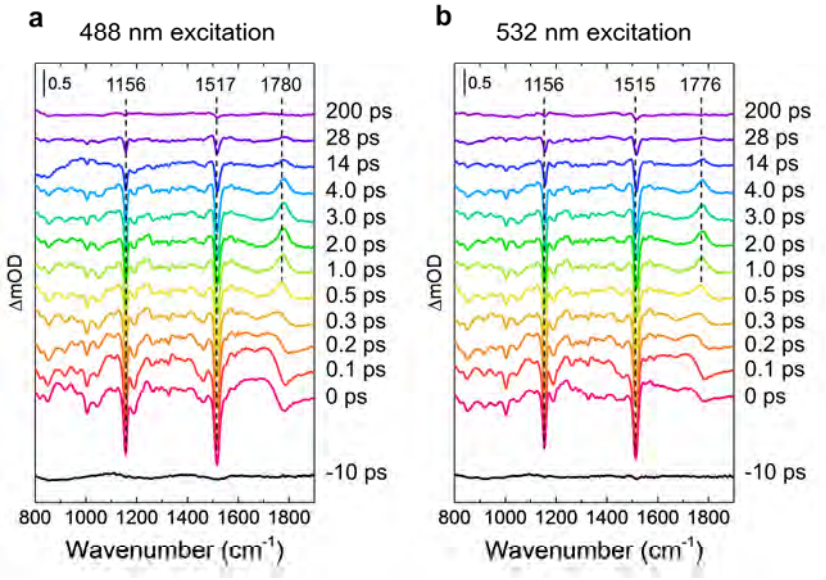

Figure 9.5. FSRS of HliC with β-car excitation. Upon excitation at (**a**) 488 nm and (**b**) 532 nm.

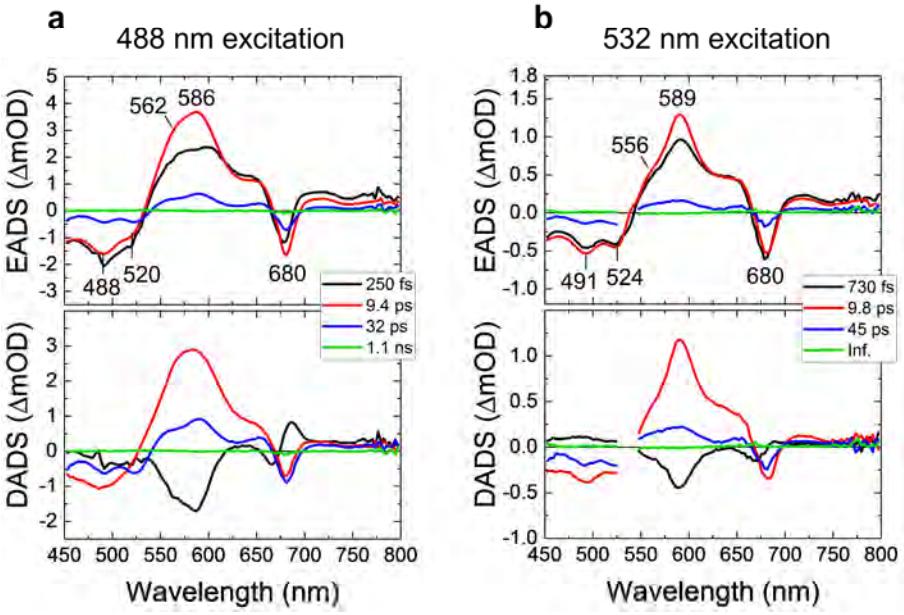

Figure 9.6. Transient absorption spectra of HliC with β-carotene excitation. Upon excitation at (**a**) 488 nm and (**b**) 532 nm. Spectral region of 524–544 nm was omitted in (**b**) because of the strong pump light scattering.

high-frequency β-carotene S_1 marker band around 1775 cm^{-1} rises in about 300 fs and upshifts with approximately the same time constant, which is assigned to ultrafast IC from the optically allowed S_2 state, followed by intramolecular vibrational cooling[136,267]. For both datasets, the β-carotene S_1 marker band decays in ~10 ps. **Fig. 9.6** shows the results of transient absorption experiments with 488 and 532 nm excitation.

Although the spectral evolution is very similar between the two datasets, significant spectral differences are observed. **Fig. 9.7** shows an overlap of the FSRS spectra at 4 ps in the C=C stretch regions of the S_0 state (panel **a**) and S_1 state (panel **b**) with excitation at 488 nm (cyan), 532 nm (green) and 675 nm (red). Strikingly, in the S_1 state (**Fig. 9.7b**) a 4 cm^{-1} difference in the band maxima is observed with 488 and 532 nm excitation, which demonstrates that the β-car_1 and β-car_2 conformers have distinct C=C stretch frequencies in the S_1 state. Note that selectivity is not 100% with either excitation wavelength[333], so the difference in S_1 state frequency of β-car_1 and β-car_2 is probably larger than 4 cm^{-1}. Smaller, but observable shifts were observed in the ground state C=C stretch manifested as the S_0 state bleaching signal (**Fig. 9.7a**).

If we now compare the FSRS data with Chl *a* excitation at 675 nm (**Fig. 9.7b**, red) with that at 488 nm excitation (**Fig. 9.7b**, cyan), we find that the former has a frequency of 1774 cm^{-1}, which is lower by 6 cm^{-1} than the latter (**Fig. 9.7b**). This observation demonstrates that the β-car_2 conformer, and not β-car_1 acts as the energy acceptor that

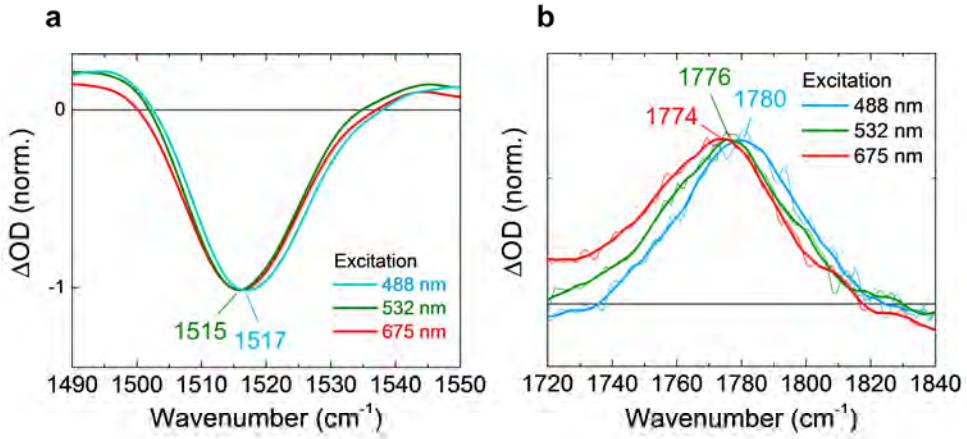

Figure 9.7. Comparison of FSRS bands of HliC at 4 ps upon excitation at different wavelengths. (**a**) The bleaches of the C=C stretch in the ground state and (**b**) the C=C stretch of the S_1 state of β-carotene. Signals upon excitation at 488, 532 and 675 nm are shown in cyan, green and red, respectively. In panel **b**, a 21 point smoothing (over 1 cm^{-1} intervals) was applied (thick lines) with Savitzky-Golay filtering. The thin lines show the watermarked data without smoothing.

quenches the excited Chl *a*. In HliC and HliD, on the basis of the linear relationship between the ground state C=C stretch frequency and effective conjugation length[338], the conjugation length of β-car$_2$ was estimated to be ~10.5, as opposed to ~9.6 for β-car$_1$[132], which would result in an up to 800 cm^{-1} (0.1 eV) energy difference between β-car$_1$ and β-car$_2$[264]. The 6 cm^{-1} shift of the C=C stretch frequency in the S_1 state observed here by FSRS corroborates this finding, though the precise relationship between the C=C stretch frequency in the S_1 state and effective conjugation has not been established yet. The S_1 C=C frequency of carotenoids is determined through the combined effects of the effective π-electron conjugation length and the vibronic coupling with the S_0 state[268]. Under the assumption that the vibronic coupling with S_0 is the same for β-car$_1$ and β-car$_2$, this result implies that the S_1 energy of β-car$_2$ indeed is lower than that of β-car$_1$. This finding implies that specific carotenoid-protein interactions induce asymmetry between the β-carotene molecules in HliC, making the β-car$_2$ the quenching site.

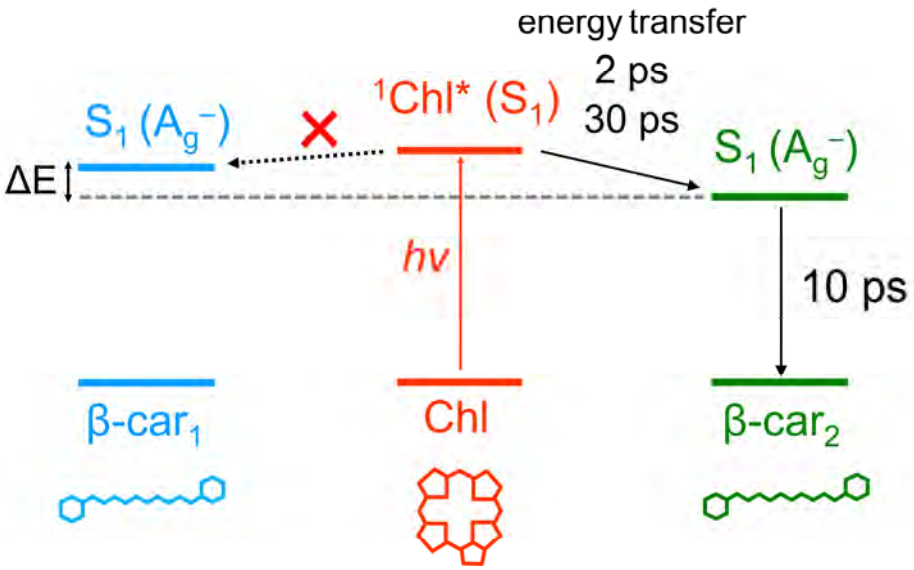

Figure 9.8. Energy transfer model of HliC upon excitation of Chl. After excitation of Chl, excited-state energy transfer occurs specifically to the lower energy β-carotene (β-car$_2$) in 2 and 30 ps. The decay of the S_1 state β-car$_2$ proceeds in 10 ps. The higher-energy β-car$_1$ is not populated because of unfavorable energetics. See text for details.

9.3. Conclusion

Fig. 9.8 summarizes our findings. Application of FSRS allowed to follow the specific vibrational mode in the S_1 state, revealing that the β-carotene S_1 energy level tuning provides a key property in creating dissipative energy transfer pathways in closely confined chlorophyll–carotenoid geometries. The carotenoid S_1 state energy is largely insensitive to environmental polarity and polarizability[264], which implies that specific pigment-protein or pigment-pigment interactions must be invoked to tune the S_1 energy. One promising avenue is provided by specific in-plane tuning of the β-carotene β-rings, which bring them in conjugation with the π-electron system of the polyene backbone, thereby lowering the overall energy levels of the electronic excited states[333]. The ramifications of these observations are very important indeed, as the same type of carotenoid molecule, β-carotene in this case, may assume a quenching and a non-quenching role in the same LHC, a mechanism that has long been hypothesized for plant LHCs[121,330,339]. Here, watermarked FSRS has revealed the vibrational signature of the β-carotene quenching state in HliC, and the technique may play an important role in elucidating quenching mechanisms in various types of LHCs that are less clear-cut and harder to assess by traditional means.

Methods

Sample preparation: The HliC protein was purified and prepared as reported previously[132]. The HliC sample at pH 6.5 in 20 mM MES buffer solution including 10 mM $CaCl_2$, 0.1% β-DM and 25% glycerol was filled in a 2-mm quartz cuvette (100-QS, Hellma Analytics) for time-resolved experiments. The sample absorbance was ~2 and ~0.4 per 2 mm at 480 nm on time-resolved Raman and transient absorption experiments, respectively. A home-built vibrating sample holder was used to avoid irradiation damage during experiments.

Baseline-free femtosecond stimulated Raman spectroscopy (FSRS): Femtosecond stimulated Raman experiments were performed with the watermarking baseline-free stimulated Raman setup reported previously. Raman pump (800 nm, ~7 μJ) and Raman probe (~840–960 nm) were spatiotemporally overlapped at the sample position with the diameter of ~100 μm. Actinic pump (675 nm, 532 or 488 nm, ~280 nJ) was focused on the sample to the diameter of ~150 μm with a time delay from -10 ps to 200 ps. A narrow-band (Δ~10 nm) interference filter was used for each excitation wavelength. In 675-nm excitation experiments, 17 time points were measured. In 532- and 488-nm excitation experiments, 25 time points were measured. The sample exposure time to the beams was ~2400 s for 675 nm excitation and ~3000 s for 532- and 488-nm excitation in total for each FSRS experiment.

Transient absorption spectroscopy: Femtosecond transient absorption measurements were performed with a pump-probe setup as reported previously[133,250]. A sapphire plate was used for supercontinuum white

light generation, and selected wavelength regions; 470–800 nm were detected by the photodiode array. The time delay was varied up to 2 ns at 95 data points with the minimum temporal step of 20 fs. The diameters of the pump and the probe beams at the sample position were ~240 μm and ~90 μm, respectively. The wavelength of the pump beam was centered at 675, 532 or 488 nm with a narrow-band (Δ~10 nm) interference filter, and the power was attenuated to ~300 nJ. The instrumental response function was ~70 fs, estimated from global analysis.

Bibliography

1. B. Alberts, "Essential cell biology", (2010).
2. E. Fernandez and R. Normann, "Introduction to Visual Prostheses", *Webvision: The Organization of the Retina and Visual System* (1995).
3. H. Kolb, "Gross Anatomy of the Eye", *Webvision: The Organization of the Retina and Visual System* (1995).
4. K. Palczewski, T. Kumasaka, T. Hori, C. A. Behnke, H. Motoshima, B. A. Fox, I. Le Trong, D. C. Teller, T. Okada, R. E. Stenkamp, M. Yamamoto and M. Miyano, "Crystal structure of rhodopsin: A G protein-coupled receptor", *Science* **289**, 739-745 (2000).
5. M. Grote, M. Engelhard and P. Hegemann, "Of ion pumps, sensors and channels - perspectives on microbial rhodopsins between science and history", *Biochim. Biophys. Acta* **1837**, 533-545 (2014).
6. F. Schneider, C. Grimm and P. Hegemann, "Biophysics of Channelrhodopsin", *Annu Rev Biophys* **44**, 167-186 (2015).
7. O. P. Ernst, D. T. Lodowski, M. Elstner, P. Hegemann, L. S. Brown and H. Kandori, "Microbial and animal rhodopsins: structures, functions, and molecular mechanisms", *Chem. Rev.* **114**, 126-163 (2014).
8. H. E. Kato, K. Inoue, H. Kandori and O. Nureki, "The light-driven sodium ion pump: A new player in rhodopsin research", *Bioessays* **38**, 1274-1282 (2016).
9. J. M. Christie, J. Gawthorne, G. Young, N. J. Fraser and A. J. Roe, "LOV to BLUF: flavoprotein contributions to the optogenetic toolkit", *Mol. Plant* **5**, 533-544 (2012).
10. N. C. Rockwell, Y. S. Su and J. C. Lagarias, "Phytochrome structure and signaling mechanisms", *Annu. Rev. Plant Biol.* **57**, 837-858 (2006).
11. Y. Shichida and T. Matsuyama, "Evolution of opsins and phototransduction", *Philos. Trans. R. Soc. Lond. B Biol. Sci.* **364**, 2881-2895 (2009).
12. A. A. Kondratova and R. V. Kondratov, "The circadian clock and pathology of the ageing brain", *Nat. Rev. Neurosci.* **13**, 325-335 (2012).
13. P. Hegemann and G. Nagel, "From channelrhodopsins to optogenetics", *EMBO Mol. Med.* **5**, 173-176 (2013).
14. Z. F. Liu, H. C. Yan, K. B. Wang, T. Y. Kuang, J. P. Zhang, L. L. Gui, X. M. An and W. R. Chang, "Crystal structure of spinach major light-harvesting complex at 2.72 angstrom resolution", *Nature* **428**, 287-292 (2004).
15. A. S. Halavaty and K. Moffat, "N- and C-terminal flanking regions modulate light-induced signal transduction in the LOV2 domain of the blue light sensor phototropin 1 from Avena sativa", *Biochemistry* **46**, 14001-14009 (2007).
16. H. E. Kato, F. Zhang, O. Yizhar, C. Ramakrishnan, T. Nishizawa, K. Hirata, J. Ito, Y. Aita, T. Tsukazaki, S. Hayashi, P. Hegemann, A. D. Maturana, R. Ishitani, K. Deisseroth and O. Nureki, "Crystal structure of the channelrhodopsin light-gated cation channel", *Nature* **482**, 369-374 (2012).
17. M. A. Van der Horst and K. J. Hellingwerf, "Photoreceptor proteins, "star actors of modern times": A review of the functional dynamics in the structure of representative members of six different photoreceptor families", *Accounts Chem. Res.* **37**, 13-20 (2004).
18. D. M. Shcherbakova, A. A. Shemetov, A. A. Kaberniuk and V. V. Verkhusha, "Natural photoreceptors as a source of fluorescent proteins, biosensors, and optogenetic tools", *Annu. Rev. Biochem.* **84**, 519-550 (2015).
19. J. T. Kennis and T. Mathes, "Molecular eyes: proteins that transform light into biological information", *Interface Focus* **3**, 20130005 (2013).
20. T. Ishizuka, A. Kamiya, H. Suzuki, R. Narikawa, T. Noguchi, T. Kohchi, K. Inomata and M. Ikeuchi, "The Cyanobacteriochrome, TePixJ, Isomerizes Its Own Chromophore by Converting Phycocyanobilin to Phycoviolobilin", *Biochemistry* **50**, 953-961 (2011).

21. A. R. Grossman, M. R. Schaefer, G. G. Chiang and J. L. Collier, "The phycobilisome, a light-harvesting complex responsive to environmental conditions", *Microbiol. Rev.* **57**, 725-749 (1993).
22. M. Chalfie, Y. Tu, G. Euskirchen, W. W. Ward and D. C. Prasher, "Green Fluorescent Protein as a Marker for Gene-Expression", *Science* **263**, 802-805 (1994).
23. R. M. Hoffman, "The multiple uses of fluorescent proteins to visualize cancer in vivo", *Nat. Rev. Cancer* **5**, 796-806 (2005).
24. N. C. Shaner, P. A. Steinbach and R. Y. Tsien, "A guide to choosing fluorescent proteins", *Nat. Methods* **2**, 905-909 (2005).
25. K. G. Chernov, T. A. Redchuk, E. S. Omelina and V. V. Verkhushaa, "Near-Infrared Fluorescent Proteins, Biosensors, and Optogenetic Tools Engineered from Phytochromes", *Chem. Rev.* **117**, 6423-6446 (2017).
26. K. Deisseroth, "Optogenetics", *Nat. Methods* **8**, 26-29 (2011).
27. F. Zhang, J. Vierock, O. Yizhar, L. E. Fenno, S. Tsunoda, A. Kianianmomeni, M. Prigge, A. Berndt, J. Cushman, J. Polle, J. Magnuson, P. Hegemann and K. Deisseroth, "The microbial opsin family of optogenetic tools", *Cell* **147**, 1446-1457 (2011).
28. L. Fenno, O. Yizhar and K. Deisseroth, "The development and application of optogenetics", *Annu. Rev. Neurosci.* **34**, 389-412 (2011).
29. S. Masuda, "Light detection and signal transduction in the BLUF photoreceptors", *Plant Cell Physiol.* **54**, 171-179 (2013).
30. C. Cosentino, L. Alberio, S. Gazzarrini, M. Aquila, E. Romano, S. Cermenati, P. Zuccolini, J. Petersen, M. Beltrame, J. L. Van Etten, J. M. Christie, G. Thiel and A. Moroni, "Engineering of a light-gated potassium channel", *Science* **348**, 707-710 (2015).
31. S. Gao, J. Nagpal, M. W. Schneider, V. Kozjak-Pavlovic, G. Nagel and A. Gottschalk, "Optogenetic manipulation of cGMP in cells and animals by the tightly light-regulated guanylyl-cyclase opsin CyclOp", *Nat. Commun.* **6**, 8046 (2015).
32. H. Murakoshi, M. E. Shin, P. Parra-Bueno, E. M. Szatmari, A. C. E. Shibata and R. Yasuda, "Kinetics of Endogenous CaMKII Required for Synaptic Plasticity Revealed by Optogenetic Kinase Inhibitor", *Neuron* **94**, 37-+ (2017).
33. M. Ormo, A. B. Cubitt, K. Kallio, L. A. Gross, R. Y. Tsien and S. J. Remington, "Crystal structure of the Aequorea victoria green fluorescent protein", *Science* **273**, 1392-1395 (1996).
34. M. Prigge, F. Schneider, S. P. Tsunoda, C. Shilyansky, J. Wietek, K. Deisseroth and P. Hegemann, "Color-tuned channelrhodopsins for multiwavelength optogenetics", *J. Biol. Chem.* **287**, 31804-31812 (2012).
35. K. Inoue, T. Tsukamoto, K. Shimono, Y. Suzuki, S. Miyauchi, S. Hayashi, H. Kandori and Y. Sudo, "Converting a Light-Driven Proton Pump into a Light-Gated Proton Channel", *J. Am. Chem. Soc.* **137**, 3291-3299 (2015).
36. A. Dawydow, R. Gueta, D. Ljaschenko, S. Ullrich, M. Hermann, N. Ehmann, S. Gao, A. Fiala, T. Langenhan, G. Nagel and R. J. Kittel, "Channelrhodopsin-2-XXL, a powerful optogenetic tool for low-light applications", *Proc. Natl. Acad. Sci. U. S. A.* **111**, 13972-13977 (2014).
37. L. A. Gunaydin, O. Yizhar, A. Berndt, V. S. Sohal, K. Deisseroth and P. Hegemann, "Ultrafast optogenetic control", *Nat. Neurosci.* **13**, 387-392 (2010).
38. T. Mathes, M. Heilmann, A. Pandit, J. Zhu, J. Ravensbergen, M. Kloz, Y. Fu, B. O. Smith, J. M. Christie, G. I. Jenkins and J. T. Kennis, "Proton-Coupled Electron Transfer Constitutes the Photoactivation Mechanism of the Plant Photoreceptor UVR8", *J. Am. Chem. Soc.* **137**, 8113-8120 (2015).
39. T. Mathes, J. Ravensbergen, M. Kloz, T. Gleichmann, K. D. Gallagher, N. C. Woitowich, R. St Peter, S. E. Kovaleva, E. A. Stojkovic and J. T. Kennis, "Femto- to Microsecond Photodynamics of an Unusual Bacteriophytochrome", *J. Phys. Chem. Lett.* **6**, 239-243 (2015).
40. Y. Hontani, M. Broser, A. Silapetere, B. S. Krause, P. Hegemann and J. T. M. Kennis, "The femtosecond-to-second photochemistry of red-shifted fast-closing anion channelrhodopsin PsACR1", *Phys. Chem. Chem. Phys.* **19**, 30402-30409 (2017).

41. Y. Hontani, K. Inoue, M. Kloz, Y. Kato, H. Kandori and J. T. Kennis, "The photochemistry of sodium ion pump rhodopsin observed by watermarked femto- to submillisecond stimulated Raman spectroscopy", *Phys. Chem. Chem. Phys.* **18**, 24729-24736 (2016).
42. Y. Hontani, M. Marazzi, K. Stehfest, T. Mathes, I. H. M. van Stokkum, M. Elstner, P. Hegemann and J. T. M. Kennis, "Reaction dynamics of the chimeric channelrhodopsin C1C2", *Sci. Rep.* **7**, 7217 (2017).
43. P. E. Konold, T. Mathes, J. Weissenhorn, M. L. Groot, P. Hegemann and J. T. M. Kennis, "Unfolding of the C-Terminal J alpha Helix in the LOV2 Photoreceptor Domain Observed by Time-Resolved Vibrational Spectroscopy", *J. Phys. Chem. Lett.* **7**, 3472-3476 (2016).
44. J. Zhu, T. Mathes, Y. Hontani, M. T. Alexandre, K. C. Toh, P. Hegemann and J. T. Kennis, "Photoadduct Formation from the FMN Singlet Excited State in the LOV2 Domain of Chlamydomonas reinhardtii Phototropin", *J. Phys. Chem. Lett.* **7**, 4380-4384 (2016).
45. R. Brust, A. Lukacs, A. Haigney, K. Addison, A. Gil, M. Towrie, I. P. Clark, G. M. Greetham, P. J. Tonge and S. R. Meech, "Proteins in action: femtosecond to millisecond structural dynamics of a photoactive flavoprotein", *J. Am. Chem. Soc.* **135**, 16168-16174 (2013).
46. A. A. Gil, S. P. Laptenok, J. B. French, J. N. Iuliano, A. Lukacs, C. R. Hall, I. V. Sazanovich, G. M. Greetham, A. Bacher, B. Illarionov, M. Fischer, P. J. Tonge and S. R. Meech, "Femtosecond to Millisecond Dynamics of Light Induced Allostery in the Avena sativa LOV Domain", *J. Phys. Chem. B* **121**, 1010-1019 (2017).
47. A. K. Sharma, J. L. Spudich and W. F. Doolittle, "Microbial rhodopsins: functional versatility and genetic mobility", *Trends Microbiol.* **14**, 463-469 (2006).
48. J. L. Spudich, C. S. Yang, K. H. Jung and E. N. Spudich, "Retinylidene proteins: structures and functions from archaea to humans", *Annu. Rev. Cell Dev. Biol.* **16**, 365-392 (2000).
49. A. Terakita, "The opsins", *Genome Biol.* **6**, (2005).
50. E. G. Govorunova, O. A. Sineshchekov, H. Li and J. L. Spudich, "Microbial Rhodopsins: Diversity, Mechanisms, and Optogenetic Applications", *Annu. Rev. Biochem.* **86**, 845-872 (2017).
51. H. Belrhali, P. Nollert, A. Royant, C. Menzel, J. P. Rosenbusch, E. M. Landau and E. Pebay-Peyroula, "Protein, lipid and water organization in bacteriorhodopsin crystals: a molecular view of the purple membrana at 1.9 angstrom resolution", *Structure* **7**, 909-917 (1999).
52. G. Nagel, D. Ollig, M. Fuhrmann, S. Kateriya, A. M. Musti, E. Bamberg and P. Hegemann, "Channelrhodopsin-1: a light-gated proton channel in green algae", *Science* **296**, 2395-2398 (2002).
53. G. Nagel, T. Szellas, W. Huhn, S. Kateriya, N. Adeishvili, P. Berthold, D. Ollig, P. Hegemann and E. Bamberg, "Channelrhodopsin-2, a directly light-gated cation-selective membrane channel", *Proc. Natl. Acad. Sci. U. S. A.* **100**, 13940-13945 (2003).
54. E. G. Govorunova, O. A. Sineshchekov, R. Janz, X. Liu and J. L. Spudich, "NEUROSCIENCE. Natural light-gated anion channels: A family of microbial rhodopsins for advanced optogenetics", *Science* **349**, 647-650 (2015).
55. J. Wietek, M. Broser, B. S. Krause and P. Hegemann, "Identification of a Natural Green Light Absorbing Chloride Conducting Channelrhodopsin from Proteomonas sulcata", *J. Biol. Chem.* **291**, 4121-4127 (2016).
56. E. G. Govorunova, O. A. Sineshchekov and J. L. Spudich, "Proteomonas sulcata ACR1: A Fast Anion Channelrhodopsin", *Photochem. Photobiol.* **92**, 257-263 (2016).
57. E. G. Govorunova, O. A. Sineshchekov, E. M. Rodarte, R. Janz, O. Morelle, M. Melkonian, G. K. Wong and J. L. Spudich, "The Expanding Family of Natural Anion Channelrhodopsins Reveals Large Variations in Kinetics, Conductance, and Spectral Sensitivity", *Sci. Rep.* **7**, 43358 (2017).
58. F. Mohammad, J. C. Stewart, S. Ott, K. Chlebikova, J. Y. Chua, T. W. Koh, J. Ho and A. Claridge-Chang, "Optogenetic inhibition of behavior with anion channelrhodopsins", *Nat. Methods* **14**, 271-274 (2017).
59. D. Oesterhelt and W. Stoeckenius, "Rhodopsin-like protein from the purple membrane of Halobacterium halobium", *Nat. New Biol.* **233**, 149-152 (1971).

60. Y. Mukohata, Y. Sugiyama, K. Ihara and M. Yoshida, "An Australian halobacterium contains a novel proton pump retinal protein: archaerhodopsin", *Biochem. Biophys. Res. Commun.* **151**, 1339-1345 (1988).
61. O. Beja, E. N. Spudich, J. L. Spudich, M. Leclerc and E. F. DeLong, "Proteorhodopsin phototrophy in the ocean", *Nature* **411**, 786-789 (2001).
62. K. Inoue, H. Ono, R. Abe-Yoshizumi, S. Yoshizawa, H. Ito, K. Kogure and H. Kandori, "A light-driven sodium ion pump in marine bacteria", *Nat. Commun.* **4**, 1678- (2013).
63. B. Schobert and J. K. Lanyi, "Halorhodopsin is a light-driven chloride pump", *J. Biol. Chem.* **257**, 10306-10313 (1982).
64. G. M. Avelar, R. I. Schumacher, P. A. Zaini, G. Leonard, T. A. Richards and S. L. Gomes, "A rhodopsin-guanylyl cyclase gene fusion functions in visual perception in a fungus", *Curr. Biol.* **24**, 1234-1240 (2014).
65. M. Luck, T. Mathes, S. Bruun, R. Fudim, R. Hagedorn, T. M. Tran Nguyen, S. Kateriya, J. T. Kennis, P. Hildebrandt and P. Hegemann, "A photochromic histidine kinase rhodopsin (HKR1) that is bimodally switched by ultraviolet and blue light", *J. Biol. Chem.* **287**, 40083-40090 (2012).
66. H. E. Kato, K. Inoue, R. Abe-Yoshizumi, Y. Kato, H. Ono, M. Konno, S. Hososhima, T. Ishizuka, M. R. Hoque, H. Kunitomo, J. Ito, S. Yoshizawa, K. Yamashita, M. Takemoto, T. Nishizawa, R. Taniguchi, K. Kogure, A. D. Maturana, Y. Iino, H. Yawo, R. Ishitani, H. Kandori and O. Nureki, "Structural basis for Na(+) transport mechanism by a light-driven Na(+) pump", *Nature* **521**, 48-53 (2015).
67. O. Shimomura, F. H. Johnson and Y. Saiga, "Extraction, purification and properties of aequorin, a bioluminescent protein from the luminous hydromedusan, Aequorea", *J. Cell. Comp. Physiol.* **59**, 223-239 (1962).
68. N. C. Shaner, R. E. Campbell, P. A. Steinbach, B. N. Giepmans, A. E. Palmer and R. Y. Tsien, "Improved monomeric red, orange and yellow fluorescent proteins derived from Discosoma sp. red fluorescent protein", *Nat. Biotechnol.* **22**, 1567-1572 (2004).
69. V. V. Verkhusha and K. A. Lukyanov, "The molecular properties and applications of Anthozoa fluorescent proteins and chromoproteins", *Nat. Biotechnol.* **22**, 289-296 (2004).
70. R. Hein and R. Y. Tsien, "Engineering green fluorescent protein for improved brightness, longer wavelengths and fluorescence resonance energy transfer", *Curr. Biol.* **6**, 178-182 (1996).
71. F. Helmchen and W. Denk, "Deep tissue two-photon microscopy", *Nat. Methods* **2**, 932-940 (2005).
72. N. G. Horton, K. Wang, D. Kobat, C. G. Clark, F. W. Wise, C. B. Schaffer and C. Xu, "In vivo three-photon microscopy of subcortical structures within an intact mouse brain", *Nature Photonics* **7**, 205-209 (2013).
73. E. A. Jares-Erijman and T. M. Jovin, "FRET imaging", *Nat. Biotechnol.* **21**, 1387-1395 (2003).
74. K. D. Piatkevich, F. V. Subach and V. V. Verkhusha, "Engineering of bacterial phytochromes for near-infrared imaging, sensing, and light-control in mammals", *Chem. Soc. Rev.* **42**, 3441-3452 (2013).
75. R. Weissleder and V. Ntziachristos, "Shedding light onto live molecular targets", *Nat. Med.* **9**, 123-128 (2003).
76. K. S. Morozova, K. D. Piatkevich, T. J. Gould, J. Zhang, J. Bewersdorf and V. V. Verkhusha, "Far-red fluorescent protein excitable with red lasers for flow cytometry and superresolution STED nanoscopy", *Biophys. J.* **99**, L13-15 (2010).
77. M. Drobizhev, S. Tillo, N. S. Makarov, T. E. Hughes and A. Rebane, "Color hues in red fluorescent proteins are due to internal quadratic Stark effect", *J. Phys. Chem. B* **113**, 12860-12864 (2009).
78. K. D. Piatkevich, V. N. Malashkevich, K. S. Morozova, N. A. Nemkovich, S. C. Almo and V. V. Verkhusha, "Extended Stokes shift in fluorescent proteins: chromophore-protein interactions in a near-infrared TagRFP675 variant", *Sci. Rep.* **3**, 1847 (2013).
79. D. M. Shcherbakova, M. Baloban, A. V. Emelyanov, M. Brenowitz, P. Guo and V. V. Verkhusha, "Bright monomeric near-infrared fluorescent proteins as tags and biosensors for multiscale imaging", *Nat. Commun.* **7**, 12405 (2016).

80. D. M. Shcherbakova and V. V. Verkhusha, "Near-infrared fluorescent proteins for multicolor in vivo imaging", *Nat. Methods.* **10**, 751-754 (2013).
81. D. M. Shcherbakova, M. Baloban, S. Pletnev, V. N. Malashkevich, H. Xiao, Z. Dauter and V. V. Verkhusha, "Molecular Basis of Spectral Diversity in Near-Infrared Phytochrome-Based Fluorescent Proteins", *Chem. Biol.* **22**, 1540-1551 (2015).
82. L. H. Otero, S. Klinke, J. Rinaldi, F. Velazquez-Escobar, M. A. Mroginski, M. Fernandez Lopez, F. Malamud, A. A. Vojnov, P. Hildebrandt, F. A. Goldbaum and H. R. Bonomi, "Structure of the Full-Length Bacteriophytochrome from the Plant Pathogen Xanthomonas campestris Provides Clues to its Long-Range Signaling Mechanism", *J. Mol. Biol.* **428**, 3702-3720 (2016).
83. G. S. Filonov, K. D. Piatkevich, L. M. Ting, J. Zhang, K. Kim and V. V. Verkhusha, "Bright and stable near-infrared fluorescent protein for in vivo imaging", *Nat. Biotechnol.* **29**, 757-761 (2011).
84. D. M. Shcherbakova, M. Baloban and V. V. Verkhusha, "Near-infrared fluorescent proteins engineered from bacterial phytochromes", *Curr. Opin. Chem. Biol.* **27**, 52-63 (2015).
85. M. E. Auldridge and K. T. Forest, "Bacterial phytochromes: More than meets the light", *Crit. Rev. Biochem. Mol.* **46**, 67-88 (2011).
86. X. K. Shu, A. Royant, M. Z. Lin, T. A. Aguilera, V. Lev-Ram, P. A. Steinbach and R. Y. Tsien, "Mammalian Expression of Infrared Fluorescent Proteins Engineered from a Bacterial Phytochrome", *Science* **324**, 804-807 (2009).
87. H. Takala, A. Bjorling, O. Berntsson, H. Lehtivuori, S. Niebling, M. Hoernke, I. Kosheleva, R. Henning, A. Menzel, J. A. Ihalainen and S. Westenhoff, "Signal amplification and transduction in phytochrome photosensors", *Nature* **509**, 245-248 (2014).
88. K. C. Toh, E. A. Stojkovic, I. H. van Stokkum, K. Moffat and J. T. Kennis, "Proton-transfer and hydrogen-bond interactions determine fluorescence quantum yield and photochemical efficiency of bacteriophytochrome", *Proc. Natl. Acad. Sci. U. S. A.* **107**, 9170-9175 (2010).
89. K. C. Toh, E. A. Stojkovic, I. H. van Stokkum, K. Moffat and J. T. Kennis, "Fluorescence quantum yield and photochemistry of bacteriophytochrome constructs", *Phys. Chem. Chem. Phys.* **13**, 11985-11997 (2011).
90. M. Gomelsky and G. Klug, "BLUF: a novel FAD-binding domain involved in sensory transduction in microorganisms", *Trends Biochem. Sci.* **27**, 497-500 (2002).
91. S. Masuda and C. E. Bauer, "AppA is a blue light photoreceptor that antirepresses photosynthesis gene expression in Rhodobacter sphaeroides", *Cell* **110**, 613-623 (2002).
92. S. Braatsch and G. Klug, "Blue light perception in bacteria", *Photosynth Res* **79**, 45-57 (2004).
93. M. Iseki, S. Matsunaga, A. Murakami, K. Ohno, K. Shiga, K. Yoshida, M. Sugai, T. Takahashi, T. Hori and M. Watanabe, "A blue-light-activated adenylyl cyclase mediates photoavoidance in Euglena gracilis", *Nature* **415**, 1047-1051 (2002).
94. S. Rajagopal, J. M. Key, E. B. Purcell, D. J. Boerema and K. Moffat, "Purification and initial characterization of a putative blue light-regulated phosphodiesterase from Escherichia coli", *Photochem. Photobiol.* **80**, 542-547 (2004).
95. M. Stierl, P. Stumpf, D. Udwari, R. Gueta, R. Hagedorn, A. Losi, W. Gartner, L. Petereit, M. Efetova, M. Schwarzel, T. G. Oertner, G. Nagel and P. Hegemann, "Light modulation of cellular cAMP by a small bacterial photoactivated adenylyl cyclase, bPAC, of the soil bacterium Beggiatoa", *J. Biol. Chem.* **286**, 1181-1188 (2011).
96. S. Schroder-Lang, M. Schwarzel, R. Seifert, T. Strunker, S. Kateriya, J. Looser, M. Watanabe, U. B. Kaupp, P. Hegemann and G. Nagel, "Fast manipulation of cellular cAMP level by light in vivo", *Nat. Methods* **4**, 39-42 (2007).
97. C. Bonetti, M. Stierl, T. Mathes, I. H. van Stokkum, K. M. Mullen, T. A. Cohen-Stuart, R. van Grondelle, P. Hegemann and J. T. Kennis, "The role of key amino acids in the photoactivation pathway of the Synechocystis Slr1694 BLUF domain", *Biochemistry* **48**, 11458-11469 (2009).

98. J. Mehlhorn, T. Lindtner, F. Richter, K. Glass, S. Beck, P. Hegemann, J. T. M. Kennis and T. Mathes, "Light-Induced Rearrangement of the beta 5 Strand in the BLUF Photoreceptor SyPixD (Slr1694)", *J. Phys. Chem. Lett.* **6**, 4749-4753 (2015).
99. S. Masuda, K. Hasegawa, A. Ishii and T. Ono, "Light-induced structural changes in a putative blue-light receptor with a novel FAD binding fold sensor of blue-light using FAD (BLUF); Slr1694 of Synechocystis sp PCC6803", *Biochemistry* **43**, 5304-5313 (2004).
100. T. Mathes, J. Y. Zhu, I. H. M. van Stokkum, M. L. Groot, P. Hegemann and J. T. M. Kennis, "Hydrogen Bond Switching among Flavin and Amino Acids Determines the Nature of Proton-Coupled Electron Transfer in BLUF Photoreceptors", *J. Phys. Chem. Lett.* **3**, 203-208 (2012).
101. M. Gauden, I. H. van Stokkum, J. M. Key, DCh Luhrs, R. van Grondelle, P. Hegemann and J. T. Kennis, "Hydrogen-bond switching through a radical pair mechanism in a flavin-binding photoreceptor", *Proc. Natl. Acad. Sci. U. S. A.* **103**, 10895-10900 (2006).
102. T. Mathes, I. H. van Stokkum, M. Stierl and J. T. Kennis, "Redox modulation of flavin and tyrosine determines photoinduced proton-coupled electron transfer and photoactivation of BLUF photoreceptors", *J. Biol. Chem.* **287**, 31725-31738 (2012).
103. A. Kita, K. Okajima, Y. Morimoto, M. Ikeuchi and K. Miki, "Structure of a cyanobacterial BLUF protein, Tll0078, containing a novel FAD-binding blue light sensor domain", *J. Mol. Biol.* **349**, 1-9 (2005).
104. S. Anderson, V. Dragnea, S. Masuda, J. Ybe, K. Moffat and C. Bauer, "Structure of a novel photoreceptor, the BLUF domain of AppA from Rhodobacter sphaeroides", *Biochemistry* **44**, 7998-8005 (2005).
105. H. Yuan, S. Anderson, S. Masuda, V. Dragnea, K. Moffat and C. Bauer, "Crystal structures of the Synechocystis photoreceptor Slr1694 reveal distinct structural states related to signaling", *Biochemistry* **45**, 12687-12694 (2006).
106. A. Jung, J. Reinstein, T. Domratcheva, R. L. Shoeman and I. Schlichting, "Crystal structures of the AppA BLUF domain photoreceptor provide insights into blue light-mediated signal transduction", *J. Mol. Biol.* **362**, 717-732 (2006).
107. J. S. Grinstead, M. Avila-Perez, K. J. Hellingwerf, R. Boelens and R. Kaptein, "Light-induced flipping of a conserved glutamine sidechain and its orientation in the AppA BLUF domain", *J. Am. Chem. Soc.* **128**, 15066-15067 (2006).
108. J. S. Grinstead, S. T. Hsu, W. Laan, A. M. Bonvin, K. J. Hellingwerf, R. Boelens and R. Kaptein, "The solution structure of the AppA BLUF domain: insight into the mechanism of light-induced signaling", *Chembiochem* **7**, 187-193 (2006).
109. Q. Wu, W. H. Ko and K. H. Gardner, "Structural requirements for key residues and auxiliary portions of a BLUF domain", *Biochemistry* **47**, 10271-10280 (2008).
110. Q. Wu and K. H. Gardner, "Structure and Insight into Blue Light-Induced Changes in the BlrP1 BLUF Domain", *Biochemistry* **48**, 2620-2629 (2009).
111. T. Domratcheva, E. Hartmann, I. Schlichting and T. Kottke, "Evidence for Tautomerisation of Glutamine in BLUF Blue Light Receptors by Vibrational Spectroscopy and Computational Chemistry", *Sci. Rep.* **6**, 22669 (2016).
112. M. Unno, S. Masuda, T. A. Ono and S. Yamauchi, "Orientation of a key glutamine residue in the BLUF domain from AppA revealed by mutagenesis, spectroscopy, and quantum chemical calculations", *J. Am. Chem. Soc.* **128**, 5638-5639 (2006).
113. T. Iwata, A. Watanabe, M. Iseki, M. Watanabe and H. Kandori, "Strong Donation of the Hydrogen Bond of Tyrosine during Photoactivation of the BLUF Domain", *J. Phys. Chem. Lett.* **2**, 1015-1019 (2011).
114. T. Domratcheva, B. L. Grigorenko, I. Schlichting and A. V. Nemukhin, "Molecular models predict light-induced glutamine tautomerization in BLUF photoreceptors", *Biophys. J.* **94**, 3872-3879 (2008).
115. K. Sadeghian, M. Bocola and M. Schutz, "A QM/MM study on the fast photocycle of blue light using flavin photoreceptors in their light-adapted/active form", *Phys. Chem. Chem. Phys.* **12**, 8840-8846 (2010).

116. P. Goyal and S. Hammes-Schiffer, "Role of active site conformational changes in photocycle activation of the AppA BLUF photoreceptor", *Proc. Natl. Acad. Sci. U.S.A.* **114**, 1480-1485 (2017).
117. K. C. Toh, I. H. van Stokkum, J. Hendriks, M. T. Alexandre, J. C. Arents, M. A. Perez, R. van Grondelle, K. J. Hellingwerf and J. T. Kennis, "On the signaling mechanism and the absence of photoreversibility in the AppA BLUF domain", *Biophys. J.* **95**, 312-321 (2008).
118. C. Bonetti, T. Mathes, I. H. van Stokkum, K. M. Mullen, M. L. Groot, R. van Grondelle, P. Hegemann and J. T. Kennis, "Hydrogen bond switching among flavin and amino acid side chains in the BLUF photoreceptor observed by ultrafast infrared spectroscopy", *Biophys. J.* **95**, 4790-4802 (2008).
119. A. Lukacs, A. Haigney, R. Brust, R. K. Zhao, A. L. Stelling, I. P. Clark, M. Towrie, G. M. Greetham, S. R. Meech and P. J. Tonge, "Photoexcitation of the blue light using FAD photoreceptor AppA results in ultrafast changes to the protein matrix", *J. Am. Chem. Soc.* **133**, 16893-16900 (2011).
120. R. Croce and H. van Amerongen, "Natural strategies for photosynthetic light harvesting", *Nat. Chem. Biol.* **10**, 492-501 (2014).
121. A. V. Ruban, R. Berera, C. Ilioaia, I. H. van Stokkum, J. T. Kennis, A. A. Pascal, H. van Amerongen, B. Robert, P. Horton and R. van Grondelle, "Identification of a mechanism of photoprotective energy dissipation in higher plants", *Nature* **450**, 575-578 (2007).
122. H. Staleva, J. Komenda, M. K. Shukla, V. Slouf, R. Kana, T. Polivka and R. Sobotka, "Mechanism of photoprotection in the cyanobacterial ancestor of plant antenna proteins", *Nat. Chem. Biol.* **11**, 287-291 (2015).
123. R. Berera, C. Herrero, I. H. van Stokkum, M. Vengris, G. Kodis, R. E. Palacios, H. van Amerongen, R. van Grondelle, D. Gust, T. A. Moore, A. L. Moore and J. T. Kennis, "A simple artificial light-harvesting dyad as a model for excess energy dissipation in oxygenic photosynthesis", *Proc. Natl. Acad. Sci. U. S. A.* **103**, 5343-5348 (2006).
124. R. Berera, R. van Grondelle and J. T. Kennis, "Ultrafast transient absorption spectroscopy: principles and application to photosynthetic systems", *Photosynth. Res.* **101**, 105-118 (2009).
125. N. Liguori, P. Xu, I. H. M. van Stokkum, B. van Oort, Y. Lu, D. Karcher, R. Bock and R. Croce, "Different carotenoid conformations have distinct functions in light-harvesting regulation in plants", *Nat. Commun.* **8**, 1994 (2017).
126. N. E. Holt, D. Zigmantas, L. Valkunas, X. P. Li, K. K. Niyogi and G. R. Fleming, "Carotenoid cation formation and the regulation of photosynthetic light harvesting", *Science* **307**, 433-436 (2005).
127. T. K. Ahn, T. J. Avenson, M. Ballottari, Y. C. Cheng, K. K. Niyogi, R. Bassi and G. R. Fleming, "Architecture of a charge-transfer state regulating light harvesting in a plant antenna protein", *Science* **320**, 794-797 (2008).
128. S. Park, A. L. Fischer, Z. Li, R. Bassi, K. K. Niyogi and G. R. Fleming, "Snapshot Transient Absorption Spectroscopy of Carotenoid Radical Cations in High-Light-Acclimating Thylakoid Membranes", *J. Phys. Chem. Lett.* **8**, 5548-5554 (2017).
129. S. Bode, C. C. Quentmeier, P. N. Liao, N. Hafi, T. Barros, L. Wilk, F. Bittner and P. J. Walla, "On the regulation of photosynthesis by excitonic interactions between carotenoids and chlorophylls", *Proc. Natl. Acad. Sci. U. S. A.* **106**, 12311-12316 (2009).
130. M. Kloz, S. Pillai, G. Kodis, D. Gust, T. A. Moore, A. L. Moore, R. van Grondelle and J. T. Kennis, "Carotenoid photoprotection in artificial photosynthetic antennas", *J. Am. Chem. Soc.* **133**, 7007-7015 (2011).
131. M. G. Muller, P. Lambrev, M. Reus, E. Wientjes, R. Croce and A. R. Holzwarth, "Singlet Energy Dissipation in the Photosystem II Light-Harvesting Complex Does Not Involve Energy Transfer to Carotenoids", *Chemphyschem* **11**, 1289-1296 (2010).
132. M. K. Shukla, M. J. Llansola-Portoles, M. Tichy, A. A. Pascal, B. Robert and R. Sobotka, "Binding of pigments to the cyanobacterial high-light-inducible protein HliC", *Photosynth. Res.* (2017).

133. J. Ravensbergen, F. F. Abdi, J. H. van Santen, R. N. Frese, B. Dam, R. van de Krol and J. T. M. Kennis, "Unraveling the Carrier Dynamics of BiVO4: A Femtosecond to Microsecond Transient Absorption Study", *J. Phys. Chem. C* **118**, 27793-27800 (2014).
134. M. T. Alexandre, T. Domratcheva, C. Bonetti, L. J. van Wilderen, R. van Grondelle, M. L. Groot, K. J. Hellingwerf and J. T. Kennis, "Primary reactions of the LOV2 domain of phototropin studied with ultrafast mid-infrared spectroscopy and quantum chemistry", *Biophys. J.* **97**, 227-237 (2009).
135. P. Kukura, D. W. McCamant and R. A. Mathies, "Femtosecond stimulated Raman spectroscopy", *Annu. Rev. Phys. Chem.* **58**, 461-488 (2007).
136. M. Kloz, J. Weissenborn, T. Polivka, H. A. Frank and J. T. M. Kennis, "Spectral watermarking in femtosecond stimulated Raman spectroscopy: resolving the nature of the carotenoid S-star state", *Phys. Chem. Chem. Phys.* **18**, 14619-14628 (2016).
137. M. Kloz, R. van Grondelle and J. T. Kennis, "Wavelength-modulated femtosecond stimulated Raman spectroscopy-approach towards automatic data processing", *Phys. Chem. Chem. Phys.* **13**, 18123-18133 (2011).
138. B. Gobets, J. T. M. Kennis, J. A. Ihalainen, M. Brazzoli, R. Croce, I. H. M. van Stokkum, R. Bassi, J. P. Dekker, H. van Amerongen, G. R. Fleming and R. van Grondelle, "Excitation energy transfer in dimeric light harvesting complex I: A combined streak-camera/fluorescence upconversion study", *J. Phys. Chem. B* **105**, 10132-10139 (2001).
139. C. Le Quiniou, "Influence of size, composition and supramolecular organization of Photosystem I on trapping efficiency", *Ph.D. Thesis* (2016).
140. I. H. van Stokkum, D. S. Larsen and R. van Grondelle, "Global and target analysis of time-resolved spectra", *Biochim. Biophys. Acta* **1657**, 82-104 (2004).
141. E. S. Boyden, F. Zhang, E. Bamberg, G. Nagel and K. Deisseroth, "Millisecond-timescale, genetically targeted optical control of neural activity", *Nat. Neurosci.* **8**, 1263-1268 (2005).
142. P. Hegemann and A. Moglich, "Channelrhodopsin engineering and exploration of new optogenetic tools", *Nat. Methods* **8**, 39-42 (2011).
143. J. Y. Lin, P. M. Knutsen, A. Muller, D. Kleinfeld and R. Y. Tsien, "ReaChR: a red-shifted variant of channelrhodopsin enables deep transcranial optogenetic excitation", *Nat. Neurosci.* **16**, 1499-1508 (2013).
144. S. Kleinlogel, K. Feldbauer, R. E. Dempski, H. Fotis, P. G. Wood, C. Bamann and E. Bamberg, "Ultra light-sensitive and fast neuronal activation with the Ca2+-permeable channelrhodopsin CatCh", *Nat. Neurosci.* **14**, 513-U152 (2011).
145. J. Wietek, J. S. Wiegert, N. Adeishvili, F. Schneider, H. Watanabe, S. P. Tsunoda, A. Vogt, M. Elstner, T. G. Oertner and P. Hegemann, "Conversion of channelrhodopsin into a light-gated chloride channel", *Science* **344**, 409-412 (2014).
146. A. Berndt, S. Y. Lee, C. Ramakrishnan and K. Deisseroth, "Structure-guided transformation of channelrhodopsin into a light-activated chloride channel", *Science* **344**, 420-424 (2014).
147. H. E. Kato, M. Kamiya, S. Sugo, J. Ito, R. Taniguchi, A. Orito, K. Hirata, A. Inutsuka, A. Yamanaka, A. D. Maturana, R. Ishitani, Y. Sudo, S. Hayashi and O. Nureki, "Atomistic design of microbial opsin-based blue-shifted optogenetics tools", *Nat. Commun.* **6**, 7177 (2015).
148. M. K. Verhoefen, C. Bamann, R. Blocher, U. Forster, E. Bamberg and J. Wachtveitl, "The photocycle of channelrhodopsin-2: ultrafast reaction dynamics and subsequent reaction steps", *Chemphyschem* **11**, 3113-3122 (2010).
149. F. Scholz, E. Bamberg, C. Bamann and J. Wachtveitl, "Tuning the primary reaction of channelrhodopsin-2 by imidazole, pH, and site-specific mutations", *Biophys. J.* **102**, 2649-2657 (2012).
150. M. K. Neumann-Verhoefen, K. Neumann, C. Bamann, I. Radu, J. Heberle, E. Bamberg and J. Wachtveitl, "Ultrafast infrared spectroscopy on channelrhodopsin-2 reveals efficient energy transfer from the retinal chromophore to the protein", *J. Am. Chem. Soc.* **135**, 6968-6976 (2013).
151. S. Ito, H. E. Kato, R. Taniguchi, T. Iwata, O. Nureki and H. Kandori, "Water-containing hydrogen-bonding network in the active center of channelrhodopsin", *J. Am. Chem. Soc.* **136**, 3475-3482 (2014).

152. Y. Guo, F. E. Beyle, B. M. Bold, H. C. Watanabe, A. Koslowski, W. Thiel, P. Hegemann, M. Marazzi and M. Elstner, "Active site structure and absorption spectrum of channelrhodopsin-2 wild-type and C128T mutant", *Chem. Sci.* **7**, 3879-3891 (2016).
153. P. Hamm, M. Zurek, T. Roschinger, H. Patzelt, D. Oesterhelt and W. Zinth, "Femtosecond spectroscopy of the photoisomerisation of the protonated Schiff base of all-trans retinal", *Chem. Phys. Lett.* **263**, 613-621 (1996).
154. R. A. Mathies, C. H. Brito Cruz, W. T. Pollard and C. V. Shank, "Direct observation of the femtosecond excited-state cis-trans isomerization in bacteriorhodopsin", *Science* **240**, 777-779 (1988).
155. F. Gai, J. C. McDonald and P. A. Anfinrud, "Pump-dump-probe spectroscopy of bacteriorhodosin: Evidence for a near-IR excited state absorbance", *J. Am. Chem. Soc.* **119**, 6201-6202 (1997).
156. S. Ruhman, B. Hou, N. Friedman, M. Ottolenghi and M. Sheves, "Following evolution of bacteriorhodopsin in its reactive excited state via stimulated emission pumping", *J. Am. Chem. Soc.* **124**, 8854-8858 (2002).
157. J. T. Kennis, D. S. Larsen, I. H. van Stokkum, M. Vengris, J. J. van Thor and R. van Grondelle, "Uncovering the hidden ground state of green fluorescent protein", *Proc. Natl. Acad. Sci. U. S. A.* **101**, 17988-17993 (2004).
158. D. S. Larsen, I. H. van Stokkum, M. Vengris, M. A. van Der Horst, F. L. de Weerd, K. J. Hellingwerf and R. van Grondelle, "Incoherent manipulation of the photoactive yellow protein photocycle with dispersed pump-dump-probe spectroscopy", *Biophys. J.* **87**, 1858-1872 (2004).
159. P. W. Kim, L. H. Freer, N. C. Rockwell, S. S. Martin, J. C. Lagarias and D. S. Larsen, "Second-Chance Forward Isomerization Dynamics of the Red/Green Cyanobacteriochrome NpR6012g4 from Nostoc punctiforme", *J. Am. Chem. Soc.* **134**, 130-133 (2012).
160. P. W. Kim, N. C. Rockwell, L. H. Freer, C. W. Chang, S. S. Martin, J. C. Lagarias and D. S. Larsen, "Unraveling the Primary Isomerization Dynamics in Cyanobacterial Phytochrome Cph1 with Multi-pulse Manipulations", *J. Phys. Chem. Lett.* **4**, 2605-2609 (2013).
161. J. T. Kennis, I. H. van Stokkum, D. S. Peterson, A. Pandit and R. M. Wachter, "Ultrafast proton shuttling in Psammocora cyan fluorescent protein", *J. Phys. Chem. B* **117**, 11134-11143 (2013).
162. A. Rupenyan, I. H. van Stokkum, J. C. Arents, R. van Grondelle, K. J. Hellingwerf and M. L. Groot, "Reaction pathways of photoexcited retinal in proteorhodopsin studied by pump-dump-probe spectroscopy", *J. Phys. Chem. B* **113**, 16251-16256 (2009).
163. M. Di Donato, L. J. van Wilderen, I. H. Van Stokkum, T. C. Stuart, J. T. Kennis, K. J. Hellingwerf, R. van Grondelle and M. L. Groot, "Proton transfer events in GFP", *Phys. Chem. Chem. Phys.* **13**, 16295-16305 (2011).
164. B. van Oort, M. J. ter Veer, M. L. Groot and I. H. van Stokkum, "Excited state proton transfer in strongly enhanced GFP (sGFP2)", *Phys. Chem. Chem. Phys.* **14**, 8852-8858 (2012).
165. B. van Oort, R. van Grondelle and I. H. van Stokkum, "A Hidden State in Light-Harvesting Complex II Revealed By Multipulse Spectroscopy", *J. Phys. Chem. B* **119**, 5184-5193 (2015).
166. I. Dokukina and O. Weingart, "Spectral properties and isomerisation path of retinal in C1C2 channelrhodopsin", *Phys. Chem. Chem. Phys.* **17**, 25142-25150 (2015).
167. C. Garcia-Iriepa, M. Gueye, J. Leonard, D. Martinez-Lopez, P. J. Campos, L. M. Frutos, D. Sampedro and M. Marazzi, "A biomimetic molecular switch at work: coupling photoisomerization dynamics to peptide structural rearrangement", *Phys. Chem. Chem. Phys.* **18**, 6742-6753 (2016).
168. D. Polli, P. Altoe, O. Weingart, K. M. Spillane, C. Manzoni, D. Brida, G. Tomasello, G. Orlandi, P. Kukura, R. A. Mathies, M. Garavelli and G. Cerullo, "Conical intersection dynamics of the primary photoisomerization event in vision", *Nature* **467**, 440-443 (2010).
169. I. Schapiro, M. N. Ryazantsev, L. M. Frutos, N. Ferre, R. Lindh and M. Olivucci, "The ultrafast photoisomerizations of rhodopsin and bathorhodopsin are modulated by bond length alternation and HOOP driven electronic effects", *J. Am. Chem. Soc.* **133**, 3354-3364 (2011).

170. J. Tittor and D. Oesterhelt, "The Quantum Yield of Bacteriorhodopsin", *FEBS Lett.* **263**, 269-273 (1990).
171. S. Bruun, D. Stoeppler, A. Keidel, U. Kuhlmann, M. Luck, A. Diehl, M. A. Geiger, D. Woodmansee, D. Trauner, P. Hegemann, H. Oschkinat, P. Hildebrandt and K. Stehfest, "Light-Dark Adaptation of Channelrhodopsin Involves Photoconversion between the all-trans and 13-cis Retinal Isomers", *Biochemistry* **54**, 5389-5400 (2015).
172. J. Becker-Baldus, C. Bamann, K. Saxena, H. Gustmann, L. J. Brown, R. C. Brown, C. Reiter, E. Bamberg, J. Wachtveitl, H. Schwalbe and C. Glaubitz, "Enlightening the photoactive site of channelrhodopsin-2 by DNP-enhanced solid-state NMR spectroscopy", *Proc. Natl. Acad. Sci. U. S. A.* **112**, 9896-9901 (2015).
173. C. Schnedermann, V. Muders, D. Ehrenberg, R. Schlesinger, P. Kukura and J. Heberle, "Vibronic Dynamics of the Ultrafast all-trans to 13-cis Photoisomerization of Retinal in Channelrhodopsin-1", *J. Am. Chem. Soc.* **138**, 4757-4762 (2016).
174. T. Stensitzki, Y. Yang, V. Muders, R. Schlesinger, J. Heberle and K. Heyne, "Femtosecond infrared spectroscopy of channelrhodopsin-1 chromophore isomerization", *Struct. Dyn.* **3**, 043208 (2016).
175. T. Stensitzki, V. Muders, R. Schlesinger, J. Heberle and K. Heyne, "The primary photoreaction of channelrhodopsin-1: wavelength dependent photoreactions induced by ground-state heterogeneity", *Front. Mol. Biosci.* **2**, 41 (2015).
176. S. Y. Hou, E. G. Govorunova, M. Ntefidou, C. E. Lane, E. N. Spudich, O. A. Sineshchekov and J. L. Spudich, "Diversity of Chlamydomonas channelrhodopsins", *Photochem. Photobiol.* **88**, 119-128 (2012).
177. B. R. Rost, F. Schneider, M. K. Grauel, C. Wozny, C. Bentz, A. Blessing, T. Rosenmund, T. J. Jentsch, D. Schmitz, P. Hegemann and C. Rosenmund, "Optogenetic acidification of synaptic vesicles and lysosomes", *Nat. Neurosci.* **18**, 1845-1852 (2015).
178. L. Zimanyi, J. Saltiel, L. S. Brown and J. K. Lanyi, "A priori resolution of the intermediate spectra in the bacteriorhodopsin photocycle: the time evolution of the L spectrum revealed", *J. Phys. Chem. A* **110**, 2318-2321 (2006).
179. I. Schapiro, O. Weingart and V. Buss, "Bicycle-pedal isomerization in a rhodopsin chromophore model", *J. Am. Chem. Soc.* **131**, 16-17 (2009).
180. M. Blanco-Lomas, P. J. Campos and D. Sampedro, "Synthesis and Photoisomerization of Rhodopsin-Based Molecular Switches", *Eur. J. Org. Chem.* 6328-6334 (2012).
181. L. Vukovic, C. F. Burmeister, P. Kral and G. Groenhof, "Control Mechanisms of Photoisomerization in Protonated Schiff Bases", *J. Phys. Chem. Lett.* **4**, 1005-1011 (2013).
182. J. Finley, P. A. Malmqvist, B. O. Roos and L. Serrano-Andres, "The multi-state CASPT2 method", *Chem. Phys. Lett.* **288**, 299-306 (1998).
183. A. D. MacKerell, D. Bashford, M. Bellott, R. L. Dunbrack, J. D. Evanseck, M. J. Field, S. Fischer, J. Gao, H. Guo, S. Ha, D. Joseph-McCarthy, L. Kuchnir, K. Kuczera, F. T. Lau, C. Mattos, S. Michnick, T. Ngo, D. T. Nguyen, B. Prodhom, W. E. Reiher, B. Roux, M. Schlenkrich, J. C. Smith, R. Stote, J. Straub, M. Watanabe, J. Wiorkiewicz-Kuczera, D. Yin and M. Karplus, "All-atom empirical potential for molecular modeling and dynamics studies of proteins", *J. Phys. Chem. B* **102**, 3586-3616 (1998).
184. W. L. Jorgensen, J. Chandrasekhar, J. D. Madura, R. W. Impey and M. L. Klein, "Comparison of Simple Potential Functions for Simulating Liquid Water", *J. Chem. Phys.* **79**, 926-935 (1983).
185. H. C. Watanabe, K. Welke, D. J. Sindhikara, P. Hegemann and M. Elstner, "Towards an understanding of channelrhodopsin function: simulations lead to novel insights of the channel mechanism", *J. Mol. Biol.* **425**, 1795-1814 (2013).
186. F. Aquilante, L. De Vico, N. Ferre, G. Ghigo, P. A. Malmqvist, P. Neogrady, T. B. Pedersen, M. Pitonak, M. Reiher, B. O. Roos, L. Serrano-Andres, M. Urban, V. Veryazov and R. Lindh, "Software News and Update MOLCAS 7: The Next Generation", *J. Comput. Chem.* **31**, 224-247 (2010).
187. J. W. Ponder and F. M. Richards, "An Efficient Newton-Like Method for Molecular Mechanics Energy Minimization of Large Molecules", *J. Comput. Chem.* **8**, 1016-1024 (1987).

188. X. Han and E. S. Boyden, "Multiple-color optical activation, silencing, and desynchronization of neural activity, with single-spike temporal resolution", *PLoS One* **2**, e299 (2007).
189. J. Wietek, R. Beltramo, M. Scanziani, P. Hegemann, T. G. Oertner and J. S. Wiegert, "An improved chloride-conducting channelrhodopsin for light-induced inhibition of neuronal activity in vivo", *Sci. Rep.* **5**, 14807 (2015).
190. M. Braiman and R. Mathies, "Resonance Raman evidence for an all-trans to 13-cis isomerization in the proton-pumping cycle of bacteriorhodopsin", *Biochemistry* **19**, 5421-5428 (1980).
191. J. K. Lanyi, "Bacteriorhodopsin", *Annu. Rev. Physiol.* **66**, 665-688 (2004).
192. V. A. Lorenz-Fonfria and J. Heberle, "Channelrhodopsin unchained: structure and mechanism of a light-gated cation channel", *Biochim. Biophys. Acta* **1837**, 626-642 (2014).
193. O. A. Sineshchekov, H. Li, E. G. Govorunova and J. L. Spudich, "Photochemical reaction cycle transitions during anion channelrhodopsin gating", *Proc. Natl. Acad. Sci. U. S. A.* **113**, E1993-E2000 (2016).
194. O. A. Sineshchekov, E. G. Govorunova, H. Li and J. L. Spudich, "Gating mechanisms of a natural anion channelrhodopsin", *Proc. Natl. Acad. Sci. U. S. A.* **112**, 14236-14241 (2015).
195. A. Campion, M. A. El-Sayed and J. Terner, "Resonance Raman kinetic spectroscopy of bacteriorhodopsin on the microsecond time scale", *Biophys. J.* **20**, 369-375 (1977).
196. R. Diller and M. Stockburger, "Kinetic Resonance Raman Studies Reveal Different Conformational States of Bacteriorhodopsin", *Biochemistry* **27**, 7641-7651 (1988).
197. K. Stehfest and P. Hegemann, "Evolution of the channelrhodopsin photocycle model", *Chemphyschem* **11**, 1120-1126 (2010).
198. L. H. Andersen, I. B. Nielsen, M. B. Kristensen, M. O. El Ghazaly, S. Haacke, M. B. Nielsen and M. A. Petersen, "Absorption of schiff-base retinal chromophores in vacuo", *J. Am. Chem. Soc.* **127**, 12347-12350 (2005).
199. J. T. M. Kennis, D. S. Larsen, K. Ohta, M. T. Facciotti, R. M. Glaeser and G. R. Fleming, "Ultrafast protein dynamics of bacteriorhodopsin probed by photon echo and transient absorption spectroscopy", *J. Phys. Chem. B* **106**, 6067-6080 (2002).
200. A. Yi, H. Li, N. Mamaeva, R. E. Fernandez De Cordoba, J. Lugtenburg, W. J. DeGrip, J. L. Spudich and K. J. Rothschild, "Structural Changes in an Anion Channelrhodopsin: Formation of the K and L Intermediates at 80 K", *Biochemistry* **56**, 2197-2208 (2017).
201. T. Friedrich, S. Geibel, R. Kalmbach, I. Chizhov, K. Ataka, J. Heberle, M. Engelhard and E. Bamberg, "Proteorhodopsin is a light-driven proton pump with variable vectoriality", *J. Mol. Biol.* **321**, 821-838 (2002).
202. J. C. D. Kaufmann, B. S. Krause, C. Grimm, E. Ritter, P. Hegemann and F. J. Bartl, "Proton transfer reactions in the red light-activatable channelrhodopsin variant ReaChR and their relevance for its function", *J. Biol. Chem.* (2017).
203. I. Gushchin, V. Shevchenko, V. Polovinkin, K. Kovalev, A. Alekseev, E. Round, V. Borshchevskiy, T. Balandin, A. Popov, T. Gensch, C. Fahlke, C. Bamann, D. Willbold, G. Buldt, E. Bamberg and V. Gordeliy, "Crystal structure of a light-driven sodium pump", *Nat. Struct. Mol. Biol.* **22**, 390-395 (2015).
204. I. Gushchin, V. Shevchenko, V. Polovinkin, V. Borshchevskiy, P. Buslaev, E. Bamberg and V. Gordeliy, "Structure of the light-driven sodium pump KR2 and its implications for optogenetics", *FEBS J.* (2015).
205. D. Xu, C. Martin and K. Schulten, "Molecular dynamics study of early picosecond events in the bacteriorhodopsin photocycle: dielectric response, vibrational cooling and the J, K intermediates", *Biophys. J.* **70**, 453-460 (1996).
206. K. C. Hasson, F. Gai and P. A. Anfinrud, "The photoisomerization of retinal in bacteriorhodospin: experimental evidence for a three-state model", *Proc. Natl. Acad. Sci. U. S. A.* **93**, 15124-15129 (1996).
207. S. Tahara, S. Takeuchi, R. Abe-Yoshizumi, K. Inoue, H. Ohtani, H. Kandori and T. Tahara, "Ultrafast Photoreaction Dynamics of a Light-Driven Sodium-Ion-Pumping Retinal Protein

from Krokinobacter eikastus Revealed by Femtosecond Time-Resolved Absorption Spectroscopy", *J. Phys. Chem. Lett.* **6**, 4481-4486 (2015).
208. J. K. Lanyi and B. Schobert, "Mechanism of proton transport in bacteriorhodopsin from crystallographic structures of the K, L, M1, M2, and M2' intermediates of the photocycle", *J. Mol. Biol.* **328**, 439-450 (2003).
209. T. Kouyama, T. Nishikawa, T. Tokuhisa and H. Okumura, "Crystal structure of the L intermediate of bacteriorhodopsin: evidence for vertical translocation of a water molecule during the proton pumping cycle", *J. Mol. Biol.* **335**, 531-546 (2004).
210. T. Althaus, W. Eisfeld, R. Lohrmann and M. Stockburger, "Application of Raman spectroscopy to retinal proteins", *Israel J. Chem.* **35**, 227-251 (1995).
211. S. O. Smith, M. S. Braiman, A. B. Myers, J. A. Pardoen, J. M. L. Courtin, C. Winkel, J. Lugtenburg and R. A. Mathies, "Vibrational Analysis of the All-Trans-Retinal Chromophore in Light-Adapted Bacteriorhodopsin", *J. Am. Chem. Soc.* **109**, 3108-3125 (1987).
212. H. Ono, K. Inoue, R. Abe-Yoshizumi and H. Kandori, "FTIR spectroscopy of a light-driven compatible sodium ion-proton pumping rhodopsin at 77 K", *J. Phys. Chem. B* **118**, 4784-4792 (2014).
213. D. W. McCamant, P. Kukura and R. A. Mathies, "Femtosecond stimulated Raman study of excited-state evolution in bacteriorhodopsin", *J. Phys. Chem. B* **109**, 10449-10457 (2005).
214. S. Shim, J. Dasgupta and R. A. Mathies, "Femtosecond time-resolved stimulated Raman reveals the birth of bacteriorhodopsin's J and K intermediates", *J. Am. Chem. Soc.* **131**, 7592-7597 (2009).
215. V. A. Lorenz-Fonfria, T. Resler, N. Krause, M. Nack, M. Gossing, G. Fischer von Mollard, C. Bamann, E. Bamberg, R. Schlesinger and J. Heberle, "Transient protonation changes in channelrhodopsin-2 and their relevance to channel gating", *Proc. Natl. Acad. Sci. U. S. A.* **110**, E1273-1281 (2013).
216. J. Sasaki, A. Maeda, C. Kato and H. Hamaguchi, "Time-resolved infrared spectral analysis of the KL-to-L conversion in the photocycle of bacteriorhodopsin", *Biochemistry* **32**, 867-871 (1993).
217. N. J. Claassens, D. Z. Sousa, V. A. Dos Santos, W. M. de Vos and J. van der Oost, "Harnessing the power of microbial autotrophy", *Nat. Rev. Microbiol.* **14**, 692-706 (2016).
218. J. M. Walter, D. Greenfield, C. Bustamante and J. Liphardt, "Light-powering Escherichia coli with proteorhodopsin", *Proc. Natl. Acad. Sci. U. S. A.* **104**, 2408-2412 (2007).
219. J. M. Kralj, D. R. Hochbaum, A. D. Douglass and A. E. Cohen, "Electrical Spiking in Escherichia coli Probed with a Fluorescent Voltage-Indicating Protein", *Science* **333**, 345-348 (2011).
220. J. M. Kralj, A. D. Douglass, D. R. Hochbaum, D. Maclaurin and A. E. Cohen, "Optical recording of action potentials in mammalian neurons using a microbial rhodopsin", *Nat. Methods* **9**, 90-U130 (2012).
221. D. R. Hochbaum, Y. Zhao, S. L. Farhi, N. Klapoetke, C. A. Werley, V. Kapoor, P. Zou, J. M. Kralj, D. Maclaurin, N. Smedemark-Margulies, J. L. Saulnier, G. L. Boulting, C. Straub, Y. K. Cho, M. Melkonian, G. K. S. Wong, D. J. Harrison, V. N. Murthy, B. L. Sabatini, E. S. Boyden, R. E. Campbell and A. E. Cohen, "All-optical electrophysiology in mammalian neurons using engineered microbial rhodopsins", *Nat. Methods* **11**, 825-833 (2014).
222. V. Gradinaru, K. R. Thompson and K. Deisseroth, "eNpHR: a Natronomonas halorhodopsin enhanced for optogenetic applications", *Brain Cell Biol.* **36**, 129-139 (2008).
223. B. Y. Chow, X. Han, A. S. Dobry, X. Qian, A. S. Chuong, M. Li, M. A. Henninger, G. M. Belfort, Y. Lin, P. E. Monahan and E. S. Boyden, "High-performance genetically targetable optical neural silencing by light-driven proton pumps", *Nature* **463**, 98-102 (2010).
224. N. C. Klapoetke, Y. Murata, S. S. Kim, S. R. Pulver, A. Birdsey-Benson, Y. K. Cho, T. K. Morimoto, A. S. Chuong, E. J. Carpenter, Z. Tian, J. Wang, Y. Xie, Z. Yan, Y. Zhang, B. Y. Chow, B. Surek, M. Melkonian, V. Jayaraman, M. Constantine-Paton, G. K. Wong and E. S. Boyden, "Independent optical excitation of distinct neural populations", *Nat. Methods* **11**, 338-346 (2014).

225. A. S. Chuong, M. L. Miri, V. Busskamp, G. A. Matthews, L. C. Acker, A. T. Sorensen, A. Young, N. C. Klapoetke, M. A. Henninger, S. B. Kodandaramaiah, M. Ogawa, S. B. Ramanlal, R. C. Bandler, B. D. Allen, C. R. Forest, B. Y. Chow, X. Han, Y. Lin, K. M. Tye, B. Roska, J. A. Cardin and E. S. Boyden, "Noninvasive optical inhibition with a red-shifted microbial rhodopsin", *Nat. Neurosci.* **17**, 1123-1129 (2014).
226. K. Erbguth, M. Prigge, F. Schneider, P. Hegemann and A. Gottschalk, "Bimodal activation of different neuron classes with the spectrally red-shifted channelrhodopsin chimera C1V1 in Caenorhabditis elegans", *PLoS One* **7**, e46827 (2012).
227. S. Ganapathy, O. Becheau, H. Venselaar, S. Frolich, J. B. van der Steen, Q. Chen, S. Radwan, J. Lugtenburg, K. J. Hellingwerf, H. J. de Groot and W. J. de Grip, "Modulation of spectral properties and pump activity of proteorhodopsins by retinal analogues", *Biochem. J.* **467**, 333-343 (2015).
228. S. Ganapathy, H. Venselaar, Q. Chen, H. J. de Groot, K. J. Hellingwerf and W. J. de Grip, "Retinal-Based Proton Pumping in the Near Infrared", *J. Am. Chem. Soc.* **139**, 2338-2344 (2017).
229. N. AzimiHashemi, K. Erbguth, A. Vogt, T. Riemensperger, E. Rauch, D. Woodmansee, J. Nagpal, M. Brauner, M. Sheves, A. Fiala, L. Kattner, D. Trauner, P. Hegemann, A. Gottschalk and J. F. Liewald, "Synthetic retinal analogues modify the spectral and kinetic characteristics of microbial rhodopsin optogenetic tools", *Nat. Commun.* **5**, 5810 (2014).
230. P. B. Coto, A. Strambi, N. Ferre and M. Olivucci, "The color of rhodopsins at the ab initio multiconfigurational perturbation theory resolution", *Proc. Natl. Acad. Sci. U. S. A.* **103**, 17154-17159 (2006).
231. A. K. Dioumaev, L. S. Brown, J. Shih, E. N. Spudich, J. L. Spudich and J. K. Lanyi, "Proton transfers in the photochemical reaction cycle of proteorhodopsin", *Biochemistry* **41**, 5348-5358 (2002).
232. R. A. Krebs, D. Dunmire, R. Partha and M. S. Braiman, "Resonance Raman characterization of proteorhodopsin's chromophore environment", *J. Phys. Chem. B* **107**, 7877-7883 (2003).
233. E. S. Imasheva, K. Shimono, S. P. Balashov, J. M. Wang, U. Zadok, M. Sheves, N. Kamo and J. K. Lanyi, "Formation of a long-lived photoproduct with a deprotonated Schiff base in proteorhodopsin, and its enhancement by mutation of Asp227", *Biochemistry* **44**, 10828-10838 (2005).
234. N. Pfleger, M. Lorch, A. C. Woerner, S. Shastri and C. Glaubitz, "Characterisation of Schiff base and chromophore in green proteorhodopsin by solid-state NMR", *J. Biomol. NMR* **40**, 15-21 (2008).
235. V. Bergo, J. J. Amsden, E. N. Spudich, J. L. Spudich and K. J. Rothschild, "Structural changes in the photoactive site of proteorhodopsin during the primary photoreaction", *Biochemistry* **43**, 9075-9083 (2004).
236. S. O. Smith, J. A. Pardoen, J. Lugtenburg and R. A. Mathies, "Vibrational Analysis of the 13-Cis-Retinal Chromophore in Dark-Adapted Bacteriorhodopsin", *J. Phys. Chem.* **91**, 804-819 (1987).
237. A. K. Dioumaev, J. M. Wang, Z. Balint, G. Varo and J. K. Lanyi, "Proton transport by proteorhodopsin requires that the retinal Schiff base counterion Asp-97 be anionic", *Biochemistry* **42**, 6582-6587 (2003).
238. R. Huber, T. Kohler, M. O. Lenz, E. Bamberg, R. Kalmbach, M. Engelhard and J. Wachtveitl, "pH-dependent photoisomerization of retinal in proteorhodopsin", *Biochemistry* **44**, 1800-1806 (2005).
239. A. G. Doukas, B. Aton, R. H. Callender and T. G. Ebrey, "Resonance Raman studies of bovine metarhodopsin I and metarhodopsin II", *Biochemistry* **17**, 2430-2435 (1978).
240. G. Varo, L. S. Brown, M. Lakatos and J. K. Lanyi, "Characterization of the photochemical reaction cycle of proteorhodopsin", *Biophys. J.* **84**, 1202-1207 (2003).
241. S. Hussain, M. Kinnebrew, N. S. Schonenbach, E. Aye and S. Han, "Functional consequences of the oligomeric assembly of proteorhodopsin", *J. Mol. Biol.* **427**, 1278-1290 (2015).
242. T. Kohler, I. Weber, C. Glaubitz and J. Wachtveitl, "Proteorhodopsin Photocycle Kinetics Between pH 5 and pH 9", *Photochem. Photobiol.* **93**, 762-771 (2017).

243. M. O. Lenz, R. Huber, B. Schmidt, P. Gilch, R. Kalmbach, M. Engelhard and J. Wachtveitl, "First steps of retinal photoisomerization in proteorhodopsin", *Biophys. J.* **91**, 255-262 (2006).
244. K. Neumann, M. K. Verhoefen, I. Weber, C. Glaubitz and J. Wachtveitl, "Initial reaction dynamics of proteorhodopsin observed by femtosecond infrared and visible spectroscopy", *Biophys. J.* **94**, 4796-4807 (2008).
245. Y. Xiao, R. Partha, R. Krebs and M. Braiman, "Time-resolved FTIR spectroscopy of the photointermediates involved in fast transient H+ release by proteorhodopsin", *J. Phys. Chem. B* **109**, 634-641 (2005).
246. M. Mehler, F. Scholz, S. J. Ullrich, J. Mao, M. Braun, L. J. Brown, R. C. Brown, S. A. Fiedler, J. Becker-Baldus, J. Wachtveitl and C. Glaubitz, "The EF loop in green proteorhodopsin affects conformation and photocycle dynamics", *Biophys. J.* **105**, 385-397 (2013).
247. P. J. Johnson, A. Halpin, T. Morizumi, V. I. Prokhorenko, O. P. Ernst and R. J. Miller, "Local vibrational coherences drive the primary photochemistry of vision", *Nat. Chem.* **7**, 980-986 (2015).
248. R. A. Mathies, "Photochemistry: A coherent picture of vision", *Nat. Chem.* **7**, 945-947 (2015).
249. L. Herwig, A. J. Rice, C. N. Bedbrook, R. J. K. Zhang, A. Lignell, J. K. B. Cahn, H. Renata, S. C. Dodani, I. Cho, L. Cai, V. Gradinaru and F. H. Arnold, "Directed Evolution of a Bright Near-Infrared Fluorescent Rhodopsin Using a Synthetic Chromophore", *Cell Chem. Biol.* **24**, 415-425 (2017).
250. Y. Hontani, D. M. Shcherbakova, M. Baloban, J. Zhu, V. V. Verkhusha and J. T. Kennis, "Bright blue-shifted fluorescent proteins with Cys in the GAF domain engineered from bacterial phytochromes: fluorescence mechanisms and excited-state dynamics", *Sci. Rep.* **6**, 37362 (2016).
251. K. Rurack and M. Spieles, "Fluorescence quantum yields of a series of red and near-infrared dyes emitting at 600-1000 nm", *Anal. Chem.* **83**, 1232-1242 (2011).
252. E. Salcedo, L. Zheng, M. Phistry, E. E. Bagg and S. G. Britt, "Molecular basis for ultraviolet vision in invertebrates", *J. Neurosci.* **23**, 10873-10878 (2003).
253. Y. Shi, F. B. Radlwimmer and S. Yokoyama, "Molecular genetics and the evolution of ultraviolet vision in vertebrates", *Proc. Natl. Acad. Sci. U. S. A.* **98**, 11731-11736 (2001).
254. M. Koyanagi, E. Kawano, Y. Kinugawa, T. Oishi, Y. Shichida, S. Tamotsu and A. Terakita, "Bistable UV pigment in the lamprey pineal", *Proc. Natl. Acad. Sci. U. S. A.* **101**, 6687-6691 (2004).
255. T. Yamashita, H. Ohuchi, S. Tomonari, K. Ikeda, K. Sakai and Y. Shichida, "Opn5 is a UV-sensitive bistable pigment that couples with Gi subtype of G protein", *Proc. Natl. Acad. Sci. U. S. A.* **107**, 22084-22089 (2010).
256. P. Kukura, D. W. McCamant, S. Yoon, D. B. Wandschneider and R. A. Mathies, "Structural observation of the primary isomerization in vision with femtosecond-stimulated Raman", *Science* **310**, 1006-1009 (2005).
257. T. Nakamura, S. Takeuchi, M. Shibata, M. Demura, H. Kandori and T. Tahara, "Ultrafast pump-probe study of the primary photoreaction process in pharaonis halorhodopsin: halide ion dependence and isomerization dynamics", *J. Phys. Chem. B* **112**, 12795-12800 (2008).
258. R. R. Birge, "2-Photon Spectroscopy of Protein-Bound Chromophores", *Acc. Chem. Res.* **19**, 138-146 (1986).
259. A. Penzkofer, M. Luck, T. Mathes and P. Hegemann, "Bistable Retinal Schiff Base Photodynamics of Histidine Kinase Rhodopsin HKR1 from Chlamydomonas reinhardtii", *Photochem. Photobiol.* (2014).
260. A. Bonvicini, B. Demoulin, S. F. Altavilla, A. Nenov, M. M. T. El-Tahawy, J. Segarra-Marti, A. Giussani, V. S. Batista, M. Garavelli and I. Rivalta, "Ultraviolet vision: photophysical properties of the unprotonated retinyl Schiff base in the Siberian hamster cone pigment", *Theor. Chem. Acc.* **135**, (2016).
261. D. M. Niedzwiedzki, J. O. Sullivan, T. Polivka, R. R. Birge and H. A. Frank, "Femtosecond time-resolved transient absorption spectroscopy of xanthophylls", *J. Phys. Chem. B* **110**, 22872-22885 (2006).

262. G. Kodis, C. Herrero, R. Palacios, E. Marino-Ochoa, S. Gould, L. de la Garza, R. van Grondelle, D. Gust, T. A. Moore, A. L. Moore and J. T. M. Kennis, "Light harvesting and photoprotective functions of carotenoids in compact artificial photosynthetic antenna designs", *J. Phys. Chem. B* **108**, 414-425 (2004).
263. H. H. Billsten, J. Pan, S. Sinha, T. Pascher, V. Sundstrom and T. Polivka, "Excited-state processes in the carotenoid zeaxanthin after excess energy excitation", *J. Phys. Chem. A* **109**, 6852-6859 (2005).
264. T. Polivka and V. Sundstrom, "Ultrafast dynamics of carotenoid excited States-from solution to natural and artificial systems", *Chem. Rev.* **104**, 2021-2071 (2004).
265. E. Papagiannakis, J. T. Kennis, I. H. van Stokkum, R. J. Cogdell and R. van Grondelle, "An alternative carotenoid-to-bacteriochlorophyll energy transfer pathway in photosynthetic light harvesting", *Proc. Natl. Acad. Sci. U. S. A.* **99**, 6017-6022 (2002).
266. H. Hashimoto, Y. Koyama, Y. Hirata and N. Mataga, "S1 and T1 Species of Beta-Carotene Generated by Direct Photoexcitation from the All-Trans, 9-Cis, 13-Cis, and 15-Cis Isomers as Revealed by Picosecond Transient Absorption and Transient Raman Spectroscopies", *J. Phys. Chem.* **95**, 3072-3076 (1991).
267. D. W. McCamant, P. Kukura and R. A. Mathies, "Femtosecond Time-Resolved Stimulated Raman Spectroscopy: Application to the Ultrafast Internal Conversion in beta-Carotene", *J. Phys. Chem. A* **107**, 8208-8214 (2003).
268. Hiroyoshi Nagae, Michitaka Kuki, Jian-Ping Zhang, Tokutake Sashima, Yumiko Mukai and Yasushi Koyama, "Vibronic Coupling through the In-Phase, CC Stretching Mode Plays a Major Role in the 2Ag-to 1Ag-Internal Conversion ofall-trans-β-Carotene", *J. Phys. Chem. A* **104**, 4155-4166 (2000).
269. S. P. Balashov and F. F. Litvin, "Phototransformation of Metabacteriorhodopsin", *Photobiochem. Photobiophys.* **2**, 111-117 (1981).
270. O. Kalisky, U. Lachish and M. Ottolenghi, "Time Resolution of a Back Photoreaction in Bacteriorhodopsin", *Photochem. Photobiol.* **28**, 261-263 (1978).
271. C. E. Eckert, J. Kaur, C. Glaubitz and J. Wachtveitl, "Ultrafast Photoinduced Deactivation Dynamics of Proteorhodopsin", *J. Phys. Chem. Lett.* **8**, 512-517 (2017).
272. N. E. Holt, J. T. M. Kennis, L. Dall'Osto, R. Bassi and G. R. Fleming, "Carotenoid to chlorophyll energy transfer in light harvesting complex II from Arabidopsis thaliana probed by femtosecond fluorescence upconversion", *Chem. Phys. Lett.* **379**, 305-313 (2003).
273. A. N. Macpherson, J. B. Arellano, N. J. Fraser, R. J. Cogdell and T. Gillbro, "Efficient energy transfer from the carotenoid S(2) state in a photosynthetic light-harvesting complex", *Biophys. J.* **80**, 923-930 (2001).
274. B. G. Levine and T. J. Martinez, "Isomerization through conical intersections", *Annu. Rev. Phys. Chem.* **58**, 613-634 (2007).
275. S. M. Bachilo and T. Gillbro, "Fluorescence of retinal Schiff base in alcohols", *J. Phys. Chem. A* **103**, 2481-2488 (1999).
276. M. L. Groot, L. J. van Wilderen and M. Di Donato, "Time-resolved methods in biophysics. 5. Femtosecond time-resolved and dispersed infrared spectroscopy on proteins", *Photochem. Photobiol. Sci.* **6**, 501-507 (2007).
277. K. D. Piatkevich and V. V. Verkhusha, "Advances in engineering of fluorescent proteins and photoactivatable proteins with red emission", *Curr. Opin. Chem. Biol.* **14**, 23-29 (2010).
278. B. Karniol, J. R. Wagner, J. M. Walker and R. D. Vierstra, "Phylogenetic analysis of the phytochrome superfamily reveals distinct microbial subfamilies of photoreceptors", *Biochem. J.* **392**, 103-116 (2005).
279. E. Giraud and A. Vermeglio, "Bacteriophytochromes in anoxygenic photosynthetic bacteria", *Photosynth. Res.* **97**, 141-153 (2008).
280. N. C. Rockwell and J. C. Lagarias, "A brief history of phytochromes", *Chemphyschem* **11**, 1172-1180 (2010).
281. A. J. Fischer and J. C. Lagarias, "Harnessing phytochrome's glowing potential", *Proc. Natl. Acad. Sci. U. S. A.* **101**, 17334-17339 (2004).

282. X. Shu, A. Royant, M. Z. Lin, T. A. Aguilera, V. Lev-Ram, P. A. Steinbach and R. Y. Tsien, "Mammalian expression of infrared fluorescent proteins engineered from a bacterial phytochrome", *Science* **324**, 804-807 (2009).
283. M. E. Auldridge, K. A. Satyshur, D. M. Anstrom and K. T. Forest, "Structure-guided Engineering Enhances a Phytochrome-based Infrared Fluorescent Protein", *J. Biol. Chem.* **287**, 7000-7009 (2012).
284. M. T. N. Tran, J. Tanaka, M. Hamada, Y. Sugiyama, S. Sakaguchi, M. Nakamura, S. Takahashi and Y. Miwa, "In Vivo image Analysis Using iRFP Transgenic Mice", *Exp. Anim. Tokyo* **63**, 311-319 (2014).
285. T. Lamparter, N. Michael, O. Caspani, T. Miyata, K. Shirai and K. Inomata, "Biliverdin binds covalently to agrobacterium phytochrome Agp1 via its ring A vinyl side chain", *J. Biol. Chem.* **278**, 33786-33792 (2003).
286. J. R. Wagner, J. Zhang, J. S. Brunzelle, R. D. Vierstra and K. T. Forest, "High resolution structure of Deinococcus bacteriophytochrome yields new insights into phytochrome architecture and evolution", *J. Biol. Chem.* **282**, 12298-12309 (2007).
287. T. Rohmer, C. Lang, J. Hughes, L. O. Essen, W. Gartner and J. Matysik, "Light-induced chromophore activity and signal transduction in phytochromes observed by 13C and 15N magic-angle spinning NMR", *Proc. Natl. Acad. Sci. U. S. A.* **105**, 15229-15234 (2008).
288. X. Yang, J. Kuk and K. Moffat, "Crystal structure of Pseudomonas aeruginosa bacteriophytochrome: photoconversion and signal transduction", *Proc. Natl. Acad. Sci. U. S. A.* **105**, 14715-14720 (2008).
289. F. Andel, K. C. Hasson, F. Gai, P. A. Anfinrud and R. A. Mathies, "Femtosecond time-resolved spectroscopy of the primary photochemistry of phytochrome", *Biospectroscopy* **3**, 421-433 (1997).
290. K. Heyne, J. Herbst, D. Stehlik, B. Esteban, T. Lamparter, J. Hughes and R. Diller, "Ultrafast dynamics of phytochrome from the cyanobacterium Synechocystis, reconstituted with phycocyanobilin and phycoerythrobilin", *Biophys. J.* **82**, 1004-1016 (2002).
291. J. J. van Thor, K. L. Ronayne and M. Towrie, "Formation of the early photoproduct lumi-R of cyanobacterial phytochrome cph1 observed by ultrafast mid-infrared spectroscopy", *J. Am. Chem. Soc.* **129**, 126-132 (2007).
292. J. Dasgupta, R. R. Frontiera, K. C. Taylor, J. C. Lagarias and R. A. Mathies, "Ultrafast excited-state isomerization in phytochrome revealed by femtosecond stimulated Raman spectroscopy", *Proc. Natl. Acad. Sci.U. S. A.* **106**, 1784-1789 (2009).
293. C. Schumann, R. Gross, N. Michael, T. Lamparter and R. Diller, "Sub-picosecond mid-infrared spectroscopy of phytochrome Agp1 from Agrobacterium tumefaciens", *Chemphyschem* **8**, 1657-1663 (2007).
294. T. Mathes, J. Ravensbergen, M. Kloz, T. Gleichmann, K. D. Gallagher, N. C. Woitowich, R. St Peter, S. E. Kovaleva, E. A. Stojkovic and J. T. M. Kennis, "Femto- to Microsecond Photodynarnics of an Unusual Bacteriophytochrome", *J. Phys. Chem. Lett.* **6**, 239-243 (2015).
295. M. G. Muller, I. Lindner, I. Martin, W. Gartner and A. R. Holzwarth, "Femtosecond kinetics of photoconversion of the higher plant photoreceptor phytochrome carrying native and modified chromophores", *Biophys. J.* **94**, 4370-4382 (2008).
296. K. C. Toh, E. A. Stojkovic, A. B. Rupenyan, I. H. van Stokkum, M. Salumbides, M. L. Groot, K. Moffat and J. T. Kennis, "Primary reactions of bacteriophytochrome observed with ultrafast mid-infrared spectroscopy", *J. Phys. Chem. A* **115**, 3778-3786 (2011).
297. B. Borucki, D. von Stetten, S. Seibeck, T. Lamparter, N. Michael, M. A. Mroginski, H. Otto, D. H. Murgida, M. P. Heyn and P. Hildebrandt, "Light-induced proton release of phytochrome is coupled to the transient deprotonation of the tetrapyrrole chromophore", *J. Biol. Chem.* **280**, 34358-34364 (2005).
298. A. Krumholz, D. M. Shcherbakova, J. Xia, L. V. Wang and V. V. Verkhusha, "Multicontrast photoacoustic in vivo imaging using near-infrared fluorescent proteins", *Sci. Rep.* **4**, 3939 (2014).

299. W. L. Rice, D. M. Shcherbakova, V. V. Verkhusha and A. T. Kumar, "In Vivo Tomographic Imaging of Deep-Seated Cancer Using Fluorescence Lifetime Contrast", *Cancer Res.* **75**, 1236-1243 (2015).
300. D. Bellini and M. Z. Papiz, "Structure of a bacteriophytochrome and light-stimulated protomer swapping with a gene repressor", *Structure* **20**, 1436-1446 (2012).
301. D. Bellini and M. Z. Papiz, "Dimerization properties of the RpBphP2 chromophore-binding domain crystallized by homologue-directed mutagenesis", *Acta Crystallogr. D Biol. Crystallogr.* **68**, 1058-1066 (2012).
302. X. Yang, E. A. Stojkovic, J. Kuk and K. Moffat, "Crystal structure of the chromophore binding domain of an unusual bacteriophytochrome, RpBphP3, reveals residues that modulate photoconversion", *Proc. Natl. Acad. Sci. U. S. A.* **104**, 12571-12576 (2007).
303. O.V. Stepanenko, M. Baloban, G.S. Bublikov, D.M. Shcherbakova, O.V. Stepanenko, K.T. Turoverov, I.M. Kutznetsova and V.V. Verkhusha, "Allosteric effects of chromophore interaction with dimeric nearinfrared fluorescent proteins engineered from bacterial phytochromes", *Sci. Rep.* **6**, 18750 (2016).
304. J. Zhu, D. M. Shcherbakova, Y. Hontani, V. V. Verkhusha and J. T. Kennis, "Ultrafast excited-state dynamics and fluorescence deactivation of near-infrared fluorescent proteins engineered from bacteriophytochromes", *Sci. Rep.* **5**, 12840 (2015).
305. A. Marin, A. B. Doust, G. D. Scholes, K. E. Wilk, P. M. Curmi, I. H. van Stokkum and R. van Grondelle, "Flow of excitation energy in the cryptophyte light-harvesting antenna phycocyanin 645", *Biophys. J.* **101**, 1004-1013 (2011).
306. J. B. Nieder, E. A. Stojkovic, K. Moffat, K. T. Forest, T. Lamparter, R. Bittl and J. T. Kennis, "Pigment-protein interactions in phytochromes probed by fluorescence line narrowing spectroscopy", *J. Phys. Chem. B* **117**, 14940-14950 (2013).
307. L. O. Essen, J. Mailliet and J. Hughes, "The structure of a complete phytochrome sensory module in the Pr ground state", *Proc. Natl. Acad. Sci. U. S. A.* **105**, 14709-14714 (2008).
308. E. Sethe Burgie, Adam N. Bussell, Joseph M. Walker, Katarzyna Dubiel and Richard D. Vierstra, "Crystal structure of the photosensing module from a red/far-red light-absorbing plant phytochrome", *Proc. Natl. Acad. Sci. U. S. A.* **111**, 10179-10184 (2014).
309. K. Tang, W. L. Ding, A. Hoppner, C. Zhao, L. Zhang, Y. Hontani, J. T. Kennis, W. Gartner, H. Scheer, M. Zhou and K. H. Zhao, "The terminal phycobilisome emitter, LCM: A light-harvesting pigment with a phytochrome chromophore", *Proc. Natl. Acad. Sci. U. S. A.* **112**, 15880-15885 (2015).
310. S. Bhattacharya, M. E. Auldridge, H. Lehtivuori, J. A. Ihalainen and K. T. Forest, "Origins of fluorescence in evolved bacteriophytochromes", *J. Biol. Chem.* **289**, 32144-32152 (2014).
311. A. R. Holzwarth, E. Bittersmann, W. Reuter and W. Wehrmeyer, "Studies on chromophore coupling in isolated phycobiliproteins: III. Picosecond excited state kinetics and time-resolved fluorescence spectra of different allophycocyanins from Mastigocladus laminosus", *Biophys. J.* **57**, 133-145 (1990).
312. L. M. Ying and X. S. Xie, "Fluorescence spectroscopy, exciton dynamics, and photochemistry of single allophycocyanin trimers", *J. Phys. Chem. B* **102**, 10399-10409 (1998).
313. A. Marx and N. Adir, "Allophycocyanin and phycocyanin crystal structures reveal facets of phycobilisome assembly", *Biochim. Biophys. Acta* **1827**, 311-318 (2013).
314. I. N. Stadnichuk, M. F. Yanyushin, G. Bernat, D. V. Zlenko, P. M. Krasilnikov, E. P. Lukashev, E. G. Maksimov and V. Z. Paschenko, "Fluorescence quenching of the phycobilisome terminal emitter LCM from the cyanobacterium Synechocystis sp. PCC 6803 detected in vivo and in vitro", *J. Photochem. Photobiol. B* **125**, 137-145 (2013).
315. P. W. Kim, N. C. Rockwell, S. S. Martin, J. C. Lagarias and D. S. Larsen, "Dynamic inhomogeneity in the Photodynamics of Cyanobacterial Phytochrome Cph1", *Biochemistry* **53**, 2818-2826 (2014).
316. P. Altoe, T. Climent, G. C. De Fusco, M. Stenta, A. Bottoni, L. Serrano-Andres, M. Merchan, G. Orlandi and M. Garavelli, "Deciphering intrinsic deactivation/isomerization routes in a phytochrome chromophore model", *J. Phys. Chem. B* **113**, 15067-15073 (2009).

317. F. Velazquez Escobar, T. Hildebrandt, T. Utesch, F. J. Schmitt, I. Seuffert, N. Michael, C. Schulz, M. A. Mroginski, T. Friedrich and P. Hildebrandt, "Structural parameters controlling the fluorescence properties of phytochromes", *Biochemistry* **53**, 20-29 (2014).
318. B. Zienicke, L. Y. Chen, H. Khawn, M. A. Hammam, H. Kinoshita, J. Reichert, A. S. Ulrich, K. Inomata and T. Lamparter, "Fluorescence of phytochrome adducts with synthetic locked chromophores", *J. Biol. Chem.* **286**, 1103-1113 (2011).
319. T. Mathes, I. H. van Stokkum and J. T. Kennis, "Photoactivation mechanisms of flavin-binding photoreceptors revealed through ultrafast spectroscopy and global analysis methods", *Methods Mol. Biol.* **1146**, 401-442 (2014).
320. S. Masuda, K. Hasegawa, H. Ohta and T. A. Ono, "Crucial role in light signal transduction for the conserved Met93 of the BLUF protein PixD/Slr1694", *Plant Cell Physiol.* **49**, 1600-1606 (2008).
321. K. Sadeghian, M. Bocola and M. Schutz, "A conclusive mechanism of the photoinduced reaction cascade in blue light using flavin photoreceptors", *J. Am. Chem. Soc.* **130**, 12501-12513 (2008).
322. A. L. Stelling, K. L. Ronayne, J. Nappa, P. J. Tonge and S. R. Meech, "Ultrafast structural dynamics in BLUF domains: transient infrared spectroscopy of AppA and its mutants", *J. Am. Chem. Soc.* **129**, 15556-15564 (2007).
323. A. Weigel, A. Dobryakov, B. Klaumunzer, M. Sajadi, P. Saalfrank and N. P. Ernsting, "Femtosecond stimulated Raman spectroscopy of flavin after optical excitation", *J. Phys. Chem. B* **115**, 3656-3680 (2011).
324. C. R. Hall, I. A. Heisler, G. A. Jones, J. E. Frost, A. A. Gil, P. J. Tonge and S. R. Meech, "Femtosecond stimulated Raman study of the photoactive flavoprotein AppA(BLUF)", *Chem. Phys. Lett.* **683**, 365-369 (2017).
325. D. H. Murgida, E. Schleicher, A. Bacher, G. Richter and P. Hildebrandt, "Resonance Raman spectroscopic study of the neutral flavin radical complex of DNA photolyase from Escherichia coli", *J. Raman Spectrosc.* **32**, 551-556 (2001).
326. A. Jung, T. Domratcheva, M. Tarutina, Q. Wu, W. H. Ko, R. L. Shoeman, M. Gomelsky, K. H. Gardner and L. Schlichting, "Structure of a bacterial BLUF photoreceptor: Insights into blue light-mediated signal transduction", *Proc. Natl. Acad. Sci. U. S. A.* **102**, 12350-12355 (2005).
327. M. G. Khrenova, A. V. Nemukhin, B. L. Grigorenko, A. I. Krylov and T. M. Domratcheva, "Quantum Chemistry Calculations Provide Support to the Mechanism of the Light-Induced Structural Changes in the Flavin-Binding Photoreceptor Proteins", *J. Chem. Theory Comput.* **6**, 2293-2302 (2010).
328. A. A Granovsky, "Firefly version 8.", (2015).
329. M. W. Schmidt, K. K. Baldridge, J. A. Boatz, S. T. Elbert, M. S. Gordon, J. H. Jensen, S. Koseki, N. Matsunaga, K. A. Nguyen, S. J. Su, T. L. Windus, M. Dupuis and J. A. Montgomery, "General Atomic and Molecular Electronic-Structure System", *J. Comput. Chem.* **14**, 1347-1363 (1993).
330. A. V. Ruban, M. P. Johnson and C. D. P. Duffy, "Natural light harvesting: principles and environmental trends", *Energ. Environ. Sci.* **4**, 1643-1650 (2011).
331. B. van Oort, L. M. Roy, P. Xu, Y. Lu, D. Karcher, R. Bock and R. Croce, "Revisiting the Role of Xanthophylls in Nonphotochemical Quenching", *J. Phys. Chem. Lett.* **9**, 346-352 (2018).
332. J. Komenda and R. Sobotka, "Cyanobacterial high-light-inducible proteins--Protectors of chlorophyll-protein synthesis and assembly", *Biochim. Biophys. Acta* **1857**, 288-295 (2016).
333. M. J. Llansola-Portoles, R. Sobotka, E. Kish, M. K. Shukla, A. A. Pascal, T. Polivka and B. Robert, "Twisting a beta-Carotene, an Adaptive Trick from Nature for Dissipating Energy during Photoprotection", *J. Biol. Chem.* **292**, 1396-1403 (2017).
334. V. Balevicius, Jr., K. F. Fox, W. P. Bricker, S. Jurinovich, I. G. Prandi, B. Mennucci and C. D. P. Duffy, "Fine control of chlorophyll-carotenoid interactions defines the functionality of light-harvesting proteins in plants", *Sci. Rep.* **7**, 13956 (2017).

335. A. M. Nuijs, V. A. Shuvalov, H. J. Vangorkom, J. J. Plijter and L. N. M. Duysens, "Picosecond Absorbency Difference Spectroscopy on the Primary Reactions and the Antenna-Excited States in Photosystem-I Particles", *Biochim. Biophys. Acta* **850**, 310-318 (1986).
336. D. Zigmantas, R. G. Hiller, V. Sundstrom and T. Polivka, "Carotenoid to chlorophyll energy transfer in the peridinin-chlorophyll-a-protein complex involves an intramolecular charge transfer state", *Proc. Natl. Acad. Sci. U. S. A.* **99**, 16760-16765 (2002).
337. M. Kloz, R. van Grondelle and J. T. M. Kennis, "Correction for the time dependent inner filter effect caused by transient absorption in femtosecond stimulated Raman experiment", *Chem. Phys. Lett.* **544**, 94-101 (2012).
338. M. M. Mendes-Pinto, E. Sansiaume, H. Hashimoto, A. A. Pascal, A. Gall and B. Robert, "Electronic absorption and ground state structure of carotenoid molecules", *J. Phys. Chem. B* **117**, 11015-11021 (2013).
339. A. Pandit, M. Reus, T. Morosinotto, R. Bassi, A. R. Holzwarth and H. J. de Groot, "An NMR comparison of the light-harvesting complex II (LHCII) in active and photoprotective states reveals subtle changes in the chlorophyll a ground-state electronic structures", *Biochim. Biophys. Acta* **1827**, 738-744 (2013).

Summary

Photoreceptor proteins are essential in living organisms (*e.g.* for photosynthesis and vision), and also important for life science applications such as fluorescence imaging and optogenetics. Clarification of the photoreaction dynamics of photoreceptor proteins is not only of great interest in physical chemistry and biochemistry, but also highly helpful for designing further functional photoreceptor proteins that will be useful in life sciences and medical applications. In this thesis, which is composed of nine chapters, the photoreaction dynamics of a variety of functional photoreceptor proteins are reported. Throughout the research studies, the photoreaction mechanisms of optogenetic proteins, fluorescent proteins and light-harvesting proteins were elucidated. Moreover, it was shown that time-resolved absorption, emission and stimulated Raman spectroscopies are powerful methods for photoreceptor research.

Chapter 1 is an introductory chapter describing the background and the aims of the researches, and also introducing time-resolved spectroscopic techniques that were used in the researches in this thesis.

In **Chapter 2**, the photoreaction dynamics of light-driven cation channelrhodopsin C1C2 is discussed. Channelrhodopsin currently is the most widely used photoreceptor protein in optogenetics, but its primary photoreaction mechanism had not been clarified despite its importance. Applying pump-probe/pump-dump-probe spectroscopies, target analysis and QM/MM calculation, it was demonstrated that two relaxation pathways from the excited state exist; a reactive pathway (proceeding in 450 fs) and a non-reactive pathway (proceeding in 2 ps and 11 ps). In the reactive pathway, the retinal chromophore undergoes isomerization, triggering the photocycle. In the non-reactive pathway, however, retinal is distorted in the opposite direction of isomerization, and goes back to the initial ground state without isomerization. It is proposed that the existence of the non-reactive pathway makes the isomerization quantum yield of channelrhodopsin (30%) significantly lower than that of a bacteriorhodopsin (60%) that is a model system of microbial rhodopsin studies.

Chapter 3 describes a complete photocycle of recently-found anion channelrhodopsin *Ps*ACR1 from femtoseconds to seconds, utilizing femto- to submillisecond transient absorption spectroscopy and flash photolysis. *Ps*ACR1 has a red-shifted absorption property and a fast channel-closing feature, which will be useful for deep tissue application and achieving higher temporal precision. Among the reactions in the

unique photocycle that was newly clarified, the most significant finding was that the all-*trans* to 13-*cis* isomerization proceeds in 500 fs accompanied with hydrogen-bond switch near the protonated retinal Schiff base.

In **Chapter 4**, the photochemistry of a light-driven Na^+ pump rhodopsin KR2 is investigated by femto- to submillisecond transient stimulated Raman spectroscopy. KR2 is a unique protein that pumps cations upon photon absorption, and of great interest for optogenetics applications. By analyzing the transient Raman data, a new photocycle of KR2 was determined; proceeding in 200 fs, 3 ps, 20 ps, 30 ns and 20 μs. Furthermore, it was proposed that the extracellularly-bound Na^+ is not involved in the photoinduced isomerization, but plays important roles in modulating the photoproduct dynamics from picoseconds to microseconds.

Chapter 5 presents studies of near-infrared driven proton pump rhodopsin equipped with retinal analogue pigments. Strong pH-dependent near-infrared fluorescence properties of the protein were shown, which will be useful in voltage and/or pH sensing. Moreover, by transient absorption spectroscopy and stimulated Raman spectroscopy, the molecular origin of the strong fluorescence was revealed. Interestingly, it was concluded unique boundary structures with additional protonated retinal Schiff base is the key structure of near-infrared absorption/emission and the high pH-dependent fluorescence property.

Chapter 6 describes new findings of molecular dynamics of unprotonated retinal in the HKR1 microbial rhodopsin. Many organisms including mammals have rhodopsins equipped with unprotonated retinal, and the photoreaction dynamics is of great interest while it is poorly understood. HKR1 is a unique microbial rhodopsin having two stable ground states; with protonated and unprotonated retinal. Importantly, HKR1 is advantageous in that high expression levels are achievable which is required for thorough biophysical characterization. The time-resolved spectroscopic experiments demonstrated that photoexcitation occurs to S_2 state, instead of optically-forbidden S_1 state, similar to carotenoids. Furthermore, it was proposed that double isomerization occurs; with S_2–S_1 (*cis*/*trans*, in ~40 fs) and S_1–S_0 (*anti*/*syn*, ~5 ps), which is totally different from photoreactions of protonated retinal. The findings in HKR1 constitute a model system for photophysical and photochemical studies of unprotonated retinal in proteins.

In **Chapter 7**, bright blue-shifted near-infrared fluorescent proteins (NIR FPs) engineered from bacteriophytochromes; specifically iRFP670, iRFP682 and BphP1-FP, are reported. NIR FPs are of great demand in deep-tissue *in vivo* imaging, and understanding the excited-state dynamics is helpful for engineering of brighter and color-tuned near-

infrared fluorescent proteins. With femtosecond transient absorption spectroscopy and picosecond emission spectroscopy, it was shown that a covalent bond between the biliverdin chromophore and the GAF domain is the origin of bright and blue-shifted fluorescence of the NIR FPs.

Chapter 8 shows the excited-state structural dynamics of a blue-light using flavin (BLUF) photoreceptor, which is a key protein in optogenetics applications. The chemical environment and its photodynamics of FAD chromophore and its adjacent amino acid residues are essential for deeper understanding of the activation mechanisms, but have remained controversial to this date. Combining femtosecond simulated Raman spectroscopy and quantum chemical calculations, it was proposed that the amino group of Gln50 that is located near the FAD is oriented towards the C4=O group of the FAD in the dark-adapted state. On the other hand, a tautomerized form of Gln50 applies to the light-adapted state.

In **Chapter 9**, the molecular origin of photoprotection processes in cyanobacteria is proposed. Photoprotection is fundamental in photosynthesis to avoid oxidative photodamage upon excess light exposure. Excited chlorophylls are quenched by carotenoids, but the precise molecular origin remains controversial. The cyanobacterial HliC protein, which is ancestral to plant light-harvesting complexes, binds chlorophylls and carotenoids, and can achieve high expression level that is desired for time-resolved spectroscopic studies. Utilizing femtosecond stimulated Raman spectroscopy, it was clearly revealed that quenching occurs from S_1-state chlorophylls to S_1-state carotenoids upon chlorophyll excitation, which is an essential process of photoprotection. It was demonstrated that only a low-energy form of HliC-bound carotenoids carries out the photoprotection function.

List of publications

- Y. Hontani*, M. Kloz* (equal contribution), T. Polívka, M. K. Shukla, R. Sobotka and J. T. M. Kennis, "Molecular Origin of Photoprotection in Cyanobacteria Probed by Watermarked Femtosecond Stimulated Raman Spectroscopy"
  The Journal of Physical Chemistry Letters 9, 1788 (2018). (**Chapter 9**)
- Y. Hontani, M. Broser, A. Silapetere, B. S. Krause, P. Hegemann and J. T. M. Kennis, "The femtosecond-to-second photochemistry of red-shifted fast-closing anion channelrhodopsin *Ps*ACR1"
  Physical Chemistry Chemical Physics 19, 30402 (2017). (**Chapter 3**)
- B. Siewert, M. Langerman, Y. Hontani, J. T. M. Kennis, V. van Rixel, B. Limburg, M. Siegler, V. Saez-Talens, R. Kieltyka and S. Bonnet, "Turning on the red phosphorescence of a [Ru(tpy)(bpy)(Cl)]Cl complex by amide substitution: self-aggregation, toxicity, and cellular localization of an emissive ruthenium-based amphiphile"
  Chemical Communications 53, 11126 (2017).
- Y. Hontani, M. Marazzi, K. Stehfest, T. Mathes, I. H. M. van Stokkum, M. Elstner, P. Hegemann and J. T. M. Kennis, "Reaction dynamics of the chimeric channelrhodopsin C1C2"
  Scientific Reports 7, 7217 (2017). (**Chapter 2**)
- Y. Hontani, D. M. Shcherbakova, M. Baloban, J. Zhu, V. V. Verkhusha and J. T. M. Kennis, "Bright blue-shifted fluorescent bacterial phytochromes with Cys in GAF domain: fluorescence mechanisms and excited-state dynamics"
  Scientific Reports 6, 37362 (2016). (**Chapter 7**)
- J. Zhu, T. Mathes, Y. Hontani, M. T. A. Alexandre, K. C. Toh, P. Hegemann and J. T. M. Kennis, "Photoadduct formation from the FMN singlet excited state in the LOV2 domain in Chlamydomonas reinhardtii phototropin"
  The Journal of Physical Chemistry Letters 7, 4380 (2016).
  DOI: 10.1021/acs.jpclett.6b02075
- Y. Hontani*, K. Inoue* (equal contribution), M. Kloz, Y. Kato, H. Kandori and J. T. M. Kennis, "The photochemistry of sodium ion pump rhodopsin observed by watermarked femto- to submillisecond stimulated Raman spectroscopy"
  Physical Chemistry Chemical Physics 18, 24729 (2016). (**Chapter 4**)
- K. Tang, W.-L. Ding, A. Höppner, C. Zhao, L. Zhang, Y. Hontani, J. T. M. Kennis, W. Gärtner, H. Scheer, M. Zhou, and K.-H. Zhao, "The terminal phycobilisome emitter, L_{CM}: A light-harvesting pigment with a phytochrome chromophore"
  Proceedings of the National Academy of Sciences of the United States of America 112, 15880 (2015).

- J. Zhu, D. M. Shcherbakova, Y. Hontani, V. V. Verkhusha and J. T. M. Kennis, "Ultrafast excited-state dynamics and fluorescence deactivation of near-infrared fluorescent proteins engineered from bacteriophytochromes" *Scientific Reports* 5, 12840 (2015).
- Y. Hontani, S. Ganapathy, S. Frehan, W. J. de Grip and J. T. M. Kennis. "The electronic structure and dynamics of a near-infrared active microbial rhodopsin analogue disclosing intense pH-dependent fluorescence", *submitted*. (**Chapter 5**)
- Y. Hontani, M. Broser, M. Kloz, M. Luck, J. Weissenborn, P. Hegemann and J. T. M. Kennis, "Double isomerization on distinct potential energy surfaces of unprotonated retinal in UV-absorbing histidine kinase rhodopsin HKR1", *in preparation.* (**Chapter 6**)
- Y. Hontani, T. Domratcheva, M. Kloz, T. Mathes, J. Mehlhorn, P. Hegemann and J. T. M. Kennis, "Excited-state dynamics of the BLUF photoreceptor on the dark-adapted and light-adapted states measured by FSRS", *in preparation*. (**Chapter 8**)

Acknowledgements

I feel strongly that I made a good decision to move to Amsterdam and carry out my PhD research here. I have enjoyed my PhD life not only because of the great research environment and the attractive city, but also because of the people around me.

First, I would like to thank my parents and sisters in Osaka, who are always my best supporters.

I am grateful to Joern and Mirek, who showed me 'Amsterdam life' in my first week here; I won't forget the experience, which I never would have had in Japan. Also I thank my colleagues Simon, Janneke, Niki, Heli, Tilo, JuanMa, Patrick, Enis, Pavel, Bart, and our collaborators Inoue-san, Vidya, Bianka, Kun, Katja and Arita for working together in the Monster lab. Drinking a celebratory beer outside with you after getting positive results was my favorite part of PhD life. All of my colleagues in the Biophysics group at VU and friends in Amsterdam helped me a lot in many ways, and we share many good memories; I greatly appreciate that. I would also like to thank all of our collaborators. I couldn't have achieved any of this without you.

Thank you to Sean Frehan, Swetta Jansen and Raisa Grotenhuis, who I mentored. You all were highly motivated and worked hard. I learned a lot through the mentoring, which was a precious experience for me. I highly appreciate it, and I wish you great success in your careers.

I would like to acknowledge Dr. Nakasone from Kyoto University, Japan, who crosslinked me with Prof. John Kennis five years ago. Also, you always cheered me up as my *senpai* researcher, I appreciate it.

Furthermore, I thank Dr. Hada and Prof. Matsuo in Kyoto University, where I got my bachelor's and master's degrees. There I experienced scientific researches for the first time, and acquired fundamental skills in experiments and scientific thinking. Thanks to your training, I had a good start to my research in Amsterdam.

Even though I worked using only English during my entire PhD study, I feel fortunate that I didn't forget my native Japanese language. This is because I had many awesome Japanese

friends in the Netherlands, especially in the J-Dream Football Club and Siebold-Kai. You are also an important part of my Amsterdam life, and I would like to thank you all.

Last but not least, I deeply appreciate the supervision by Prof. John Kennis. You offered me a great research environment with state-of-the-art laser setups and ensured me complete freedom, with which I could fully enjoy science. Moreover, you were always a good advisor and open for discussion anytime, which was extremely helpful when I had problems with my projects. I was very lucky to have such a great PhD supervisor and working with you.